UNIVERSITÀ DEGLI STUDI DI PADOVA

Dipartimento di Fisica e Astronomia "Galileo Galilei"

Master Degree in Physics

FINAL DISSERTATION

Opacity Effects on the Evolution of Massive Stars

Thesis supervisor

Prof. Paola Marigo

Candidate

Annachiara Picco

Academic Year 2020/2021

UNIVERSITY OF PADOVA

Abstract

Faculty of Physics

Department of Physics and Astronomy

Master of Science in Physics

Opacity Effects on the Evolution of Massive Stars

by Annachiara Picco

An in-depth analysis of the stellar matter resistance to energy transport, the ***opacity***, in the context of massive stars with high Zero Age Main Sequence (ZAMS) mass is performed. The opacity of astrophysical plasmas stands up as key in Stellar Evolution Codes (SECs) input physics, as it is know to dramatically affect model predictions of structural as well as evolutionary properties of stellar objects; by virtue of this paramount role, stellar plasma's opaqueness is examined both as a stand-alone micro-physical process *and* as the possible origin of consistent evolutionary effects.

The implementation, in the PAdova TRieste Evolutionary Code (PARSEC), of a refined subroutine for relativistic electron scattering, with arbitrary degree of degeneracy, is followed by a thorough discussion of its consequent evolutionary impacts, within a varied stellar models grid. Furthermore, the author argues about the importance of thermal conductivity in the most advanced evolutionary stages, thus proceeding with its inclusion in the code at the highest temperature range. Lastly, the work tests a new prescription, for atomic and molecular transitions, still in preparation at the Padova group; model tracks of selected ZAMS from the grid are comprehensively described, offering great insights on the cooler temperatures' opacity effects on massive stars evolution.

Contents

List of Figures

Physical Constants

Symbol	Quantity	Value	CGS unit
c	Speed of Light	$2.997\,924\,58 \times 10^{10}$	$\mathrm{cm\,s^{-1}}$
e	Electron charge	$4.803\,26 \times 10^{-10}$	esu
e^2		$1.440\,00 \times 10^{-7}$	$\mathrm{eV\,cm}$
m_u	Atomic mass unit	$1.660\,538\,8 \times 10^{-24}$	g
m_n	Neutron rest mass	$1.674\,927\,2 \times 10^{-24}$	g
m_p	Proton rest mass	$1.672\,621\,6 \times 10^{-24}$	g
m_e	Electron rest mass	$9.109\,382 \times 10^{-28}$	g
m_α	α-particle mass	$6.644\,656\,2 \times 10^{-24}$	g
h	Planck's constant	$6.626\,069 \times 10^{-27}$	$\mathrm{erg\,s}$
$\hbar$	Dirac's constant $\left(\frac{h}{2\pi}\right)$	$1.054\,572\,66 \times 10^{-27}$	$\mathrm{erg\,s}$
a	Radiation constant	$7.565\,78 \times 10^{-15}$	$\mathrm{erg\,cm^{-3}\,K^{-4}}$
σ	Stefan-Boltzmann constant $\left(\frac{1}{4}ac\right)$	$5.670\,40 \times 10^{-5}$	$\mathrm{erg\,cm^{-2}\,s^{-1}\,K^{-4}}$
k	Boltzmann's constant	$1.380\,650 \times 10^{-16}$	$\mathrm{erg\,K^{-1}}$
G	Gravitational constant	6.6743×10^{-8}	$\mathrm{cm^3\,g^{-1}\,s^{-2}}$
N_A	Avogadro constant $\left(\frac{1}{m_u}\right)$	$6.022\,142 \times 10^{23}$	$\mathrm{g^{-1}}$
$\mathcal{R}$	Gas constant $\left(\frac{k}{m_u}\right)$	$8.314\,47 \times 10^{7}$	$\mathrm{erg\,g^{-1}\,K^{-1}}$
a_0	Bohr radius	5.292×10^{-9}	cm
R_∞	Rydberg constant	$2.179\,874\,1 \times 10^{-11}$	erg
λ_c	Compton wavelength $\left(\frac{h}{m_e c}\right)$	2.42×10^{-10}	cm
σ_Th	Thomson cross section	6.652×10^{-25}	$\mathrm{cm^2}$
$\mathrm{M}_\odot$	Solar Mass	1.9884×10^{33}	g
	$G\mathrm{M}_\odot$	$1.327\,124\,42 \times 10^{26}$	$\mathrm{cm^3\,s^{-2}}$
$R_\odot$	Solar radius	6.957×10^{10}	cm
$L_\odot$	Solar luminosity	3.842×10^{33}	$\mathrm{erg\,s^{-1}}$
$T_\odot$	Solar surface temperature	5.780×10^{3}	K
1 ly	Light year	9.461×10^{17}	cm
1 AU	Astronomical Unit	$1.495\,978\,71 \times 10^{13}$	cm
1 pc	Parsec	$3.085\,678 \times 10^{18}$	cm
1 yr	Year	$3.155\,76 \times 10^{7}$	s

Table 1: Physical constants in CGS units (mostly from CODATA 2006, Astronomical Almanac 2008).

List of Symbols

Symbol	Description	First Appearance
z	cosmological redshift	Sect.(1.1)
$N\,(\mathrm{M})$	number density of masses M	Sect.(1.1)
$f_{\mathrm{M}}\,(\mathrm{M})$	mass fraction of masses M	Sect.(1.1)
M_i	initial star mass	Sect.(1.1)
M	star mass	Sect.(1.1)
R	total radius	Sect.(4.3.1)
$\mathrm{L},\ \mathrm{L}_{\mathrm{Edd}}$	surface, Eddington luminosity	Sect.(1.1)
Γ_{Edd}	Eddington parameter	Sect.(1.3.3)
κ_{surf}	surface opacity	Sect.(1.1)
κ	local (Rosseland mean) opacity	Sect.(1.2.2)
$\kappa_{\mathrm{rad}},\ \kappa_{\mathrm{cd}}$	radiative, conductive opacity	Sect.(2.1)
$\kappa_{\nu},\ \kappa_{\nu,\mathrm{i}}$	monochromatic opacity, process i	Sect.(2.1)
κ_e	electron scattering opacity	Sect.(2.1)
κ_{H^-}	negative hydrogen H^- opacity	Sect.(2.1.1)
κ_{P83}	**P83** Rosseland mean opacity	Sect.(2.1)
κ_{P17}	**P17** Rosseland mean opacity	Sect.(3.2.3)
κ_{Th}	free electrons Thomson scattering opacity	Sect.(2.1.1)
$\kappa^{\mathrm{abs}}(\nu),\ \kappa^{\mathrm{scatt}}(\nu)$	absorption, scattering opacity at ν	Sect.(2.1.2)
σ	total cross section	Sect.(2.1.1)
$\langle\sigma v\rangle$	thermally weighted cross section	Sect.(1.2.2)
$\sigma_{\nu,\mathrm{i}}$	monochromatic cross section for process i	Sect.(2.1.1)
σ_e	electron scattering cross section	Sect.(2.2)
σ_{coll}	collisional cross section	Sect.(2.2)
$\sigma^{\mathrm{abs}}(\nu),\ \sigma^{\mathrm{scatt}}(\nu)$	absorption, scattering cross section at ν	Sect.(2.1.2)
r	lagrangian radial coordinate	Sect.(1.2.1)
$r_{\mathrm{p}},\ r_{\mathrm{eq}}$	pole, equator coordinate	Sect.(1.3.4)
m	lagrangian mass coordinate	Sect.(1.2.1)
m_{ph}	photospheric lagrangian mass coordinate	Sect.(1.2.3)
ρ	local density	Sect.(1.2.1)
ρ_α	density in units of 10^α	Sect.(2.2)
ρ_{c}	core density	Sect.(1.3.1)
$n_{\mathrm{ion}},\ n_e$	total ions, electrons number density	Sect.(1.2.1)
n_i	ion i number density	Sect.(1.2.1)
P	local pressure	Sect.(1.2.1)

Symbol	Description	First Appearance
$P_i,\ P_e,\ P_{\rm rad}$	ions, electrons, radiation pressure	Sect.(1.2.1)
t	lagrangian time coordinate	Sect.(1.2.1)
$\rm T$	temperature	Sect.(1.2.1)
$\rm T_\alpha$	temperature in units of 10^α	Sect.(2.2)
U	energy density	Sect.(3.2.1)
$\rm T_{eff},\ T_c$	effective, core temperature	Sect.(1.3.1)
s	specific entropy	Sect.(1.2.1)
u	specific internal energy	Sect.(1.2.2)
l	local luminosity	Sect.(1.2.1)
ϵ	energy production rate	Sect.(1.2.1)
∇	temperature gradient	Sect.(1.2.1)
$\nabla_{\rm ad},\ \nabla_{\rm rad}$	adiabatic, radiative temperature gradient	Sect.(1.2.1)
∇_μ	chemical composition gradient	Sect.(1.3.2)
$\Delta\nabla$	super adiabaticity	Sect.(1.2.1)
$\rm X_i$	abundance in mass fraction of element i	Sect.(1.2.1)
$\rm X,\ Y,\ Z$	Hydrogen Helium, metals abundance	Sect.(1.2.2)
$\rm A_i,\ Z_i$	atomic weight, number of element i	Sect.(1.2.1)
$\rm \tilde{H}$	hydrogenic atom	Sect.(2.1.1)
r_{ij}	reaction rate of specie i with j	Sect.(1.2.1)
Q_{ij}	reaction of specie i with j Q-value	Sect.(1.2.2)
δ_{ij}	Kronecker's delta	Sect.(1.2.1)
μ	mean molecular weight	Sect.(1.2.2)
$\mu_{\rm ion},\ \mu_e$	total ions, electrons molecular weight	Sect.(1.2.2)
μ_i	ion i molecular weight	Sect.(1.2.1)
$\tau_{\rm ph}$	photosphere's optical depth	Sect.(1.2.3)
$r_{\rm ph}$	photospheric radius	Sect.(1.2.3)
e^+/e^-	positron/electron	Sect.(1.2.2)
γ	photon	Sect.(2.1.1)
N	a nucleus (fundamental processes)	Sect.(2.1.1)
M	a molecule (fundamental processes)	Sect.(2.1.2)
$E_{\rm nuc},\ E_{\rm KH}$	gravitational, nuclear energy	Sect.(1.3.1)
ΔE	energy difference	Sect.(2.1.1)
$\tau_{\rm grav},\ \tau_{\rm nuc},\ \tau_{\rm dyn}$	nuclear, Kelvin-Helmholtz, dynamical timescale	Sect.(1.3.1)
$\tau_{\rm mix}$	mixing timescale	Sect.(1.3.2)
$\tau_{\rm rot-mix}$	rotational mixing timescale	Sect.(1.3.4)
$\tau_{\rm MS},\ \tau_{\rm He}$	MS, He MS timescales	Sect.(1.3.1)
$\tau_{\rm H-shell},\ \tau_{\rm He-shell}$	shell H, He-burning timescales	Sect.(1.3.1)
$\rm T_{X_i}$	ignition temperature of $\rm X_i$	Sect.(1.3.1)
$\rm L_{nuc}\ ,L_{grav}$	nuclear, gravitational integrated luminosity	Sect.(1.3.1)
$\rm L_\gamma\ ,L_\nu$	photons, neutrinos integrated luminosity	Sect.(1.3.1)
$v_{\rm rot}/v_{\rm crit}$	fraction of critical surface rotation	Sect.(1.3.1)
$\bar{v}$	average thermal velocity	Sect.(2.1.1)

Symbol	Description	First Appearance
$v_{\rm rel}$	Møller's velocity	Sect.(3.1)
d	typical system dimension	Sect.(2.1.1)
$\theta,\ \phi$	polar, azimuthal angles	Sect.(1.3.3)
$v_{\rm r}$	rotation at $r(\theta,\phi)$	Sect.(1.3.4)
$\Omega_{\rm r}$	angular velocity at $r(\theta,\phi)$	Sect.(1.3.4)
Γ_1	first adiabatic index	Sect.(1.3.1)
$\langle\Gamma_1\rangle_{\rm tot}$	average first adiabatic index	Sect.(4.3.4)
$l, \alpha_{\rm MLT}$	mixing length, MLT parameter	Sect.(1.3.2)
H_P	pressure scale height	Sect.(1.3.2)
D	total diffusion coefficient	Sect.(1.3.4)
$\mathrm{D}_{\rm mix}$	convective mixing diffusion coefficient	Sect.(1.3.2)
$\mathrm{D}_{\rm shear}$	meridional circulation diffusion coefficient	Sect.(1.3.4)
$\mathrm{D}_{\rm med}$	shear instability diffusion coefficient	Sect.(1.3.4)
$v_{\rm conv}$	convective eddy velocity	Sect.(1.3.2)
$\chi_\mu,\ \chi_{\rm T}$	thermodynamic exponents	Sect.(1.3.2)
$\mathrm{d}_{\rm ov},\ \alpha_{\rm ov}$	overshooting length, parameter	Sect.(1.3.2)
$\tau_{\rm last}$	time of the last computed model	Sect.(1.3.2)
$\mathrm{M}_{\rm CO},\ \mathrm{M}_{\rm He}$	CO, Helium core	Sect.(1.3.2)
$\mathrm{M}_{\rm Schw}$	Schwarzschild unstable core	Sect.(1.3.2)
$\mathrm{M}_{\rm Schw}^{\rm core-Ov}$	Schwarzschild with OV unstable core	Sect.(1.3.2)
$\mathrm{M}_{\rm Conv}$	convective region mass	Sect.(1.3.2)
$\mathrm{M}_{\rm bce}$	bottom of the convective envelope mass	Sect.(1.3.2)
$\dot{\mathrm{M}}$	mass loss rate	Sect.(1.3.3)
$g_{\rm eff},\ g_{\rm rad},\ g$	effective, radiation, surface gravity	Sect.(1.3.4)
$J,\ \Delta J$	total, transferred angular momentum	Sect.(1.3.4)
λ	photon wavelength	Sect.(2.1.1)
ν	photon frequency	Sect.(2.1)
$\Delta\nu$	linewidth	Sect.(2.1.2)
ν_0	system characteristic oscillation	Sect.(2.1.1)
$l_\nu,\ l_x$	photon mean free path at ν, x	Sect.(2.1)
Λ	Rosseland mean free path	Sect.(2.1)
$\Lambda_{\rm P83}$	**P83** Rosseland mean free path	Sect.(2.1.1)
$\Lambda_{\rm P17}$	**P17** Rosseland mean free path	Sect.(3.2.3)
$\tilde{l}_\nu,\ \tilde{l}_x$	adimensional photon mean free path at ν, x	Sect.(2.1)
B_ν	Planckian of radiation at ν	Sect.(2.1)
b_ν	phase-space distribution of radiation at ν	Sect.(2.1)
$g_{\rm ff}(\nu)$	free-free Gaunt factor at ν	Sect.(2.1.1)
$g_{\rm bf}(\nu)$	bound-free Gaunt factor at ν	Sect.(2.1.1)
η	degeneracy parameter	Sect.(2.1.1)
$\eta_\pm$	degeneracy parameter of $e^\pm$	Sect.(3.2.1)
d	typical system dimension	Sect.(2.1.1)
$n,\ m$	Kramer's coefficients	Sect.(2.1.1)

Symbol	Description	First Appearance
$\chi_{\rm ion}$	ionization energy of ion	Sect.(2.1.1)
$\chi_{\rm H}$	ionization energy of H	Sect.(3.2.1)
$\Gamma_i,\ \Gamma$	Coulomb coupling parameter of ion i, total	Sect.(2.2)
a_e	electron-sphere radius	Sect.(2.2)
f	oscillator strength	Sect.(2.1.2)
g_m	statistical weight of level m	Sect.(2.1.2)
Q	partition function	Sect.(2.1.2)
$\mathrm{R_C}$	ratio of C to C-O mass fractions	Sect.(2.3)
R	density proxy in SECs	Sect.(2.3)
$k^\mu,\ \tilde{p}^\mu$	photon, electron dimensionful 4-momenta	Sect.(3.1)
$x^\mu,\ p^\mu$	photon, electron adimensional 4-momenta	Sect.(3.1)
$E_e,\ E_{k,e}$	electron relativistic total, kinetic energy	Sect.(3.1)
$\hat{\omega},\ \hat{\Omega}$	photon, electron direction	Sect.(3.1)
$\beta,\ \gamma_e$	usual relativity parameters for $e^\pm$	Sect.(3.1)
$s,\ t,\ u$	Mandelstam variables	Sect.(3.1)
$x^\mu_{\rm wl}(\lambda)$	photon worldline with affine parameter λ	Sect.(3.1)
S	scattering matrix	Sect.(3.1)
S_{fi}	scattering matrix element from state f to i	Sect.(3.1)
$A^\dagger_s,\ A_s$	creation, destruction operator with spin s	Sect.(3.1)
$\otimes$	Fock space product	Sect.(3.1)
$\delta^{(n)}(x-y)$	Dirac delta in nD	Sect.(3.1)
V	volume element	Sect.(3.1)
$\mathcal{M}_{fi}$	Feynman amplitude	Sect.(3.1)
$\lvert\tilde{\mathcal{M}}_{fi}\rvert^2$	unpolarized squared Feynman amplitude	Sect.(3.1)
$\mathcal{M}^*_{fi}$	conjugate Feynman amplitude	Sect.(3.1)
F	Klein-Nishina reaction rate	Sect.(3.1)
w	transition rate	Sect.(3.1)
dP/dt	transition probability	Sect.(3.1)
$[A]_{\rm n.u.}$	natural units of quantity A	Sect.(3.1)
$d\sigma$	differential cross section	Sect.(3.1)
Φ	incident flux	Sect.(3.1)
$d\Pi$	phase-space factor	Sect.(3.1)
Θ	adimensional temperature	Sect.(3.2.1)
$\mu_\pm$	chemical potentials for $e^\pm$	Sect.(3.2.1)
$\tilde{n}(\boldsymbol{p}), n(\boldsymbol{x})$	electron, photon distributions	Sect.(3.2.1)
$N_\pm$	number densities for $e^\pm$, individually	Sect.(3.2.1)
$N_e,\ N_{e,\rm matter}$	number densities for $e^\pm$ combined, only e^-	Sect.(3.2.1)
$\hat{\mathbb{L}},\ \hat{\mathbb{C}}$	Liouville's, Collision operator	Sect.(3.2.1)
$\vec{\nabla}_\tau$	dimensionless gradient	Sect.(3.2.1)
$R_\pm$	Compton's scattering redistribution functions	Sect.(3.2.1)
R_n	redistribution functions n-th moment	Sect.(3.2.1)
b	dimensionless relativistic parameter	Sect.(3.3.3)

Symbol	Description	First Appearance
r_s	electron density parameter	Sect.(3.3.3)
$\xi_{2.5}$	bounce compactness parameter	Sect.(4.3.1)
$\mathrm{C/N}$	atmospheric C/N ratio	Sect.(4.3.1)
$\mathrm{C/O}$	atmospheric C/O ratio	Sect.(4.3.1)
Q	relative mass coordinate	Sect.(4.3.1)

Table 1: List of symbols used in the work, also with first appearance in the text. All quantities in CGS units, unless specified otherwise. Also, when unspecified, the evolutionary quantities are referring to a chosen time step. Due to the quite extended arguments and matter literature, some symbols, e.g. μ, might assume a different role in different Chapters: μ is both the molecular weight in Chp.(1) and Chp.(2), while indicates the chemical potential in Chp.(4). The meaning is *always* made explicit in text, in these cases.

List of Abbreviations

Symbol	Meaning	First Appearance
ISM	Interstellar Medium	Sect.(1.1)
SN	Supernova	Sect.(1.1)
UV	Ultraviolet	Sect.(1.1)
BH	Black Holes	Sect.(1.1)
AGN	Active Galactic Nucleus	Sect.(1.1)
CR	Cosmic Ray	Sect.(1.1)
GW	Gravitational Wave	Sect.(1.1)
GRB	Gamma Ray Burst	Sect.(1.1)
LBV	Luminous Blue Variable	Sect.(1.1)
VMS	Very Massive Stars	Sect.(1.1)
IMF	Initial Mass Function	Sect.(1.1)
HE	Hydrostatic Equilibrium	Sect.(1.2)
LTE	Local Thermodynamic Equilibrium	Sect.(1.2.1)
MLT	Mixing Lenght Theory	Sect.(1.2.1)
EoS	Equation of State	Sect.(1.2.2)
CNO	Carbon-Nitrogen-Oxygen	Sect.(1.2.2)
SE(C)	Stellar Evolution (Code)	Sect.(1.2.2)
HR	Hertzsprung-Russel	Sect.(1.3)
MW	Milky Way	Sect.(1.3.1)
LMC	Large Magellanic Cloud	Sect.(1.3.1)
BSG, RSG	Blue, Red SuperGiant	Sect.(1.3.1)
WR	Wolf Rayet	Sect.(1.3.1)
PPI	Pair Production Instability	Sect.(1.3.1)
ZAMS	Zero Age Main Sequence	Sect.(1.3.2)
CMD	Color-Magnitude Diagram	Sect.(1.3.2)
DLEB	Double-Lined Eclipsing Variable	Sect.(1.3.2)
MS	Main Sequence	Sect.(1.3.2)
MR	Mass Ratio	Sect.(1.3.2)
BCE	Bottom of the Convective Envelope	Sect.(1.3.2)
CAK	Castor-Abbot-Klein	Sect.(1.3.3)
PARSEC	PAdova-tRieSte Evolutionary Code, [Bre+12]	Sect.(1.4)
NR, UR	Non, Utra Relativistic	Sect.(2.1.1)
CIA	Collision Induced Absorption	Sec.(2.1.2)
OP	Opacity Project, [Sea+94]	Sec.(2.1.2)

Symbol	Meaning	First Appearance
ÆSOPUS	Accurate Equation of State and OPacity Utility Software, [MA09]	Sec.(2.1.2)
OPAL	Opacity Project At Livermore, [IR96]	Sec.(4.1)
P83	Paczyński prescription [Pac83]	Sec.(3.2.2)
P17	Poutanen prescription [Pou17]	Sec.(3.2.3)
QFT	Quantum Field Theory	Sect.(3.1)
IP	Interaction Picture	Sect.(3.1)
GR, SR	General, Special Relativity	Sect.(3.1)
QED	Quantum Electrodynamics	Sect.(3.1.1)
FD, BE	Fermi-Dirac, Bose-Einstein	Sec.(3.2.1)
RF	Redistribution Function	Sec.(3.2.1)
B(T)E	Boltzmann (Transport) Equation	Sec.(3.2.1)
NS	Neutron Stars	Sec.(3.2.3)
OCP	One Component Plasma	Sec.(3.3.3)
EOv	Envelope Overshooting	Sec.(1.3)
1DU	First Dredge Up	Sec.(4.3)
CI	Configuration Interaction	Sec.(4.2)
AGB	Asymptotic Giant Branch	Sec.(4.3.1)
MK	Morgan-Keenan	Sec.(4.3.1)
2DU	Second Dredge Up	Sec.(4.3.4)
PISN	Pair Instability SuperNova	Sec.(4.3.4)
PPISN	Pulsation Pair Instability SuperNova	Sec.(4.3.4)

Table 1: List of abbreviations used in the work, also with first appearance in the text.

Synopsis

ἦμος δ᾽ ἠριγένεια φάνη ῥοδοδάκτυλος Ἠώς,
δὴ τότ᾽ ἐγὼν ἑτάρους προΐειν ἐς δώματα Κίρκης[1]
– **Ὅμηρος**

Massive stars, namely those who share Zero Age Main Sequence (ZAMS) masses M>9 $M_{\odot}$, are known to play a crucial role in the evolution of our Universe, and the need to understand the details of their structure and evolution stands out in a variety of branches of astrophysics. Feedback mechanisms enrich the inter-stellar medium (ISM) with kinetic energy and heavy isotopes; high luminosities from remote red-shifts shed light on Universe cosmological features; powerful electromagnetic signals from supernovae (SNs) often travel along with other cosmic messengers.

Structural properties of stars are expected to affect all their evolutive stages and, amongst them, ***opacity*** is of special interest: literature has known many examples of consistently different model evolutionary tracks yielded by varying the input physics of media opaqueness to radiation [BKD10]; opacities have also been postulated as the actual source of discrepancies between observations of pulsating β-Cepheids and their modeling [DDW09]; furthermore, models of the Sun's seismic activity are known to depend critically on the input opacities [Ser+09].
What has been the major approach to modeling is the usage of extensive opacity tables (the most relevant efforts being the OPAL project [IR96] and ÆSOPUS tool [MA09]) and multidimensional interpolations, with several updates during the last decades to include the most precise microphysics: this comprises, but is not limited to, the Klein-Nishina corrections to the electron scattering at high temperatures [BY76], atomic bound-bound absorptions with fine structure precision [IR96] and molecular band transitions for both surface and atmospheric structure.

In modern routines, however, the present treatment of opacity suffers from some important limitations: if a valuable effort has been made to correctly describe the variations of the opacity on the cool atmospheres of Asymptotic Giant Branch (AGB) stars, as a function of the C/O ratio [MA09], on the other hand the situation has not improved as much in the domain of massive stars. In fact, any changes in chemical composition that occur during the red supergiant (RSG) phase, e.g. following convective dredge-up (DU) episodes, or during the Wolf-Rayet (WR) phases due to intense mass loss, are typically absorbed in the opacity

[1] ’Οδύσσεια **XII**, 8-9.

as a global increase in an average initial metallicity Z, without considering the individual variations of the most important metal mass fractions, such as carbon C, nitrogen N and oxygen O.

A substantial revision of opacity treatment in stellar evolutionary codes (SECs) can lead to consistent improvements on the evolutionary description of massive stars, as well as a deeper understanding of observational properties and final outcomes for the advanced evolutive phases. On one hand, the update of the opacities in the most extreme temperatures, $\mathbf{\log T(K) \gtrsim 9}$, offers the possibility to gain insights on microphysics of the deep interior of massive stars: electron and positron Compton scattering [Pou17], or pair production, fundamental ingredient to model the progenitors of Pair Instability Supernovae (PISN), which paves the route for the investigation of Gravity Waves (GWs) sources and the Black Hole (BH) mass gap, [Cos+20]. Having a proper description of the middle to high-temperature opacities, $\mathbf{4 \lesssim \log T(K) \lesssim 9}$, consistently coupled to the changes of the chemical abundances across the stellar structure, may have a notable impact on various stages of massive-stars evolution, including the transition along the WR classes characterized by drastic changes of the surface chemical composition.

On the other hand, the study of the cool counterpart of opacity tables, $\mathbf{\log T(K) \lesssim 4}$, may have striking developments in the field of asteroseismology, with important consequences on opacity-driven radial pulsations of variables [GFF18]; on strong absorption features of metals in the envelopes, leading to convective instability. This can also be at the origin of peculiar surface compositions of massive stars via opacity-driven deep dredge-up episodes during the RSG phases. Depending on their efficiency, these mixing events are also responsible for a dramatic reduction of the core mass, a key parameter that controls the most advanced stages and the final fate of massive and Very Massive stars (VMS).

Outline of the work This work **a)** aligns with the need of a substantial revision of the opacity treatment in the PAdova TRieSte Evolutionary Code (PARSEC) over the entire relevant temperature range, $3 \leq \log T(K) \leq 9.5$, standing up as first step into this thorough effort which will be surely put in full operation in the future; **b)** serves the purpose of the study of evolutionary effects, in the context of massive stars, of some first, but key, updates to the new PARSEC's opacities, gaining insights on future flamboyant possibilities.

CHAPTER **I.**
A review of well established structural Sec.(1.2) and evolutionary Sec.(1.3) properties of massive stars, to be tested with PARSEC within the built stellar models grid Sec.(1.4);

Chapter **II.**
A complete overview of opacity sources, comprising radiation continuum Sec.(2.1.1) and lines Sec.(2.1.2) as well as thermal conduction Sec.(2.2), lays the groundwork for the subsequent chapters. The state of the art of modern SECs, with particular attention to PARSEC Sec.(2.3), is also included;

Chapter **III.**
A new theoretical framework for Compton scattering opacity in the stellar matter, namely Relativistic Kinetic Equation formalism Sec.(3.2.1) is presented, with the new prescription P17 implemented in PARSEC; structural Sec.(3.3.1) and evolutionary Sec.(3.3.2) results from PARSEC's runs are shown Sec.(3.3), and the implementation of COND routine for thermal conductivity is discussed and commented too Sec.(3.3.3);

Chapter **IV.**
The standard opacity look-up tables approach Sec.(4.1) is outlined and the new approach, in preparation at the Padova group for PARSEC, to atomic and molecular transition is expanded Sec.(4.2); selected case-study for metallicity Z=0.0003 are examined in Sec.(4.3), with several tests of the known literature as in Chp.(1), a focus on evolutionary effects of radiation opaqueness and insights onto future prospectives.

1

Massive Stars Features

This chapter introduces the general structural and evolutionary properties of ***massive stars***, namely those that are born with initial masses of more than about $10\ M_{\odot}$. Massive stars are know to play a *crucial role* in the history of our Universe and in varied fields of astrophysical interest, as highlighted in Sec.(1.1). Their *structural properties* share the treatment of less massive objects, with some peculiarities outlined in Sec.(1.2); on the other hand, their *evolutionary properties* are so distinctive to deserve a detailed summary in Sec.(1.3). Lastly, a presentation of the main instrument for this work, the PARSEC *code* and the stellar models' grid under study is due in Sec.(1.4).

This review lays the groundwork for the following chapters, in which we will verify most of the here outlined properties through various runs of the PARSEC code.

1.1 A crucial role

Massive stars are known to play a crucial role in the physical and chemical evolution of our Universe, and the need to understand them stands out in a variety of branches of astrophysics. These include

I. *Evolution of Galaxies*
Massive stars interact with the interstellar medium (ISM) both as energy sources and sources of isotope enrichment prior to the supernova (SN) explosion. For these objects, the so called *stellar feedback*, namely the combined effects of stellar winds, (UV) radiation and SNe, becomes a prominent feature on which models of galaxies chemical evolution heavily rely on; besides, gravitational instabilities from feedback mechanisms influence regions of stellar birth.

II. *Cosmology*
Massive stars are among the main sources of reionization of the Universe and, as ensembles, they can be seen at redshifts $z \gtrsim 5$; as individuals, they become probes for remote regions in which they can be still resolved, thanks to very high luminosities. Being the progenitors of massive remnants such as Black Holes (BHs), they also classify as a possible explanation to Active Galactic Nuclei (AGN), being also responsible for pregalactic chemical enrichment.

III. *Multimessenger Astroparticle Physics*
SNs shells' coronal gas are known to source X-rays, while shock fronts of galactic remnants are the most promising candidates for acceleration sites of the highly energetic charged particles that continuously hit Earth's atmosphere, cosmic rays (CRs), thanks to their prominent magnetic fields. Additionally, neutrinos from massive stars late evolution could unravel future possibilities of synching detections of Gravity Waves (GWs), Gamma Ray Bursts (GRBs) together with the well known electromagnetic counterpart. Finally, massive stars' nucleosynthesis is responsible for the production of long-lived radioactive isotopes contributing to the galactic X-ray background, such as $^{26}\mathrm{Al}$.

Number density and Mass fraction Massive stars typical number density $N(\mathrm{M}_i > 10\,\mathrm{M}_\odot)$ in stellar populations is emiyrically determined to be highly suppressed, as opposed to low- and intermediate-mass stars $N(\mathrm{M}_i < 10\mathrm{M}_\odot)$. We can consider a common simplified version of Initial Mass Function (IMF)

Salpeter's Initial Mass Function

$$\frac{\mathrm{d}N}{\mathrm{d}(\mathrm{M}/\mathrm{M}_\odot)} = N_0 \left(\frac{\mathrm{M}}{\mathrm{M}_\odot}\right)^{-2.35} , \quad \text{with} \quad 0.1\,\mathrm{M}_\odot < \mathrm{M}_i < 120\,\mathrm{M}_\odot ,$$

where N_0 is a normalization constant related to the local stellar density, which reads $N_0 \simeq 0.06$ by imposing the normalizing condition over the indicated validity range. This $N(\mathrm{M}_i)$ distribution leads to the estimates of both $N(\mathrm{M}_i > 10\,\mathrm{M}_\odot)$ and its first moment, i.e. the mass fraction $f_{\mathrm{M}_i}(\mathrm{M}_i > 10\,\mathrm{M}_\odot)$:

$$N(\mathrm{M}_i > 10\,\mathrm{M}_\odot) \simeq 0.20\% , \qquad f_{\mathrm{M}_i}(\mathrm{M}_i > 10\,\mathrm{M}_\odot) \simeq 13\% ,$$

namely only 0.20% of stars are massive, but they contain roughly 13% of all the mass in a given population with a Salpeter IMF.

Very Massive Stars (VMS) The existence of a limiting Eddington luminosity, L_{Edd}, assuring hydrostatic equilibrium of a (spherically symmetric) star of mass M,

Eddington Limit

$$\boxed{\mathrm{L} < \mathrm{L}_{\mathrm{Edd}} \equiv \frac{4\pi c G M}{\kappa_{\mathrm{surf}}}} , \tag{1.1}$$

with κ_{surf} being the surface opacity, suggests the theoretical impossibility for gravitationally bound, super-Eddington gaseous structures to exist. However, several structures are nowadays known to reside very close to the so called Humphrey-Davidson limit, undergoing episodic and violent mass losses, an example being Luminous Blue Variables (LBVs). The issue of *Very Massive Stars* (VMS), namely those with initial masses $\mathrm{M} > 100\,\mathrm{M}_\odot$, has been recently reassessed, with renewed interest in both modeling their peculiar evolution and pursuing their observation since, by now, very few of them are known. In this work we will try to include these objects to compare their evolutive properties with that of massive stars.

1.2 Structural Properties

Stars are self-gravitating objects of hot plasma which radiate energy from the photosphere and host nuclear fusion in the core, maintaining hydrostatic equilibrium (HE) throughout most of their lifetimes. Basic laws of physics coupled to constitutive relations lay the ground to the *structural properties* of a star: let us briefly review these building blocks and specialize them to the massive case.

1.2.1 Stellar Structure Equations

Conservation Laws A general fluid dynamical treatment for the stellar matter, with a Lagrangian description and spherical symmetry approximation, immediately leads to the well known *conservation laws* for mass, momentum and energy. These hold at each spherical mass shell $\mathrm{d}m$ of mass coordinate m, such that

$$\begin{aligned} &\textsc{Continuity Equation} && \frac{\partial r}{\partial m} = \frac{1}{4\pi r^2 \rho}\,, \\ &\textsc{Euler Equation} && \frac{\partial P}{\partial m} = -\frac{Gm}{4\pi r^4} - \frac{1}{4\pi r^2}\frac{\mathrm{d}^2 r}{\mathrm{d}t^2}\,, \\ &\textsc{Energy Conservation} && \frac{\partial l}{\partial m} = \epsilon_{\mathrm{nuc}} - \epsilon_\nu - \mathrm{T}\frac{\partial s}{\partial t}\,. \end{aligned} \tag{1.2}$$

Here $P\,(m,t)$, $\mathrm{T}\,(m,t)$, $\rho\,(m,t)$, $s\,(m,t)$ and $l\,(m,t)$ are the local pressure, temperature, density, specific entropy and luminosity fields, with an explicit time-dependence allowing to solve for stellar properties evolution, see Sec.(1.3).
The energy production rates ϵ, such that $[\epsilon] = \mathrm{erg\,g^{-1}\,s^{-1}}$, are referred to nuclear reactions, ϵ_{nuc}, and neutrinos net leakage, ϵ_ν. The latter shall be the leading parameter for advanced massive stars evolution.

Energy Transport Local Thermodynamic Equilibrium (LTE) in stellar interiors assures a tight coupling between radiation and matter, allowing for heat diffusion processes as an efficient mean for *energy transport* from the core to the surface. Furthermore, the onset of local dynamical instabilities leads to bulk motion of macroscopic gas bubbles, whence a convective enegy transfer.

$$\textsc{Energy Transport} \qquad \frac{\partial \mathrm{T}}{\partial m} = -\frac{Gm}{4\pi r^4}\frac{\mathrm{T}}{P}\nabla\,, \tag{1.3}$$

$$\text{with} \quad \nabla = \begin{cases} \nabla_{\rm rad} = \dfrac{3\kappa}{16\pi ac\, G}\dfrac{lP}{m\mathrm{T}^4} & \text{if } \nabla_{\rm rad} \leq \nabla_{\rm ad}\,, \\ \nabla_{\rm ad} + \Delta\nabla & \text{if } \nabla_{\rm rad} > \nabla_{\rm ad}\,. \end{cases}$$

Here the radiative $\nabla_{\rm rad}$ and adiabatic $\nabla_{\rm ad}$ gradients quantify the logarithmic response of local temperature T to a change in pressure and of pressure P to an adiabatic change in density, respectively:

$$\nabla_{\rm rad} \equiv \left(\frac{\mathrm{d}\log \mathrm{T}}{\mathrm{d}\log P}\right)\bigg|_{\rm rad}\,, \qquad \nabla_{\rm ad} \equiv \left(\frac{\mathrm{d}\log \mathrm{T}}{\mathrm{d}\log P}\right)\bigg|_{\rm ad}\,. \tag{1.4}$$

The entity of ∇ depends on the Schwarzschild stability criterion against convection and, in massive stars, large convective cores throughout the nuclear burning phases are expected to appear, sometimes along with convective envelopes, too. Notice also that a superadiabaticity term $\Delta\nabla$ is allowed: this has to be specified by the Mixing Lenght Theory (MLT) and is often neglected when treating stellar interiors.
Lastly, the opacity κ expresses the resistance of the medium to the flow of energy and, in massive stars, results from various contributions, as we will see in Chp.(2).

Nucleosynthesis and Mixing Nuclear reactions in the deep interior, at sufficiently high temperatures and densities, provide the energy supply for the star to radiate and sustain secular equilibrium. In massive stars all the nuclear burning phases, up to the last energetically favorable fusion of ^{56}Fe, are ignited quietly, giving rise to a complex *nucleosynthesis* of elements with mass fraction X_i and mass number A_i:

NUCLEOSYNTHESIS & MIXING

$$\frac{\mathrm{dX}_i}{\mathrm{d}t} = \mathrm{A}_i\frac{m_u}{\rho}\left(-\textstyle\sum_j (1+\delta_{ij})\, r_{ij} + \sum_{k,l} r_{kl,i}\right) + [\mathrm{mix}]\,, \qquad \text{with} \qquad [r_{ij}] = \mathrm{cm}^{-3}\,\mathrm{s}^{-1}\,. \tag{1.5}$$

Here r_{ij} represents the number of reactions per unit volume and time, and the indexes i, j are referring to the two species involved in the initial state of a general reaction. The first addendum on the right-hand side is understood to be a sinking term, the second being instead the sourcing one. Of course, Eq.(1.5) is solved subject to boundary conditions for the abundance gradients in the core and at the surface, that is

$$\left(\frac{\partial \mathrm{X}_i}{\partial m}\right)\bigg|_{\rm core} = \left(\frac{\partial \mathrm{X}_i}{\partial m}\right)\bigg|_{\rm surface} = 0\,.$$

The term [mix] accounts for the presence of *compositional mixing*, so that the redistribution of composition between different mass shells is considered too. A collection of mixing mechanisms can intervene:

MIXING MECHANISMS

1) (Semi-)convective and Diffusive mixing ,
2) Convective Overshooting ,
3) Rotational, shear-induced,
pulsationally induced, magnetic fields mixing...

These several mechanisms have been extensively treated in literature but some degree of uncertainty still persists. Above all, (semi-)convection and overshooting shall play a key role in massive stars evolution; we will see this in Sec.(1.3.2).

1.2.2 Constitutive Relations

Equation of State (EoS) Local pressure P depends on the local density ρ, temperature T fields and abundances X_i via a proper *Equation of State* (EoS), which needs to be specified at each mass coordinate in the star's structure as well as in every evolutionary stage:

$$\textsc{Equation of State} \qquad P = P\left(\rho, \mathrm{T}, \mathrm{X}_i\right) \ .$$

Massive stars share a relatively simple EoS from their Main Sequence until prior the iron core collapse onset. A perfect, thermal gas treatment for electrons and positrons, combined with an ideal gas of ions and a Planckian distribution for the radiation, happens to be well suited for most of their lives:

$$P = P_{\text{ion}} + P_e + P_{\text{rad}}$$

$$\text{with} \qquad P_{\text{ion}} = \frac{\mathcal{R}}{\mu}\rho\mathrm{T} \ , \quad P_e = P_e(\rho, T, \mathrm{X}_i) \ , \quad P_{\text{rad}} = \frac{1}{3}a\mathrm{T}^4 \ ,$$

where we have allowed for a general form of P_e, to be specified with regards to degeneracy and relativity, while the much higher masses of ions prevents them to become relativistic (with the exception of very late evolutionary stages) during the examined phases.
The mean molecular weight μ is defined with respect to the ones of ions μ_{ion} and electrons (positrons) μ_e through the following:

$$\boxed{\frac{1}{\mu} \equiv \frac{1}{\mu_{\text{ion}}} + \frac{1}{\mu_e}} \tag{1.6}$$

$$\text{with} \qquad \frac{1}{\mu_{\text{ion}}} \equiv \sum_i \frac{\mathrm{X}_i}{\mathrm{A}_i} = \frac{n_{\text{ion}} m_u}{\rho} \ , \qquad \frac{1}{\mu_e} \equiv \sum_i \frac{\mathrm{Z}_i \mathrm{X}_i}{\mathrm{A}_i} = \frac{n_e m_u}{\rho} \ , \qquad [\mu] = \# \ .$$

Here we are summing over all ions i with electric charge $\mathrm{Z}_i e$ and mass number A_i; these expressions shall depend on the ionization degree of the stellar layer. By considering a fully ionized plasma, for which $\mathrm{Z}_i/\mathrm{A}_i \approx 1/2$ for heavy elements, one can easily show that

$$\frac{1}{\mu_\mathrm{e}} \approx \frac{1+\mathrm{X}}{2} \ , \qquad \frac{1}{\mu} = \sum_i \frac{\left(\mathrm{Z}_i + 1\right)\mathrm{A}_i}{\mathrm{A}_i} \approx 2\mathrm{X} + \frac{3}{4}\mathrm{Y} + \frac{1}{2}\mathrm{Z} \ , \tag{1.7}$$

and we have also used the fact that for elements heavier than helium $\mathrm{A}_i \approx 2\mathrm{Z}_i \approx 2\left(\mathrm{Z}_i + 1\right)$.

Opacity κ Stellar interiors exert, in general, a resistance to the energy flow, either transported by radiation or conductively by electrons at high densities. Such behavior is quantitatively described by the *opacity* κ, which shall be the focus of our work and is usually given in the following terms

Opacity

$$\boxed{\kappa = \kappa\,(\rho, \mathrm{T}, \mathrm{X}_i)} \qquad \text{with} \qquad [\kappa] = \mathrm{cm}^2\,\mathrm{g}^{-1}\,.$$

In massive stars, radiative opaqueness has a twofold nature: photo-absorption by molecules and atoms prevails in the cool envelopes, while convective cores are dominated by electron scattering. A detailed description is postponed until Chp.(2).

Rate of Energy Generation ϵ In Eq.(1.2) we have seen that the local mass divergence of luminosity, $\partial l/\partial m$, is balanced by the local energy generation rate, which is the sum of thermonuclear, gravothermal effects and neutrino leakage:

Rate of Energy Generation

$$\epsilon = \epsilon\,(\rho, \mathrm{T}, \mathrm{X}_i) \qquad \text{with} \qquad [\epsilon] = \mathrm{erg}\,\mathrm{g}^{-1}\,\mathrm{s}^{-1}\,.$$

1. *Thermonuclear Rate*
Nuclear reactions act as supplier of energy lost by radiation and neutrinos, maintaining the nuclear equilibrium till a given fuel is depleted in the core; once a thin shell surrounding the core is ignited, the star contracts until the subsequent, heavier fuel can undergo fusion. The rate of energy generation ϵ_{nuc},

Thermonuclear Rate

$$\epsilon_{\mathrm{nuc}} = \textstyle\sum_{ij} \epsilon_{ij} \qquad \text{with} \qquad \epsilon_{ij} = \epsilon_{0,\,ij}\,\mathrm{X}_i\mathrm{X}_j\,\rho^{\lambda}\mathrm{T}^{\nu}$$

is known to be strongly dependent on temperature, due to the Gamow-peaked nuclear cross sections. Above we sum over all the reactions occuring between species i, j, and the amplitude $\epsilon_{0\,ij}$ is related to the Q-value of the reaction, Q_{ij}, the mass numbers involved A_i, A_j, and the thermally weighted cross section $\langle \sigma v \rangle$.
The slopes λ and ν are defined as

$$\lambda \equiv \left.\frac{\partial \ln \epsilon}{\partial \ln \rho}\right|_{\mathrm{T}} = 1\,, \qquad \nu \equiv \left.\frac{\partial \ln \epsilon}{\partial \ln \mathrm{T}}\right|_{\rho} = \frac{\tau(\mathrm{T}) - 2}{3} \gg 1\,,$$

where the linear dependence on ρ holds for non-resonant, $2 \to \ldots$ reactions and $\tau(\mathrm{T}) \propto \mathrm{T}^{-1/3}$, inheriting a temperature-dependence from the thermally averaged nuclear cross section $\langle \sigma v \rangle$.

In massive stars, the first stable and long-lasting nuclear burning stage is the core H-burning, which is powered by the Carbon-Nitrogen-Oxygen (CNO) cycle; this engine is characterized by $\nu \simeq 18$, implying a high sensitivity to T fluctuations and peaked nuclear energy flux.

2. *Gravothermal Energy Rate*

The gravothermal rate $\epsilon_{\rm grav}$ describes the response of the star to contraction or expansion, in terms of thermodynamic variables

Gravothermal Rate

$$\epsilon_{\rm grav} = -\mathrm{T}\frac{\partial s}{\partial t}$$
$$\text{with} \quad \mathrm{T}\mathrm{d}s = \mathrm{d}u - \frac{P}{\rho^2}\,\mathrm{d}\rho\,,$$

where we have reported the II law of thermodynamics with the specific energy per unit mass being u.

NB If $\epsilon_{\rm grav} > 0$ the energy is released by the mass shell (typically when contracting), while $\epsilon_{\rm grav} < 0$ leads to an absorption of energy by the mass shell (typically when expanding).

3. *Neutrino Energy Loss*
   The neutrino leakage ϵ_ν represents a net energy loss, being stellar matter (at ordinary temperatures and densities) extraordinarily transparent to them.
   In massive stars, neutrinos are released in nuclear chains already from core H-burning but, in advanced nuclear burning cycles, ϵ_ν becomes a key evolutionary parameter: thermally produced neutrinos rate, chiefly from e^+e^- annihilation, quickly overcomes any energy leakage, driving an extremely accelerated Stellar Evolution (SE) through subsequent stages.

1.2.3 Boundary conditions

The solution of Eq.(1.2) and Eq.(1.3) requires *four boundary conditions*. These conditions for the differential equations of stellar evolution constitute an important problem for evolutionary codes, mainly because they have to be set at *two opposite sides*, i.e. at the stellar center and at a suitable point in the outer surface. This also means that codes have to deal with two boundaries problems, and the influence of these conditions on the solutions is often not easy to foresee.

- **Stellar Center**
  The natural conditions in the stellar center assure that both the density ρ and the energy generation rate ϵ must remain finite, so

  $$\boldsymbol{m=0} \quad : \qquad r = 0 \;\; \text{and} \;\; l = 0\,,$$

  as one can understand by looking at the Continuity and Energy conservation equations in Eq.(1.2) and Eq.(1.3).

- **Photospheric radius**
  There is general agreement, in the astrophysical community, to take the **photospheric radius** as the radial coordinate at which outer boundary conditions are set. From the photosphere, the bulk of radiation escapes and the stellar interior models can match the structure resulting from stellar atmospheres' models. By defining the

photospheric radius $r_{\rm ph} = \tau_{\rm ph}$ as

Photosheric Radius

$$\tau_{\rm ph} = \int_{r_{\rm ph}}^{\infty} \kappa\rho\, \mathrm{d}r \approx \kappa_{\rm ph} \int_{r_{\rm ph}}^{\infty} \rho\, \mathrm{d}r \stackrel{!}{=} \frac{2}{3}$$
$$\Leftrightarrow \quad r_{\rm ph} = r(\tau_{\rm ph})$$

we obtain the following boundary conditions for the lagrangian mass coordinate $m = m_{\rm ph} = m(r = r_{\rm ph})$:

$$\boldsymbol{m = m_{\rm ph}} \ : \qquad P = P(m_{\rm ph}) \ \text{ and } \ \mathrm{T} = \mathrm{T}(m_{\rm ph})\ .$$

1.3 Evolutionary Properties

The aim of this section is to outline the *pre-supernova evolution* of massive stars, comprising core H, He burning and the so called "advanced" stages, until the iron core formation. Models of such phases are strongly affected by the input physics concerning

Input Physics

1) Convection and Overshooting
2) Mass Loss
3) Rotation
4) Further effects: Opacity, Binarity, Magnetic Fields...

After an overview of evolutionary tracks of massive stars over the Hertzsprung-Russel (HR) diagram in Sec.(1.3.1), we will discuss here the main effects of 1)-3) on such tracks in Sec.(1.3.2), Sec.(1.3.3) and Sec.(1.3.4). The question about microphysics, namely opacity effects on evolution of massive stars, shall be the major focus of Chp.(3) and Chp.(4).

1.3.1 Evolutionary Tracks

The general picture Massive stars show a peculiar journey through the HR diagram, very different from low ($\lesssim 2\,\mathrm{M}_\odot$) and intermediate ($2\,\mathrm{M}_\odot \lesssim \mathrm{M} \lesssim 8\,\mathrm{M}_\odot$) mass objects. Such journey in the $\log \mathrm{T}_{\rm eff} - \log \mathrm{L}$ plane shall reflect the succession of burning phases, each one lasting approximately $\tau_{\rm nuc}$, leading to core contraction and equilibrium ignition of the subsequent fuel burning, within the Kelvin-Helmholtz timescale $\tau_{\rm KH}$:

$$\tau_{\rm nuc} \sim \frac{E_{\rm nuc}}{\mathrm{L}}\ , \qquad \tau_{\rm KH} \sim \frac{|E_{\rm gr}|}{2\mathrm{L}}\ ,$$

where we reasoned with dimensional arguments, $E_{\rm gr}$ is the total gravitational energy and $E_{\rm nuc}$ the supplied nuclear energy. Every time the core contracts, an active burning shell surrounding it acts as a mirror for the outer envelope, which expands and cools down. Expressly:

CORE H BURNING
$10^6\ \mathrm{yr} \lesssim \tau_{\mathrm{MS}} \lesssim 10^7\ \mathrm{yr}$
$T_{\mathrm{ign}} \simeq 4 - 6 \times 10^7\ \mathrm{K}$
for
$13\ \mathrm{M}_\odot < \mathrm{M} < 120\ \mathrm{M}_\odot$

▶ During core H burning the luminosity $\mathrm{L} \propto \mu^4$ of massive stars progressively increases as opposing to the decreasing effective temperature $\mathrm{T}_{\mathrm{eff}}$, necessary for HE:

$$\mathrm{L}(\mathrm{L}_\odot) \nearrow \quad \text{and} \quad \mathrm{T}_{\mathrm{eff}} \searrow$$

▶ This phase is usually spent in (or in proximity to) the *O spectral type* region.

▶ A typical ***hook feature*** manifests the process of activating the H burning in a surrounding shell, after the central H depletion.

▶ Key parameter → He core mass M_{He}, which increases with the star's initial mass, but minimum mass for He core ignition, $\mathrm{M}_{\mathrm{He}} > \mathrm{M}_{\mathrm{He,min}} = 0.3\ \mathrm{M}_\odot$, is always reached (at the end of shell burning).

$$\text{INITIAL M} \nearrow \ \Rightarrow \mathrm{M}_{\mathrm{He}} \nearrow$$

SHELL H BURNING
$\tau_{\text{H-shell}} \overset{?}{\sim} 10^6\ \mathrm{yr}$

▶ Shell H burning ignites, after central H depletion, in a surrounding layer, driving the formation of a *convective zone* and feeding the core.

▶ All stars evolve towards the red, mostly at constant L, as a consequence of the mirror principle, whilst the core contracts: convective envelopes penetrate deeper and deeper as the ***Hayashi line*** is approaching.

$$\mathrm{L}(\mathrm{L}_\odot) \simeq \mathbf{const} \quad \text{and} \quad \mathrm{T}_{\mathrm{eff}} \searrow\searrow$$

▶ The timescale of H shell burning is uncertain: an *Hertzsprung gap* is observationally known for the Milky Way (MW) and Large Magellanic Cloud (LMC), so a $\tau \sim \tau_{\mathrm{KH}}$ seems appropriate.

CORE HE BURNING
10^5 yr $\lesssim \tau_{\rm He} \lesssim 10^6$ yr
for
$13\ \mathrm{M}_\odot < \mathrm{M} < 120\ \mathrm{M}_\odot$

▶ Depending on initial mass, core He burning begins when the star is still a Blue SuperGiant (BSG) or has already become a Red SuperGiant (RSG):

- Stars that start core He burning as **RSGs** become cool enough to develop strong *dust-driven winds*, favouring the evolution to Wolf Rayet (WR) objects.
- Stars with initial masses $\mathrm{M} \gtrsim \mathrm{M}_\star\,(\mathrm{M}, Z, v)$ do not reach a RSG phase due to heavy mass loss and they appear as **LBVs**, then as WR.

▶ A **Blue Loop** is developed by a range of masses $8\ \mathrm{M}_\odot \lesssim \mathrm{M} \lesssim 12\ \mathrm{M}_\odot$, namely in those stars in which strong $\dot{\mathrm{M}}$ is not yet present. These loops correspond to a slow, $\tau_{\rm nuc}$, phase, resulting in well populated HR diagrams.

$$\text{INITIAL M} \nearrow\ \Rightarrow \mathrm{T}_{\rm loop} \nearrow$$

▶ Key parameter → CO core mass $\mathrm{M}_{\rm CO}$ at the end of He-burning, which depends on several factors (see below), but in general it increases with initial mass:

$$\text{INITIAL M} \nearrow\ \Rightarrow \mathrm{M}_{\rm CO} \nearrow$$

Also the ${}^{12}\mathrm{C}/{}^{16}\mathrm{O}$ ratio is determinant for subsequent phases.

SHELL HE BURNING
$\tau_{\rm He\ shell} \overset{?}{\sim}$ kyr

▶ Shell He burning ignites, after central He depletion, in a surrounding layer, driving the formation of a convective zone.

▶ In stars where the He core remains constant in mass, the He convective shell forms a region where the He profile is flat. In this case, the shell increases in mass thanks to the advancing H burning layer.

▶ Short lifetimes of the following nuclear burning stages allow for just a small amount of He to be burnt inside the shell.

Advanced nuclear burning stages
$T_{^{12}\mathrm{C}} \sim 5 \times 10^8$ K
$T_{^{20}\mathrm{Ne}} \sim 1.5 \times 10^9$ K
$T_{^{16}\mathrm{O}} \sim 2 \times 10^9$ K
$T_{^{28}\mathrm{Si}} \sim 3 \times 10^9$ K

▶ The evolution proceeds in a series of alternating nuclear burning and core contraction cycles, with ^{12}C and ^{16}O as basic fuel and CO core mass governing the thermodynamics.

▶ The position in the HR diagram remains, usually, *almost unchanged* during these phases; the stellar envelope hardly has time to respond to the rapid changes in the core:

- $\mathrm{M} \lesssim 30\ \mathrm{M}_\odot$ explode as **RSGs**
- $\mathrm{M} \gtrsim 30\ \mathrm{M}_\odot$ explode as **BSGs**

▶ Each burning stage begins at the center, forming a convective core, which increases in mass, and then shifting into convective shells; the number of shells depends upon CO core mass.

▶ Neutrino energy losses speed up the evolution enormously: during burning cycles, in which $\tau_{\mathrm{nuc}} = E_{\mathrm{nuc}}/\mathrm{L}_\nu \ll E_{\mathrm{nuc}}/\mathrm{L}_\gamma$, the generation rates $\epsilon_{\mathrm{nuc}} = \epsilon_\nu$ are in balance.

▶ Onion-skin structure: an iron core of mass between $1.3\ \mathrm{M}_\odot \lesssim \mathrm{M}_{\mathrm{Fe}} \lesssim 1.8\ \mathrm{M}_\odot$, surrounded by active burning shells.

In figure Fig.(1.1), an example of evolutionary track through the HR diagram of a massive star, with M=10 $\mathrm{M}_\odot$, is shown, compared with a model in which a convective overshooting of the envelope is incorporated too. Conversely, Fig.(1.2) shows the structural properties of the same star in the $\log \mathrm{T}_c - \log \rho_c$ plane: consistent deviations from the homologous trend appear in correspondece of startings (endings) of burning cycles, when the structure experiences readjustments. A complete degeneracy locus is also highlighted (and reached in the final evolutionary phase): this shall be discussed in Chp.(3).

Very Massive Stars Tracks Evolutionary tracks of *Very Massive Stars VMS* show some peculiarities with respect to the ones of ordinary massive stars.

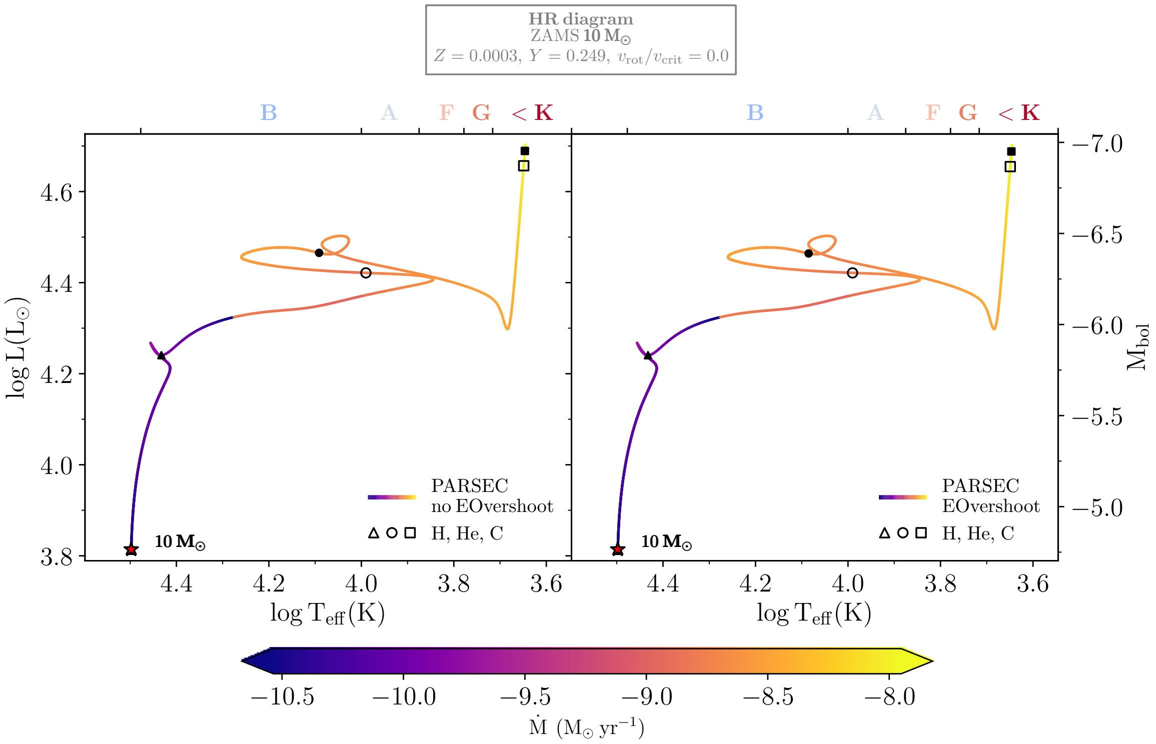

Figure 1.1: Evolutionary track for a star with Zero Age Main Sequence (ZAMS) mass $\mathrm{M} = 10\ \mathrm{M}_\odot$, metallicity Z=0.0003 and rotation velocity $v_{\mathrm{rot}}/v_{\mathrm{crit}} = 0$, up to the end of C core burning. Color coding describes mass loss rates $\dot{\mathrm{M}}$ throughout the evolution, and (filled) symbols states the start (end) of corresponding nuclear burning cycle. Spectral types are also highlighted. Left – PARSEC output without convective overshooting of the envelope (EOvershooting); Right – same as Left, but with EOvershooting incorporated. Differences between the two models are completely negligible. The characteristic *blue loop* is performed during He-burning, and the hook feature after H-depletion in the core is also evident.

- **Track** Mainly vertical evolution, spanning a large luminosity range but a restricted range in $\mathrm{T}_{\mathrm{eff}}$.
- **Colors** The colors of VMS in general do not change much with M, so one expects to find different initial masses stars occupying similar position in HR diagram.
- **Timescales** The core H burning phase lasts about few Myr, while core He burning ~ 0.1 Myr; the lifetime dependence on the initial mass is very weak:

$$\tau_{\mathrm{MS}} \sim \frac{E_{\mathrm{nuc}}}{\mathrm{L}} \sim \frac{\mathrm{M}}{\mathrm{L}} \propto \mathrm{M}^{-0.3} ,$$

where we have used the fact that $E_{\mathrm{nuc}} \propto \mathrm{M}$ and the observational, steep law $\mathrm{L} \propto \mathrm{M}^k$ with $k = 1.3$ for VMS.

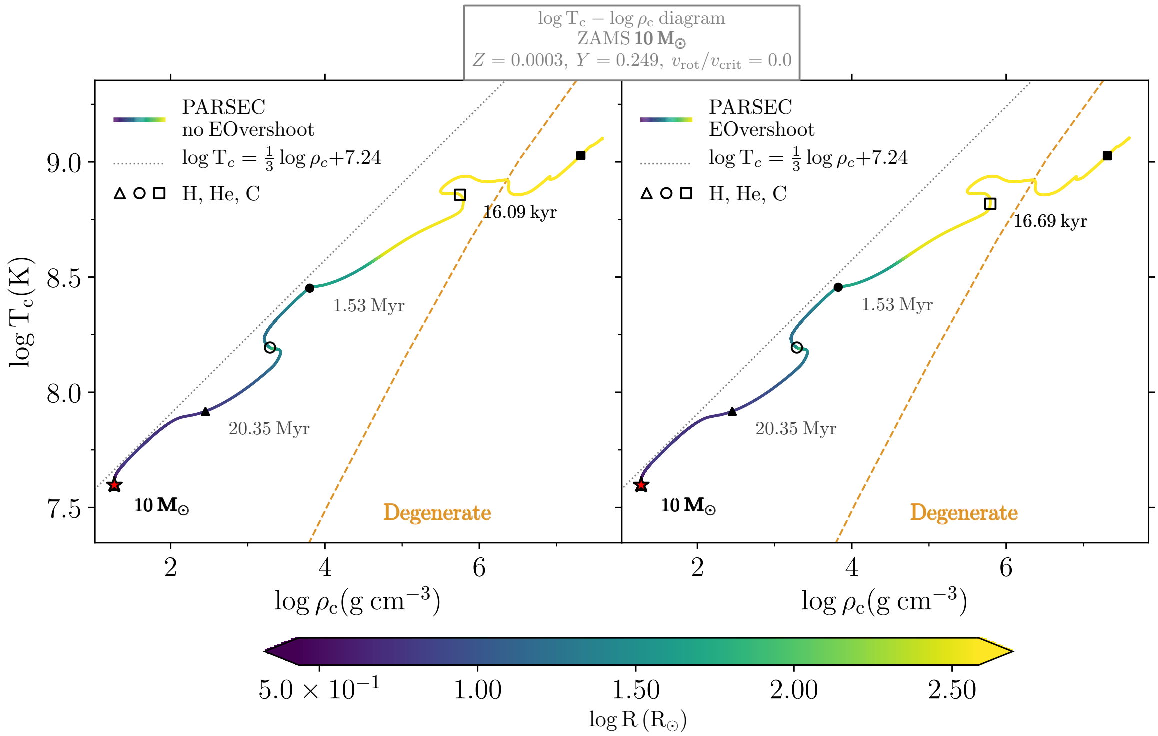

Figure 1.2: Structure $\log T_c - \log \rho_c$ for a star with Zero Age Main Sequence (ZAMS) mass $\mathrm{M} = 10\ \mathrm{M}_\odot$, metallicity Z=0.0003 and rotation velocity $v_{\mathrm{rot}}/v_{\mathrm{crit}} = 0$, up to the end of C core burning. Color coding describes the radius R, with its expansions and contractions throughout the evolution, and (filled) symbols states the start (end) of corresponding nuclear burning cycle. Duration of core H and He burning are also highlighted. Left – PARSEC output without convective overshooting of the envelope (EOvershooting); Right – same as Left, but with EOvershooting incorporated.

- **End** After the end of the core He burning phase the VMS may evolve towards the red and terminate its lifetime around $\log \mathrm{T_{eff}} \sim 4$, due to the core contraction.

These features are mainly determined by a mass loss-governed evolution, together with a typical strong internal mixing, see below.

In figure Fig.(1.3) an example of evolutionary track through the HR diagram of a very massive star is shown, again with a comparison with a model in which convective overshooting of the envelope is incorporated too. The latter effect is the subject of the next section, Sec.(1.3.2). Fig.(1.4), instead, shows the structural properties of the same VMS in the $\log \mathrm{T}_c - \log \rho_c$ plane: the interesting fact is the quasi-homologous evolution in the ideal gas phase, confirming what was said in Sec.(1.2.2). One should also notice the consistently shortened duration of MS and He-burning phases; also, the degeneracy region is completely avoided throughout the evolution.

Finally, Fig.(1.5) and Fig.(1.6) show the HR plot and structural properties of relevant massive stars, namely $9\mathrm{M}_\odot \lesssim \mathrm{M} \lesssim 20\mathrm{M}_\odot$, which shall be studied in details in Chp.(3). Blue loops is subtituted by a simple hook feature as M increases, and there is a maximum mass for

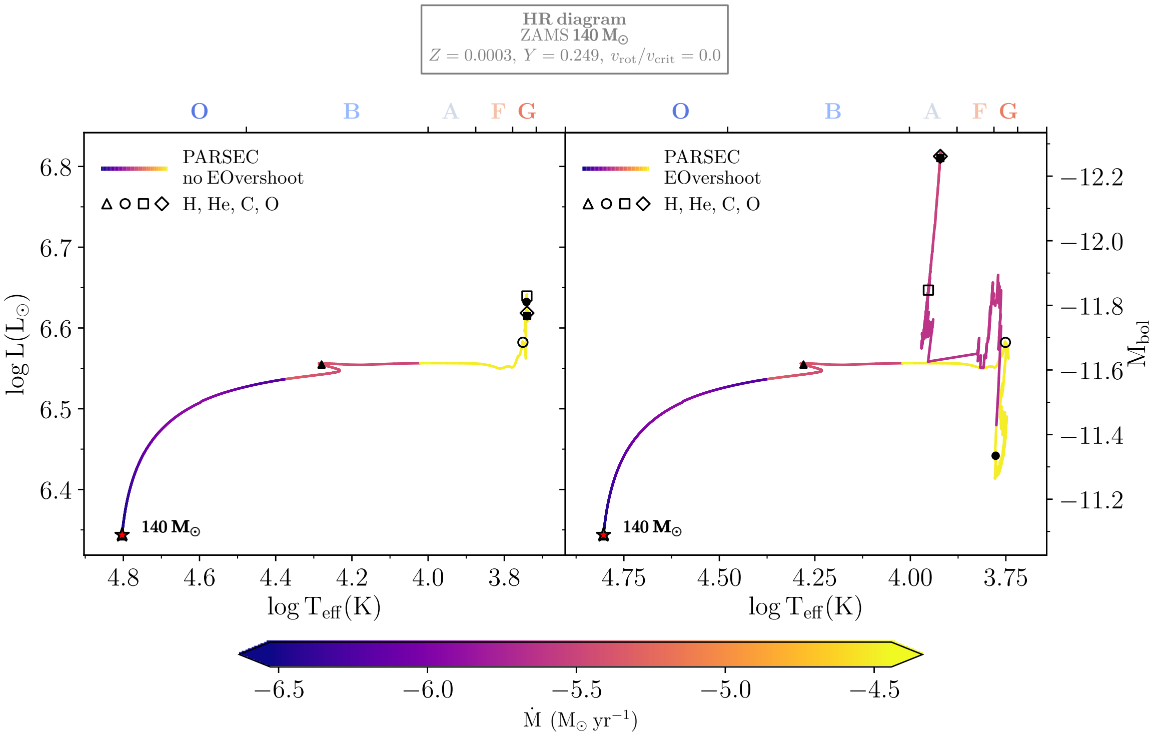

Figure 1.3: Evolutionary track for a star with Zero Age Main Sequence (ZAMS) mass $M = 140\ M_{\odot}$, metallicity Z=0.0003 and rotation velocity $v_{\rm rot}/v_{\rm crit} = 0$, up to the end of O core burning. Color coding describes mass loss rates $\dot{M}$ throughout the evolution, and (filled) symbols states the start (end) of corresponding nuclear burning cycle. Spectral types are also highlighted. Left – PARSEC output without convective overshooting of the envelope (EOvershooting); Right – same as Left, but with EOvershooting incorporated. In this case it is also evident a computational difficulty for the solver, due to the fragmented and complex convective envelope.

which the degeneracy region can be touched in the later evolutionary stages. The region in which a dynamical instability sets on, $\Gamma_1 < 4/3$, is also highlighted, but not touched by our models; this is the regime of Pair Production Instability (PPI) in the core of the hottest stars. Also, one can notice that after C-burning ignition the position of the stars in the HR diagram does not change much: this is due to the surface properties slower response to core readjustments.

1.3.2 Convection and Overshooting

Convective mixing As can have been already glimpsed from the previous section, i.e. Sec.(1.3.1), *convective mixing* plays a pivotal role in evolutionary modeling, intervening at each stage with relevant consequences. Saying that it is one of the greatest sources of uncertainty in the input physics of SECs is, indeed, not an exaggeration, especially regarding the lacking of a complete 3D hydrodinamical theory.

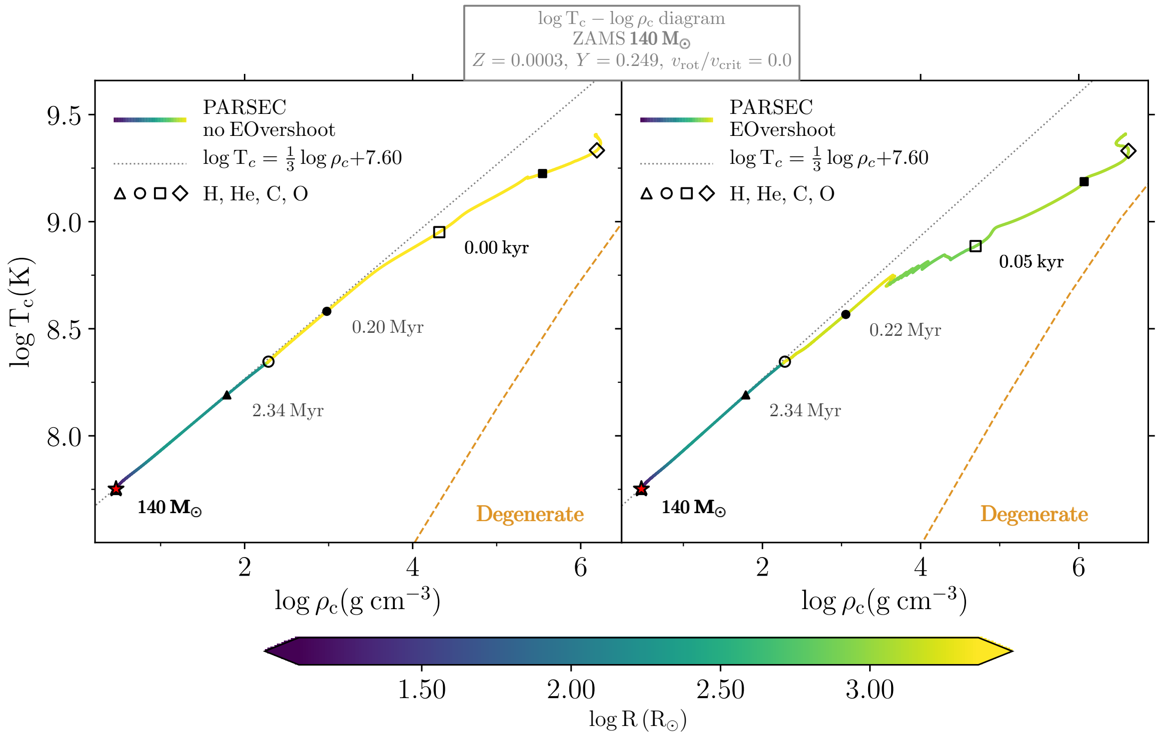

Figure 1.4: Structure $\log T_c - \log \rho_c$ for a star with Zero Age Main Sequence (ZAMS) mass $\mathrm{M} = 140\ \mathrm{M}_\odot$, metallicity Z=0.0003 and rotation velocity $v_{\mathrm{rot}}/v_{\mathrm{crit}} = 0$, up to the end of O core burning. Color coding describes the radius R, with its expansions and contractions throughout the evolution, and (filled) symbols states the start (end) of corresponding nuclear burning cycle. Duration of core H and He burning are also highlighted. Left – PARSEC output without convective overshooting of the envelope (EOvershooting); Right – same as Left, but with EOvershooting incorporated.

Basically, all models use some variation of the 1D MLT, in which macroscopic gas bubbles travel an average distance of the order of the *mixing lenght* l

$$\textsc{Mixing Lenght} \qquad l = \alpha_{\mathrm{MLT}} H_P \,, \tag{1.8}$$

which is a fraction of the local pressure scale height H_P. This quantity has the meaning of the distance travelled by convective eddies before dissolving; usually it is calibrated with the Sun, and a fixed value is commonly adopted in codes. In the context of MLT, convective mixing timescale τ_{mix} is such that

$$\tau_{\mathrm{mix}} \ll \tau_{\mathrm{KH}} \ll \tau_{\mathrm{nuc}}$$

for most of massive stars' evolution, except for the latest, neutrino-driven stages, in which convective and nuclear timescales become comparable.

Modern evolutionary codes account for a ***diffusive convection***, where elements in the turbulent regions are mixed by solving a system of diffusion equations coupled with the

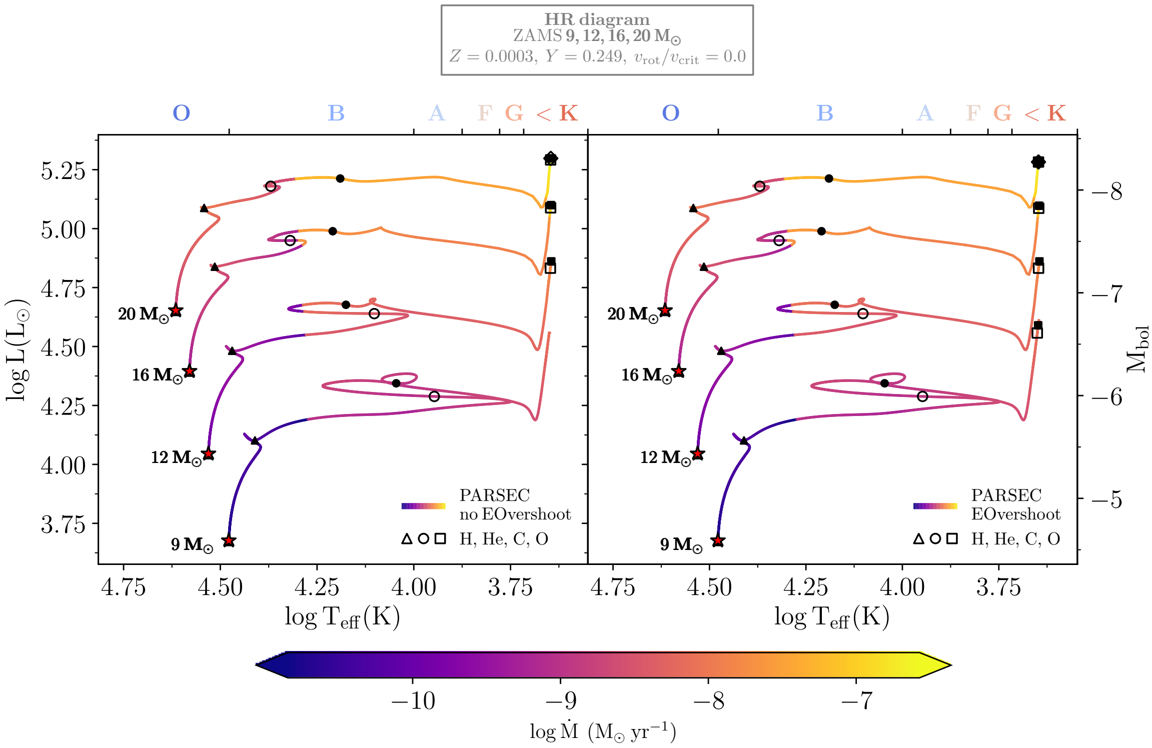

Figure 1.5: Evolutionary track for stars with Zero Age Main Sequence (ZAMS) mass $M = 9 - 12 - 16 - 20\ M_\odot$, metallicity Z=0.0003 and rotation velocity $v_{\rm rot}/v_{\rm crit} = 0$. Same color coding for $\dot{M}$ and symbols for phases as in Fig(1.1) are adopted. Left – PARSEC output without convective overshooting of the envelope (EOvershooting); Right – same as Left, but with EOvershooting incorporated.

nuclear reaction rates. In particular, a diffusion coefficient, $D_{\rm mix}$, for both compositional mixing and energy transport is employed

Diffusion Equation Convective Mixing

$$\left.\frac{\partial X_i}{\partial t}\right|_{\rm conv} = \frac{\partial}{\partial m}\left[(4\pi r^2\rho)^2\ D_{\rm mix}\frac{\partial X_i}{\partial m}\right]\,, \qquad \text{with} \qquad D_{\rm mix} = \frac{1}{3}v_{\rm conv}\,l \tag{1.9}$$

where $v_{\rm conv}$ is the eddy convective velocity. A term such as the one appearing at the RHS of the 1D diffusion equation is promptly added to Eq.(1.5) to account for mixing.

Semiconvection The regions of the star that are unstable by the Schwarzschild criterion but stable by the, more stringent, Ledoux criterion are called <u>*semiconvective*</u>. The two stability criteria against convection read

$$\begin{array}{lll} \textbf{Schwarzschild} & \nabla_{\rm rad} < \nabla_{\rm ad} & \text{(stable)} \\ \textbf{Ledoux} & \nabla_{\rm rad} < \nabla_{\rm ad} - \dfrac{\chi_\mu}{\chi_T}\nabla_\mu & \text{(stable)} \end{array} \tag{1.10}$$

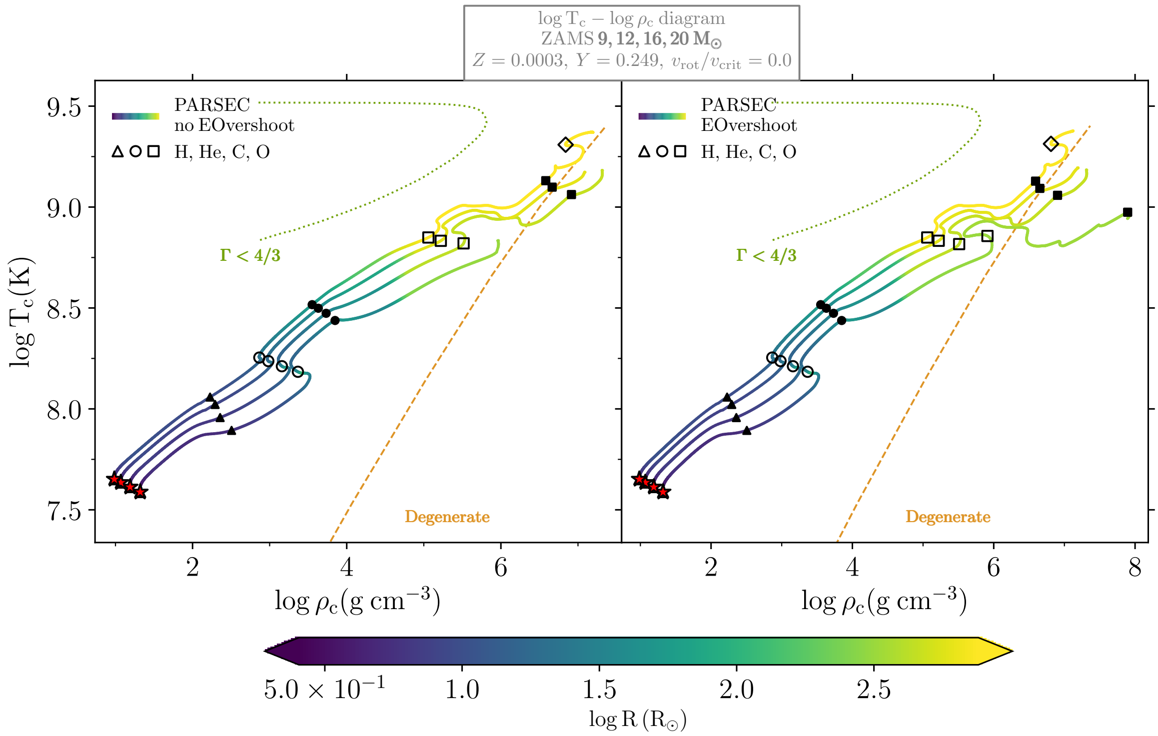

Figure 1.6: Structure $\log T_c - \log \rho_c$ for stars with Zero Age Main Sequence (ZAMS) mass $\mathrm{M} = 9 - 12 - 16 - 20\,\mathrm{M}_\odot$, metallicity Z=0.0003 and rotation velocity $v_{\mathrm{rot}}/v_{\mathrm{crit}} = 0$. Same color coding for R and symbols for phases as in Fig(1.1) are adopted. Left – PARSEC output without convective overshooting of the envelope (EOvershooting); Right – same as Left, but with EOvershooting incorporated.

$$\text{with} \qquad \chi_T \equiv \left.\frac{\partial \log P}{\partial \log \mathrm{T}}\right|_{\rho,\mathrm{X}_i}, \qquad \chi_\mu \equiv \left.\frac{\partial \log P}{\partial \log \mu}\right|_{\rho,\mathrm{T}}, \qquad \nabla_\mu \equiv \left.\frac{\partial \log \mu}{\partial \log P}\right|_{\mathrm{ad}},$$

where χ_T and χ_μ are the logarithmic derivatives of pressure with respect to the correspondent thermodynamic variable, while ∇_{rad} and ∇_{ad} are defined in Eq.(1.4). The (stabilizing) chemical composition gradient ∇_μ has the net effect of reducing the extent of convective regions, exerting some influence on evolutionary properties of massive stars.

Consistent uncertainties in semiconvection treatment in codes are still present, essentially because a physical model of semiconvective regions requires the description of the non-linear hydrodynamic instabilities and turbulent processes.

Overshoot mixing *Convective overshooting* is a phenomenon caused by inertial motion of gas bubbles when they reach the boundary of a convective zone: the eddies shall have, in general, a non-zero velocity, causing them to travel some distance and maybe originate a turbulent cascade.
The effect is highly non-linear, and the actual overshooting lenght d_{ov} is very uncertain: usually, this process is treated ballistically, by assuming a fixed fraction of the pressure

scale height such that

$$\textsc{Overshooting Lenght} \qquad \boxed{\mathbf{d_{ov}} = \boldsymbol{\alpha_{ov} H_P}}\ . \tag{1.11}$$

Here α_{ov} is a free parameter, to be calibrated against observations, and this has been performed via several types of data, comprising color-magnitude diagrams (CMDs) of star clusters, asteroseismology or double-lined eclipsing binaries (DLEBs). A series of works (see e.g. Bressan et al. [Bre+12]) suggests that the best choice for the overshoot parameter α_{ov} is mass-dependent, particularly for the transition ($1 - 1.2\,\mathrm{M}_\odot \lesssim \mathrm{M} \lesssim 1.6 - 2\,\mathrm{M}_\odot$) between models with radiative and convective cores of Main Sequence (MS).

We shall stress that also the base of the convective envelope can give rise to a sizable envelope overshooting (EOvershooting) region; this was demonstrated, in the past, to explain observational effects such as the extension of blue loops of intermediate mass stars, wih a typical value of $\alpha_{ov} \sim 0.25 - 1.0\,\mathrm{H}_P$. Modern codes accounts for this possibility, with a similar treatment as the one for core overshooting. Similarly to the latter, envelope overshooting is expected to have significant effects on the evolutionary properties of stars, affecting also some observable features (surface abundances of light elements, e.g. ^{7}Li); in this work we shall discuss these effects too.
Fig.(1.7) shows an example of the evolution of surface mass fractions X_i of isotopes in a (very) massive star, both without and with EOvershooting, as a PARSEC's output. As a comparison, Fig.(1.8) shows the same quantity for a $\mathrm{M} = 10\ \mathrm{M}_\odot$ star.

Effects on evolution Effects of these three mechanisms on the evolutionary properties of massive stars are relevant in almost all phases, here we list them in order.

Core H burning
10^6 yr $\lesssim \tau_{\mathrm{MS}} \lesssim 10^7$ yr
$T_{\mathrm{ign}} \simeq 4 - 6 \times 10^7$ K

▶ The convective core, created by the high energy flux of CNO cycle, is reduced as the burning proceeds. This is a consequence of the X dependence of the predominant electron scattering opacity $\kappa_e \propto 1 + \mathrm{X}$:

Convective Core ↘

We can see this in Fig.(1.9).

▶ The size of the convective core, which in turn depends on the amount of convective core overshooting, influences the total He core mass at core H depletion.

▶ Convection contributes to the *angular momentum transport* from innermost zones towards the more external ones, where it is dispersed by stellar winds.

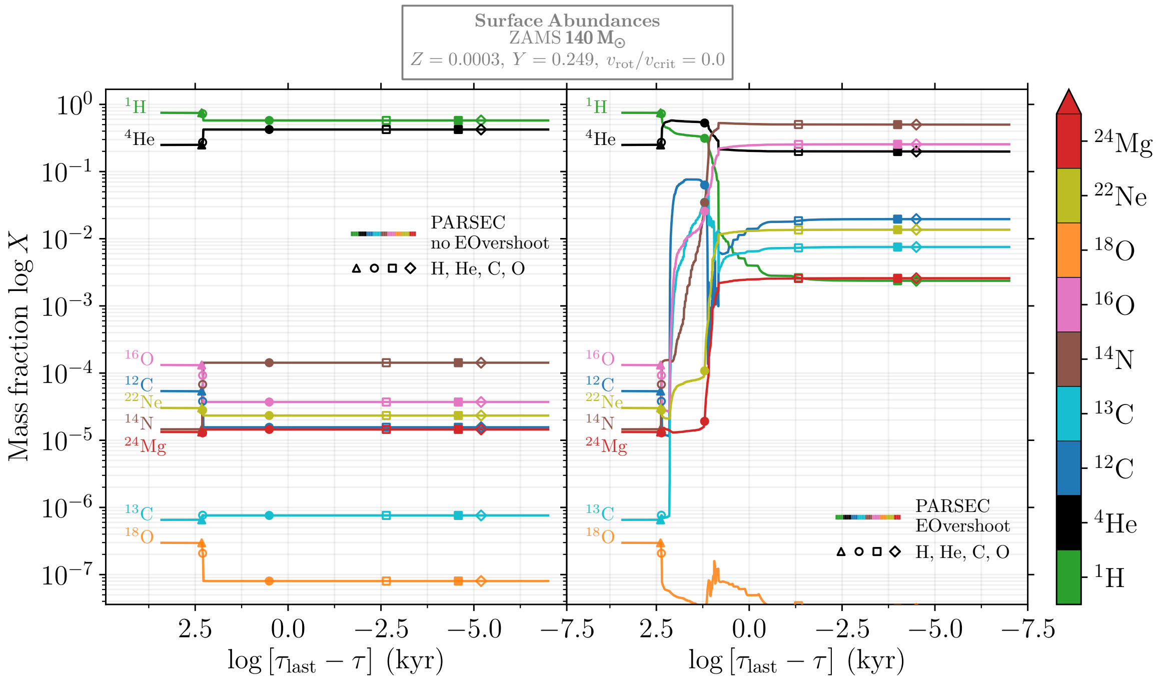

Figure 1.7: Surface abundances mass fractions X_i as a function of age τ remaining till the O burning onset at $\tau_{^{16}O}$, for a star with Zero Age Main Sequence (ZAMS) mass $M = 140\ M_\odot$, metallicity Z=0.0003 and rotation velocity $v_{rot}/v_{crit} = 0$, up to the end of O core burning. Color coding describes the highlighted isotopes throughout the evolution. Left – PARSEC output without convective overshooting of the envelope (EOvershooting); Right – same as Left, but with EOvershooting incorporated. An evident mixing of species is present in the last phases, due to the dredge up boosting the He mass fraction with respect to H.

▶ The ***additional mixing*** due to overshooting is usually responsible for the tracks to be more extended towards *lower* T_{eff}.

$$\text{Mixing} \nearrow\ \Rightarrow T_{eff} \searrow$$

Shell H burning

$\tau_{\text{H-shell}} \overset{?}{\sim} 10^6$ yr

▶ A semiconvective region develops in the layers of variable composition left by the receding convective core.

▶ Convection prescriptions during H core burning determine either the gradient of hydrogen to helium effectively mixes or not; this affects the time at which the hydrogen shell burning timescale.

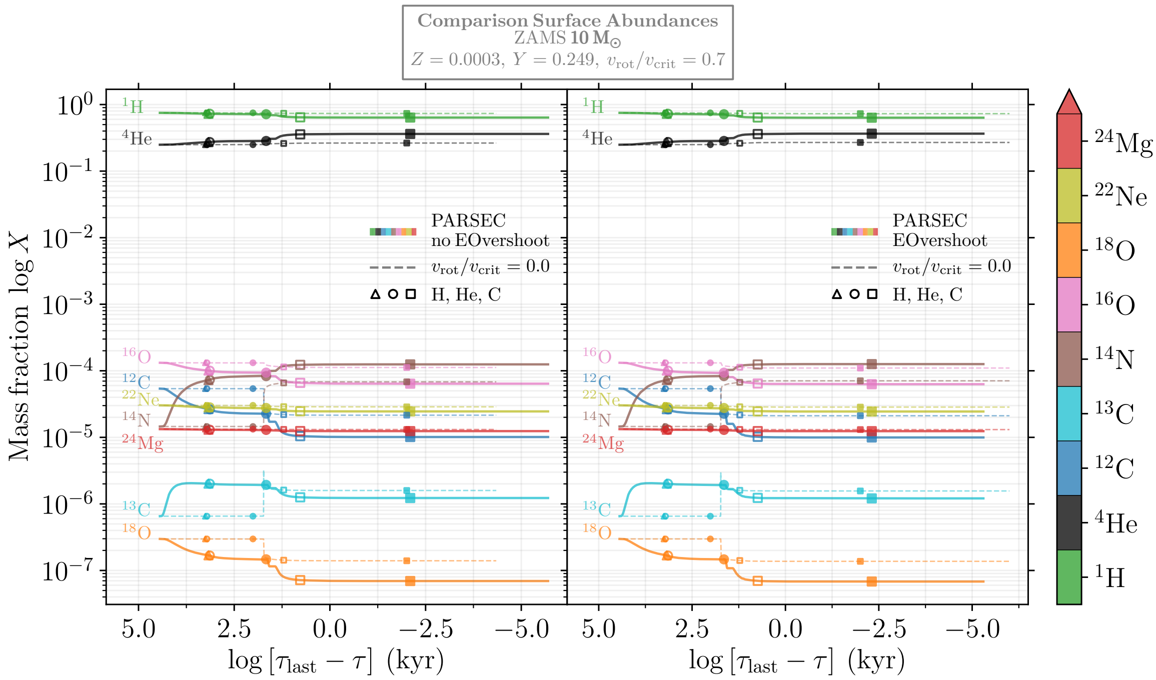

Figure 1.8: Surface abundances mass fractions X_i as a function of age τ remaining till the C burning onset at $\tau_{^{12}\mathrm{C}}$, for a star with Zero Age Main Sequence (ZAMS) mass $\mathrm{M} = 10\mathrm{M}_\odot$, metallicity Z=0.0003 and rotation velocity $v_{\rm rot}/v_{\rm crit} = 0.7$, up to the end of C core burning. Color coding describes the highlighted isotopes throughout the evolution. Left – PARSEC output without convective overshooting of the envelope (EOvershooting); Right – same as Left, but with EOvershooting incorporated. As a contrast with the $\mathrm{M} = 140\mathrm{M}_\odot$ in Fig(1.7), a relevant mixing of surface abundances is not present. the difference with respect to the non rotating models shall be highlighted in Sec.(1.3.4).

In particular:

- Schwarzschild criterion $\Rightarrow$ efficient mixing $\tau_{\rm mix} \sim \tau_{\rm dyn} \Rightarrow \tau_{\text{H-shell}} \sim \tau_{\rm nuc} \Rightarrow$ well populated horizontal branch (not observed).
- Ledoux criterion $\Rightarrow$ suppressed mixing $\tau_{\rm mix} \gg \tau_{\rm dyn} \Rightarrow \tau_{\text{H-shell}} \sim \tau_{\rm KH} \Rightarrow$ observed (in MW and LMC) gap. ⚠ Lack of robustness: ∇_μ may be reduced by any turbulence.

This, in turn, affects whether the star is a RSG or a BSG, so that ratio RSGs/BSGs is a powerful semiconvection diagnostic.

▶ As stars evolve towards the red, convective envelopes of the cooler and cooler external layers penetrate deep into the stars: this can originate a **dredge up**, modifying surface abundances.

Core He burning
$10^5 \text{ yr} \lesssim \tau_{\mathrm{He}} \lesssim 10^6 \text{ yr}$

▶ The convective core, mainly enpowered by triple-α and $^{12}\mathrm{C}\,(\alpha,\gamma)^{16}\,\mathrm{O}$, is increased by H burning shell, as opposed to core H burning.

Convective Core $\nearrow$

You can see this in Fig.(1.9).

▶ The **Blue Loop** extension in $8\ \mathrm{M}_\odot \lesssim \mathrm{M} \lesssim 10\ \mathrm{M}_\odot$ is sensitive to the convective overshooting treatment, since it depends on the shape of the H profile above the core. This makes loops a significant mean for observational tests of overshooting using He-burning stars.

Advanced nuclear burning stages

▶ The ^{12}C mass fraction at core He depletion, key parameter in advanced stages, depends on the treatment of convection.

▶ Several convective regions are formed as subsequent fuels are ignited; their overlap determine the mass-ratio (MR) and the chemical stratification of the star.

▶ In general: lower ^{12}C mass fraction $\Rightarrow$ fewer convective zones $\Rightarrow$ higher contraction of the CO core and $\Rightarrow$ steeper M-R relation, i.e. the more compact shall be the pre-supernova structure,

$^{12}\mathrm{C} \searrow\ \Rightarrow$ Compactness $\nearrow$

▶ The use of mixing-lenght theory during oxygen and silicon burning is particularly problematic, since $\tau_{\rm mix} \sim \tau_{\rm nuc}$, i.e. the nuclear and convective time scales become comparable.

Very Massive Stars Convection VMS usually posses very large (extending over more than 75% of M) convective cores during MS phase, evolving quasi-chemically homogeneously. This can be observed in Fig.(1.10—Left). We will discover more details about the convective history of a VMS in the Chp.(4).

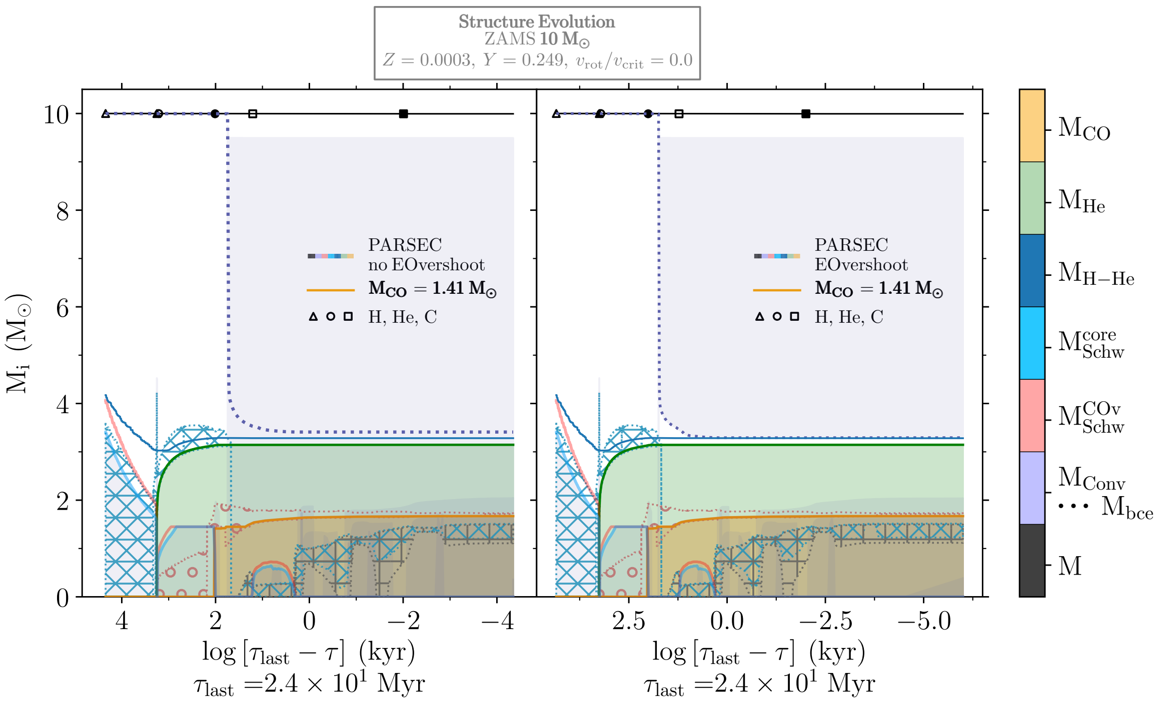

Figure 1.9: Stratification history for a star with Zero Age Main Sequence (ZAMS) mass $M = 10\ M_\odot$, metallicity Z=0.0003 and rotation velocity $v_{\rm rot}/v_{\rm crit} = 0.0$. Same notation symbols for phases as in Fig(1.1) are adopted. Respectively, M_{CO}, M_{He}, M_{H-He}, $M^{\rm COv}_{\rm Schw}$, $M_{\rm Conv}$, $M_{\rm bce}$ and M stand for the mass coordinates of: final mass of the CO core, mass of He core at H-burning end, mass of the H-He discontinuity, Schwarzschild-unstable convective core, Schwarzschild-unstable convective core with overshooting, mass coordinate of the Bottom of the Convective Envelope (BCE), total mass as a function of (logarithmic) time coordinate, until the last model at $\tau_{\rm last}$. The latter is a constant shift of coordinate time, reported below x-axis. Left – PARSEC output without convective overshooting of the envelope (EOvershooting); Right – same as Left, but with EOvershooting incorporated. The negligible effects of the mass loss rate, treated in Sec.(1.3.3), is due to the very low metallicity Z.

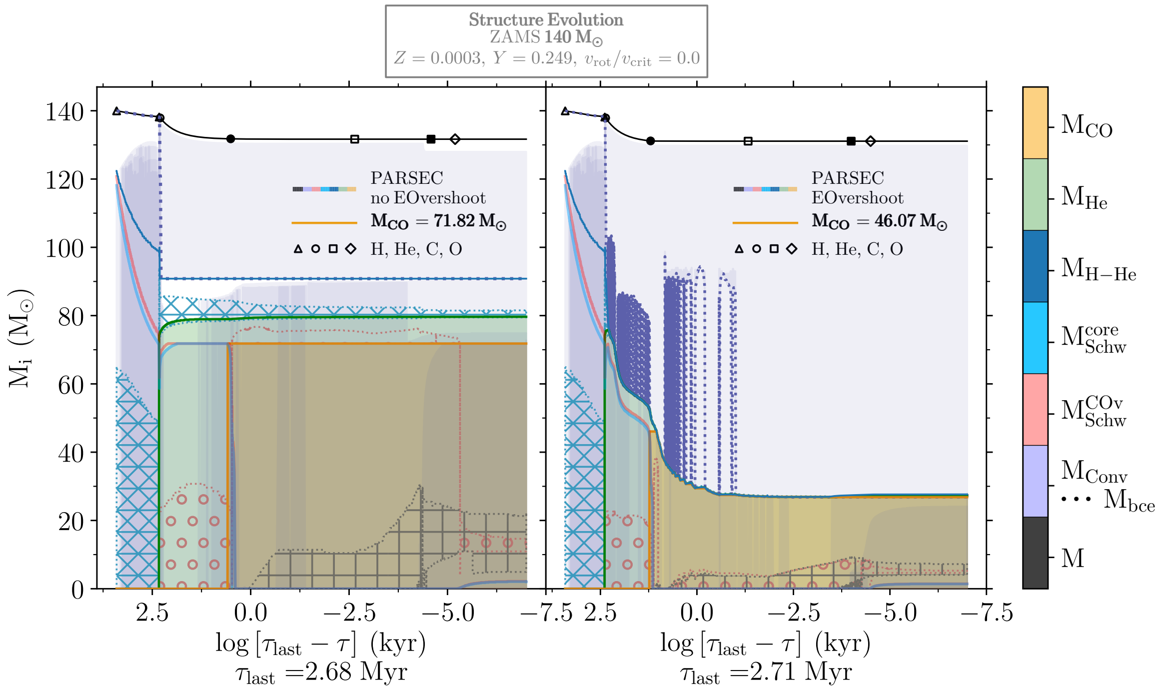

Figure 1.10: Stratification history for a star with Zero Age Main Sequence (ZAMS) mass $M = 140\ M_\odot$, metallicity Z=0.0003 and rotation velocity $v_{rot}/v_{crit} = 0.0$. Same notation symbols for phases as in Fig(1.1) are adopted, as well as same mass coordinates highlighted in Fig.(1.9). Left – PARSEC output without convective overshooting of the envelope (EOvershooting); Right – same as Left, but with EOvershooting incorporated.

1.3.3 Mass Loss

Typical P-cygni profiles of resonant spectral lines around hot (O-B) stars reveal that, already starting from $15\ M_\odot$, strong, line-driven, stellar winds lead to high *mass loss rates* $\dot{M}$. On the other hand, atmospheres of luminous cool giants are characterized by dust grains' continuum (mainly infrared) absorption of radiation, probably combined with pulsations, with same mass loss effect and even higher resulting rates.

Empirical and theoretical prescriptions The involved physical mechanisms are by now well understood, but the consequences of mass loss on evolution properties and final fates of massive stars are so relevant that continuous efforts have been put into refining *empirical and theoretical rates*. As we have seen in Sec.(1.3.1), depending on their initial mass, massive stars can undergo He core burning as RSGs or BSGs so, in principle, input physics of models should account for both line- and dust- driven winds.

Literature has known several prescriptions, but of course they must be adapted to the specific case. In particular:

a) For **massive luminous stars**, of O-B spectral type, the commonly adopted theoretical prescription for radiative line-driven winds is the one from Vink et al. (2001), [VKL01], which compares rather well with observations.

b) For **WR objects** the prescription in simulations depends on the WR subtype, a recent model being the one from Costa et al. (2020), [Cos+20].

c) For **cooler parts** of HR diagram the prescriptions are much more uncertain, so we must rely on observations only.

The seminal expression in de Jager et al. (1988), [JNH88], is generally used for parts of the HR diagram not covered by modern, accredited prescriptions:

$$\log\left(-\dot{\mathrm{M}}\right) = -8.16 + 1.77 \log\left(\frac{L}{L_\odot}\right) - 1.68 \log\left(\frac{T_{\mathrm{eff}}}{\mathrm{K}}\right) . \tag{1.12}$$

The metallicity Z dependence of the mass loss rate is commonly included with a scaling factor, resembling the well known Castor-Abbot-Klein (CAK) theory for line driven winds:

$$\dot{\mathrm{M}}\,(Z) = \dot{\mathrm{M}}\,(\mathrm{Z}_\odot)\left(\frac{Z}{Z_\odot}\right)^{\alpha} \qquad \text{with} \quad \alpha \simeq 0.66 - 0.85\,, \tag{1.13}$$

where $\alpha = 0.85$ is set for O-type and WN, while $\alpha = 0.66$ for WC and WO. In the above formula the initial metallicity, rather than the actual surface one, is used. Furthermore, in the presence of rotation, we shall see that the mass loss rates should be modified accordingly.

Effects on evolution Effects of mass loss on the evolutionary properties of massive stars are prominent during all the HR journey. Actually, as one can see from Eq.(1.12), $\dot{\mathrm{M}}$ depends mainly on both the luminosity and the effective temperature, i.e. on the HR diagram position (and on the interior properties of the star). Expressly

Core H burning
10^6 yr $\lesssim \tau_{\mathrm{MS}} \lesssim 10^7$ yr
$T_{\mathrm{ign}} \simeq 4 - 6 \times 10^7$ K

▶ Mass loss is quite efficient during H core burning, reaching peaks of $\dot{\mathrm{M}} = 10^{-6} - 10^{-5}\ \mathrm{M}_\odot\ \mathrm{yr}^{-1}$, and stars approach their ***Eddington luminosities***.

▶ Substantial reduction of the total mass and exposure to the surface of zones partially modified by the core H burning; some stars ($\mathrm{M} \gtrsim 60\ \mathrm{M}_\odot$) even become WR objects already during H core burning. In general bluer tracks are expected for higher $\dot{\mathrm{M}}$.

▶ In more massive stars, mass loss is strong enough to induce a reduction of the H convective core, such that

$$\dot{\mathrm{M}} \nearrow \;\Rightarrow \mathrm{M}_{\mathrm{He}} \searrow$$

i.e. the key He core at core H depletion M_{He} is reduced too.

▶ **Surface velocity reduction** in the case of rotating stars (see Sec.(1.3.4)); mass loss in general removes angular momentum, working just like a normal expansion of a rotating rigid body:

$$\dot{M} \nearrow \;\Rightarrow v_{\text{surf}} \searrow$$

This is particularly true during the MS phase, when $\dot{M}$ can be very high.

▶**NB** The above effect can be balanced by an enhanced *angular momentum transport* at low Z. In this case,

$$\dot{M} \searrow \;\Rightarrow v_{\text{surf}} \longrightarrow v_{\text{crit}} \,,$$

where v_{crit} stands for critical velocity, see Sec.(1.3.4).

Core He burning
$10^5\ \text{yr} \lesssim \tau_{\text{He}} \lesssim 10^6\ \text{yr}$

▶ Mass loss in this stage continues to peel off external layers of the stars, influencing their development into WR objects.

▶ Depending on $\dot{M}$, stars can reach RSGs or BSGs regions of HR diagram; strong *dust driven winds* on RSGs determines whether the star remains a RSG or become a WR (BSG).

- Stars entering the dust-driven wind phase at late stage of core He burning will have less time to lose mass, so they will remain RSG
- Stars entering the dust-driven wind phase at early stage of core He burning will have more time to lose mass, so they will evolve as BSG-WR

▶ Effects on CO core mass M_{CO}: strong $\dot{M}$ can progressively reduce He core, leading to WNE or even WC stage.

$$\dot{M} \nearrow \;\Rightarrow M_{\text{He}} \searrow$$

This reduction has the following effetcs:

- Thermostatic reaction to core reduction makes the He convective core **shrink** in mass, leaving a region of variable chemical composition;
- $\tau_{\text{He}} \nearrow$ ▸ $\text{L} \searrow$ ▸ $^{12}\text{C} \nearrow$ ▸ $\text{M}_{\text{CO}} \searrow$

▶ Mass loss during WNE/WC phase affects the CO core mass relation with initial star mass M, $\text{M}_{\text{CO}} - \text{M}$.

Low metallicity models evolve essentially at constant M, so that none of them becomes a WR; in particular, the most massive, non rotating ones, can develop an enhanced CO core mass,at the end of He-burning, which may overcome the limit for the onset of pair instabiity SN, i.e. $\text{M} \gtrsim 60\ \text{M}_{\odot}$, as the one in Fig.(1.10–Left).

Shell He burning

$\tau_{\text{He shell}} \overset{?}{\sim} \text{kyr}$

▶ In stars in which the He core is reduced by mass loss, the He convective shell forms in the region left by the receding He convective core. In this case, the He convective shell results hotter:

$$\text{M}_{\text{He}} \searrow \Rightarrow T_{\text{He-shell}} \nearrow$$

This can have some implications on nucleosynthesis.

Advanced nuclear burning stages

▶ Even in these stages, mass loss progressively reduces the mass of the H-rich envelope and of the He core, with sufficiently high masses.

Very Massive Stars Mass Loss In VMS mass loss plays the *pivotal role* in every stage of the evolution; with sufficient metallicities, its role overcomes every other factors' impact for evolution, determining the formation scenario of many WR species. This generally comes from the very high luminosities reached by these objects; highest values for $\dot{\text{M}}$ are reached after the C-burning ignition.

▶ **Similar final masses** are usually achieved by VM models with same metallicity, thanks to the very relevant mass loss. Of course, the chosen $\dot{\text{M}}$ prescription shall influence the fate of the VMS.

Fig(1.11) shows the evolution of the mass loss rates for various models at Z=0.0003 metallicity, following from left to right the age until the last model; the same is shown in Fig.(1.12) for Z=0.001 metallicity. One can see that higher masses are indeed subject to higher $\dot{\mathrm{M}}$; also a non trivial, mass-dependent evolution is expected in the more advanced stages; lastly, a systematically higher $\dot{\mathrm{M}}$ is present for higher Z.

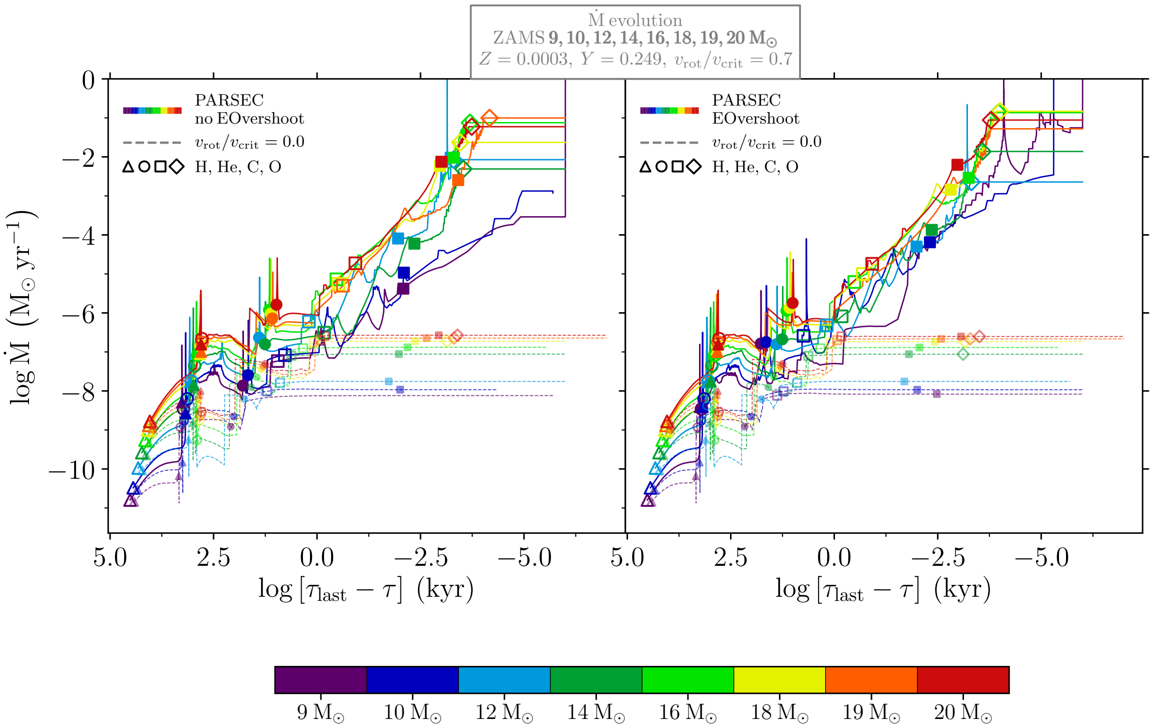

Figure 1.11: Evolution of mass loss rate $\dot{\mathrm{M}}$ for stars with Zero Age Main Sequence (ZAMS) mass $\mathrm{M} = 9 - 10 - 12 - 14 - 16 - 18 - 19 - 20\ \mathrm{M}_\odot$, metallicity Z=0.0003 and rotation velocity $v_{\rm rot}/v_{\rm crit} = 0.7$, until the last model. Color coding differentiate the masses, and same symbols for phases as in Fig(1.1) are adopted. Left — PARSEC output without convective overshooting of the envelope; Right — same as Left, but with EOvershooting incorporated. We can see that, for masses $\mathrm{M} \lesssim 18\ \mathrm{M}_\odot$, a consistently higher $\dot{\mathrm{M}}$ is achieved at the onset of C-burning, while for $\mathrm{M} \gtrsim 18\ \mathrm{M}_\odot$ the onset of C-burning sets the regime of slightly lower $\dot{\mathrm{M}}$ with respect to the previous phases. In all cases, the rate $\dot{\mathrm{M}}$ increases slightly during the MS; the difference with respect to the non rotating models shall be highlighted in Sec.(1.3.4).

Eddington parameter $\Gamma_{\rm Edd}$ As already said in Sect.(1.1), HE implies the existence of a maximum, Eddington luminosity $\mathrm{L}_{\rm Edd}$, setting the limit for the radiation pressure-driven luminosity. The more massive the star is, the larger the radiation pressure component, so essentially radiation gets to drive most of the luminosity L beyond $\mathrm{M} \gtrsim 100\ \mathrm{M}_\odot$, but for less massive stars a good fraction of radiation is present, too. A proper tool to know the

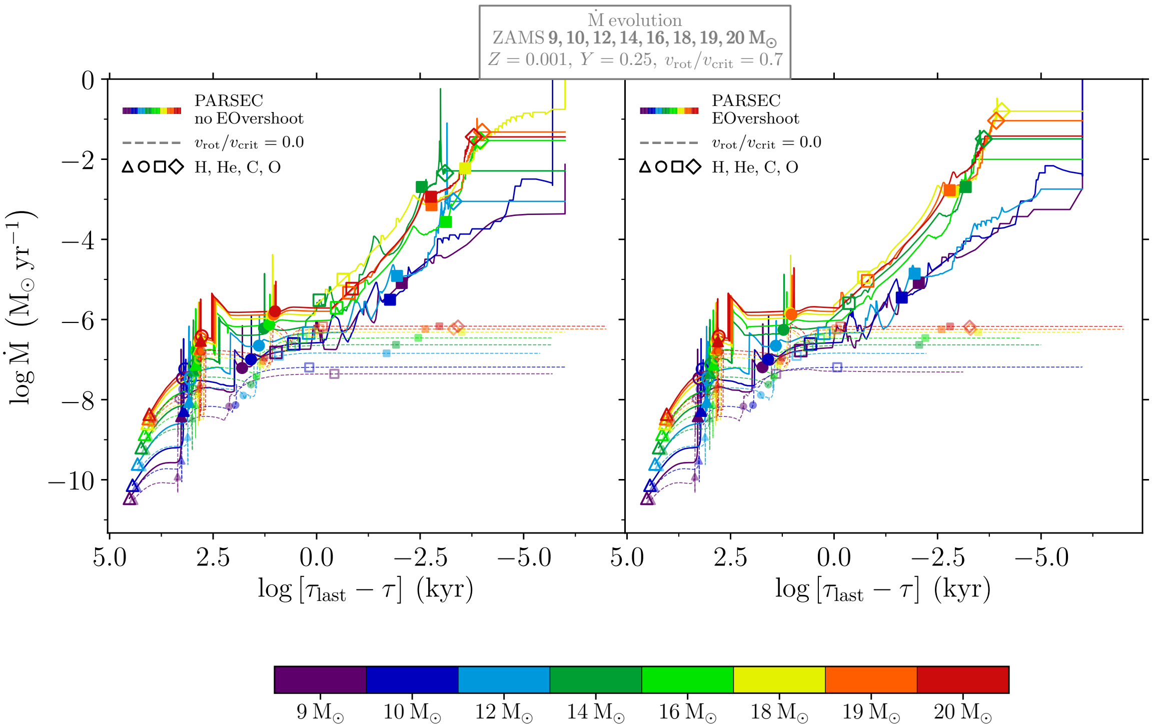

Figure 1.12: Evolution of mass loss rate $\dot{\rm M}$ for stars with Zero Age Main Sequence (ZAMS) mass $\rm M = 9 - 10 - 12 - 14 - 16 - 18 - 19 - 20\ M_\odot$, metallicity Z=0.0003 and rotation velocity $v_{\rm rot}/v_{\rm crit} = 0.7$, until the last model. Color coding differentiate the masses, and same symbols for phases as in Fig(1.1) are adopted. Left — PARSEC output without convective overshooting of the envelope; Right — same as Left, but with EOvershooting incorporated. We can see that, for all masses $\rm M \lesssim 20\ M_\odot$, a consistently higher $\dot{\rm M}$ is achieved at the onset of C-burning, differently as compared to the $\rm Z = 3 \times 10^{-3}$ case. In all cases, the rate $\dot{\rm M}$ increases slightly during the MS.

entity of $\rm L_{Edd}$ departure for massive stars is the so called *Eddington parameter* $\Gamma_{\rm Edd}$:

Eddington & Parameter

$$\Gamma_{\rm Edd} \equiv \frac{\rm L}{\rm L_{Edd}} \simeq \\ \simeq 2.63 \times 10^{-5} \left(\frac{\rm M_\odot}{\rm M}\right) \left(\frac{0.34\ {\rm cm^2\ g}}{\kappa}\right)^{-1} \left(\frac{\rm L}{\rm L_\odot}\right) , \tag{1.14}$$

where the value of $0.34\ {\rm cm^2\ g^{-1}}$ corresponds to the electron scattering opacity for $\rm X = 0.7$. Actually, the opacity κ in the atmosphere is larger than the electron scattering one, decreasing with temperature, and this motivates the generalized HD limit. Fig(1.13) shows the Eddington parameter evolution for model with Z=0.0003, with κ computed as if just electron scattering was present.

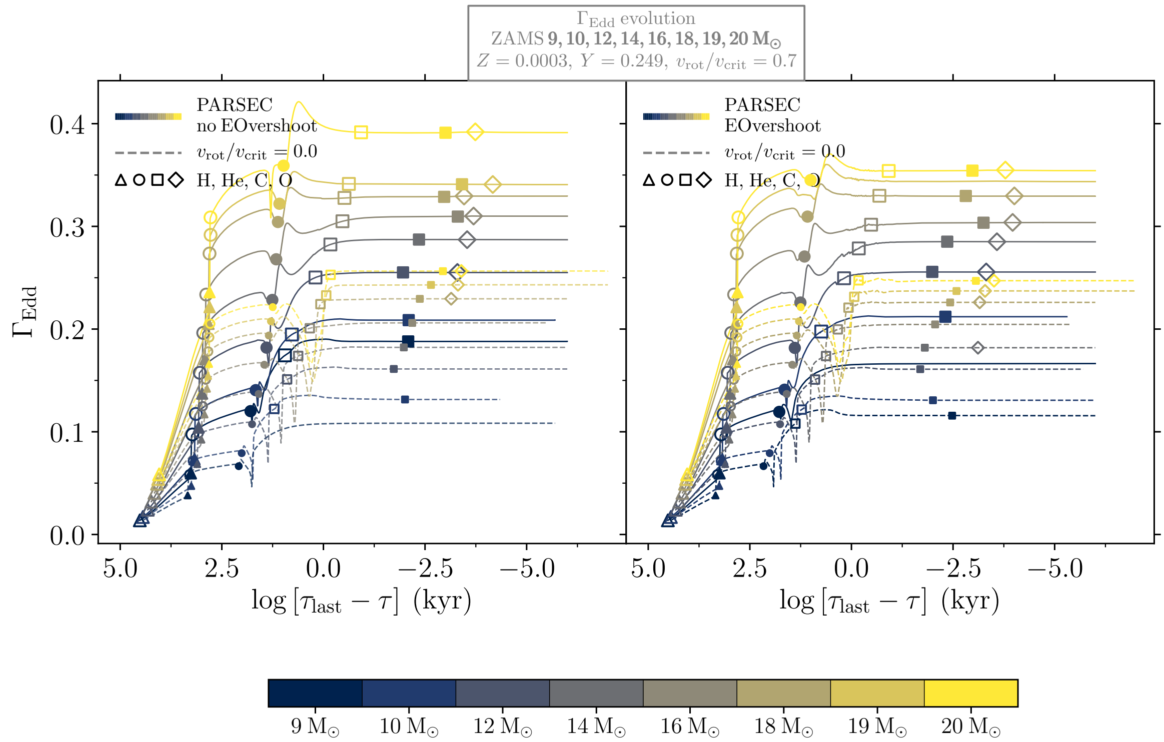

Figure 1.13: Evolution of the Eddington parameter $\Gamma_{\rm Edd}$ for stars with Zero Age Main Sequence (ZAMS) mass $M = 10M_\odot$, metallicity Z=0.0003 and rotation velocity $v_{\rm rot}/v_{\rm crit} = 0$, until the last model. Color coding differentiate the masses, and same symbols for phases as in Fig(1.1) are adopted. Left — PARSEC output without convective overshooting of the envelope; Right — same as Left, but with EOvershooting incorporated. One can immediately see that more massive stars approach the unstable limit $\Gamma_{\rm Edd} \gtrsim 1$ in the more advanced phases; the difference with respect to the non rotating models shall be highlighted in Sec.(1.3.4)

1.3.4 Rotation

Another very influent ingredient in SECs is given by *rotation*, which shall be acknowledged as equally important to convection and mass loss. With regards to massive stars, it is a well known fact that they are generally rapid rotators already starting from the MS phase; this rotation is also enhanced on advanced phases by the exceptional contraction leading to the presupernova stage. The main physical consequences of rotation are **a)** the centrifugal force, **b)** the angular momentum transport and **c)** the rotational mixing.

Centrifugal Force Rapidly rotating objects are naturally subject to a *centrifugal force* acting on the plane orthogonal to the rotation axis. Some important effects are

- **Spheroidal stellar shape**, spherical symmetry is no longer a good assumption and stellar structure equations need to be modified accordingly. This implies a latitude dependence of all interesting quantities, comprising radiative energy flux and effective temperature.

- **Gravity darkening** near the stellar equators, an (observationally confirmed) property caused by the fact that the stellar surface gravity is modified by the centrifugal force; the local surface flux of a rotating star, conversely, is proportional to the *effective surface gravity* g_{eff}, as shown by von Zeipel (1924) [von24].
  The surface gravity g is defined as

  Surface Gravity
  $$g \equiv \frac{GM}{r^2} \qquad \text{with} \quad [g] = \text{cm s}^{-2}$$

  In the above we obviously assumed a spherical object. To account for deformations of most real astrophysical objects, affected by the centrifugal force, one introduces the effective surface gravity g_{eff} as follows:

  Effective Surface Gravity
  $$g_{\text{eff}}(r) \equiv g + g_{\text{rot}} = \frac{GM}{r^2} - \frac{v_r^2}{r} \qquad \text{with} \quad g_{\text{eff}} \geq 0 \;\Rightarrow\; \text{Stability},$$

  and we have called v_r the rotational velocity at the radial coordinate $r(\theta, \phi)$; the stability criterion is usually referred to $g_{\text{eff}}(r_{\text{eq}})$, with r_{eq} being the photospheric radius at the equator. As a ruler, we report the value of $\log g$ for our Sun: $\log g_{\odot} \simeq 4.44$.
  NB Sometimes, for more massive stars, a relevant contribution to g_{eff} can be exerted by radiation pressure, with a term g_{rad} adding to g_{rot}.
- **Break-up rotation** occurs when gravity and centrifugal acceleration cancel each other at the equator, limiting the value of rotation rate for HE. This *critical velocity* v_{crit} is achieved when $g_{\text{eff}}(r_{\text{eq}}) \stackrel{!}{=} 0$, so that

  Break-Up Rotational Velocity
  $$\boxed{v_{\text{crit}} \equiv v_{\text{eq}} = \left(\frac{GM}{r_{\text{eq}}}\right)^{1/2} = \left(\frac{2}{3}\frac{GM}{r_{\text{p}}}\right)^{1/2}} \qquad \text{with} \quad r_{\text{eq}} = \frac{3}{2} r_{\text{p}},$$

  where we have used the fact that the pole, with coordinate R_{p}, is on the same potential surface as the equator, i.e. the virial theorem. As a ruler, we report the value of v_{crit} for our Sun: $v_{\text{crit}\odot} \simeq 357 \text{ km s}^{-1}$.
  NB Again, for massive stars near their Eddington luminosities radiation pressure slightly modifies this critical rotation.

Nowadays 1D routines usually account for these effects by adopting a *shellular* rotation law, namely each mass coordinate in the star is an isobaric layer with a constant angular velocity $\Omega_r = \Omega(r)$.

Angular Momentum Transport Due to the high rotation rates in massive stars, an efficient mechanism of *angular momentum transport* between the dense cores of massive stars and their expanded envelopes is needed, assuring the core does not reach a critical rate. As is done for convection, often a diffusive approximation is adopted,

DIFFUSION EQUATION MOMENTUM TRANSPORT

$$\rho r^2 \frac{\mathrm{d}r^2\Omega_r}{\mathrm{d}t} = \frac{\partial}{\partial r}\left(\rho r^4\, D \frac{\partial \Omega_r}{\partial r}\right) ,$$
$$\text{with} \qquad D = D_{\text{mix}} + D_{\text{shear}} + D_{\text{mer}} .$$

The total diffusive coefficient is produced by the sum of the different rotation instabilities:

- **Convective** diffusive coefficient, D_{mix}, namely the diffusion coefficient in the convective zones, introduced in Eq.(1.9) and computed with the MLT. It is properly the complex, turbulent mean of transport which in principle has to be treated with full 3D hydrodynamics.
- **Shear instability** diffusive coefficient, D_{shear}, originated by differentially rotating layers.
- **Meridional circulation** diffusive coefficient, D_{mer}, accounts for the transport of angular momentum by meridional flows, the latter being common features of all rotating fluids; they are required to maintain LTE conditions, and are essentially determined by the *rotation profile* of the star. When the star is initially in uniform rotation, the proper name is *Eddington-Sweet* circulation.
- (▶) **Magnetic torques & Gravity waves**, possibly additional angular momentum transport mechanisms are needed to find agreement with the slow spins of observed young neutron stars and white dwarfs. Both of the above can be present due to differential rotation, exerting significant torques to couple the rotation of the core with that of the stellar envelope.

Rotationally induced mixing The same processes that transport angular momentum in stars may also induce mixing, but *rotationally induced mixing* is worth a separate discussion in massive stars. The introduction of this additional mixing source is supported by both direct and more indirect observations; the first regards the need to explain enhanced surface abundances of He for fast, MS rotators; the latter comprise the Blue to Red (B/R) Supergiants number ratio and the nucleosynthesis signature of massive rotators in low-mass stars.
The relevant predicted effects of rotation with respect to mixing are

- **Larger cores** of He for a given MS mass and of CO for a given He-core mass, respectively; this altered ratio of core mass to envelope is expected to affect the late evolution of stars. Larger He-cores means also $\Rightarrow$ higher luminosities as supergiants and, consequently, higher mass loss rates.
- **Reduced disparity of Ledoux and Schwarzschild** criteria for stability against convection, by virtue of the additional mixing and effects on molecular weight gradients.
- **Quasi-chemically homogeneous** evolution: once a chemical stratification is established in a star, the gradients in composition usually prevent efficient rotationally induced transport processes in the interested layer; however, when the timescale of rotational mixing $\tau_{\text{mix,rot}}$ becomes shorter than the nuclear timescale τ_{nuc} (namely

the timescale over which the star evolves off the ZAMS and builds chemical stratification), these barriers may never establish, and the evolution is said to be *chemically homogeneous*.

However, **direct evidence** for rotational mixing, e.g. an observed correlation of surface enrichment with rotation in massive MS stars, has yet to be found. The reason can be twofold: **a)** most of abundance determinations for massive MS stars have been obtained for slow rotators (narrower absorption widths, easier recognitions); **b)** the effects of binarity, mass loss and magnetic fields might dominate in the vast majority of cases.

Effects on evolution Effects of these physical consequences of rotation on the evolutionary properties of massive stars are relevant in almost all phases, here we list them in order.

CORE H BURNING
$10^6 \text{ yr} \lesssim \tau_{\text{MS}} \lesssim 10^7 \text{ yr}$
$T_{\text{ign}} \simeq 4 - 6 \times 10^7 \text{ K}$

▶ Effective gravity g reduction due to both the centrifugal force and the angular momentum transport; this essentially makes the track *redder*.

$$g \searrow \Rightarrow \mathrm{T_{eff}} \searrow$$

▶ Additional rotational mixing determines

- a nearly **vertical evolution** of the tracks, since chemical homogeneity is favored.
- an increase of the size of the H-depleted core, making the track *brighter* and *cooler*; it is indeed a similar effect as the one due to convective core overshooting.

$$\textsc{Mixing} \nearrow \Rightarrow \mathrm{T_{eff}} \searrow$$

- an enrichment of the radiative envelope with ^{4}He and ^{14}N, with a consequent reduction of the opacity and *brighter* and *bluer* tracks.

$$\textsc{Mixing} \nearrow \Rightarrow \mathrm{T_{eff}} \nearrow$$

This mixing is due to both meridional circulation and shear turbulence in radiative zones, and due to convection in the convective ones.

▶ ***Mass loss rate modification*** due to the substantial changes in the evolutionary tracks. This is an indirect, though relevant, effect of stellar rotation.

▶ Efficient angular momentum transport, which increases with initial rotation velocity (as well as with initial mass):

$$\textsc{Mixing} \nearrow \Rightarrow \Delta J \nearrow$$

Which one of the above effects is predominant is usually determined by some factors, like metallicity Z, initial mass M or initial rotation velocity. Fig.(1.14) and Fig.(1.15) shows the HR plot and structural properties of relevant massive stars, namely $9\,\mathrm{M}_{\odot} \lesssim \mathrm{M} \lesssim 20\,\mathrm{M}_{\odot}$, in which a relatively high fraction of $v_{\mathrm{rot}}/v_{\mathrm{crit}}$ is ignited. These are the rotating counterparts of Fig.(1.5), and are expected to highlight the impact of different Z and M on the rotational effects regarding the tracks.

In general, brighter and redder tracks result in an enhanced rate of mass loss $\dot{\mathrm{M}}$, thus in a reduction of the total mass of the star during core H-burning, with important consequences on the minimum initial mass entering the WR stage during this phase. This can be observed in Fig.(1.11) and Fig.(1.12).
Finally, the enhancement of the ^{4}He and ^{14}N surface abundances with respect to the non-rotating models is evident from Fig.(1.8); the increase of He core mass at H-burning end can be also seen in Fig.(1.16), which serves as a rotating counterpart for Fig.(1.9).

Core He burning
$10^5\ \mathrm{yr} \lesssim \tau_{\mathrm{He}} \lesssim 10^6\ \mathrm{yr}$

▶ Influence whether the star becomes a RSG or remains RSG, key factor together with mass loss, see Sec.(1.3.3). In general, redward evolutions are favored, such that the number of RSG increases:

$$v_{\mathrm{rot}}/v_{\mathrm{crit}} \nearrow \Rightarrow \mathrm{RSG} \nearrow$$

▶ Super-Eddington luminosities are favored by rotation velocity for higher masses, as one can see in Fig.(1.13):

$$v_{\mathrm{rot}}/v_{\mathrm{crit}} \nearrow \Rightarrow \Gamma_{\mathrm{Edd}} \nearrow$$

▶ CO core mass greatly influenced, see Fig.(1.16), due to rotation-driven mixing, which adds up to the other mixing mechanisms and determines

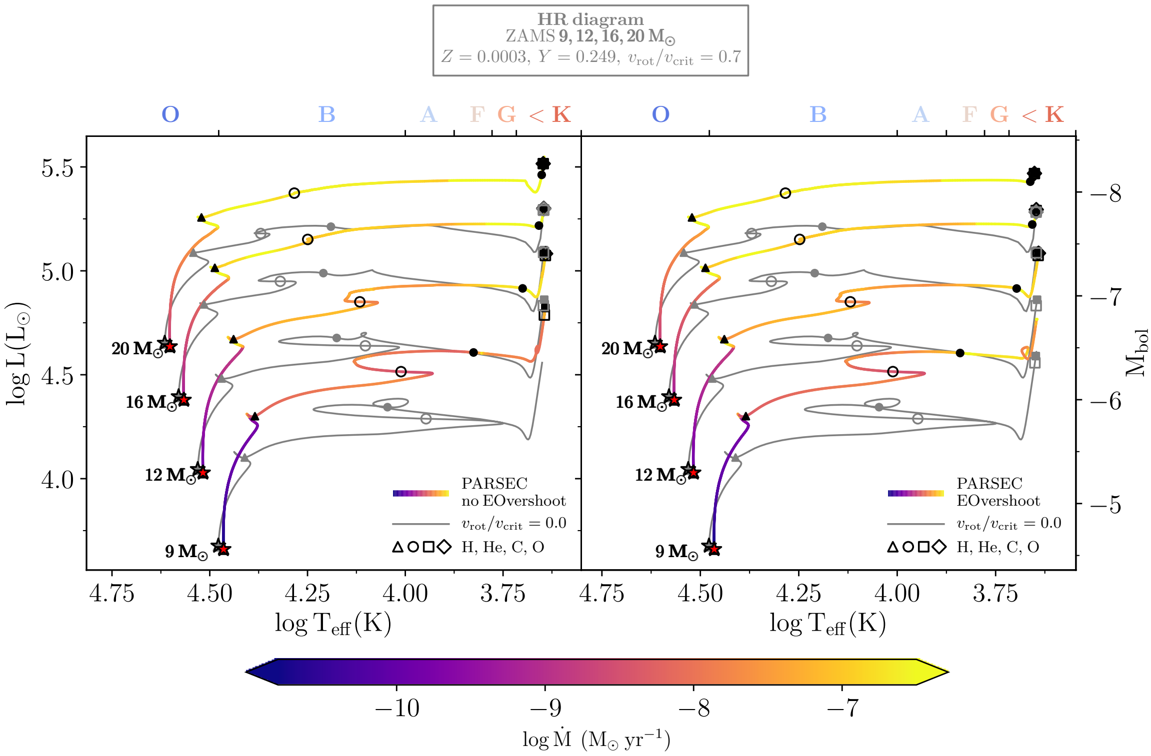

Figure 1.14: Evolutionary track for stars with Zero Age Main Sequence (ZAMS) mass $M = 9 - 12 - 16 - 20\ M_\odot$, metallicity Z=0.0003 and rotation velocity $v_{\rm rot}/v_{\rm crit} = 0.7$. Same color coding for $\dot{M}$ and symbols for phases as in Fig(1.1) are adopted. Left – PARSEC output without convective overshooting of the envelope (EOvershooting); Right – same as Left, but with EOvershooting incorporated. We can see that, for such very low metallicity, the evolutionary tracks are consistently *brighter* and *redder* at the end of the MS, which reveals a more relevant effect from g reduction and $M_{\rm He}$ increase.

- $M_{\rm CO} \nearrow$ ▸ ^{12}C $\searrow$

$\Rightarrow$ Compactness

- Diffusion of He burning products up to the base of the H-burning shell, that activates a primary ^{14}N.
- The effect of $M_{\rm CO} \nearrow$ can be challenged by the $\dot{M}$ one, see Sec.(1.3.3), especially with higher Z.

These effects are less important as the initial M increases: the larger M, the smaller the timescale over which the rotation-driven secular instabilities may operate.

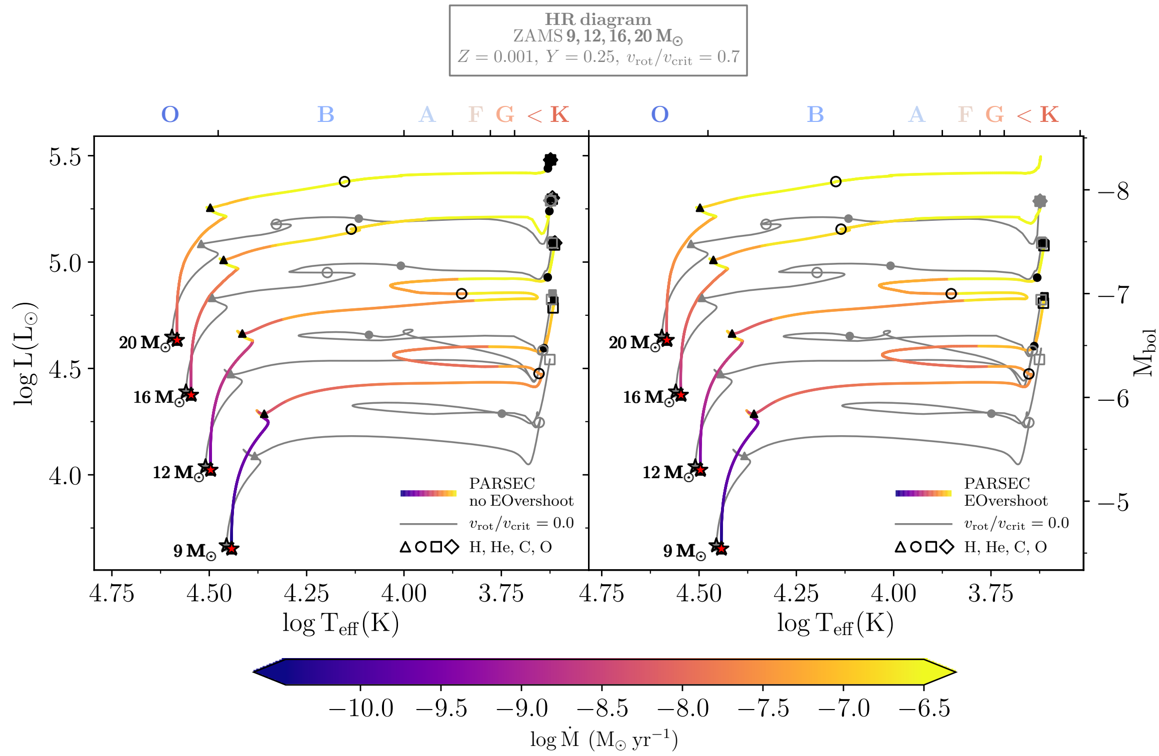

Figure 1.15: Evolutionary track for stars with Zero Age Main Sequence (ZAMS) mass $\mathrm{M} = 9-12-16-20\ \mathrm{M}_\odot$, metallicity Z=0.001 and rotation velocity $v_{\mathrm{rot}}/v_{\mathrm{crit}} = 0.7$. Same color coding for $\dot{\mathrm{M}}$ and symbols for phases as in Fig(1.1) are adopted. Left – PARSEC output without convective overshooting of the envelope (EOvershooting); Right – same as Left, but with EOvershooting incorporated.

Shell He burning

$\tau_{\text{He shell}} \overset{?}{\sim}$ kyr

▶ In stars in which the He core is increased by rotation-driven mixing, the He convective shell forms in the region produced by the continuous diffusion of He burning products driven by rotational mixing. In this case, as in the case of $\dot{\mathrm{M}}$-reduced He core, the He convective shell results hotter:

$$\mathrm{M_{He}} \searrow \;\Rightarrow\; \mathrm{T_{He\text{-}shell}} \nearrow$$

This can have some implications on nucleosynthesis.

Advanced nuclear burning stages

▶ Internal and total distribution of angular momentum adds to the CO core mass and $^{12}\mathrm{C}/^{16}\mathrm{O}$ ratio as a key evolutive parameter.

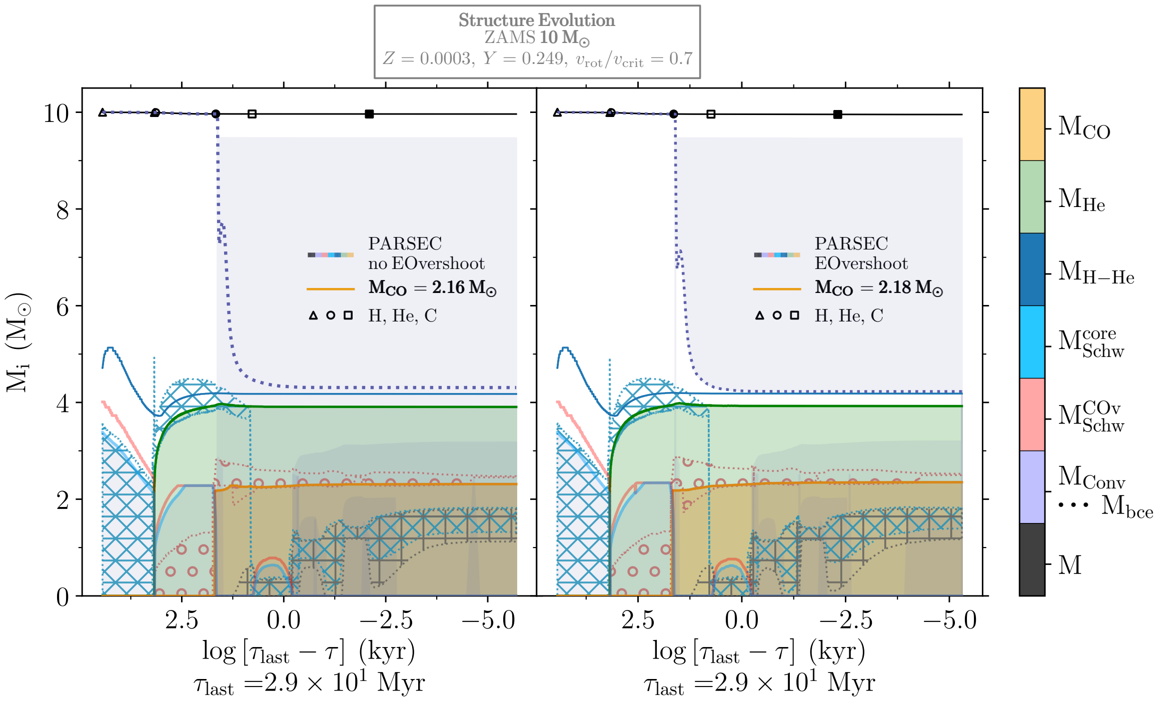

Figure 1.16: Stratification history for a star with Zero Age Main Sequence (ZAMS) mass $M = 10M_\odot$, metallicity Z=0.0003 and rotation velocity $v_{rot}/v_{crit} = 0.7$. Same color coding, notation and symbols for phases as in Fig(1.9) are adopted. Left – PARSEC output without convective overshooting of the envelope (EOvershooting); Right – same as Left, but with EOvershooting incorporated. An important difference in the core H-depletion mass M_{He} and also in the CO core mass M_{CO} can be immediately noticed, with respect to the non-rotating model.

▶ Deformation factor parameter, which enters the hydrostatic equilibrium equation to account for centrifugal force, starts to depart from unity only from Si burning,

> $\Rightarrow$ differences come mainly from the increased CO mass and the central ^{12}C mass fraction.

▶ Behavior like more massive stars, since the rotating models end up with more compact structures as a general rule.

▶ Increase of RSG explosions due to the reduced limiting mass for entering WR stage; this impacts the kind of expected supernova progenitors.

Very Massive Stars Rotation Some peculiarities of rotating Very Massive Stars are indeed expected.

- **Track** is even more vertically extended with respect to the, nearly vertical as well, tracks of less massive stars.
- **Timescales** The H-burning (thus, the total) lifetimes of VMS are lengthened by rotation, as in lower mass stars. The WR lifetimes is also increased, for the lowest Z, with possible consequences on the WR/O-type stars ratio.
- **WR limiting mass** Even more the with the lower mass counterparts, VMS limiting mass for entering the WR stage is *greatly* reduced; this would constitute an invaluable observational probe for VMS, when observing WR objects at young ages in starburst regions.
- **Evolutive parameter** was shown to be simply the CO core mass M_{CO}, which alone determines the final fate of a VMS (as a PISN or BH), differently with respect to lower masses.

1.4 The PARSEC code

We are lastly going to briefly present the main instrument of this work: the **PA**dova & **TR**ieste **S**tellar **E**volution **C**ode, PARSEC v2.0, a thorough revision and update of the stellar evolution code used in Padova for decades. Most of the following description is based on the original paper from A. Bressan et al. (2012), [Bre+12], but we will hint also at some recent developments in G. Costa et al. (2019), [Cos+19], and X. Fu (2018), [Fu+18].

Equation of State The more recent version of PARSEC, v2.0, adopts different tools to compute the *Equation of State* of stellar matter, depending on the temperature range:

- $\log \mathrm{T(K)} \leq 8.5$
  The FreeEOS code, version 2.2.1 [Irw], by A. W. Irwin is used and completely integrated in PARSEC, such that the EoS can be computed *on-the-fly*, with a higher degree of accuracy and computational cost, or be retrieved by means of pre-computed look-up tables with different combinations of abundances. As shown in A. Bressan et al. (2012), [Bre+12], this second method is accurate enough and preferred.
- $\log \mathrm{T(K)} > 8.5$
  For the highest temperatures, PARSEC adopts the routine from Timmes & Arnett (1999), [TA99], thanks to which a detail treatment of ***pair-creation*** is possible. An example of Timmes & Arnett outcome for the electrons' chemical potential in stellar matter is shown also in Fig.(3.7 – Left).

Nuclear reaction network The *nuclear reaction network* in PARSEC consists in 72 different reactions and 33 isotopic elements, from H to Zn. All reaction rates and Q-values are taken from the JINA REACLIB Database, Cyburt et al. (2010), [Cyb+10]. In the network, all the most important reactions from H to O burning are comprised, including pp chains, CNO tri-cycle, Ne-Na and Mg-Al chains and (reversed) α-captures. Electron neutrino energy losses and screening factors for all the reactions are included too.

Convection and Overshooting *Convection* in PARSEC is described by means of the mixing-legth theory, as explained in Sec.(1.3.2). The mixing length parameter $\alpha_{\rm MLT}$ in Eq.(1.8) is calibrated via a Solar model tested against helioseismologic constraints, and its value is set to $\alpha_{\rm MLT} = 1.74$. To test the stability of radiative zones against convection the Schwarzschild criterion in Eq.(1.10) is adopted, notwithstanding the possibility of large chemical gradients ∇_μ.
As for the convective *Overshooting*, PARSEC describes differently two types of regions in which this phenomenon can occur:

- **Core** Overshooting from the ***convective core*** is estimated within the framework of the MLT, Eq.(1.11), allowing the penetration of convective elements into the stable regions. The adopted mean free path, $\mathrm{d}_{\rm ov}^{\rm core}$, of convective elements *accross* the border of the unstable region, is calibrated with several methods (e.g., individual stars, DLEBs) and the overshooting parameter $\alpha_{\rm ov}^{\rm core}$ assumes different values, depending on the ZAMS masses on the considered models. In the context of massive stars, the following value is commonly adopted:

$$\boldsymbol{\alpha_{\rm ov}^{\rm core} = 0.4}\,.$$

- **Envelope Overshooting (EOv)** PARSEC also accounts for overshooting at the base of the ***convective envelope***, which is simply modelled by mixing the radiative region down to a distance of $\mathrm{d}_{\rm ov}^{\rm env} = \alpha_{\rm ov}^{\rm env} H_P$ from the formal Schwarzschild border. The overshooting parameter $\alpha_{\rm ov}^{\rm env}$ can assume the following values:

$$\boldsymbol{0.0 \leq \alpha_{\rm ov}^{\rm env} \leq 0.7}\,.$$

  This parameter is purely theoretical and thus it cannot be calibrated; we can nevertheless switch it on or off and discuss its implications on the evolution of stars, and this is precisely what we are going to do, see Sec.(1.4.1).

Mass loss rate The *mass loss rate* $\dot{\mathrm{M}}$ in PARSEC is treated with different prescriptions, depending on the HR diagram position of the models:

- $\log \mathbf{T_{eff}(K)} \gtrsim \mathbf{3.1}$
  This range is described by the relations from Vink et al. (2001), [VKL01], specifically designed to describe the BSGs phases. This formulation shows an almost linear, overall, dependence of the mass loss rates on the metallicity, as in Eq.(1.13), and PARSEC adopts $\alpha = 0.85$.

- **$\log \mathrm{T_{eff}(K)} \lesssim 3.1$**
  This range is described by the relations from de Jager et al. (1988), [JNH88], specifically designed to describe the RSGs phases. PARSEC adopts the same metallicity dependence of the BSGs prescription, i.e. as in Eq.(1.13) with $\alpha = 0.85$.

- **Wolf-Rayet stars**
  For these objects PARSEC adopts the recent mass loss prescription by Costa et al. (2020), [Cos+20], which includes an adapted formulation for the metallicity dependence, too.

Besides these seminal prescriptions, some recent results (e.g., Vink (2011), [Vin11]) are utilized to include the effects of evolution at near-Eddington luminosities, which can be quite interesting in the neighborhood of $\Gamma_{\mathrm{Edd}} \sim 1$ since **a)** enhanced $\dot{\mathrm{M}}$ are shown to be achieved; **b)** $\dot{\mathrm{M}}$ becomes almost independent of Z.

Rotation The *rotation* in PARSEC was implemented in recent years, Costa et al. (2019), [Cos+19]. The treatment follows the reasoning explained in Sec.(1.3.4): a ***shellular rotation*** law allows to include rotational effects into the stellar structure equations, preserving at the same time the 1D description. Overall, the models are are treated as differentially rotating rigid bodies, with isobaric surfaces which have to be computed under the Roche approximation. At each time step, PARSEC's tracks conserve angular momentum along the structure and atmosphere of the star, assuring conservation laws to hold throughout the age.
The parameter governing the evolutionary tracks and related to the rotational properties is, in PARSEC, the ***angular rotation rate*** $\Omega/\Omega_{\mathrm{crit}} = v_{\mathrm{rot}}/v_{\mathrm{crit}}$,

$$\boxed{\frac{\Omega}{\Omega_{\mathrm{crit}}} = \frac{v_{\mathrm{rot}}}{v_{\mathrm{crit}}}}\,, \tag{1.15}$$

that is the ratio between the angular velocity Ω and the break-up angular velocity Ω at the stellar surface, and we remembered the relation between the linear and angular velocities $v = \omega r$. This parameter is purely theoretical, and we will switch it on and off to discuss possible differences in the following, see Sec.(1.4.1).

Opacity We defer the discussion of *opacities in PARSEC* untill the following Chp.(2), in Sec.(2.3), since it deserves a separate, detailed treatment, being the protagonist of this work.

1.4.1 The stellar models grid

In this section we present the *stellar models grid* employed in this work, Tab.(1.1), Tab.(1.2) and Tab.(1.3). We are including all the computed models during the course of the thesis, but not each one of them has been considered for a detailed analysis: the studied ones are to be presented in the inherent chapters, Chp.(3) and Chp.(4), in their respective contexts of interest. As for the other ones: we have nevertheless used them as a test of PARSEC's new implementations, stability into convergence, and finally as a useful check for many of the above cited evolutionary properties of massive stars.

ZAMS masses M PARSEC model coverage on *ZAMS masses M* is $0.1 \leq \mathrm{M}(\mathrm{M}_\odot) \leq 350$. We are going to concentrate on the massive models, and we will run our code, at least once, for ZAMS masses ranging from 9 $\mathrm{M}_\odot$ to 140 $\mathrm{M}_\odot$, as in Tab.(1.1) and here below:

$$\mathbf{M = 9,\ 10,\ 12,\ 14,\ 16,\ 18,\ 19,\ 20,\ 40,\ 60,\ 140\ M_\odot}\ .$$

This means that we are producing both massive and very massive stellar models, at least up to the core C-burning start and at most up to the core O-burning start.

Metallicity Z PARSEC model coverage on *metallicity Z* is $0.0005 \leq \mathrm{Z} \leq 0.07$. We are going to produce models assuming only *three distinct* values for Z, chosen as a reference for a very poor, middle range and solar-like metal mass fraction. The reference compositions are the following:

Z=0.0003	Y=0.249	X=0.751	$[\mathrm{Fe/H}] \simeq [\mathrm{M/H}] = -1.714$
Z=0.001	Y=0.250	X=0.749	$[\mathrm{Fe/H}] \simeq [\mathrm{M/H}] = -1.190$
Z=0.014	Y=0.273	X=0.713	$[\mathrm{Fe/H}] \simeq [\mathrm{M/H}] = -0.023$.

These values are chosen assuming scaled solar mixtures based on Caffau et al.(2011), [Caf+11]. At a given initial metal content Z, the initial Helium, Hydrogen and metal contents, Y, X and [Fe/H] respectively, are given by

$$\mathrm{Y} = \frac{\Delta \mathrm{Y}}{\Delta \mathrm{Z}} = \mathrm{Z} + \mathrm{Y_P} = 1.78 \times \mathrm{Z} + 0.2485\,,$$

$$[\mathrm{Fe/H}] \simeq [\mathrm{M/H}] = \log\left[\frac{\mathrm{Z/X}}{0.0207}\right]\,,$$

$$\mathrm{X} = 1 - \mathrm{Y} - \mathrm{Z}\,,$$

where we used the primordial Helium abundance $\mathrm{Y_P}$, obtained from the solar calibration in Bressan et al. (2012), [Bre+12], and the $\Delta\mathrm{Y}/\Delta\mathrm{Z}$ is commonly known as helium-to-metals enrichment ratio.

Angular rotation rate $v_{\mathrm{rot}}/v_{\mathrm{crit}}$ We are switching on and off an *angular rotation rate* $v_{\mathrm{rot}}/v_{\mathrm{crit}} = 0.7$ at each value of ZAMS mass M$< 20\ \mathrm{M}_\odot$ and for each metallicity Z listed above. This fraction is chosen to be quite high, with the purpose to enhance differences with the non-rotating ounterparts. Summarizing:

$$\boldsymbol{v_{\mathrm{rot}}/v_{\mathrm{crit}} = 0.0} \qquad \mathrm{M} \in [9, 140]\ \mathrm{M}_\odot$$

$$\boldsymbol{v_{\mathrm{rot}}/v_{\mathrm{crit}} = 0.7} \qquad \mathrm{M} \in [9, 20]\ \mathrm{M}_\odot$$

The higher masses as M>20 M$_\odot$ indeed are expected, from observations, to have rotating counterparts; however, these models are also highly unstable in PARSEC, and we defer the study of these to future works.

Envelope Overshooting $\boldsymbol{\alpha_{\mathrm{ov}}^{\mathrm{env}}}$ We are lastly switching on and off an Envelope Overshooting (EOv), characterized by overshooting parameter $\boldsymbol{\alpha_{\mathrm{ov}}^{\mathrm{env}} = 0.7}$, at each value of ZAMS mass M and for each metallicity Z listed above. Summarizing:

$$\boldsymbol{\alpha_{\mathrm{ov}}^{\mathrm{env}} = 0.0} \qquad \mathrm{M} \in [9, 140]\ \mathrm{M}_\odot$$
$$\boldsymbol{\alpha_{\mathrm{ov}}^{\mathrm{env}} = 0.7} \qquad \mathrm{M} \in [9, 140]\ \mathrm{M}_\odot$$

Z=0.0003		$v_{\rm rot}/v_{\rm crit}$ = 0.0		$v_{\rm rot}/v_{\rm crit}$ = 0.7	
		no EOv	EOv	no EOv	EOv
ZAMS ($M_\odot$)	9	✓	✓	✓	✓
	10	✓	✓	✓	✓
	12	✓	✓	✓	✓
	14	✓	✓	✓	✓
	16	✓	✓	✓	✓
	18	✓	✓	✓	✓
	19	✓	✓	✓	✓
	20	✓	✓	✓	✓
	40	✓	✓	✗	✗
	60	✓	✓	✗	✗
	140	✓	✓	✗	✗

Table 1.1: Stellar models grid for Z=0.0003 and all the ZAMS masses M, rotational rate $v_{\rm rot}/v_{\rm crit}$ and EOv parameter $\alpha_{\rm ov}^{\rm env}$ used for this work. The following notation for the symbols is adopted:

- ✓ Black checkmarks indicate that the model has been computed but did not reach the core C-burning start; a single re-run of PARSEC, with relaxed conditions for convergence, would have probably do the work up until the end of AGB stage, which is often numerically difficult;
- ✗ Red-crossed models has not been computed, mainly because of the need of multiple runs with different conditions for convergence;
- ✓ Green checkmarks label the computed models which ignited core C-burning and went also beyond the stage. We see that this is the majority of cases.

Z=0.001		$v_{\rm rot}/v_{\rm crit} = 0.0$		$v_{\rm rot}/v_{\rm crit} = 0.7$	
		no EOv	EOv	no EOv	EOv
ZAMS ($M_\odot$)	9	✓	✓	✓	✓
	10	✓	✓	✓	✓
	12	✓	✓	✓	✓
	14	✓	✓	✓	✓
	16	✓	✓	✓	✓
	18	✓	✓	✓	✓
	19	✓	✓	✓	✓
	20	✓	✓	✓	✓
	40	✓	✓	✗	✗
	60	✓	✓	✗	✗
	140	✓	✓	✗	✗

Table 1.2: Stellar models grid for Z=0.001 and all the ZAMS masses M, rotational rate $v_{\rm rot}/v_{\rm crit}$ and EOv parameter $\alpha_{\rm ov}^{\rm env}$ used for this work. The same notation for the symbols as in Tab.(1.1) is adopted.

Z=0.014		$v_{\rm rot}/v_{\rm crit} = 0.0$		$v_{\rm rot}/v_{\rm crit} = 0.7$	
		no EOv	EOv	no EOv	EOv
ZAMS ($M_\odot$)	9	✓	✓	✓	✓
	10	✓	✓	✓	✓
	12	✓	✓	✓	✓
	14	✓	✓	✓	✓
	16	✓	✓	✓	✓
	18	✓	✓	✓	✓
	19	✓	✓	✓	✓
	20	✓	✓	✓	✓
	40	✗	✗	✗	✗
	60	✗	✗	✗	✗
	140	✗	✗	✗	✗

Table 1.3: Stellar models grid for Z=0.014 and all the ZAMS masses M, rotational rate $v_{\rm rot}/v_{\rm crit}$ and EOv parameter $\alpha_{\rm ov}^{\rm env}$ used for this work. The same notation for the symbols as in Tab.(1.1) is adopted.

2

Opacity: Physics and Prescriptions

This chapter introduces a general picture of stellar opacities, with a special stress on those of interest for massive stars. The whole range of temperatures, for astrophysical interest, is covered, and a hint on how the different contributions are usually implemented in Stellar Evolution Codes (SECs) is also comprised. The discussion starts with the *radiative opacities* $\kappa_{\rm rad}$, which is perhaps the most essential ingredient, for the energy transport theory, in governing the structure and evolution of massive stars, see Sec.(2.1); a brief comment on an alternative source of energy transport, the *conductive opacities* $\kappa_{\rm cd}$, is reported in Sec.(2.2), for future utility; lastly, an overview of PARSEC *code's input physics*, with an example of a run's outcome, is given in Sec.(2.3).

The chapter **a)** lays the basis of the following treatments in Chp.(3), where we will discuss a renewed treatment of the high energy, $\log {\rm T(K)} \gtrsim 8.7$, conductive and continuum radiative opacity, and describe the consequent update implemented in PARSEC; **b)** it will help on the presentation of a new approach to the middle range energy, $4.1 \leq \log {\rm T(K)} \leq 8.7$, continuum and line radiative opacity, presented in Chp.(4).

2.1 Radiative opacity $\kappa_{\rm rad}$

Radiative opacity, $\kappa_{\rm rad}$, is a fundamental property of a material, determining the amount of radiation absorbed and scattered and being the key ingredient for any efficient energy transport theory describing the (stellar) matter. In general, the opacity is dependent on the radiation, material temperature and density of the medium, as well as on the wavelength of the incoming radiation. Furthermore, past literature have known several examples of opacity playing a ***major role*** in stellar modeling, including stellar evolution, but also pulsation and large-scale quantities determination.

As for the massive stars, we know that usually large convective cores are developed during the first phases of evolution, and often deep convective envelopes are shared towards the cooler parts of their HR diagram, see e.g. Fig.(1.9) of Fig.(1.10); however, radiative opacity is expected to play a pivotal role, both in the deep interiors once more advanced stages are encountered, and in the outer layers, during their Blue Loops.
It is therefor of prior importance to introduce $\kappa_{\rm rad}$, with all of its contributions which go

under the name of *monochromatic opacities* κ_ν, and subsequently present their harmonic sum, the *Rosseland mean* κ, suitable for diffusive media.

The monochromatic opacity κ_ν The energy transport by random thermal motions of particles, either radiation or gas particles, is described by Eq.(1.3). A lot of physical processes contribute to the resistance of the stellar medium to the flow of energy and, in general, for a given process' mean free path l_ν, we can define a monochromatic mass absorption coefficient, or *monochromatic opacity*, κ_ν, as follows

MONOCHROMATIC OPACITY
$$\kappa_\nu \equiv \frac{1}{l_\nu\,\rho} \qquad \text{with} \qquad [\kappa_\nu] = \mathrm{cm}^2\,\mathrm{g}^{-1}\,. \tag{2.1}$$

In the case of radiative equilibrium, namely when energy is majorly transported by radiation, the monochromatic opacity is built up by several addenda, which are to be distinguished into *continuum* and *line* terms. These are listed below:

	SCATTERING $\kappa_\nu^{(\mathrm{s})}$	ABSORPTION $\kappa_\nu^{(\mathrm{a})}$
CONTINUUM	Rayleigh $\kappa_{\nu,\mathrm{R}}$ Electron κ_e	Bound-free $\kappa_{\nu,\mathrm{bf}}$ Free-free $\kappa_{\nu,\mathrm{ff}}$ Collision-induced $\kappa_{\nu,\mathrm{CIA}}$
LINES		Atoms bound-bound $\kappa_{\nu,\mathrm{bb}}$ Molecular band $\kappa_{\nu,\mathrm{mol}}$

where we notice that electron scattering (Thomson) opacity κ_e is the only contribution independent from wavelength. The above picture leads to the total monochromatic opacity κ_ν as a function of wavelength, for each specie j:

$$\kappa_\nu = \sum_j \kappa_\nu^{(\mathrm{s}),j} + \kappa_\nu^{(\mathrm{a}),j} = \tag{2.2}$$
$$= \sum_j \underbrace{\kappa_{\nu,\mathrm{R}}^j + \kappa_\mathrm{e}^j}_{(\mathrm{s})} + \underbrace{\kappa_{\nu,\mathrm{bf}}^j + \kappa_{\nu,\mathrm{ff}}^j + \kappa_{\nu,\mathrm{CIA}}^j + \kappa_{\nu,\mathrm{bb}}^j + \kappa_{\nu,\mathrm{mol}}^j}_{(\mathrm{a})}\,.$$

We expect that $\kappa_\nu = \kappa_\nu\,(\nu, \rho, \mathrm{T}, \mathrm{Z})$, namely the monochromatic opacity should depend on chemical composition and two of the three state variables T, P or ρ.

The Rosseland Mean κ Once one is able to add up all the monochromatic mass absorption coefficients as in Eq.(2.2), the usual procedure is to obtain a measure of a mean opacity κ, by means of an appropriate average. In stellar interiors, where both LTE and diffusion approximation are fulfilled, it is customary to take the *Rosseland mean* of κ_ν in Eq.(2.2), due to the Norwegian astronomer Svein Rosseland (1894-1985). It basically consists in a harmonic mean with the weighting function $\partial B_\nu/\partial \mathrm{T}$:

Rosseland Mean Opacity

$$\frac{1}{\kappa} \equiv \frac{\int_0^\infty \frac{1}{\kappa_\nu}\frac{\partial B_\nu}{\partial \mathrm{T}}\,d\nu}{\int_0^\infty \frac{\partial B_\nu}{\partial \mathrm{T}}\,d\nu}$$

$$\text{with} \quad B_\nu(\mathrm{T}) = \frac{2h}{c^2}\frac{\nu^3}{e^{h\nu/k\mathrm{T}}-1}$$

$$[B_\nu] = \mathrm{erg\ cm^2\ s^{-1}\ Hz^{-1}\ sr^{-1}}\,.$$

Here, of course, B_ν is the LTE specific intensity, or simply the Planckian of the radiation field. This function weights the high frequencies more than the low ones, since $\partial B_\nu/\partial \mathrm{T}$ has a maximum at $h\nu \simeq 3.83\,k\mathrm{T}$; this means that Rosseland mean tends to emphasize spectral regions of weak absorption, i.e. low-κ, being consequently appropriate for optically thick (diffusive) regions.

It is instructive to look at the form of κ when the total monochromatic opacity κ_ν can be written in a simple power-law form, $\kappa_\nu \propto \nu^{-n}$:

$$\frac{\partial B_\nu}{\partial \mathrm{T}} = \frac{\partial}{\partial \mathrm{T}}\left[\frac{2h}{c^2}\frac{\nu^3}{e^{h\nu/k\mathrm{T}}-1}\right] = \frac{2h^2\nu^4}{c^2k\mathrm{T}^2}\frac{e^{h\nu/k\mathrm{T}}}{\left(e^{h\nu/k\mathrm{T}-1}\right)^2}\,,$$

$$\frac{1}{\kappa} \propto \frac{\int_0^\infty \nu^{n+4}\frac{e^{h\nu/k\mathrm{T}}}{\left(e^{h\nu/k\mathrm{T}}-1\right)^2}\,d\nu}{\int_0^\infty \nu^4\frac{e^{h\nu/k\mathrm{T}}}{\left(e^{h\nu/k\mathrm{T}}-1\right)^2}\,d\nu} \propto \left(\frac{k\mathrm{T}}{h}\right)^n \underbrace{\frac{\int_0^\infty x^{n+4}\frac{e^x}{\left(e^x-1\right)^2}\,d\nu}{\int_0^\infty x^4\frac{e^x}{\left(e^x-1\right)^2}\,d\nu}}_{(\star)} \propto \mathrm{T}^n\,,$$

$$\kappa_\nu \propto \nu^{-n} \quad \Rightarrow \quad \kappa \propto \mathrm{T}^{-n}\,, \tag{2.3}$$

where we have called $x = h\nu/k\mathrm{T}$ and in the last line we have used that fact that the integral $(\star)$ is a known numerical quantity. This behavior follows since the mean opacity must drop as the number of high energy photons increases.
We lastly present a useful way to express the Rosseland mean, for a process with mean free path l_ν:

$$\frac{1}{\kappa} = \frac{\int_0^\infty \frac{1}{\kappa_\nu}\frac{\partial B_\nu}{\partial \mathrm{T}}\,d\nu}{\int_0^\infty \frac{\partial B_\nu}{\partial \mathrm{T}}\,d\nu} \overset{\text{Eq.(2.1)}}{=} \frac{\int_0^\infty \rho\, l_\nu \frac{\partial}{\partial \mathrm{T}}\left[\frac{\nu^3}{e^{h\nu/k\mathrm{T}}-1}\right]d\nu}{\int_0^\infty \frac{\partial}{\partial \mathrm{T}}\left[\frac{\nu^3}{e^{h\nu/k\mathrm{T}}-1}\right]d\nu} =$$

$$= \frac{\rho}{n_e\sigma_{\mathrm{Th}}}\underbrace{\frac{\int_0^\infty \tilde{l}_\nu \frac{\partial}{\partial \mathrm{T}}\left[\nu^3 b_\nu\right]\,d\nu}{\int_0^\infty \frac{\partial}{\partial \mathrm{T}}\left[\nu^3 b_\nu\right]\,d\nu}}_{:=\Lambda} = \frac{\rho}{n_e\sigma_{\mathrm{Th}}}\Lambda(\mathrm{T})$$

$$\Rightarrow \quad \boxed{\boldsymbol{\kappa = \frac{n_e \sigma_{\mathrm{Th}}}{\rho} \frac{1}{\Lambda\,(\mathrm{T})}}} \,, \tag{2.4}$$

where we have defined an adimensional mean free path $\tilde{l}_\nu = l_\nu n_e \sigma_{\mathrm{Th}}$, the phase-space distribution $b_\nu = \left[\exp\left(h\nu/k\mathrm{T}\right) - 1\right]^{-1}$ and an adimensional *Rosseland mean free path* $\Lambda\,(\mathrm{T})$. This last quantity shall be useful for parameterizations of electron scattering, see Sec.(2.1.1), and inherits the dependences of the (dimensioful) mean free path l_ν.

Summary In the following subsections, Sec.(2.1.1) and Sec.(2.1.2), we will give a description of the several processes quoted above. Each of them is particularly relevant in different temperature ranges, and we can *summarize* this as

High Temperatures $\log\mathrm{T} \gtrsim 6$	▸ $\mathbf{6 \lesssim \log T \lesssim 8.7}$ Thomson	$\kappa_{\mathrm{Th}} \propto$ cost
	▸ $\mathbf{\log T \gtrsim 8.7}$ Compton	$\kappa_{\mathrm{P83}} \propto \rho \mathrm{T}^{-2}$
Mid Temperatures $4 \lesssim \log\mathrm{T} \lesssim 6$	▸ Free-free	$\kappa_{\mathrm{ff}} \propto \rho \mathrm{T}^{-7/2}$
	▸ Bound-free	$\kappa_{\mathrm{bf}} \propto \mathrm{Z} \rho \mathrm{T}^{-7/2}$
	▸ Bound-bound	κ_{bb}
Low Temperatures $3.2 \lesssim \log\mathrm{T} \lesssim 4$	▸ $\mathbf{3.5 \lesssim \log T \lesssim 4}$ H^-	$\kappa_{\mathrm{H}^-} \propto \mathrm{Z} \rho^{1/2} \mathrm{T}^{9}$
	▸ $\mathbf{3.2 \lesssim \log T \lesssim 3.6}$ Molecules	κ_{mol}
	▸ $\mathbf{\log T \lesssim 3.2}$ Dust grains	κ_{dust}

Here we have introduced the opacity for Compton and Thomson scattering, κ_{P83} and κ_{Th}, see Chp.(3), for the negative hydrogen ion κ_{H^-}, which is a bound-free process, and for dust grains κ_{dust}, of interest for very cool stellar atmospheres.
The simple power-law form quoted arise as a consequence of $\kappa_\nu \propto \nu^{-n}$, as seen above. For lines absorptions there is no simple approximation for those millions of transitions to be taken into account; one has to rely on complex *line lists*, as we shall see in Sec.(2.1.2).

2.1.1 Continuum sources

This section describes the physical processes sourcing stellar matter opacity for a *continuous spectrum* of energies of photons. These are both scattering and absorption phenomena, and comprise

1) Electron scattering $\quad e^- + \gamma \rightarrow e^- + \gamma$

2) Rayleigh scattering $\quad N + \gamma \rightarrow N + \gamma'$

3) Free-free absorption $\quad N + (\pm) + \gamma \rightarrow N + (\pm)$

4) Bound-free absorption $\quad N + \gamma \rightarrow N^{(\pm)} + (\pm)$

where N denotes a nucleus, γ' is a photon with a frequency ν' and $(\pm)$ is an elementary charge, allowed by charge conservation laws. These sources were the first to be introduced in early radiative transfer studies in stellar matter, due to their major importance in fully ionized plasmas, i.e. the deep stellar interiors, and their relatively simple theoretical framework; this latter consent the usage of analytic prescriptions, often depending on the mixture properties in a simple way, facilitating the implementation in SECs.

Electron scattering $\quad e^- + \gamma \rightarrow e^- + \gamma$

We are treating both the classical Non Relativistic (NR) and Ultra Relativistic (UR) limits of the electron scattering, since this lays the basis of Chp.(3) and both limits are invaluably important in the context of massive stars.

- ***Thomson scattering*** $\quad h\nu \ll m_e c^2$

  Thomson scattering is a conservative ($\nu = \nu'$) and isotropic process, which can be assimilated to an absorption. It happens when an impingant electromagnetic wave hits a free electron, which emits (classical) dipole radiation, with

$$\sigma_{\rm Th} = \frac{8\pi}{3}\left(\frac{e^2}{m_e c^2}\right)^2 = 6.652 \times 10^{-25}\ \mathrm{cm}^2\ ,$$

  namely the Thomson cross section. The monochromatic opacity, $\kappa_{\rm e}$, for Thomson scattering can be found by dividing $\sigma_{\rm Th}$ by the unit mass of the gas of targets, namely $\rho/n_e \overset{\text{Eq.(1.6)}}{=} \mu_{\rm e} m_u$, so that

$$\kappa_{\rm Th} = \frac{\sigma_{\rm Th}}{\mu_{\rm e} m_u} \overset{\text{Eq.(1.7)}}{=} 0.20\,(1+\mathrm{X})\ \ \mathrm{cm}^2\ \mathrm{g}^{-1}\ , \tag{2.5}$$

  which is explicitly independent of frequency, giving also directly the expression for its Rosseland mean, if Thomson scattering was the only source of opacity. We have also used the fact that, when stellar material is completely ionized, $\mu_{\rm e} = 2/(1+\mathrm{X})$, from Eq.(1.7). When the degree of ionization drops, $\mu_{\rm e} \nearrow$ and $\kappa_{\rm Th} \swarrow$.

- ***Compton scattering*** $\quad h\nu \gtrsim m_e c^2$

  Compton scattering is the relativistic limit of the Thomson process, and is expected to occur at temperatures as high as $\log \mathrm{T} \gtrsim 8.7$. The electromagnetic wave is impinging with a reduced differential cross section,

$$\left.\frac{d\sigma_{\nu,\rm e}}{d\Omega}\right|_{\substack{\rm lab\\ \rm unpol}} = \frac{1}{32\pi^2}\left(\frac{e^2}{m_e c^2}\right)^2\left(\frac{\nu'}{\nu}\right)^2\left(\frac{\nu}{\nu'} + \frac{\nu'}{\nu} - \sin^2\theta\right)\ \mathrm{cm}^2\ \mathrm{sr}^{-1}\ , \tag{2.6}$$

  namely the **fully unpolarized Klein-Nishina cross section**. This is evaluated in the laboratory frame, in which the electron is at rest; ν' is the (reduced) frequency of the scattered photon, θ the scattering angle of the deflected photon; fully unpolarized refers to the unknown spin polarization states of both initial and final state particles.

The electron scattering opacity is *reduced* with respect to the classical limit: this is due to the fact that $\nu' < \nu$, since the electron recoils by a non-negligible amount and energy must be conserved. In **SECs**, such as PARSEC, a Paczyński prescription is usually implemented:

Paczyński Prescription

$$\kappa_{\rm P83} = \frac{\overbrace{n_e \sigma_{\rm Th}}^{=\kappa_{\rm Th}}}{\rho} \frac{1}{\Lambda_{\rm P83}\,(\mathrm{T}, \rho)} \qquad \text{with}$$
$$\Lambda_{\rm P83}\,(\mathrm{T}, \rho) = \left[1 + \left(\frac{k\mathrm{T}}{38.8\ \mathrm{keV}}\right)^{0.86}\right] \left[1 + 2.7 \times 10^{11}\ \rho \mathrm{T}^{-2}\right] , \tag{2.7}$$

This arises from a Boltzmann equation formalism as we will see in Chp.(3), and traces its roots back to a seminal paper by Paczyński (1983) [Pac83]. Fig.(2.1) shows the prescription for $\mu_e = 2$ and different values of degeneracy parameter $\eta \equiv \mu/k\mathrm{T}$, see Chp.(3) for more details.

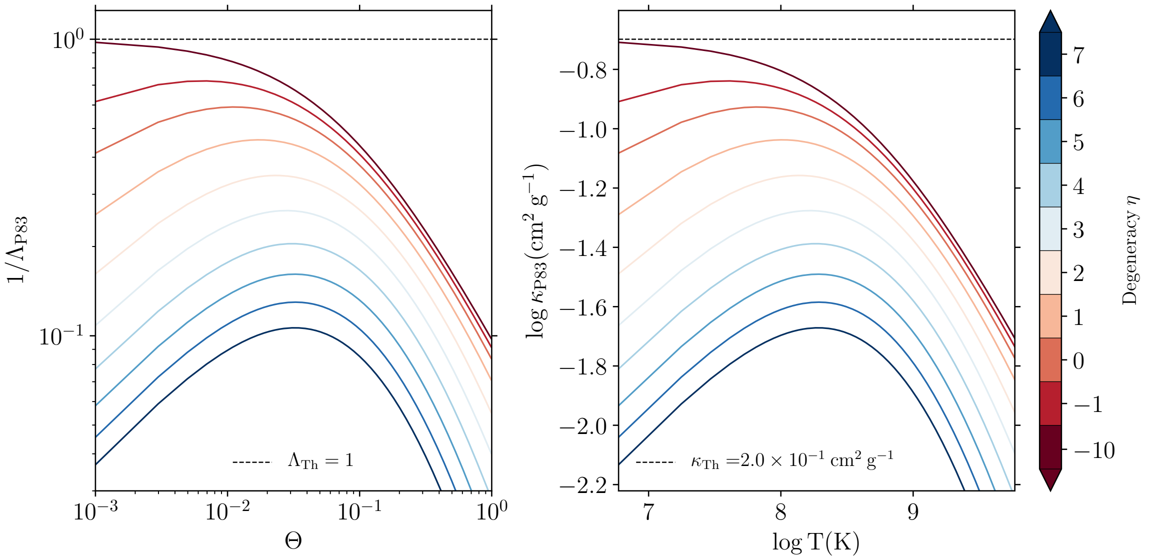

Figure 2.1: Left – Paczyński prescription in Eq.(2.7) for the (inverse of the) Rosseland mean free path $\Lambda_{\rm P83}\,(\mathrm{T})$ as a function of temperatures of interest for stellar matter. The dashed line shows the Thomson scattering limit, in which $\Lambda_{\rm Th} = 1$, Eq.(2.5). Fixed degeneracy parameters are color coded, and $\mu_e = 2$; Right – Compton opacity $\kappa_{\rm P83}$ as in Eq.(2.7) as a function of temperatures of interest for stellar matter. The dashed line shows again the Thomson scattering limit, $\kappa_{\rm Th}$, for $\mu_e = 2$, and degeneracy parameter η is fixed and color coded.

Rayleigh scattering $\quad N + \gamma \to N + \gamma'$

The solution to the scattering of light by atoms or molecules when the target particle has dimension d much smaller than the light's wavelenght λ is called *Rayleigh scattering*. Qualitatively, when an electromagnetic wave interacts with an atom or molecule, the oscillating electric field creates an oscillating dipole, which

a) Radiates with the same frequency $\nu = \nu'$ of the incoming light.

b) Scatters with different **efficiency** for different electronic configurations.

c) Is essentially **isotropic**.

The process of Rayleigh scattering is complex and has to be described by the second-order time dependent perturbation theory, with the *Krammers-Heisenberg formula* for the differential cross-section.
For neutral hydrogen H, the classical theory of dipoles and low energy approximation (which is essentially equivalent to say that $d \ll \lambda$) can, however, give an idea of the Rayleigh scattering cross section $\sigma^{\mathrm{H}}_{\nu,\mathrm{R}}$,

$$\sigma^{\mathrm{H}}_{\nu,\mathrm{R}} = \frac{8\pi}{3}\left(\frac{e^2}{m_e c^2}\right)^2 \left(\frac{\nu^2}{\nu^2-\nu_0^2}\right)^2 \xrightarrow{\nu\ll\nu_0} \frac{8\pi}{3}\left(\frac{e^2}{m_e c^2}\right)^2 \left(\frac{\nu}{\nu_0}\right)^4 \mathrm{cm}^2 ,$$

where ν_0 is the characteristic oscillation of the system (atom or molecule), in this case the Lyman-α transitions. This is strongly, $\sigma_{\nu,\mathrm{R}} \propto \nu^4$, dependent on the scattered light frequency ν, thus shorter wavelengths are scattered more than longer wavelengths in the Rayleigh limit.

Rayleigh scattering processes are very important in **stellar atmospheres**, mainly for cool stars in which major contributors are neutral H and molecular H_2 hydrogen and helium He, since the cross section $\sigma_{\nu,\mathrm{R}}$ is smaller for atoms with a higher atomic number. Conversely, it is often neglected in hot star atmospheres because of the low abundance of bound electrons species.

In **SECs**, well known Rayleigh cross sections from literature are included under convenient prescriptions, which usually perform a *polynomial expansion* (in $\nu/\nu_0 \ll 1$ for the red vicinity) of Krammers-Heisenberg formula away from resonances. For the neutral hydrogen H, e.g.,

$$\frac{\sigma^{\mathrm{H}}_{\nu,\mathrm{R}}}{1\ \mathrm{cm}^2} \simeq \frac{5.5758\times10^{-25}}{1\ \mathrm{cm}^2}\left(\frac{\nu}{\nu_0}\right)^4 + \frac{1.8567\times10^{-24}}{1\ \mathrm{cm}^2}\left(\frac{\nu}{\nu_0}\right)^6 + \ldots$$
$$\ldots + \frac{4.9480\times10^{-24}}{1\ \mathrm{cm}^2}\left(\frac{\nu}{\nu_0}\right)^8 + \mathcal{O}\left(\nu^{10}\right) ,$$

used in the ÆSOPUS tool, see below, for $\mathrm{H}+\gamma \to \mathrm{H}+\gamma'$, from et al. (2016) [Fis+16]. The zeroth order is eloquently dependent on ν^4, admitting an immediate classical interpretation. Consequently, the monochromatic mass absorption coefficient $\kappa^j_{\nu,\mathrm{R}}$ is computed by

Rayleigh Opacity $$\kappa^j_{\nu,\mathrm{R}} = \frac{n_j \sigma^j_{\nu,\mathrm{R}}}{\rho} ,$$

where n_j is the number density of target particles of type j.

Free-free absorption $\quad \boldsymbol{N + (\pm) + \gamma \rightarrow N + (\pm)}$
When a free electron passes in vicinity of a charged ion, they temporarily form an unbound system capable of absorbing electromagnetic radiation of any frequency. The associated opacity $\kappa_{\nu,\mathrm{ff}}$ is called *free-free absorption* opacity, and was firstly classically derived by Kramers. For a system of N ions with charge $Z_j e$ each coupled with a free electron and in the dipole approximation, the complete, quantum mechanical result for the cross section $\sigma_{\nu,\mathrm{ff}}$ is

$$\sigma_{\nu,\mathrm{ff}} = \underbrace{\left(\frac{2m_e}{3\pi k}\right)^{1/2} \frac{2e^6}{3chm_e^2}}_{:=C} n_e \,\mathrm{T}^{-1/2}\, \mathrm{Z}_j^2 g_{\mathrm{ff}}(\nu)\, \nu^{-3} \left(1 - e^{-h\nu/k\mathrm{T}}\right) \mathrm{cm}^2 ,$$

where $g_{\mathrm{ff}}(\nu)$ is the so called *Gaunt factor*, a slowly varying function of ν of order unity for most interesting values of $h\nu/k\mathrm{T}$. The last factor in round brackets is the traditional LTE correction for stimulated emission; also, the cross section is $\sigma_{\nu,\mathrm{ff}} \propto n_e$, proportional to the target's number. The constant C is such that

$$C \equiv \left(\frac{2m_e}{3\pi k}\right)^{1/2} \frac{2e^6}{3chm_e^2} \simeq 1.43 \times 10^{43} \text{ [cgs units]} .$$

The monochromatic mass absorption coefficient $\kappa_{\nu,\mathrm{ff}}$ can be obtained by summing over all the ions n_j in the mixture and dividing by ρ:

FREE-FREE $$\kappa_{\nu,\mathrm{ff}} = C\,\frac{n_e}{\rho} \sum_j n_j \mathrm{Z}_j^2\, \mathrm{T}^{-1/2} g_{\mathrm{ff}}(\nu)\; \nu^{-3} \left(1 - e^{-h\nu/k\mathrm{T}}\right) \mathrm{cm}^2\, \mathrm{g}^{-1} \tag{2.8}$$

This expression has several features:

a) It heavily depends on **composition**, however the primary contribution to the free-free opacity comes from hydrogen and helium.

b) For $\boldsymbol{h\nu \gg k\mathrm{T}}$ it reduces to $\kappa_{\nu,\mathrm{ff}} \propto \nu^{-3}$, which is a thermal cut-off, since e^- have average energy of $\sim k\mathrm{T}$. This is expected to translate into a T^{-3} dependence in κ_{ff}, due to Eq.(2.3).

c) For $\boldsymbol{h\nu \ll k\mathrm{T}}$ it goes as $\kappa_{\nu,\mathrm{ff}} \propto \nu^{-2}$, a Rayleigh regime.

d) The dependence $\boldsymbol{\kappa_{\nu,\mathrm{ff}} \propto \mathrm{T}^{-1/2}}$ comes from the thermal velocity $\bar{v} \propto (k\mathrm{T}/m_e)^{1/2}$ of target electrons.

e) The sum over n_j can be written as $\sum_j n_j \mathrm{Z}_j^2 \overset{\mathrm{Eq.(1.6)}}{=} (\rho/m_u) \sum_j (\mathrm{X}_j \mathrm{Z}_j^2/A_j) = (\rho/m_u)(\mathrm{X} + \mathrm{Y} + \mathrm{B}) \simeq (\rho/m_u)$ with $\mathrm{B} = \sum_{j>2} (\mathrm{X}_j \mathrm{Z}_j^2/\mathrm{A}_j)$ is the contribution of elements heavier than He.

In **SECs**, e.g. in ÆSOPUS, the complete expression of $\kappa_{\nu,\mathrm{ff}}$ is used for the most important species, namely H, He, H_2, H_3 and some ionization stages of these; often simply $\sigma^{\mathrm{H}}_{\nu,\mathrm{ff}}$ is used. Lastly, if the free-free contribution were all that existed, the Rosseland mean opacity $\kappa_{\rm ff}$ would be given by a well known power-law, *Kramer opacity*:

$$\kappa_{\rm ff} \propto \rho^n\, \mathrm{T}^{-m} \qquad \text{with} \quad n = 1\,, \;\; m = 7/2\,,$$

with n and m as Kramer's coefficients.

Bound-free absorption $\quad \boldsymbol{N + \gamma \to N^{(\pm)} + (\pm)}$

When the impinging photon's energy $h\nu$ is greater than the ionization energy $\chi_{\rm ion}$ of a bound electron, an atom can promote the latter into a free state, with the difference $\Delta E = h\nu - \chi_{\rm ion} = m_e v^2/2$ feeding the kinetic energy of the freed e^-. This process is called *bound-free absorption*, or also photoionization.

The photoionization cross section for a hydrogenic atom $\tilde{\mathrm{H}}$ with charge $\mathrm{Z}_j e$ in the (n,l) state, $\sigma_{\nu,\rm ion}$, is well known

$$\sigma^{\tilde{\rm H}}_{\nu,\rm ion} = \frac{64\pi^4}{3\sqrt{3}}\,\frac{m_e e^{10}}{ch^6}\,\frac{\mathrm{Z}_j^4}{n^5}\, g_{\rm bf}\,(\nu)\;\nu^{-3} \qquad \text{with} \quad h\nu > \chi_{\rm ion} \equiv \frac{2\pi^2 m_e e^4}{h^2}\frac{\mathrm{Z}_j^2}{n^2}\,, \tag{2.9}$$

where $g_{\rm bf}\,(\nu)$ is a slowly-varying, order unity, bound-free Gaunt factor; (n,l) is the principal and orbital quantum number state. This cross section is such that

a) It drops to zero below threshold; reaches a maximum value at $\chi_{\rm ion}$; **declines** as ν^{-3} for higher frequencies.

b) When an atom is **not hydrogenic**, the charge Z_j must be replaced by an effective charge, accounting for the screening effects of bound electrons.

c) **Ionization edges**: as $\nu \nearrow$, we get $\sigma^{\tilde{\rm H}}_{\nu,\rm bf} \searrow$, but suddenly the energy is high enough to eject electrons from a deeper shell and the cross section raises steeply to decline again in ν^{-3}, until the next jump at the subsequent step.

d) **Electron degeneracy**, if present, shall be expected to decrease $\kappa^{\tilde{\rm H}}_{\nu,\rm bf}$, since many cells of the phase space of free electrons are occupied.

The total bound-free monochromatic opacity $\kappa_{\nu,\rm bf}$ can be obtained by summing over all the ions n_j, the ionization states i and the excitation levels n, taking also into account a stimulated emission correction:

Bound-Free Opacity

$$\kappa^{\tilde{\rm H}}_{\nu,\rm bf} = \textstyle\sum_{j,n} \dfrac{n_j}{\rho}\, \sigma^{\tilde{\rm H}}_{\nu,\rm bf}\, \left(1 - e^{-h\nu/k\mathrm{T}}\right)\,. \tag{2.10}$$

It is understood that, as a consequence, the opacity law for a single specie j shall have a number of ionization edges, which are partially smeared out by taking a Rosseland mean. In SECs, the bound free opacity is computed numerically, since a complete description of atomic physics of the mixture is indeed needed.

However, if one were to write a simple analytical prescription for the Rosseland mean $\kappa_{\rm bf}^{\tilde{\rm H}}$ of a hydrogenic mixture, a general Kramer's like behavior can be found even in this case:

$$\kappa_{\rm bf}^{\tilde{\rm H}} \propto {\rm Z}\,\rho^n\,{\rm T}^{-m} \qquad \text{with} \quad n = 1\,,\ m = 7/2\,,$$

even if ionization edges prevent $\kappa_{\rm bf}^{\tilde{\rm H}}$ to behave exactly as $\propto {\rm T}^{-7/2}$. The additional dependence on global metallicity Z can lead to a prominence of bound-free with respect to free-free absorption at high metallicities.

H⁻ bound-free opacity $\quad {\rm H}^- + \gamma \rightarrow {\rm H} + e^-$

Absorption by the *negative ion H⁻* is a dominant feature of the continuous spectrum of relatively low mass stars. This ion H⁻ is very fragile and easily ionized at temperatures of a few thousands K, due to an ionization potential of 0.747 eV.
Due to the relatively simple system, cross sections for such a process have been calculated in the literature through to standard *Hartree-Fock methods* (Configuration Interaction), and known prescriptions for $\kappa_{\nu,{\rm H}^-}$ are usually employed in **SECs**, such as the one from John (1988), [Joh88]. Then, $\kappa_{\nu,{\rm H}^-}$ is built in the usual way

$$\textbf{H}^-\ \textbf{Absorption} \qquad \kappa_{\nu,{\rm H}^-} = \frac{n_{{\rm H}^-}}{\rho}\sigma_{\nu,{\rm H}^-}\left(1 - e^{-h\nu/k{\rm T}}\right)\ .$$

Of course H⁻ can be created only in presence of both H and free electrons, the latter being provided mainly by singly ionized metals (e.g. alkali). Therefore, H⁻ absorption is present only for a limited range of temperatures, and for purely descriptive purposes we report a famous approximate formula for $\kappa_{{\rm H}^-}$:

$$\kappa_{{\rm H}^-} \approx 2.5\times10^{-31}\left(\frac{\rm Z}{0.02}\right)\rho^{1/2}\,{\rm T}^9\ {\rm cm}^2\ {\rm g}^{-1}\ ,$$

which is valid in the range $3.48 \lesssim \log{\rm T} \lesssim 3.78$, $-10 \lesssim \log\rho \lesssim .5$ and $0.001 < {\rm Z} < 0.02$.
Lastly, **1)** at ${\rm T} \lesssim 3000$ K the H⁻ opacity becomes ineffective due to low abundance of free e^-; **2)** at ${\rm T} \gtrsim 10^4$ K most of the H⁻ has disappeared and the Kramers opacity and electron scattering take over.

2.1.2 Line sources

This section briefly describes the physical processes sourcing stellar matter opacity for a *discrete spectrum* of energies of the radiation field. These can comprise both atomic and molecular species and go usually under the names

1) Bound-Bound absorptions $\qquad N + \gamma \rightarrow N + \gamma'$

2) Molecular band transitions $\qquad M + \gamma \rightarrow M + \gamma'$

where N denotes a nucleus, γ' is a photon with frequency ν' and M is a molecular state. In both cases, we refer to photon-induced transitions between bound states in atoms, ions or molecules; in the latter case, rovibronic states are to be considered. These sources of opacity were actually neglected for long time in the past literature, mainly because of **a)** the non-trivial physics involved; **b)** the fact that there are relatively limited incompletely ionized states in the deep interior of stars. However, continuous efforts were put in their inclusion in standard radiative transfer studies, as bound-bound absorption was found to be a major source of opaqueness in regions where stellar matter is partially ionized, i.e. towards external layers.

Bound-bound absorption The *bound-bound process* involves the absorption of a line photon which causes an electron in an incompletely ionized atom to make an upward transition, from a lower atomic energy level, to a higher one. This is possible only giving the following two conditions:

- ***Low temperatures*** of the radiation field, such that the incident photon has a low probability of residing in the ionization tail of the ambient Planckian; this is always true at approximately $\log \mathrm{T} \lesssim 6$, i.e. when outer stellar layers are considered.
- ***Transition frequencies***, specific to the atomic specie under consideration, are matched, within a narrow range $\Delta\nu$ around the exact value ν_0; the $\Delta\nu/\nu_0$ is never much above a percent.

  The *line width* $\Delta\nu$ is set by the type of transition, but experiences a whole lot of **broadening** which makes the process more probable and the net result, in the end, can also be that of largely superimposed lines giving rise to an additional absorption continuum. The latter is a case called *line blanketing*, a famous example being the IRON BUMP, which is created by millions of overlapping spectral lines from the iron M-shell levels, split thanks to spin orbit interaction.

From the usual very small $\Delta\nu/\nu_0$, it may seem that bound-bound opacity can never make a significant contribution to the Rosseland mean κ, as compared to the other sources of absorption continuum. However, despite their narrowness, lines contain a huge amount of opacity due to the *resonances* of systems and the possibility to create blankets.

In **SECs**, e.g. in ÆSOPUS, the monochromatic true absorption and scattering opacity per unit mass are calculated as

$$\boldsymbol{\kappa_{\mathrm{j}}^{\mathrm{abs}}(\nu) = \frac{n_{\mathrm{j}}}{\rho}\,\sigma_{\mathrm{j}}^{\mathrm{abs}}(\nu)\,\left(1 - e^{-h\nu/k\mathrm{T}}\right)}\ ,$$

$$\boldsymbol{\kappa_{\mathrm{j}}^{\mathrm{scatt}}(\nu) = \frac{n_{\mathrm{j}}}{\rho}\,\sigma_{\mathrm{j}}^{\mathrm{scatt}}(\nu)}\ ,$$

where we denoted with $\sigma_{\mathrm{j}}(\nu)$ the monochromatic cross section of the j^{th} absorption process, and $\sigma_{\mathrm{j}}^{\mathrm{scatt}}(\nu)$ the scattering cross section; the last factor, $\left(1 - e^{-h\nu/k\mathrm{T}}\right)$, is the usual correction for stimulated emission. Usually, the monochromatic opacity cross sections for atoms can be taken from

- An accredited ***database of nuclear data***, e.g. the Opacity Project (OP) database from J. Seaton et al. (1994), [Sea+94]. One can then interpolate in frequency, T and n_e as needed. In this case, sources of line-broadening are already taken into account with the degree of detail the authors of the database find suitable to their purposes.

- A compilation of ***line lists***, providing oscillator strengths and occupation number for the desired species' transitions. In this case, one has to introduce it's own model broadening function $\phi(\nu)$, accounting at least for Doppler, microturbulence, radiation damping and pressure broadenings. More precisely, for a transition from state m to n,
$$\sigma_{\mathrm{bb}}^{\mathrm{abs}}(\nu) = \frac{\pi e^2}{m_e c}\,\frac{gf}{Q(\mathrm{T})}\,e^{-E_0/k\mathrm{T}}\left(1 - e^{-h\nu/k\mathrm{T}}\right) \,,$$
where $Q(\mathrm{T})$ stands for the total partition function, gf the usual product of the statistical weight g_m times the oscillator strength f, and the correction for stimulated emission is also there. An example of a line list can be the one from Rothman et al. (2005), [Rot+05].

Molecules transitions An important source of opacity in very cool stars or, as we will find in Chp.(4), in the envelopes of completely convective massive stars, come from the *molecules band transitions*. The nature of these molecules are mainly determined by the ambient properties, like the C/O ratio in the stellar surface; just to count the most popular species, we list water H_2O, di-atomic hydrogen H_2, titanium oxide TiO, carbon monoxide CO.

From structure of matter theory, we know that molecules, in addition to electron energy levels, exhibit a range of levels associated with rotational and vibrational degrees of freedom, which are put together in ***rovibronic states***. These are typically so close together that they merge to form continuous *energy bands*, and the transitions between these bands lead to bound-bound opacity over wide frequency ranges.

In **SECs**, e.g. in ÆSOPUS, mostly the same techniques outlined above are employed to obtain the monochromatic molecular absorption coefficients; ***line lists*** is actually the main method, but one can also rely on ***opacity sampling files***, which are pre-calculated (mostly) from line lists themselves. Once one has all the contributions, $\sigma_{\mathrm{bb}}^{\mathrm{abs}}(\nu)$, from the (known) lines, the sum
$$\sigma_{\mathrm{mol}}^{\mathrm{abs}}(\nu) = \sum_{\mathrm{lines}} \sigma_{\mathrm{bb}}^{\mathrm{abs}}(\nu)$$
is performed, each coefficient with its own broadening function $\phi(\nu)$ and characteristic oscillator strengths; this gives the *total* monochromatic absorption coefficient of a molecular species.

Collision Induced Absorption *Collision Induced Absorption* (CIA) is an additional source of opacity expected to play a relevant role at low temperatures, such as in the atmospheres of cool white dwarfs (WDs), and its features are usually recognizable in the microwaves and infrared regions of the electromagnetic spectrum.

The phenomenon describes the peculiar property of weakly interacting (via van der Waals forces) couples of colliding molecules to absorb radiation, as opposed to the ordinary, single bound molecule absorption; whether the absorption is dominated by bound or colliding molecules depends on the temperature, i.e. on whether the thermal energy kT is small or large with respect to the binding energy. The interacting couple, which can be formed by homonuclear diatomic nuclei (without electric dipole moment), becomes a *collision complex* and develops, by virtue of an inelastic scattering, a non-zero electric dipole; the collision complexes are a proper short lived phase, whose absorption spectrum is typically broad in frequency, but nevertheless discrete.

We are briefly commenting these processes because **a)** they are ***included*** in PARSEC in the ÆSOPUS tool, and **b)** they can be relevant also in the atmospheres of ***low metallicity stars*** as the ones we will encounter in Chp.(4): in these cases, molecules such as CIA by H_2-H_2 and H_2-He will be a quite important opacity source; **c)** it is of fundamental importance to calibrate ***transit transmission spectroscopy*** measurements, devoted to the atmospheric abundances determination.

2.2 Conductive opacities κ_{cd}

The Rosseland mean κ is precisely the quantity appearing in Eq.(1.3), in the case of radiative equilibrium. Anyway, random collisions between the gas particles (ions and electrons for fully ionized matter, otherwise atoms) can also transport heat, and this gives rise to the *conductive opacity* κ_{cd}. We can define this quantity completely analogously to the radiative opacity, and account for it by rewriting Eq.(1.3) as

$$\frac{\partial \mathrm{T}}{\partial m} = -\frac{3}{64\pi^2 ac}\frac{\kappa l}{r^4 \mathrm{T}^3} \qquad \text{with}$$

$$\boxed{\frac{1}{\kappa} = \frac{1}{\kappa_{\mathrm{rad}}} + \frac{1}{\kappa_{\mathrm{cd}}}}\,, \tag{2.11}$$

where κ_{rad} is the Rosseland mean for all the radiative processes, which was called κ in the previous paragraphs to simplify the notation. In the following we shall use simply κ again. **NB** For ideal gas EoS, heat conduction is very much suppressed with respect to radiative diffusion, due to a consistent difference in the mean free path

$$\sigma_{\mathrm{e}} \ll \sigma_{\mathrm{coll}} \quad \Rightarrow \quad l_{\nu,e} \ll l_{\nu,\gamma}$$

arising from hugely different collisional cross sections at subluminal thermal velocities, $\bar{v} \ll c$. Above, σ_e and σ_{coll} stand for electron scattering and e^- collisional cross sections, respectively, whilst $l_{\nu,\gamma}$ and $l_{\nu,e}$ stand for the mean free paths of the respective fundamental process. By virtue of this argument, for **massive stars**, one usually accounts for just κ_{rad}, unless the more advanced evolutionary stages comprehend very high densities in degenerate cores. In the following chapter, Chp.(2), we shall discuss this possibility for selected stellar models. Considering, hence, sufficiently degenerate gas, in which $\sigma_e \simeq \sigma_{\mathrm{coll}}$, a simple analytic prescription can be used as a reference:

Conductive Opacity

$$\kappa_{\rm cd} \approx 4.4 \times 10^{-3} \frac{\sum_{\rm i} Z_{\rm i}^{5/3} X_{\rm i}/A_{\rm i}}{(1+X)^2} \frac{(T/10^7 K)^2}{(\rho/10^5 \text{ g cm}^{-3})^2} \text{ cm}^2 \text{ g}^{-1} . \tag{2.12}$$

Deviating from the ideal EoS: liquid metal phase We are briefly commenting on *departure from ideality* in the stellar matter theoretical treatment of gas, for future utility in the context of thermal conduction. Neglecting the effects of Coulomb interactions between ions and electrons in the gas is reasonable when the interaction energies of the species are small as compared to the kinetic ones. This condition can be translated into a lower constraint on the ***Coulomb coupling parameter***, $\Gamma_{\rm i}$:

Coulomb Coupling Parameter

$$\Gamma_i = \frac{Z_j^{5/3} e^2}{a_e k T} = 0.2275 \frac{Z_i^{5/3}}{T_8} \left(\sum_j X_j \frac{Z_j}{A_j} \rho_6 \right)^{1/3} \quad \text{with} \quad a_e \equiv \left(\frac{3}{4\pi n_e} \right)^{1/3} , \tag{2.13}$$

which has to be $\Gamma_{\rm i} \gtrsim 1$ for the Coulomb interactions to be relevant. We notice that this definition is specific to a ion specie i, following Itoh et al. (2008) [Ito+08], and is both T and ρ dependent, as well as on the mixture properties. The quantity a_e is the electron-sphere radius, namely an approximated average electrons' distance.

Since we notice that $\Gamma_{\rm i} \gtrsim 1$ for sufficiently high ρ and low T, which are exactly the same dependences for the conductive opacity, Eq.(2.12), to become important, we are naturally lead to think of a deep connection between the two properties; indeed, any effective theory of thermal conduction ***must*** take into account Coulomb screening effects with some degree of approximation, and we shall see an example in Chp.(3).

When the matter is so highly degenerate that Coulomb interactions are relevant and of prior importance, the stellar matter is often in the so called ***liquid metal phase***, i.e. it is completely **pressure-ionized**: when the ions distance becomes less smaller than an atomic radius, electrons can reside in fewer bound excited states, and are forming a Fermi's sea around the ionic centers.
Fig.(2.2) shows an example of PARSEC's outputs, for two stellar models with ZAMS M=10 $M_\odot$, for the Coulomb coupling parameter of different elements, the ones expected to be relevant at the considered stages of evolution: we see that, indeed, some of our runs of PARSEC will comprise $\Gamma_{\rm i} \gtrsim 1$, and we will discuss the implications.

2.3 Opacity in Stellar Evolution Codes: PARSEC

We are finally going to present the treatment of *opacities in the stellar evolution code* employed in this work: PARSEC. Following a standard procedure, PARSEC's description of the absorption properties of matter, in the gas phase, is based on **pre-computed**, static

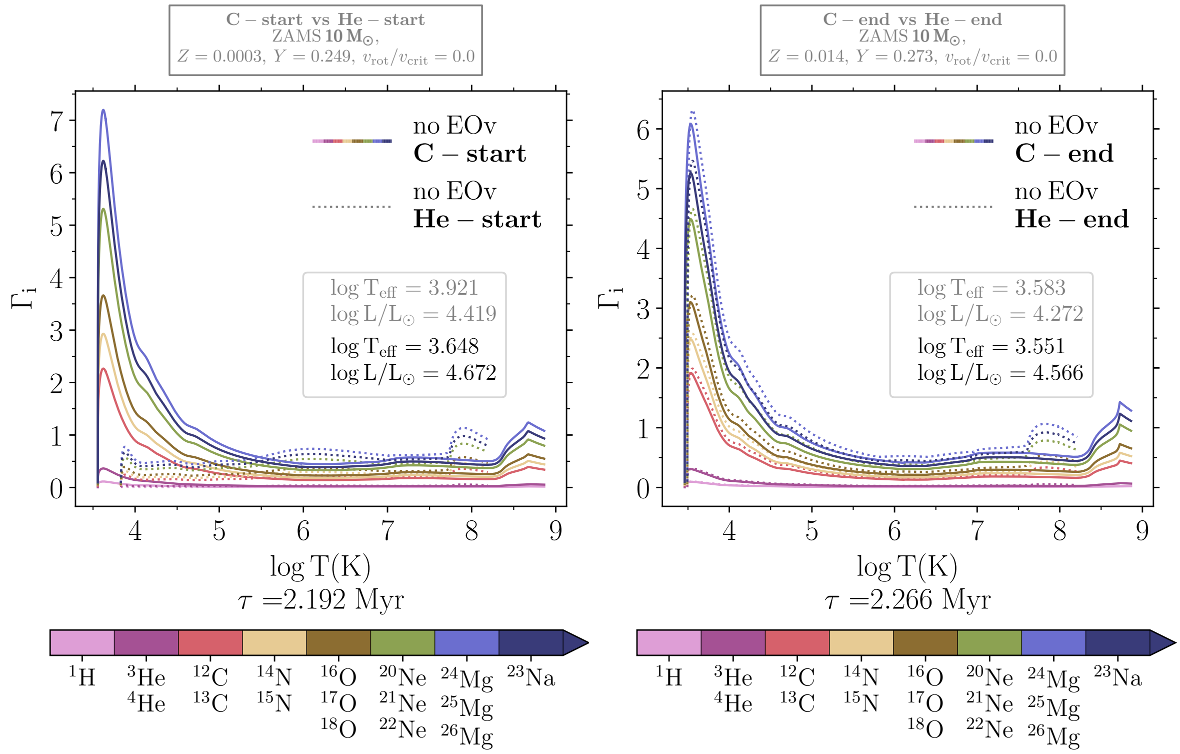

Figure 2.2: Coulomb coupling parameter Γ_i for the nuclear specie $(Z_i,\ A_i)$, as a function of stratification temperature T, for a star with ZAMS mass M=10 M$_\odot$ and rotation velocity $v_{\rm rot}/v_{\rm crit} = 0$. The quantity is shown at two different evolutionary stages, one more (solid color) and the other less advanced (dotted color), with the colorbar as explicit label for the considered i element. The HR position of the evolutionary stage is reported in an insert, with gray being referred to the less advanced stage. Left – PARSEC output, without EOvershooting (no EOv), for a metallicity Z=0.0003; Right – same as Left, but for a metallicity Z=0.014.

tables of Rosseland mean opacities, $\kappa(\rho,\ T)$, which are suitably arranged to encompass density-temperature ranges wide enough to cover all values met across the stellar structure during the evolution. Opacity tables are properly interpolated in ρ and T, as well as in the additional variable of the hydrogen mass fraction H; the latter uniquely identifies the chemical mixture at work, once the total metallicity Z and the distributions X_i/Z of heavy elements are chosen.

Various methods are jointly employed to compute the tables and describe the varied input physics:

- **$\log T(K) \geq 8.7$**
  To date of the present work, PARSEC employs the Paczyński prescription **P83** of Eq.(2.7), Paczyński (1983) [Pac83], in the highest temperature range. This means that, at such high radiation field energy, the matter is treated as completely ionized and only *Compton scattering* opacity on free electrons is taken into account. In the following chapter, Chp.(3), we shall extensively discuss the goodness of this description

and provide a new theoretical framework.

- **$4.2 \leq \log \mathrm{T(K)} \leq 8.7$**
  This quite large, high temperature range is fully covered by the opacity tables from Opacity Project At Livermore (**OPAL**) by Iglesias & Rogers (1996), [IR96], which will be described in more details in Chp.(4). OPAL opacities are, at the present date, describing continuum and discrete *atomic processes* but only few molecular transitions, under safe temperature and density conditions to justify such a simplification. The interactive web mask, [IR], is used to generate suitable tables for specified number fractions of 19 metals from C to Ni, as implied by the relative fractions $\mathrm{X_i/Z}$.

- **$3.2 \leq \log \mathrm{T(K)} \leq 4.1$**
  In the low temperature regime the **ÆSOPUS** tool, by Marigo & Aringer (2009), [MA09], is employed, which generates opacity tables for any specified set of chemical abundances for 92 elements, from H to U. ÆSOPUS solves the equation of state of matter in the gas for ≈ 800 chemical species consisting of almost 300 atoms (neutral and ios up to the 5^{th} ionization stage) and 500 molecular species.

  This tool provides the most complete molecular opacity data available now in the community, accounting for many continuum and discrete sources including atomic opacities, *molecular band transitions* and CIA. An interactive web interface, [Mar], allows the user to run ÆSOPUS according to the specific requirements, generating desired tables with suitable metals partitions, Z and reference solar composition.

- **$4.0 \leq \log \mathrm{T(K)} \leq 4.1$**
  This transition interval is treated with a linear interpolation between the opacities derived from **OPAL** and **ÆSOPUS**; it was extensively shown that both opacity sources provide values in good agreement in this temperature interval, see Marigo & Aringer (2009), [MA09].

- **Conductive Opacities**
  Conduction by sufficiently degenerate ($\eta \gtrsim 8$) electrons is included following the routine by Itoh et al. (2008), [Ito+08]. For any specified chemical mixture, the total *thermal conductivity* accounts for the contribution of 11 atomic species, (^{1}H, ^{4}He, ^{12}C, ^{14}N, ^{16}O, ^{20}Ne, ^{24}Mg, ^{28}Si, ^{32}S, ^{40}Ca and ^{56}Fe), each weighted by the corresponding abundance.

PARSEC opacity tables: an example Given the total reference metallicity Z and the partitions of heavy elements $\mathrm{X_i/Z}$, PARSEC builds two sets of *opacity tables*: a family of H-rich tables, with $\mathrm{X} \in [0.0, 1 - \mathrm{Z}]$, and a family of H-free tables, with $\mathrm{X} = 0.0$ and $\mathrm{Y} \in [0.0, 1 - \mathrm{Z}]$. These latter are specifically designed to describe the opacity in the He-burning regions. In addition, PARSEC considers also three combinations of C and O abundances, defined by the ratios $\mathrm{R_C} \equiv \mathrm{X_C}/(\mathrm{X_C} + \mathrm{X_O})$.

Fig.(2.3) shows an example of PARSEC *tables*, in the $(\log \mathrm{R}, \log \mathrm{T(K)})$ plane. The proxy for the density, i.e. the variable R, is customarily chosen due to the behavior of opacity in radiative regions, where $\mathrm{P/P_{rad}} \simeq \mathrm{const} \Rightarrow \rho/\mathrm{T} \simeq \mathrm{const}$. We see that the tables are rectangular, covering a region defined by the intervals

$$3.2 \leq \log \mathrm{T(K)} \leq 8.7\,, \qquad -8 \leq \log \mathrm{R} \equiv \frac{\rho}{\mathrm{T}_6} \leq 1\,,$$

and of course $\mathrm{T}_6 \equiv \mathrm{T}/10^6\mathrm{K}$. To limit as much as possible the accuracy loss due to subsequent interpolation, PARSEC adopts a fine grid spacing, with $\Delta \log \mathrm{T} = 0.01$ for $3.2 \leq \log \mathrm{T(K)} \leq 3.7$, then $\Delta \log \mathrm{T} = 0.02$ for the range $3.7 \leq \log \mathrm{T(K)} \leq 8.7$ and overall $\Delta \log \mathrm{R} = 0.2$. The colormaps in Fig.(2.3) are *not* obtained with this same spacing; nevertheless they give an idea of the $\log \kappa$ values and plane $(\log \mathrm{R}, \log \mathrm{T})$ coverage.

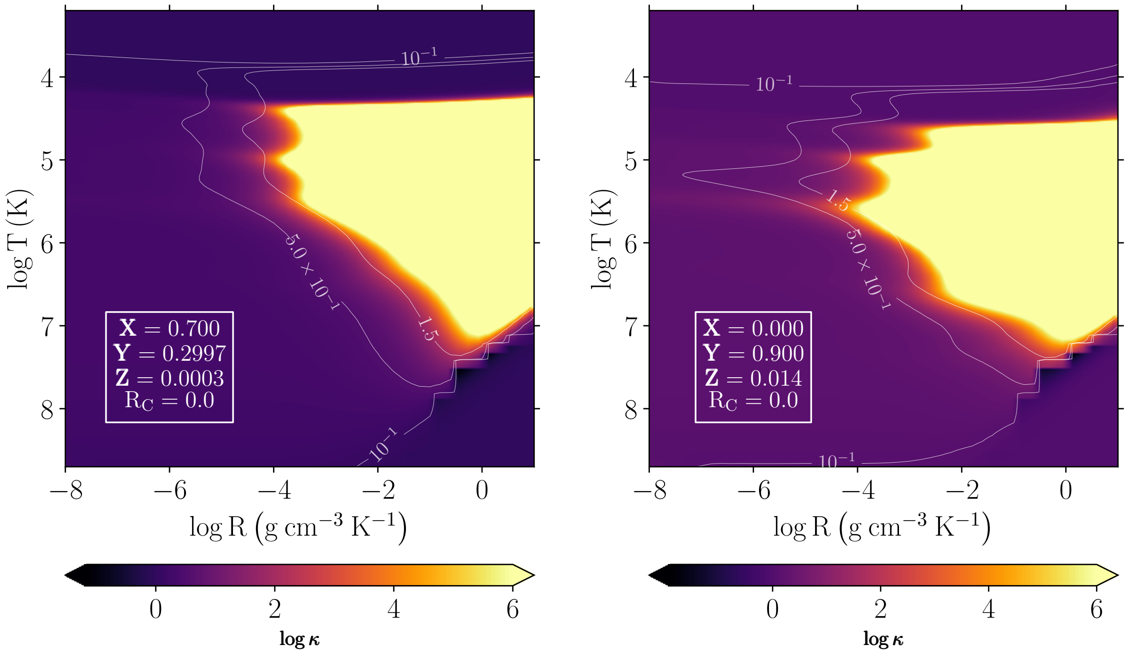

Figure 2.3: PARSEC opacity $\log \kappa$ table in the plane $(\log \rho, \log \mathrm{T})$, as output from the multiple programs described in text and combined in the range $3.2 \leq \log \mathrm{T(K)} \leq 8.7$ and $-8 \leq \log \mathrm{R} \leq 1$, with R being a proxy for the density such as R$= \rho/\mathrm{T}_6$. Some interesting contour levels are also reported explicitly, and the mixture under consideration is specified in the insert. Left – Table for a H-rich composition; Right – Same as left, but for a H-deficient mixture, suitable to describe the opacity of a gas in which all helium has been burnt and converted into O alone, since we chose $\mathrm{X_C} = 0.0$.

The interpolations performed over the tables have the following schemes:

	Bilinear	**Parabolic**	**Linear**
H-rich	R, T	X, Z	✗
H-free	R, T	Y, Z	$\mathrm{R_C}$

As for the stability into the convergence of the stellar models, PARSEC adopts a scheme in which logarithmic derivatives of the opacities, $\partial \log \kappa/\partial \mathrm{T}$ and $\partial \log \kappa/\partial \mathrm{R}$, are computed and stored over the same grid of the opacity tables. This allows to obtain these derivatives by bilinear interpolation, in the same way as for the opacity values.

Lastly, PARSEC is also able to follow in detail any significant ***change in the local metal*** content Z, e.g. the ones due to dredge up episodes or diffusion of heavy elements, by preliminarily loading a suitable number of opacity tables prior to any run. Let us summarize PARSEC's opacity, at the date of the present work, in the table below.

VERY HIGH TEMPERATURES $\log \mathrm{T} \gtrsim 8.7$	▸ **P83** κ_{P83}	[Pac83]
HIGH-MID TEMPERATURES $4.2 \lesssim \log \mathrm{T} \lesssim 8.7$	▸ **OPAL**	[IR96]
TRANSITION REGION $4.0 \lesssim \log \mathrm{T} \lesssim 4.1$	▸ **OPAL+ÆSOPUS**	
LOW TEMPERATURES $3.2 \lesssim \log \mathrm{T} \lesssim 4.1$	▸ **ÆSOPUS**	[MA09]
+ CONDUCTIVE	▸ **Itoh et al.**	[Ito+08]

PARSEC opacity output: an example We are lastly going to comment on an example of PARSEC *opacity output*, computed in the context of real two stellar models' runs, both for a model with ZAMS M=10 $\mathrm{M}_{\odot}$. The aim is to identify some interesting features, for future utility in Chp.(3) and Chp.(4).

- ▸ LEFT PANEL: C-START VS HE-END $\mathrm{Z} = 0.0003,\ v_{\mathrm{rot}}/v_{\mathrm{crit}} = 0.0$
  The left panel shows the comparison between two structures, caught at the start of the core C-burning (solid purple line) and at the end of core He-burning (solid black line). We immediately recognize a much higher opacity, in the atmospheric regions, for the model towards the more advanced evolutionary stage: this is motivated by the fact that $\log \mathrm{T_{eff}} \simeq 3.649 \ll \mathbf{\log T_{eff} \simeq 3.921}$, the C-start structure being approaching the Hayashi line for M=10 $\mathrm{M}_{\odot}$. As for the features:

  - ***Electron scattering*** dominates the higher temperatures, $\log \mathrm{T(K)} \gtrsim 8.5$, as expected. The Thomson plateaux is fairly different from PARSEC's actual curve, and this is due to Compton scattering (see Chp.(3)).

  - ***Free-free & Bound-free*** absorptions are responsible for the rising, at lower temperatures until the first peaks, as a linear-like curve; this is due to the exponential dependency on T, Eq.(2.8) and Eq.(2.10), which in a log-log plot translates in linear curves. Of course, some small steps are evident, and these can be due to sudden changes in density (or composition!).

- ***H and He ionization*** zones are showing, around $\log \mathrm{T_{eff}} \simeq 4$ and $\log \mathrm{T_{eff}} \simeq 5$, as small bumps towards the lowest T.
- ***H⁻ recombination***, for $\log \mathrm{T(K)} \lesssim 4$, decreases drastically the opacity.

► **RIGHT PANEL: C-START VS H-END** $\mathrm{Z} = 0.014,\ v_{\mathrm{rot}}/v_{\mathrm{crit}} = 0.0$
The right panel shows the comparison between two structures, caught at the start of the core C-burning (solid purple line) and at the end of core H-burning (solid black line). Again we acknowledge a much higher opacity, in the atmospheric regions, for the model towards the more advanced evolutionary stage: this is motivated by the fact that $\log \mathrm{T_{eff}} \simeq 3.551 \ll \mathbf{\log T_{eff} \simeq 4.106}$, the C-start structure being approaching the Hayashi line for M=10 $\mathrm{M_\odot}$. As for the features, we can highlight the same tendencies as in the Left panel. Additionally,

- ***Molecules & dust*** transitions are causing a small bump (which actually can be quite drastic in cooler atmospheres, see e.g. Fig.(4.6) – bottom row), interrupting the drastic decrease due to $\mathrm{H^-}$ recombination.
- ***Electron scattering*** in the core of the model towards the end of the MS is in excellent agreement with the Thomson plateaux (thin, black dotted line): this is due to the fact that the core is not too hot, at the MS's end, to satisfy the condition for Compton scattering $k\mathrm{T} \gtrsim m_e c^2$.
- ***Iron bump*** feature, in both evolutionary stages, is fairly evident at $\log \mathrm{T_{eff}} \simeq 5.5$: this is caused by the millions of lines from Fe bound-bound transitions and by Fe free-bound processes. It is usually evident in massive stars, and becomes more pronounced as one increases the metallicity.

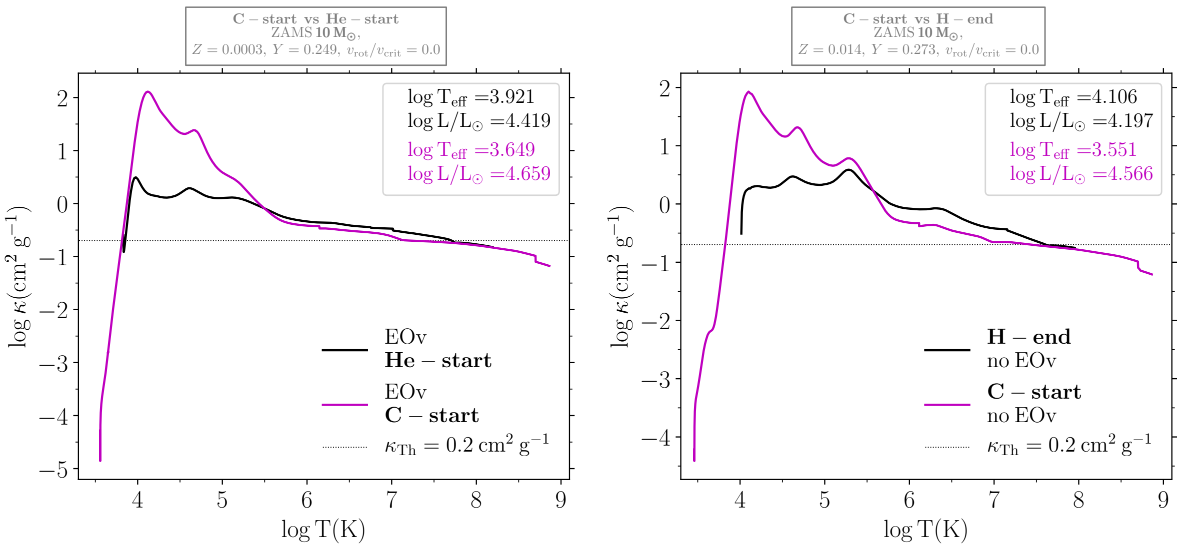

Figure 2.4: Overview of opacity $\log \kappa$, as a function of the stratification temperature $\log \mathrm{T}$, at two different evolutionary stages (see the grey heading), with an insert which specify the location in the HR diagram (($\log \mathrm{T_{eff}}, \log \mathrm{L/L_{\odot}}$), color-coded). The Thomson scattering plateaux κ_{Th} is reported (thin, black dotted line). Left – PARSEC output for Z=0.0003 and Envelope Overshooting (EOv) incorporated; Right – PARSEC output for Z=0.014, without Envelope Overshooting (no EOv).

3

Opacity: Compton scattering

This chapter focuses on the relativistic electron scattering, i.e. *Compton scattering*, in stellar matter, the main source of opacity in massive stars cores during the advanced evolutionary stages. It begins with a brief description of the well known physics of the Compton process in Sec.(3.1), comprising a presentation of the relativistic kinematic in the old quantum theory fashion and the Klein-Nishina full field theoretical result; then, the formulation of the relativistic kinetic theory is introduced in Sec.(3.2), to allow for placing the isolated Compton process into the stellar matter framework; finally, the included prescriptions in PARSEC are motivated in Sec.(3.2.2) and Sec.(3.2.3), with the relevant results from the analysis presented in Sec.(3.3).

3.1 Physics of Compton Scattering

As it is said in Sec.(2.1.1), a Compton scattering describes the scattering of an X (or gamma)-ray photon γ by a charged particle, usually an electron e; calling $h\nu_c = m_e c^2$ the rest mass energy of an electron, the condition for the incoming photon energy to produce a Compton scattering is usually

$$\boldsymbol{h\nu \gtrsim m_e c^2} \tag{3.1}$$

$$\Rightarrow \qquad h\nu \gtrsim h\nu_{\mathrm{c}} \simeq 8.18 \times 10^{-7}\,\mathrm{erg} \qquad \Leftrightarrow \qquad \log \mathrm{T} \gtrsim \log\left(\frac{h\nu_{\mathrm{c}}}{4.96\,k}\right) \simeq 9\,,$$

but, usually, already at $\log \mathrm{T} \gtrsim 8.7$ in stellar matter it makes sense to consider a relevant Compton scattering fraction, as stated in Sec.(2.1.1). It results in a variation of the photon's initial frequency ν, which is reduced by the transfer of energy E_e to the recoiling electron:

$$\begin{array}{ccccccc} \gamma & + & e^- & \longrightarrow & \gamma & + & e^- \\ \downarrow & & \downarrow & & \downarrow & & \downarrow \\ k^\mu & & \tilde{p}^\mu & & k_1^\mu & & \tilde{p}_1^\mu \end{array} \tag{3.2}$$

Fig.(3.1) shows a pictorial view of the process; above we have introduced also the four momenta $\tilde{p}^\mu$, k^μ of the particles in the initial and final states, see below for the definitions.

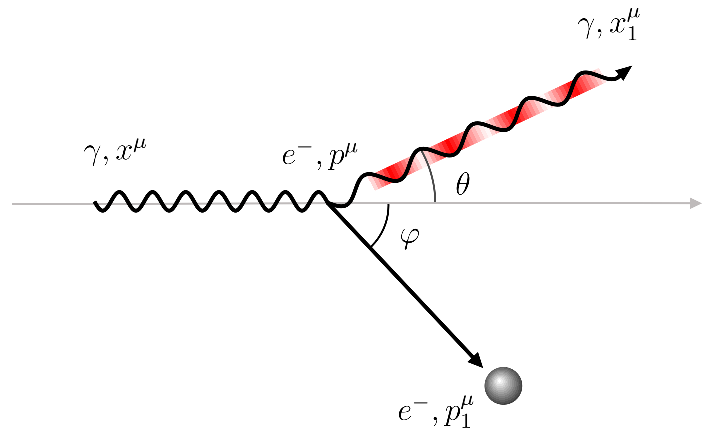

Figure 3.1: Pictorial view of the Compton scattering process, the color gradients representing the redshift of the incoming photon γ. Also, the adimensional four-momenta of the particles are indicated, for future utility in the text. The angles θ and ϕ describe the direction of the particles in the final state.

Adimensional four-momenta Let us lay the basis for a fully relativistic treatment of this process, starting with the *adimensional four-momenta*. By subscripting with a 1 index the final state and introducing a contravariant index μ in the (locally) Minkowski spacetime, we can write

ADIMENSIONAL PHOTON 4-MOMENTUM

$$x^\mu \equiv \frac{k^\mu}{m_e c} \equiv (|\vec{x}|, \vec{x}) = x\,(1, \hat{\omega})$$

$$\text{with} \quad k^\mu \equiv \left(h\nu/c, |\vec{k}|\right) , \qquad k^\mu k_\mu = 0\,.$$

Here we have called $\hat{\omega}$ the unit vector of photon direction, and of course $x \equiv |\vec{x}|$; also, the frequency ν of the photon satisfies the wave relation: $\nu = c/\lambda$. Analogously we define

ADIMENSIONAL ELECTRON 4-MOMENTUM

$$p^\mu \equiv \frac{\tilde{p}^\mu}{m_e c} \equiv (\gamma_e, \vec{p}) = \left(\gamma_e, p\hat{\Omega}\right) = \gamma_e \left(1, \beta\hat{\Omega}\right)$$

$$\text{with} \quad \tilde{p}^\mu \equiv \left(E_e/c, |\vec{\tilde{p}}|\right)\,.$$

In the above, E_e stands for the electron relativistic energy and we have used the fact that $|\vec{p}| \equiv p = \sqrt{\gamma_e^2 - 1}$, while introducing also a unitary electron direction $\hat{\Omega}$ for future utility. Lastly, we can formulate the condition Eq.(3.1) as

$$\boldsymbol{x \gtrsim 1}$$

The old quantum theory: wavelength and energy shift The historical treatment of relativistic electron scattering comes from A.H. Compton in 1923, who explained the effect in the *old quantum theory* fashion: as an inelastic collision with quantized particles' energy. The redshift of the scattered X-ray could, in fact, be motivated by simple relativistic theory, i.e. by applying the conservation of the total 4-momentum s of the system:

$$s \equiv (k^\mu + \tilde{p}^\mu)^2 \stackrel{!}{=} (k_1^\mu + \tilde{p}_1^\mu)^2 \qquad \Leftrightarrow$$

- **Energy Conservation** $$h\nu + m_e c^2 \stackrel{!}{=} h\nu_1 + \underbrace{\sqrt{\tilde{p}_1^2 c^2 + m_e^2 c^4}}_{:= E_{e1}}$$
- **Momentum Conservation** $$\frac{h\nu}{c}\hat{\omega} \stackrel{!}{=} \frac{h\nu_1}{c}\hat{\omega}_1 + \tilde{p}_1 \hat{\Omega}_1$$

The electron is supposed at rest in the initial state in this simplified case, and in the final state it acquires the energy E_{e1}. The famous Compton equation for the *wavelength shift* $\lambda_1 - \lambda$ can be easily derived by these conservation laws

Compton Wavelength Shift

$$\frac{x_1}{x} = \frac{1}{1 + x(1 - \cos\theta)} \,,$$

$$\text{or} \quad \lambda_1 - \lambda = \underbrace{\frac{h}{m_e c}}_{:= \lambda_c} (1 - \cos\theta)$$

and this result expresses the frequency x_1 of the scattered wave in the direction of the angle θ and measured from the incident direction $\hat{\omega}$, such that $\cos\theta \equiv \hat{\omega} \cdot \hat{\omega}_1$; we have also defined the Compton wavelength $\lambda_c \equiv h/m_e c \simeq 2.42 \times 10^{-10}$ cm.

NB The shift in wavelength $\lambda_1 - \lambda$ is *independent* of the incident photon energy x.

By using the same laws, completely analogously one can deduce the *energy shift* $x - x_1$, which in fact corresponds also to the acquired kinetic energy by the electron:

Compton Energy Shift

$$x - x_1 = \frac{x^2(1 - \cos\theta)}{1 + x(1 - \cos\theta)} \,,$$

$$\text{with} \quad \gamma_e - 1 \equiv \frac{E_{k,e1}}{m_e c^2} \stackrel{\text{Energy Cons}}{=} x - x_1 \,,$$

where also the kinetic energy of the electron in the final state $E_{k,e1} = E_{e1} - m_e c^2$ is introduced.

NB Since $\gamma_e - 1$ can only be a fraction of x, it is evident that a stationary, *free electron cannot absorb a photon* by itself, but scattering must occur with a bound charged particle. Also, this energy shift is actually *dependent* of the incident photon energy x.

The affine parameter and the null geodesic Let us also point out the photon's 4-momentum definition in more (General) Relativistic terms. With this purpose, we call $x^\mu_{\text{wl}}(\lambda) \in \mathcal{M}$ the worldline, or better the null geodesic, of our initial state photon, well defined curve on the (locally flat) manifold $\mathcal{M}$.

The (coordinate basis) components $k^\mu(x^\mu_{\text{wl}}(\lambda))$ of a vector field $V \equiv k^\mu(x^\mu_{\text{wl}}(\lambda))\partial_\mu$, tangent to a null geodesic curve $x^\mu_{\rm wl}(\lambda) \in \mathcal{M}$, are given in these terms

$$k^\mu(x^\mu_{\rm wl}(\lambda)) \equiv \frac{dx^\mu_{\rm wl}(\lambda)}{d\lambda} \qquad \text{with} \quad \frac{d}{d\lambda} \equiv k^\mu(x_{\rm wl}(\lambda))\frac{\partial}{\partial x^\mu_{\rm wl}} \,,$$

with λ being an appropriate *affine parameter*, completely fixed, affine transformations aside, by the choice of the curve; also, we have defined the derivative $d/d\lambda$ of a vector field V along the geodesic path. An affine transformation such $\lambda \to \lambda'$ shall result in

$$k^\mu(x^\mu_{\rm wl}(\lambda)) \xrightarrow{\lambda\to\lambda'} x^\mu(x^\mu_{\rm wl}(\lambda')) \equiv \frac{dx^\mu_{\rm wl}(\lambda')}{d\lambda'}$$

$$\text{with} \qquad x^\mu = \frac{d\lambda}{d\lambda'}\frac{dx^\mu_{\rm wl}}{d\lambda} \stackrel{!}{=} \frac{d\lambda}{d\lambda'}k^\mu \quad \Leftrightarrow \quad \frac{d\lambda}{d\lambda'} = \frac{1}{m_e c} \,.$$

We are thus able to write the *null geodesic*, namely the equation of parallel transport of the tangent vector V along the null curve:

$$\textsc{Null Photon Geodesic} \qquad \frac{dx^\mu}{d\lambda'} + \cancel{\Gamma^\mu_{\nu\rho}(x^\mu_{\rm wl}(\lambda'))}\, x^\nu x^\rho = \frac{d^2 x^\mu_{\rm wl}(\lambda')}{d\lambda'} \stackrel{!}{=} 0 \tag{3.3}$$

The Riemaniann connection $\Gamma^\mu_{\nu\rho}$ is here cancelled, because we are going to study our collision with standard Quantum Field Theory (QFT) in the Interaction Picture (IP), in which the interaction is highly localized: the manifold $\mathcal{M}$ is thus approximately flat and we can use Minkowski spacetime and Special Relativity (SR). Finally, the photon geodesic is given by simple double integration of Eq.(3.3):

$$x^\mu_{\rm wl}(\lambda) = (ct, \vec{x}_{\rm wl}) \quad \xrightarrow{\lambda\to\lambda'} \quad x^\mu_{\rm wl}(\lambda') = (ct, \vec{x}_{\rm wl}) \,. \tag{3.4}$$

We have of course used the coordinate time t as an affine parameter $\lambda \to t$ to the proper time, since we are in a Minkowski-like spacetime.

3.1.1 The Klein-Nishina cross section

Once the Dirac relativistic wave equation for spin-1/2 massive particles outburst in 1928, O. Klein and Y. Nishina adopted the fully quantum field theoretical framework to derive the famous, homonymous result: the *Klein-Nishina cross section* for Compton scattering of an X-ray from a free electron, see Klein, Nishina (1929) [KN29].
This paragraph will not follow the full calculation, but rather present the hypothesis and the full result, as it will be useful for the treatment of Compton scattering in stellar plasma in Sec.(3.2.1). For this entire paragraph we shall stick to the very common *natural units* ($c = \hbar = 1$) in particle physics; we will adjust, in the following, the quantities of interest back to the cgs.

The Compton scattering matrix element The first step in the QFT IP framework to build the probability amplitude for a transition from an initial to a final state is to build the *scattering matrix element* $S_{fi} = \langle f|S|i\rangle$ for the specific process under study, from which all

observables can be derived.
As we know, the scattering matrix S in IP admits an expansion in perturbation theory; for Compton scattering, it is sufficient to stick to standard QED, i.e. stop the expansion at the second $n = 2$ order, writing

$$S_{e^-\gamma\to e^-\gamma} \equiv \left\langle f \left| \overbrace{\sum_n S^{(n)}}^{:=S} \right| i \right\rangle \simeq \delta_{fi} + S^{(2)}_{e^-\gamma\to e^-\gamma}$$

$$S^{(2)}_{e^-\gamma\to e^-\gamma} \equiv \langle f \left| S^{(2)} \right| i \rangle = (2\pi)^4 \, \delta^{(4)} \left(\sum_f p_f - \sum_i p_i \right) \times \; \dots \tag{3.5}$$

$$\dots \times \prod_i \left(\frac{1}{2E_i V} \right)^{1/2} \prod_f \left(\frac{1}{2E_f V} \right)^{1/2} \mathcal{M}_{e^-\gamma\to e^-\gamma}$$

We are calling p_f and p_i the (dimensionfull) 4-momenta of the final and initial state particles, respectively, and we have introduced the Feynmann amplitude $\mathcal{M}_{e^-\gamma\to e^-\gamma}$. The figure below pictorially shows the IP framework for Compton scattering, for which we can define the initial $|i\rangle$ and final $|f\rangle$ states as follows:

$$|i\rangle \equiv \left|e^-_s\left(\tilde{p}\right)\right\rangle \otimes \left|\gamma_\lambda\left(k\right)\right\rangle$$
$$|f\rangle \equiv \left|e^-_s\left(\tilde{p}_1\right)\right\rangle \otimes \left|\gamma_{\lambda_1}\left(k_1\right)\right\rangle$$

with

$$\left|e^-_s\left(\tilde{p}\right)\right\rangle \equiv \frac{1}{\sqrt{2E_e V}}(2\pi)^{3/2} \times$$
$$\times \sqrt{2\omega_p}\, C^\dagger_s\left(\tilde{p}\right) \left|0\left(\tilde{p}\right)\right\rangle$$
$$\left|\gamma_\lambda\left(k\right)\right\rangle \equiv \frac{1}{\sqrt{2E_\gamma V}}(2\pi)^{3/2} \times$$
$$\times \sqrt{2\omega_k}\, A^\dagger_\lambda\left(k\right) \left|0\left(k\right)\right\rangle$$

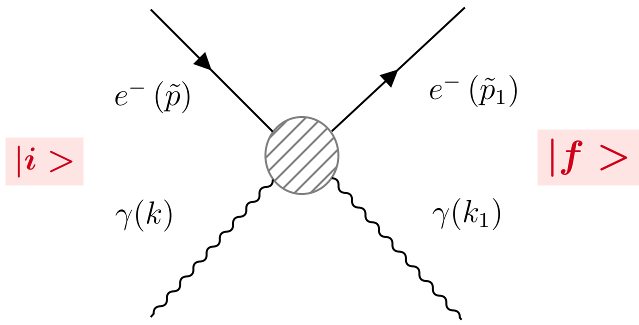

Figure 3.2: Pictorial view of Interaction Picture (IP) framework for Compton scattering. The evolution of the initial state $|i>$ into $|f>$, which stand at formally infinite time interval distance, is highlighted. The gray shaded area is the scattering region, in which we do not know what happens.

We have defined the single particle eigenstates $|e^-_s(\tilde{p})\rangle$ and $|\gamma_\lambda(k)\rangle$ in the continuum normalization in finite volume V framework of canonical quantization; the polarization and spin states are indexed by λ and s; the vacuum, Fock-like momentum eigenstate is called $|0\rangle$. Such a normalization of states reads

$$\left\langle e^-_r\left(\tilde{q}\right)\right| \left. e^-_s\left(\tilde{p}\right)\right\rangle = \frac{1}{V}\,(2\pi)^3\, \langle 0| \left\{ A_r\left(\vec{\tilde{q}}\right), A^\dagger_s\left(\vec{\tilde{p}}\right) \right\} |0\rangle =$$

$$= \delta_{rs}\,(2\pi)^3\,\frac{\delta^{(3)}(\vec{\tilde{q}}-\vec{\tilde{p}})}{V}\ ,$$

where the last factor is adimensional and we have used the canonical quantization with anticommutators $\{.\}$ for the creation/destruction operators $A_s^\dagger$ and A_r, with the different spin states s and r; also, plainly $\langle 0|0\rangle = 1$ in Fock space.

The Feynman amplitude $\mathcal{M}$ The further step is to obtain the *Feynman amplitude* for the Compton scattering $\mathcal{M}_{e^-\gamma\to e^-\gamma}$. The fastest way to achieve this quantity is to use the Feynman rules for QED vertices, once one has recognized the $2\to 2$ processes contributing to the total amplitude. Defining the two Mandelstam variables

$$s \equiv (\tilde{p}^\mu + k^\mu)^2 = (\tilde{p}_1^\mu + k_1^\mu)^2\ ,$$

$$u \equiv (\tilde{p}^\mu - k_1^\mu)^2 = (\tilde{p}_1^\mu - k^\mu)^2\ ,$$

the two contributions $\mathcal{M}_s$ and $\mathcal{M}_u$ can be easily identified as the ones in Figure below; these are conserving the total s and the total u, respectively.

Feynman Rules

- The QED vertex is $ie\gamma^\mu$.
- The fermion propagator is

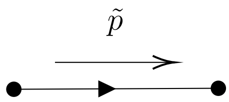

- Fermion legs cannot clash for total charge conservation.
- Spinor factors must be written from left to right in the same order as the opposite one to the arrows.
- A closed fermion loop corresponds to a trace and brings a factor (-1).

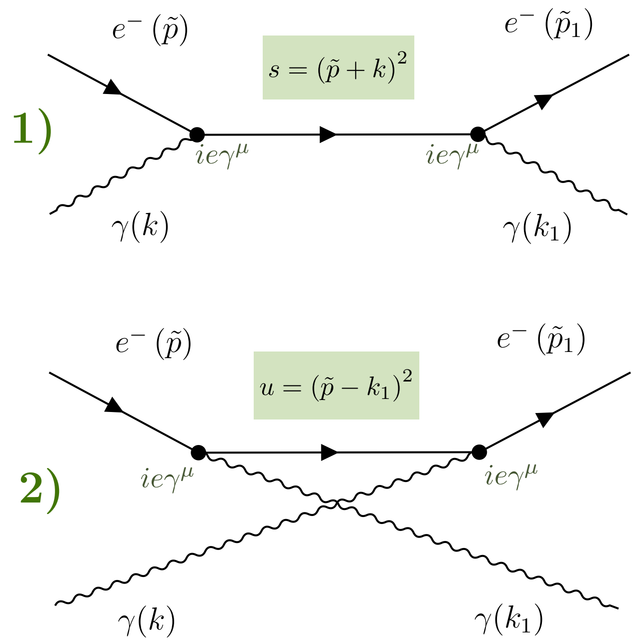

Figure 3.3: The two contributing Feynman diagrams for the Compton scattering process, respectively regarding the s and u-channel.

Going through these passages is beyond the scope of this work, and it is also a standard QED exercise; the resulting scattering amplitude for the Compton effect can, at the end, be written as the sum of the two contributions

$$\mathcal{M}_{e-\gamma\to e^-\gamma} = \mathcal{M}_s + \mathcal{M}_u\ ,$$

where 1) and 2) are added since we notice an identical fermion flow.

The unpolarized Feynman amplitude squared $|\tilde{\mathcal{M}}|^2$ All the observable quantities are derived from another entity: the *squared, unpolarized Feynman amplitude* $|\tilde{\mathcal{M}}_{e^\gamma \to e^-\gamma}|^2$. This quantity contains all the information about the kinematics of the process, and can be derived by standard (though lengthy) trace techniques.
It is defined as

$$\left|\tilde{\mathcal{M}}_{e^-\gamma\to e^-\gamma}\right|^2 \equiv \prod_i \frac{1}{(2j_i+1)} \sum_s \sum_f |\mathcal{M}_{e^-\gamma\to e^-\gamma}|^2 =$$

$$= \frac{1}{4} \underbrace{\sum_s \sum_\lambda}_{\text{initial}} \underbrace{\sum_{s_1} \sum_{\lambda_1}}_{\text{final}} |\mathcal{M}_{e^-\gamma\to e^-\gamma}|^2 = \frac{1}{4} \sum_{s,\lambda} |\mathcal{M}_{e^-\gamma\to e^-\gamma}|^2 \ ,$$

where the sum is carried over the initial and final polarization states, s and λ, of both particles, where j_i stands for the number of i particles states. This quantity is motivated by the fact that often

a) in experiments, the final spin of particles cannot be measured;

b) the initial polarization states are unknown unless contrarily specified.

By defining the conjugate process $\mathcal{M}^* \equiv T(\mathcal{M}) \times -1^{(\#\text{ vertices})}$, where the contribution $T(\mathcal{M})$ is obtained by an exchange of final and initial states, one can go through all the trace gymnastics to find

$$\left|\tilde{\mathcal{M}}_{e^-\gamma\to e^-\gamma}\right|^2 = |\mathcal{M}_s|^2 + |\mathcal{M}_u|^2 + \mathcal{M}_s^*\mathcal{M}_u + \mathcal{M}_u^*\mathcal{M}_s = \tag{3.6}$$

$$= 2e^4 \left[m^4 \left(\frac{1}{(\tilde{p}_\mu k^\mu)} - \frac{1}{\tilde{p}_\mu k_1^\mu} \right)^2 + 2m^2 \left(\frac{1}{(\tilde{p}_\mu k^\mu)} - \frac{1}{\tilde{p}_\mu k_1^\mu} \right) + \left(\frac{(\tilde{p}_\mu k_1^\mu)}{(\tilde{p}_\mu k^\mu)} + \frac{(\tilde{p}_\mu k^\mu)}{(\tilde{p}_\mu k_1^\mu)} \right) \right] =$$

$$\equiv 2e^4 F \ .$$

This result refers to a completely general reference frame. Notice that, in natural units (n.u.), this quantity is *adimensional*: $[e^4]_{\text{n.u.}} = \#$, $[F]_{\text{n.u.}} = \#$.
NB Notice, lastly, that we have defined the *Klein-Nishina reaction rate* F, due to Berestetskii et al. (1982) [BPL15], which will be very useful in Sec.(3.2.1):

KLEIN-NISHINA REACTION RATE

$$\begin{aligned} F \equiv m^4 & \left(\frac{1}{(\tilde{p}_\mu k^\mu)} - \frac{1}{\tilde{p}_\mu k_1^\mu} \right)^2 + \ \dots \\ \dots \ + 2m^2 & \left(\frac{1}{(\tilde{p}_\mu k^\mu)} - \frac{1}{\tilde{p}_\mu k_1^\mu} \right) + \left(\frac{(\tilde{p}_\mu k_1^\mu)}{(\tilde{p}_\mu k^\mu)} + \frac{(\tilde{p}_\mu k^\mu)}{(\tilde{p}_\mu k_1^\mu)} \right) \\ \text{with} \quad & [F]_{\text{n.u.}} = \# \end{aligned} \tag{3.7}$$

The transition probability per unit time w In order to introduce the cross sections, which is the natural quantity to measure experimentally, we need to identify the quantum mechanical equivalent of the number dN/dt of scattered particles per unit time dt by a target. This is called the *transition probability per unit time*, or simply transition rate w:

TRANSITION RATE

$$w \equiv \frac{|S_{fi}|^2}{dt} = \frac{|\langle f\,|S|\,i\rangle|^2}{dt} \quad \text{with} \quad [w]_{\text{n.u.}} = 1\,. \tag{3.8}$$

By accounting for the space and time (formal) regularization $(2\pi)^4\delta^{(4)}(0) = V dt$, we can explicitly write w fot the Compton scattering as

$$w = \frac{|S_{e^-\gamma\to e^-\gamma}|^2}{dt} = \tag{3.9}$$

$$\overset{\text{Eq.(3.5)}}{=} V(2\pi)^4\delta^{(4)}\left(\sum_f p_f - \sum_i p_i\right) \times \prod_i \left(\frac{1}{2VE_i}\right) \prod_f \left(\frac{1}{2VE_f}\right) |\mathcal{M}_{e^-\gamma\to e^-\gamma}|^2\,,$$

where we have used Eq.(3.5) for the expression of $S^{(2)}_{e^-\gamma\to e^-\gamma}$. Notice the n.u. dimensions of this quantity: $[w]_{\text{n.u.}} = 1$, since $[\delta^{(4)}(p_f)]_{\text{n.u.}} = -4$ and $[V]_{\text{n.u.}} = -3$.
Let us also introduce, for future utility, the differential *transition probability per unit time* dP/dt as follows:

TRANSITION PROBABILITY

$$\frac{dP}{dt} \equiv \textstyle\sum_{p_f} w \overset{V\to\infty}{=} \int_V \prod_f \frac{d^3p_f}{(2\pi)^3}\, V\, \frac{|S_{fi}|^2}{dt} \quad \text{with} \quad [dP/dt]_{\text{n.u.}} = 1\,.$$

Here, the limit for a large volume $V \longrightarrow \infty$ is used, which motivates the substitution of the sum over p_f into a regularized integral over the phase-space; this integration is needed to obtain the transition probability into a final state with all (kinematically allowed) final momentum p_f values.
Specializing to the Compton scattering case, we get for $dP_{e^-\gamma\to e^-\gamma}/dt$:

$$\frac{dP_{e^-\gamma\to e^-\gamma}}{dt} = \int_V \prod_f \frac{d^3p_f}{(2\pi)^3}\, V\, \frac{|S_{e^-\gamma\to e^-\gamma}|^2}{dt}\,. \tag{3.10}$$

This quantity, again, is such that $[dP/dt]_{\text{n.u.}} = 1$, appropriate for a probability per unit time.

The Klein-Nishina differential cross section We finally have all the ingredients to introduce the quantum mechanical *differential cross section* $d\sigma$. This quantity finds its classical counterpart in the cross-sectional geometrical area $d\sigma = dN/(dt \cdot \Phi)$, where Φ plays the role of the incoming flux of particles.

The differential cross section $d\sigma$ is defined as

Differential Cross Section

$$d\sigma \equiv \frac{1}{\Phi}\, w\, d\Pi = \frac{1}{\Phi}\frac{|S_{fi}|^2}{dt}\, d\Pi \qquad \text{with} \quad [d\sigma]_{\text{n.u.}} = -2\,, \tag{3.11}$$

where the *phase-space factor* $d\Pi$ is needed to obtain the transition to a final state with momenta in the intervals $[p_f, p_f + dp_f]$. Combining this definition with Eq.(3.9), one immediately finds the Compton scattering differential cross section

$$d\sigma = \frac{V}{v_{\text{rel}}}\, w \prod_f \frac{d^3 p_f}{(2\pi)^3} V = \tag{3.12}$$

$$= (2\pi)^4 \delta^{(4)}\left(\sum_f p_f - \sum_i p_i\right) \frac{1}{4E_e E_\gamma v_{\text{rel}}} \left(\prod_f \frac{d^3 p_f}{(2\pi)^3 2E_f}\right) |\mathcal{M}_{e^-\gamma\to e^-\gamma}|^2\,,$$

where we have also substituted $\Phi = v_{\text{rel}}/V$, with v_{rel} being the relative, often called Møller's, velocity of between initial particles. Notice also the correct natural units of the cross section: $[d\sigma]_{\text{n.u.}} = -2$.

This result for $d\sigma$ is generally valid, without any assumption regarding a preferred reference frame, as it holds for Eq.(3.6). We shall focus on the case in which the photon is incident on a fixed electron, in the *laboratory frame*, since we want to recover the famous form of the *Klein-Nishina differential cross section*, as in Eq.(2.6). Without going through all the calculations, we can simply state

$$\left|\tilde{\mathcal{M}}_{e^-\gamma\to e^-\gamma}\right|^2_{\text{lab}} = e^4\left(\frac{\nu}{\nu_1} + \frac{\nu_1}{\nu} - \sin^2\theta\right)\,,$$

where we have used some properties of laboratory frame, in which $\tilde{p} = (m_e, \vec{0})$ and $k = (2\pi\nu, \vec{k}) \Rightarrow \tilde{p}\cdot k = m_e 2\pi\nu$, or $\tilde{p}_1 = (E_1, \vec{\tilde{p}}_1)$, $k_1 = (2\pi\nu_1, k_1) \Rightarrow \tilde{p}\cdot k_1 = m_e 2\pi\nu_1$. Lastly, with similar manipulations, from Eq.(3.11) one obtains

$$\left.\frac{d\sigma}{d\Omega}\right|_{\substack{\text{lab}\\ \text{unpol}}} = \frac{1}{32\pi^2}\left(\frac{1}{m_e}\right)\left(\frac{\nu_1}{\nu}\right)^2 \left|\tilde{\mathcal{M}}_{e^-\gamma\to e^-\gamma}\right|^2_{\text{lab}} = \tag{3.13}$$

$$= \frac{1}{32\pi^2}\left(\frac{e^2}{m_e}\right)^2\left(\frac{\nu_1}{\nu}\right)^2\left(\frac{\nu}{\nu_1} + \frac{\nu_1}{\nu} - \sin^2\theta\right)\,,$$

which is nothing but Eq.(2.6), with this Chapter's notation and in natural units. Recovering the cgs system into this expression is very simple: one can immediately notice that a simple substitution allows to recover the right dimensionality of the observable quantity:

$$[e^2]_{\text{cgs}} = \text{g cm}^3\,\text{s}^{-2}\,, \quad [m_e]_{\text{cgs}} = \text{g} \quad \Rightarrow \quad \left(\frac{e^2}{m_e}\right) \xrightarrow{\text{cgs}} \left(\frac{e^2}{m_e c^2}\right)\,.$$

What about the positrons? Up till now we have kept the discussion focused on just the Compton scattering of X-rays to electrons, since this is the most common process of interest for massive stars, and it shall be the focus of the thesis. However, the formalism we are going to encounter in Sec.(3.2.1) is completely general, able to account also for Compton scattering to *positrons*:

$$e^+(\tilde{p}) + \gamma(k) \longrightarrow e^+(\tilde{p}_1) + \gamma(k_1) \,. \tag{3.14}$$

The QED formalism outlined above is obviously the same, since in QFT the spin-$1/2$ Dirac field equally describes both leptons as positive/negative energy eigenstates of the same fermion field. Nevertheless, one does not need to compute $\left|\tilde{\mathcal{M}}_{e^+\gamma\to e^+\gamma}\right|^2$: QED is invariant under charge conjugation, which implies invariance of the observables as well:

$$\left|\tilde{\mathcal{M}}_{e^+\gamma\to e^+\gamma}\right|^2 = \left|\tilde{\mathcal{M}}_{e^-\gamma\to e^-\gamma}\right|^2 \,.$$

In the following Sec.(3.2.1) we shall treat both positrons and electrons, since the invariance of QED makes this task fairly easy; we will explicitly drop the positrons, furtherly, as a first approximation, but highlighting this as a possible future improvement of the work.

3.2 Compton Scattering in Stellar Matter

As already said in Sec.(1.2), the stellar matter is always treated as a thermodynamic, perfect fluid system, whose many-body properties are generally overlooked in favor of a statistical description of the macroscopic quantities, i.e. thermodynamic state variables. The cores of massive stars during their advanced stages of evolution are not an exception, and we expect that the Compton scattering of X-rays to free charged leptons shall be important in those conditions precisely.
This section describes the theoretical treatment of *Compton scattering in stellar matter*, starting with **a)** an overview of the assumptions on the stellar plasma, progressing with **b)** the Boltzmann transport equation solution for the photon mean free path and concluding with **c)** the actual prescriptions for Compton opacity used in SECs.

3.2.1 Relativistic kinetic theory formulation

The kinetic theory of perfect gases characterizes the many-body systems with a statistical approach, in terms of one-particle distribution functions. On the ***macroscopic*** level, these systems' states are described by

Particle Density N , Energy Density U , Pressure P ,

where the latter can actually be a proxy for the hydrodynamic velocity. These fundamental quantities are, in principle, functions of the spacetime coordinates, and when the theoretical implant in which the spacetime is embedded is relativistic we say that we are formulating a *relativistic kinetic theory*, see e.g. [Gro80].

On the ***microscopic*** level, the specific interactions of the constituent particles of the many-body system nevertheless enter the statistical formulation, in the form of a dynamical quantity: the **transition probability**. We have already defined the latter in a relativistic (field theoretical) framework in Sec.(3.1.1), in general, and in Eq.(3.10) for the Compton scattering; this will indeed prove useful within the present description.

Reviewing the entire framework of a covariant hydrodynamic theory from conservation laws is far beyond the scope of this work; in the following, we would rather present the interesting quantities for our treatment, namely only the ones useful for building a transport equation for Compton scattering.

The distribution function The fundamental building block of relativistic kinetic theory, from which the macroscopic state variables can be obtained, is a *distribution function* $n(t, \boldsymbol{x}, \boldsymbol{p})$, function of space $\boldsymbol{x}$ and time t coordinates as well as (dimensionfull) momenta $\boldsymbol{p}$. It is defined in such a way thet

$$n(t, \boldsymbol{x}, \boldsymbol{p})\; d^3x\; d^3p \quad \Longrightarrow \quad \begin{array}{l} \#\text{ particles at } d^3x\; d^3p(t, \boldsymbol{x}, \boldsymbol{p}) \\ \text{with } \boldsymbol{p} \in (\boldsymbol{p}, \boldsymbol{p} + \boldsymbol{dp})\ , \end{array}$$

$d^3x\; d^3p(t, \boldsymbol{x}, \boldsymbol{p})$ being the spatial volume element at the specific spacetime coordinates; plainly, bolded symbols stand for 3-vectors to ease the notation, e.g. $\boldsymbol{x} = \vec{x}$.
NB This definition presupposes that **a)** the number of particles contained in the volume element d^3x is large; b) the size of d^3x is small from a macroscopic point of view.

A ionized, relativistic plasma of e^-, H^+ Temperatures such as in Eq.(3.1) are reached, in the core of massive stars, only in the most advanced stages of evolution, namely towards the ignition of C-burning, as one can see in Fig.(1.6). These extreme conditions make the assumptions of a *ionized, relativistic plasma* very appropriate.

I. e^- , $\mathbf{H}^+$ As the C-burning approaches, H is already efficiently depleted in the core; we can imagine a plasma made of free e^- and H^+, plus a fraction of e^+ which depends on processes like pair production.

II. ***Ionized*** The ionization energy of hydrogen $\chi_{\mathrm{H}} \simeq 13.6\,\mathrm{eV}$ is, in any case, much lower that the average temperatures in stellar interiors:

$$\log \mathrm{T}_{\mathrm{H,\,ion}} \simeq \log\left(\frac{\chi_{\mathrm{H}}}{4.96\,k}\right) \simeq 4.5 \ll \log \mathrm{T} \gtrsim 8\ .$$

This assures that a full Saha equation treatment for partial ionization is not needed; also, the expression in Eq.(1.7) for μ_e is also good.

III. ***Relativistic*** Highly energetic photons interact with electrons which, at the highest densities ρ and degeneracies η, are relativistic. The relativity indeed enters in the treatment with the expressions for the energies E_k of particles and the collision rate.

The highly energetic radiation field, lastly, will be tightly coupled to the matter plasma, in the well known hypothesis of LTE.

LTE and beyond As fairly known, in *Local Thermodynamic Equilibrium* ▶ the properties of matter are dominated by matter collisions, which establish thermodynamic equilibrium locally at $(t, \boldsymbol{x})$; ▶ if the radiation field deviates from the classical Planckian, it is such that it does not affect this equilibrium.
Thus, the components $e^{\pm}$ and γ of the stellar plasma can be described by simple distribution functions; we are again calling p and x the adimensional momenta of $e^{\pm}$ and γ, since we want to use adimensional quantities throughout.

FERMI-DIRAC DISTRIBUTION

$$\tilde{n}_{\pm}(\gamma) \equiv \frac{1}{\exp\left(\dfrac{E_k - \mu_{\pm}}{kT}\right) + 1} = \frac{1}{\exp\left(\dfrac{\gamma - 1}{\Theta} - \eta_{\pm}\right) + 1}$$

$$\text{with} \quad \eta_{\pm} \equiv \frac{\mu_{\pm}}{kT}\,, \quad \Theta \equiv \frac{kT}{m_e c^2}$$

BOSE-EINSTEIN DISTRIBUTION

$$n(x) \equiv \frac{1}{\exp\left(\dfrac{h\nu}{kT}\right) - 1} = \frac{1}{\exp\left(\dfrac{x}{\Theta}\right) - 1}$$

Notice that we have introduced the degeneracy parameter $\eta_{\pm}$ of positrons and electrons in terms of their chemical potential $\mu_{\pm}$, and the adimensional temperature proxy Θ; also, we have used the relation $E_k \equiv E_{k,e} = m_e c^2(\gamma_e - 1)$. These are the well known Fermi-Dirac (FD) and Bose-Einstein (BE) distribution functions, accounting for the statistics of quantum particles.

To advance with our study, we need to go *beyond* these *equilibrium* distributions, allowing for a general dependence $\tilde{n}(\boldsymbol{p})$ and/or $n(\boldsymbol{x})$; we could expect that these will take a perturbed shape with respect to the equilibrium FD and BE ones, but this will depend on the considered case and processes.
In total generality, the $e^{\pm}$ concentrations $N_{\pm}$ are given by the integrals of the out-of-equilibrium distribution over the momentum space:

$$N_{\pm} = \frac{g_{e^{\pm}}}{h^3} \int d^3\tilde{\boldsymbol{p}}\, \tilde{n}_{\pm}(\tilde{\boldsymbol{p}}) = \frac{2}{\lambda_c^3}\, 4\pi \int_0^{\infty} p^2 dp\, \tilde{n}_{\pm}(\boldsymbol{p}) = \frac{2}{\lambda_c^3}\, 4\pi \int_1^{\infty} \sqrt{\gamma^2 - 1}\, d\gamma\, \tilde{n}_{\pm}(\gamma)$$

$$\text{with} \quad p = \sqrt{\gamma^2 - 1}\,, \quad pdp = \gamma d\gamma\,,$$

and we have made explicit the change of variables; also, $g_{e^{\pm}} = 2$ accounts for the spin states of the fermions $e^{\pm}$. Analogously, one can define the γ number density N_{γ}

$$N_{\gamma} = g_{\gamma} \frac{V}{h^3} \int d^3\boldsymbol{k}\, n(\boldsymbol{k}) = g_{\gamma} \frac{V}{\lambda_c^3} \int d^3\boldsymbol{x}\, n(\boldsymbol{x}) \tag{3.15}$$

$$\text{with} \quad d\boldsymbol{k} = m_e c\, d\boldsymbol{x}\,, \quad d^3\boldsymbol{k} = (m_e c)^3 d^3\boldsymbol{x}\,.$$

Again, the polarization states of photons $g_\gamma = 2$. Finally, the total mass density ρ (not including $e^\pm$ created by pair production or radiation) is given by

Total Mass Density
$$\rho = (N_- - N_+)\,\mu_e m_u \quad \text{with} \quad \mu_e^{-1} \equiv \textstyle\sum_i Z_i X_i / A_i \simeq 0.5\,,$$

while the total number density of both electrons and positrons is given by $N_e = N_- + N_+$. This is given by charge neutrality, which states that the number density of free electrons in matter $N_{\text{e, matter}} \equiv \rho/\mu N_{\text{ion}}$ must satisfy the following:

Charge Neutrality
$$N_{\text{e, matter}} = N_- - N_+\,.$$

The Boltzmann Transport Equation (BTE) formalism The formal instrument for the treatment of out-of-equilibrium evolution of thermodynamical systems is called *Boltzmann Transport Equation* (BTE): this is a closed equation for the spacetime behavior of the distribution function, which relies on a number of assumptions.

a) ***Stosszahlansatz*** Absence of particle correlation is postulated before each individial collision; this is known also as the *molecular chaos hypothesis*.

b) ***Macroscopic description*** Changes of the distribution function on microscopic scales of length and time are negligibly small, for the macroscopic description to be possible.

The general, relativistic form of the Boltzmann equation postulates the equality between two operators, Liouville's and Collision's, both acting on the distribution function. For the Compton scattering, we need to follow the photon's $n(\boldsymbol{x})$, so

Boltzmann Equation
$$\hat{\mathbb{L}}\left[n(\boldsymbol{x})\right] = \hat{\mathbb{C}}\left[n(\boldsymbol{x})\right]\,. \tag{3.16}$$

The photons' distribution $n(\boldsymbol{x})$ is our unknown, while for $e^\pm$ we shall adopt the FD throughout, since actually the out-of-equilibrium nature of these distributions can be encoded in the $\mu_\pm$, accounting for diffusive equilibrium of the system.

Liouville operator $\hat{\mathbb{L}}$ The *Liouville's operator* $\hat{\mathbb{L}}$ plays the role of the total derivative of the distribution function $n(\boldsymbol{x})$, with respect to an affine parameter λ. It is supposed to describe the changes of $n(\boldsymbol{x})$ along the photon trajectory:

$$\hat{\mathbb{L}}\left[n(\boldsymbol{x})\right] = \frac{d}{d\lambda'}\left[n\left(x^\mu_{\text{wl}}(\lambda'), k^\mu(\lambda')\right)\right] = \left[x^\mu \frac{\partial}{\partial x^\mu_{\text{wl}}} + \cancel{\frac{dx^\mu}{d\lambda'}\frac{\partial}{\partial x^\mu}}\right] n(\boldsymbol{x}) \overset{\text{Eq.(3.3)}}{=}$$
$$= x^\mu \frac{\partial n(\boldsymbol{x})}{\partial x^\mu_{\text{wl}}} \overset{\text{Eq.(3.4)}}{=} x\left[\frac{\partial}{c\,\partial t} + \hat{\omega}\cdot\vec{\nabla}\right] n(\boldsymbol{x})$$

Liouville Operator
$$\hat{\mathbb{L}}\left[n(\boldsymbol{x})\right] = x\left[\frac{\partial}{c\,\partial t} + \hat{\omega}\cdot\vec{\nabla}\right] n(\boldsymbol{x})\,. \tag{3.17}$$

Notice the cgs dimensions of this operator, since we will have to adjust the collision operator's ones accordingly: $[\hat{\mathbb{L}}_{e^-\gamma\to e^-\gamma}[n(\boldsymbol{x})]]_{\text{cgs}} = \text{cm}^{-1}$.
Let us also compute, in the same fashion, the time derivative $dn(\boldsymbol{x})/dt$ of the distribution function in terms of the Liouville's operator, for future utility:

$$\frac{dn(\boldsymbol{x})}{dt} = c\,\frac{d\lambda'}{c\,dt}\,\frac{dn(\boldsymbol{x})}{d\lambda'} = \frac{c}{x}\,\frac{dn(\boldsymbol{x})}{d\lambda'}\ . \tag{3.18}$$

Collision operator $\hat{\mathbb{C}}$ The *collision operator* $\hat{\mathbb{C}}$ describes the change of $n(\boldsymbol{x})$ caused by any kind of process, both elastic (Compton scattering) and inelastic (annihilations). Its explicit form changes according to the selected process, since it also comprises the microscopic dynamical information. Let us deduce it, for Compton scattering, with some simple arguments.
We can start with the time derivative of the concentration N_γ:

$$\frac{dN_\gamma}{dt} \overset{\text{Eq.(3.15)}}{=} g_\gamma \frac{V}{\lambda_c^3}\int d^3\boldsymbol{x}\,\frac{dn(\boldsymbol{x})}{dt} \overset{\text{Eq.(3.18)}}{=} g_\gamma \frac{V}{\lambda_c^3}\int d^3\boldsymbol{x}\,\frac{c}{x}\,\hat{\mathbb{L}}\,[n(\boldsymbol{x})] = \tag{3.19}$$
$$\overset{\text{Eq.(3.16)}}{=} g_\gamma \frac{V}{\lambda_c^3}\int d^3\boldsymbol{x}\,\frac{c}{x}\,\hat{\mathbb{C}}_{e^-\gamma\to e^-\gamma}\,[n(\boldsymbol{x})]\ .$$

Here, we have simply applied Eq.(3.18) and the Boltzmann equation Eq.(3.16) itself, to find an expression of dN_γ/dt in terms of $\hat{\mathbb{C}}$; notice that we are concentrating on the specific process $\hat{\mathbb{C}}_{e^-\gamma\to e^-\gamma}$. If we are able to find, by other means, another expression for dN_γ/dt, we will be able to compare these two to successfully find $\hat{\mathbb{C}}_{e^-\gamma\to e^-\gamma}$.
More precisely, we recall that the change dN_γ/dt in the number of γ, due to Compton scattering, in the time interval dt is given by the collision rate $dP_{e^-\gamma\to e^-\gamma}/dt$, integrated within the number N_{in} of initial state particles:

$$\frac{dN_\gamma}{dt} = \overbrace{g_\gamma g_e \frac{V}{\lambda_c^3}\frac{V}{\lambda_c^3}\int d^3\boldsymbol{x}\,d^3\boldsymbol{p}\,\tilde{n}_-(\boldsymbol{p})\,n(\boldsymbol{x})}^{:=N_{\text{in}}}\,\frac{dP_{e^-\gamma\to e^-\gamma}}{dt}\ .$$

Let us elaborate further on the transition probability $dP_{e^-\gamma\to e^-\gamma}/dt$ of Eq.(3.10):

$$\frac{dP_{e^-\gamma\to e^-\gamma}}{dt} \overset{\text{Eq.(3.10)}}{=} \int_V \prod_f \frac{d^3\boldsymbol{p}_f}{\lambda_c^3}\,V\,\frac{|S_{e^-\gamma\to e^-\gamma}|^2}{dt} =$$
$$= \int \frac{V}{\lambda_c^3}\,d^3\boldsymbol{p}_1 \int \frac{V}{\lambda_c^3}\,d^3\boldsymbol{x}_1\,\frac{h^4}{(m_e c)^4}\,\delta^{(4)}\left(x_1^\mu + p_1^\mu - p^\mu - x^\mu\right)\,V\times$$
$$\times\,|\mathcal{M}_{e^-\gamma\to e^-\gamma}|^2 \prod_i \left(\frac{1}{2Vp_i}\right)\prod_f\left(\frac{1}{2Vp_f}\right) =$$
$$= \int \frac{1}{\lambda_c^3}\,d^3\boldsymbol{p}_1 \int \frac{1}{\lambda_c^3}\,d^3\boldsymbol{x}_1\,\frac{\lambda_c^4}{(m_e c)^4}\,\delta^{(4)}\left(x_1^\mu + p_1^\mu - p^\mu - x^\mu\right)\,\times$$

$$\times \frac{|\mathcal{M}_{e^-\gamma\to e^-\gamma}|^2}{V} \frac{1}{2c\gamma_e} \frac{1}{2c\gamma_{e1}} \frac{1}{2cx} \frac{1}{2cx_1} =$$

$$= \int \frac{1}{\lambda_c^3} \frac{d^3\boldsymbol{p}_1}{2\gamma_{e1}} \int \frac{1}{\lambda_c^3} \frac{d^3\boldsymbol{x}_1}{2x_1} \left[\frac{\lambda_c^4}{(m_e c^2)^4} \delta^{(4)} \left(x_1^\mu + p_1^\mu - p^\mu - x^\mu \right) \frac{|\mathcal{M}_{e^-\gamma\to e^-\gamma}|^2}{V} \frac{1}{2\gamma_e} \frac{1}{2x} \right] \longrightarrow$$

$$\xrightarrow{\text{cgs}} (\hbar c)^4 c \int \frac{1}{\lambda_c^3} \frac{d^3\boldsymbol{p}_1}{2\gamma_{e1}} \int \frac{1}{\lambda_c^3} \frac{d^3\boldsymbol{x}_1}{2x_1} \times$$

$$\times \left[\frac{\lambda_c^4}{(m_e c^2)^4} \delta^{(4)} \left(x_1^\mu + p_1^\mu - p^\mu - x^\mu \right) \frac{|\mathcal{M}_{e^-\gamma\to e^-\gamma}|^2}{V} \frac{1}{2\gamma_e} \frac{1}{2x} \right] .$$

In the last line we have simply observed that the transition probability $dP_{e^-\gamma\to e^-\gamma}/dt$ must have the dimensions of inverse time; thus we restored the cgs units by a multiplication $\times c(\hbar c)^4$. We thus obtain for dN_γ/dt:

$$\frac{dN_\gamma}{dt} = g_\gamma \frac{V}{\lambda_c^3} \int d^3\boldsymbol{x} \, \frac{c}{x} \left[x \, g_e \frac{V}{\lambda_c^3} \int d^3\boldsymbol{p} \, n(\boldsymbol{x}) \tilde{n}_-(\boldsymbol{p}) \frac{dP_{e^-\gamma\to e^-\gamma}}{dt} \right] =$$

$$= g_\gamma \frac{V}{\lambda_c^3} \int d^3\boldsymbol{x} \, \frac{c}{x} \left\{ \frac{n(\boldsymbol{x})\tilde{n}_-(\boldsymbol{p})}{2} \left[\int \overbrace{\frac{g_e}{\lambda_c^3} \frac{d^3\boldsymbol{p}}{2\gamma_e}}^{:= d\Pi_e} \int \overbrace{\frac{g_e}{\lambda_c^3} \frac{d^3\boldsymbol{p}_1}{2\gamma_{e1}}}^{:= d\Pi_{e1}} \int \overbrace{\frac{g_\gamma}{\lambda_c^3} \frac{d^3\boldsymbol{x}_1}{2x_1}}^{:= d\Pi_\gamma} \times \right.\right.$$

$$\left.\left. \times \left(\frac{\lambda_c^4}{(m_e c^2)^4} \delta^{(4)} \left(x_1^\mu + p_1^\mu - p^\mu - x^\mu \right) \overbrace{\frac{|\mathcal{M}_{e^-\gamma\to e^-\gamma}|^2}{g_e g_\gamma}}^{:= |\tilde{\mathcal{M}}|^2} \right) \right] (\hbar c)^4 \right\} \stackrel{!}{=}$$

$$\stackrel{!}{=} g_\gamma \frac{V}{\lambda_c^3} \int d^3\boldsymbol{x} \, \frac{c}{x} \, \hat{\mathbb{C}}_{e^-\gamma\to e^-\gamma}[n(\boldsymbol{x})] \qquad \Leftrightarrow$$

$$\hat{\mathbb{C}}_{e^-\gamma\to e^-\gamma}[n(\boldsymbol{x})] =$$

$$= -\frac{1}{2} \int d\Pi_e \, d\Pi_{e1} \, d\Pi_\gamma \, \frac{\lambda_c^4 \, \hbar^4}{(m_e c)^4} \delta^{(4)} \left(x_1^\mu + p_1^\mu - p^\mu - x^\mu \right) \left| \tilde{\mathcal{M}}_{e^-\gamma\to e^-\gamma} \right|^2 n(\boldsymbol{x}) \tilde{n}_-(\boldsymbol{p}) =$$

$$\stackrel{\text{Eq.(3.7)}\times(\hbar c)^{-2}}{=} -\frac{r_e^2}{2} \frac{2}{\lambda_c^3} \int \frac{d^3\boldsymbol{p}_1}{\gamma_{e1}} \frac{d^3\boldsymbol{x}_1}{x_1} \frac{d^3\boldsymbol{p}}{\gamma_e} \delta^{(4)} \left(x_1^\mu + p_1^\mu - p^\mu - x^\mu \right) \, F \, n(\boldsymbol{x}) \tilde{n}(\boldsymbol{p}) \, .$$

In the second row we have identified the fully unpolarized Feynman amplitude squared $|\tilde{\mathcal{M}}_{e^-\gamma\to e^-\gamma}|^2$; in defining the collision operator $\hat{\mathbb{C}}_{e^-\gamma\to e^-\gamma}$ we have also reintroduced the cgs units multiplying by $(\hbar c)^{-2}$, since we wanted the $|\tilde{\mathcal{M}}_{e^-\gamma\to e^-\gamma}|^2$ to be dimensionless $\Rightarrow$ $[\hat{\mathbb{C}}_{e^-\gamma\to e^-\gamma}[n(\boldsymbol{x})]]_{\text{cgs}} = \text{cm}^{-1}$, as wanted.

We have thus obtained the expression for the collision operator of Compton scattering $\hat{\mathbb{C}}_{e^-\gamma\to e^-\gamma}$ by a direct comparison with Eq.(3.19); notice also the form, which is explicitly covariant.

Quantum corrections The final state, in our direct process $e^-\gamma \to e^-\gamma$, is populated by quantum particles which follow their own statistics; the effect of this has to be accounted by *quantum corrections*, which translates into a simple multiplication of the $n(\boldsymbol{x})$ distribution function by

$$\times\ \left[(1+n(\boldsymbol{x}_1))\,(1-\tilde{n}_-(\boldsymbol{p}_1))\right]\ .$$

One can easily see that these new factors describe a BE enhancing / FD blocking in the final state.

The BTE for Compton scattering Up to now we have focused on the direct Compton scattering process, $e^-\gamma \to e^-\gamma$. Of course, due to QED symmetry (see Sec.(3.1.1)), we need to account for **a)** ***positrons***; **b)** their respective ***time-reversed*** process, since $|\tilde{\mathcal{M}}_{ab\to cd}|^2 = |\tilde{\mathcal{M}}_{cd\to ab}|^2$ (CPT invariance of QED). All of these can be summarized in the following expression for the Boltzmann equation:

$$\hat{\mathbb{L}}[n(\boldsymbol{x})] \stackrel{!}{=} \hat{\mathbb{C}}[n(\boldsymbol{x})] = \sum_{b,c,d} \hat{\mathbb{C}}_{\gamma b\to cd}[n(\boldsymbol{x})]\ ,$$

where $b, c, d = e^{\pm}, \gamma$, depending on the selected process.
We can see that a different expression for $\hat{\mathbb{C}}[n(\boldsymbol{x})]$ is required for each of them, but thanks to the QED properties we do not need to perform the above calculations everytime, we can simply change the multiplicative factors. Additionally, each of these processes needs their proper quantum corrections:

$$\begin{array}{lll}
\textbf{1)} & e^-(p)\gamma(k) \to e^-(p_1)\gamma(k_1) & \times -\left[(1+n(\boldsymbol{x}_1))\,(1-\tilde{n}_-(\boldsymbol{p}_1))\right] \\
\textbf{2)} & e^-(p)\gamma(k) \leftarrow e^-(p_1)\gamma(k_1) & \times \left[(1+n(\boldsymbol{x}))\,(1-\tilde{n}_-(\boldsymbol{p}))\right] \\
\textbf{3)} & e^+(p)\gamma(k) \to e^+(p_1)\gamma(k_1) & \times -\left[(1+n(\boldsymbol{x}_1))\,(1-\tilde{n}_+(\boldsymbol{p}_1))\right] \\
\textbf{4)} & e^+(p)\gamma(k) \leftarrow e^+(p_1)\gamma(k_1) & \times \left[(1+n(\boldsymbol{x}))\,(1-\tilde{n}_+(\boldsymbol{p}))\right]
\end{array}$$

The $\pm$ signs basically decide whether the process is a source or a sink term for the population of $\gamma(k)$. Putting everything together and remembering the expression of the Liouville's operator in Eq.(3.17), we can write the complete ***Boltzmann Transport Equation*** for $n(\boldsymbol{x})$ in this way:

$$x\left[\frac{\partial}{c\partial t} - \hat{\omega}\cdot\vec{\nabla}\right] n(\boldsymbol{x}) = \frac{r_e^2}{2}\,\frac{2}{\lambda_c^3}\int \frac{d^3\boldsymbol{p}_1}{\gamma_{e1}}\,\frac{d^3\boldsymbol{p}}{\gamma_e}\,\frac{d^3\boldsymbol{x}_1}{x_1}\,F\times \tag{3.20}$$

$$\times\left\{n(\boldsymbol{x}_1)\,(1+n(\boldsymbol{x}))\,[\overbrace{\tilde{n}_-(\boldsymbol{p}_1)\,(1-\tilde{n}_-(\boldsymbol{p}))}^{\textbf{2)}} + \overbrace{\tilde{n}_+(\boldsymbol{p}_1)\,(1-\tilde{n}_+(\boldsymbol{p}))}^{\textbf{4)}}] + \right.$$

$$\left. n(x)\,(1+n(\boldsymbol{x}_1))\,[\overbrace{\tilde{n}_-(\boldsymbol{p})\,(1-\tilde{n}(\boldsymbol{p}_1))}^{\textbf{1)}} + \overbrace{\tilde{n}_+(\boldsymbol{p})\,(1-\tilde{n}_+(\boldsymbol{p}_1))}^{\textbf{3)}}]\right\}\ .$$

Redistribution functions The form of the BTE Eq.(3.20) can be simplified by introducing the so called <u>*Redistribution Functions*</u> (RF) $R_\pm(\boldsymbol{x} \to \boldsymbol{x}_1)$. These represent a prior component of radiative transfer theory, since they essentially represent the *differential scattering coefficient*, being then tightly connected to the scattering kernel, see e.g. [PP29]. In our case of a highly energetic radiation field scattering from a relativistic plasma of free $e^\pm$, this kernel will have distinct characteristics:

- ***Detailed balance principle*** Since the FD is the LTE distribution for $e^\pm$, the scattering kernel must also satisfy the detailed balance condition:

$$R_\pm(\boldsymbol{x} \to \boldsymbol{x}_1)\, e^{-x/\Theta} = R_\pm(\boldsymbol{x}_1 \to \boldsymbol{x})\, e^{-x_1/\Theta} \,,$$

  which is basically asserting that, in LTE, the number of photons scattering from $\boldsymbol{x} \to \boldsymbol{x}_1$ must equal the number scattered as $\boldsymbol{x}_1 \to \boldsymbol{x}$, stimulated emissions comprised.

- ***Angular dependence*** Since, in absence of strong magnetic fields, the matter is assumed to be isotropic, the dependence on the emission solid angle is reduced to a scattering angle μ dependence:

$$R_\pm(\boldsymbol{x} \to \boldsymbol{x}_1) = R_\pm(x, x_1, \mu) \,.$$

- ***Accounts for all the physics*** For Compton scattering, it basically accounts for all the physical effects expected by theory: **a)** photon's wavelength increase; **b)** classical Doppler broadening from scattering by moving $e^\pm$; **c)** photon's wavelength reduction upon relativistic effect on the target density.

These functions are defined in the following fashion:

Redistribution Functions

$$R_\pm(\boldsymbol{x}_1 \to \boldsymbol{x}) \equiv \frac{3}{16\pi}\,\frac{2}{\lambda_c^3}\,\frac{1}{N_\pm} \int \frac{d^3\boldsymbol{p}}{\gamma_e}\,\frac{d^3\boldsymbol{p}_1}{\gamma_{e1}} \times$$
$$\times\, \tilde{n}_\pm(\boldsymbol{p}_1)\,[1 - \tilde{n}_\pm(\boldsymbol{p})]\; F\, \delta^{(4)}\left(p_1^\mu + x_1^\mu - p^\mu - x^\mu\right) \,.$$

A total redistribution function $R(x, x_1, \mu)$ can be also introduced to ease the notation:

Total Redistribution Functions

$$R(x, x_1, \mu) \equiv \frac{N_-}{N_e}\, R_-(x, x_1, \mu) + \frac{N_+}{N_e}\, R_+(x, x_1, \mu) \,.$$

Finally, the BTE Eq.(3.20) in a steady state (i.e. for $\partial n(\boldsymbol{x})/\partial t$=0) can be recast in the same standard form of the radiative transfer equation with just the scattering term:

$$\hat{\omega} \cdot \vec{\nabla}_\tau n(\boldsymbol{x}) = \tag{3.21}$$

$$-\frac{n(\boldsymbol{x})}{x} \int \frac{d^3\boldsymbol{x}_1}{x_1}\, R(x, x_1, \mu)\; [1 + n(\boldsymbol{x}_1)] + \frac{[1 + n(\boldsymbol{x})]}{x} \int \frac{d^3\boldsymbol{x}_1}{x_1}\, R(x, x_1, \mu)\, n(\boldsymbol{x}_1) =$$
$$= -\frac{n(\boldsymbol{x})}{x} \int_0^\infty x_1\, dx_1 \int d^2\hat{\omega}_1\, R(x, x_1, \mu)\; [1 + n(\boldsymbol{x})] + \;\ldots$$

$$\ldots + \frac{[1+n(\boldsymbol{x})]}{x} \int_0^\infty x_1\, dx_1 \int d^2\hat{\omega}_1\, R(x, x_1, \mu)\, n(\boldsymbol{x}_1)\,.$$

In the last equality we have simply make explicit the 2D angles integral in $d\hat{\boldsymbol{\omega}}_1$ and the radial one in dx_1; also, we defined the ***dimensionless gradient*** $\vec{\nabla}_\tau \equiv \vec{\nabla}/\sigma_{\mathrm{Th}} N_e$. In the following, we shall closely follow the treatment by J. Poutanen (2017), [Pou17].

Diffusion approximation As it is often the praxis, to solve a radiative transfer problem a level of approximation is needed. A suitable one is the Eddington or *diffusion approximation*: the radiation field is taken to be nearly isotropic, with a small anisotropy along the scattering direction $\hat{\omega}$; this anisotropy is however essential, since it is responsible for the entire monochromatic flux transported in stellar layers. Of course, we can expect that this approximation must be quite good deep in thermonuclear burning regions of massive stars. The approximation amounts to write $n(\boldsymbol{x})$ as

$$\boldsymbol{n(x) = b_x - \tilde{l}_x \hat{\omega} \cdot \vec{\nabla}_\tau b_x}\,, \qquad \text{with} \quad b_x \equiv \left\{\exp\left(x/\Theta\right) - 1\right\}^{-1}\,,$$

and we are calling b_x the BE distribution, which constitutes the isotropic, zeroth order solution of the BTE; $\tilde{l}_x$, in the fashion of Chp.(2), is the *adimensional mean free path*, see below. A substitution of this form into Eq.(3.21) leads, after straightforward algebra, to

$$\hat{\omega} \cdot \vec{\nabla}_\tau n(\boldsymbol{x}) = \tag{3.22}$$

$$= \frac{1}{x} \int_0^\infty x_1\, dx_1 \int d^2\hat{\omega}_1\, R(x_1, x, \mu) \times$$

$$\times \left[\tilde{l}_x \hat{\omega} \cdot \vec{\nabla}_\tau b_x \left(\frac{1 - e^{-x/\Theta}}{1 - e^{-x_1/\Theta}} \right) - \tilde{l}_{x_1} \hat{\omega} \cdot \vec{\nabla}_\tau b_{x_1} \left(\frac{e^{x_1/\Theta} - 1}{e^{x/\Theta} - 1} \right) \right]\,.$$

We notice that zeroth order terms cancel each other out, leaving us with just $\vec{\nabla}_\tau b_x$ terms.

Adimensional photon mean free path $\tilde{l}_x$ Together with the Debye length λ_D, a quantity which is often used to characterize the interaction between the radiation field and matter is the *adimensional photon's mean free path* $\tilde{l}_x$. It is defined, in terms of the dimensionfull mean free path l_x, as

Adimensional Photon Mean Free Path

$$\tilde{l}_x \equiv \frac{l_x}{\sigma_{\mathrm{Th}} N_e}\,, \tag{3.23}$$

and, in general, is expected to describe the average distance traveled by a photon of energy x before experiencing an interaction. In our case, we are accounting for Compton scatterings, and we can recast Eq.(3.22) into a linear integral equation for $\tilde{l}_x$:

$$1 = \frac{1}{x} \int_0^\infty x_1\, dx_1 \int d^2\hat{\omega}_1\, R(x_1, x, \mu) \left(\frac{1 - e^{-x/\Theta}}{1 - e^{-x_1/\Theta}} \right) \left[\tilde{l}_x - \tilde{l}_{x_1} \frac{x_1}{x} \frac{\hat{\omega}_1 \cdot \vec{\nabla}_\tau \Theta}{\hat{\omega} \cdot \vec{\nabla}_\tau \Theta} \right]$$

This is the final form of our equation, since we precisely want to find $\tilde{l}_x$, as it is fundamental to compute the rosseland mean free path $\Lambda(\Theta, \eta)$ and, ultimately, the Compton scattering opacity, in the fashion of Sec.(**??**), see Eq.(2.4). Now it is a matter of choosing the appropriate reference system. We shall adopt the description illustrated below, which allows us to single out the azimuthal integral over $d\phi$.

Reference system

$$\hat{\omega} = (0, 0, 1) \ ,$$

$$\hat{\omega}_1 = \left(\sqrt{1-\mu^2}\cos\phi, \sqrt{1-\mu^2}\sin\phi, \mu\right) \ ,$$

with $\mu = \cos\theta = \hat{\omega}_1 \cdot \hat{\omega}$,

$$\vec{\nabla}_\tau \Theta \propto (\sin\theta, 0 \cos\theta)$$

$$\Downarrow$$

Azimuthal integral

$$\int_0^{2\pi} d\phi \left[\frac{\hat{\omega}_1 \cdot \vec{\nabla}_\tau \Theta}{\hat{\omega} \cdot \vec{\nabla}_\tau \Theta}\right] =$$

$$\int_0^{2\pi} d\phi \left[\sqrt{1-\mu^1}\tan\theta\cos\phi + \mu\right] =$$

$$= 2\pi\mu$$

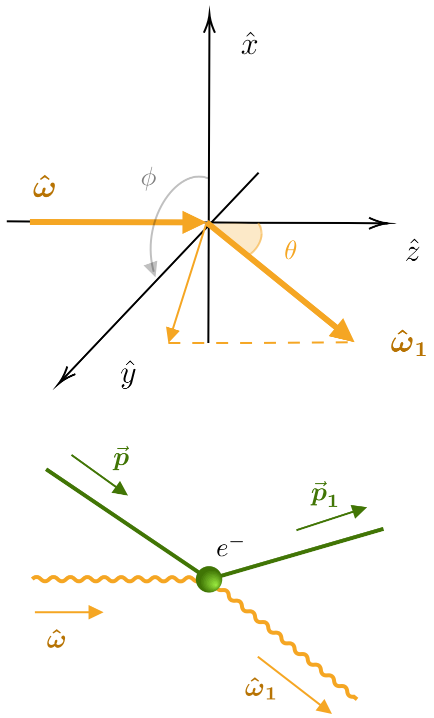

Figure 3.4: Pictorial view of polar reference system for Compton scattering. Here $\cos\theta = \hat{\omega}_1 \cdot \hat{\omega}$, and ϕ is simply the azimuth.

Finally, after the integration over the angles of the scattered photon $d\theta$, we can write the definitive form of our Eq.(3.22), introducing also the ***angular moments*** $R_0(x_1, x)$, $R_1(x_1, x)$ of the total redistribution function $R(x_1, x, \mu)$:

$$1 = 4\pi \int_0^\infty \frac{x_1}{x}\, dx_1 \left(\frac{1-e^{-x/\Theta}}{1-e^{-x_1/\Theta}}\right) \left[\tilde{l}_x\, R_0(x_1, x) - \tilde{l}_{x_1}\, \frac{x_1}{x}\, R_1(x_1, x)\right] \tag{3.24}$$

$$\text{with} \quad R_0(x_1, x) \equiv \frac{1}{2}\int_{-1}^{1} R(x_1, x, \mu)\, d\mu \ ,$$

$$R_1(x_1, x) \equiv \frac{1}{2}\int_{-1}^{1} R(x_1, x, \mu)\, \mu\, d\mu \ .$$

There are several methods to compute these functions, and one is indeed described in J. Poutanen (2017), [Pou17]. It is not completely straightforward, and reporting all the passages here is beyond the scope of this work.

The numerical solution Undoubtedly, Eq.(3.24) is very complicated. In order to achieve a full *numerical solution*, one needs to perform an iterative procedure at low temperatures and a classic Gauss Seidel at the higher T.

- **Low T** An *iterative procedure* can be performed starting from a suitable approximation. In literature, the *on-spot* approximation is usually employed, namely $\tilde{l}_x \simeq \tilde{l}_{x_1}$: this allows to simplify our equation a bit,

$$\frac{1}{\tilde{l}_x} \simeq r_0(x) - r_1(x)$$

$$\text{with} \quad r_i(x) \equiv \frac{4\pi}{x^{i+1}} \int x_1^{i+1}\, dx_1\, R_i(x_1, x)\, \frac{1 - e^{-x/\Theta}}{1 - e^{-x_1/\Theta}}\,,$$

and we see that we can tabulate the $r_i(x)$ in advance. The integrals over the energy x_1 for every x have to be taken over a dense grid around x.
NB Let us point out that the in-spot approximation is motivated by the fact that, at low T, the RFs are extremely peaked at $x_1 \simeq x$.

- **High T** In principle, one can replace the integral by the discrete sum on a logarithmic grid of photon energies x_i, and directly solve Eq.(3.24) with standard *Gauss-Seidel* methods, i.e. as a system of linear equations for $l_i = l_{x_i}$:

$$\frac{1}{4\pi} = \tilde{l}_i\, a_1 + \sum_j \tilde{l}_j\, (b_{ij} + a_{ij}\delta_{ij})$$

$$\text{with} \quad a_i = \sum_j w_j\, \frac{x_j}{x_i}\, \frac{1 - e^{-x_i/\Theta}}{1 - e^{-x_j/\Theta}}\, R_0(x_j, x_i)\,,$$

$$b_i = \sum_j w_j \frac{x_j^2}{x_i^2}\, \frac{1 - e^{-x_i/\Theta}}{1 - e^{-x_j/\Theta}}\, R_1(x_j, x_i)\,.$$

The w_j are the integration weights, equal to $x_j \Delta \ln x$ for a logarithmic grid, and δ_{ij} the Kronecker's delta. What can be found is that the mean free path computed using the on-spot approximation is actually in good agreement with the exact $\tilde{l}_x$ at all photon energies x, both for low T and large T with $x \gtrsim \Theta$.

Once we have the solution for the adimensional mean free path $\tilde{l}_x$, it is straightforward to compute the Rosseland mean free path $\Lambda(\Theta, \eta) \to \Lambda(\mathrm{T}, \rho)$ as illustrated in Sec.(2.1), see Eq.(2.4).

Dropping the positrons Up to now, the presented formalism accounted for both positrons and electrons. We are now going to *drop the positrons*, the reason being essentially the fact that Compton scattering on e^- is expected to be the major source of opacity in the cores of massive stars, at least during the phases we are going to encouter.
A twofold motivation can also support this choice:

a) **Low T** or **high η** there is no pair production happening;

b) **High T** or **low η**, we have that $\eta_+ > \eta-$, which comes from the condition $\Theta > -1/\eta_-$; this means that, in theory, the number of positrons exceeds the number of electrons, which is practically unphysical.

Therefore, in the following we will present our results taking opacity by electrons only, as was also done by past literature; we will also replace η_- by η for clarity. However, we also recognize that the inclusion, in future works, of Compton opacity by positrons can be an interesting development: the most advanced phases of (very)massive are expected to comprise also a fraction of pairs e^-e^+, which are actually key to the final dynamical instabilities in the core for SN outcomes.

3.2.2 The P83 prescription

We are now going to present the well known Paczyński prescription for the Rosseland mean free path $\Lambda(\mathrm{T}, \rho)$, due to B. Paczyński (1983), [Pac83]; we will call it throughout as *P83 prescription*. This represents the included prescription in the PARSEC code since the happening of this work, in which an update of P83 is included and the resulting differences are discussed, see the following Sec.(3.2.3).

Motivation and assumptions The P83 prescription was first introduced by Paczyński in a study of nuclear reactions in the surface of accreting Neutron Stars (NS), as a possible explanation for X-ray bursts. Although this *motivation* may seem quite detached, the theoretical background was based on the seminal work by J. R. Buchler and W. R. Yueh (1976), [BY76], which actually employed the RTE formalism too.

Buchler & Yueh solved a similar form of Eq.(3.22) by using the techniques described in Sec.(3.2.1), and Paczyński used the tabulated values from them to derive an approximated formula with the *assumption* of a matter with a mean number of nucleons per free electrons $\mu_e = 2$. This indeed works good for us too, if one remembers Eq.(1.7) and the fact that H is completely depleted in the core of massive stars towards C-burning.

The P83 prescription Let us call $N_{\mathrm{e,matter}} = N_- - \cancel{N_+}$ as n_e, to reconvene with Chp.(2)'s notation. The P83 prescription, in the fashion of Eq.(2.4), reads

P83 PRESCRIPTION

$$\kappa_{\mathrm{P83}} = \frac{\overbrace{n_e \sigma_{\mathrm{Th}}}^{=\kappa_{\mathrm{Th}}}}{\rho} \frac{1}{\Lambda_{\mathrm{P83}}(\mathrm{T}, \rho)} \quad \text{with}$$
$$\Lambda_{\mathrm{P83}}(\mathrm{T}, \rho) = \left[1 + \left(\frac{k\mathrm{T}}{38.8\,\mathrm{keV}}\right)^{0.86}\right] \left[1 + 2.7 \times 10^{11}\,\rho \mathrm{T}^{-2}\right] . \tag{3.25}$$

This simple, analytic form is shown in Fig.(3.5), together with the full numerical solution of Eq.(3.20), over a broad range of temperatures T and electron degeneracies η. We can see that Paczyński's approximation is rather good for small η, while at larger degeneracies it becomes highly inaccurate at low T.

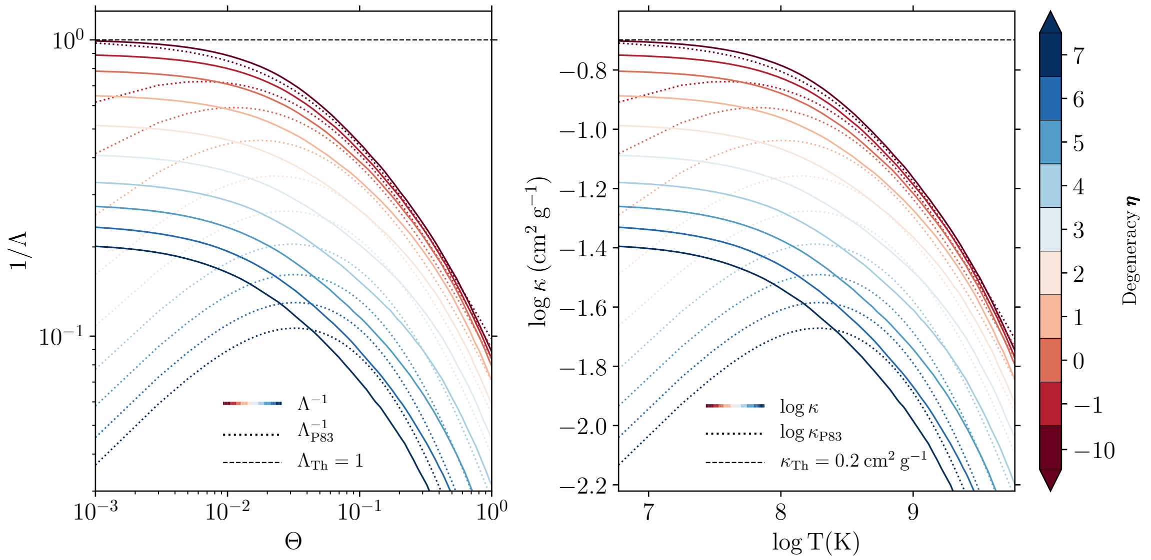

Figure 3.5: Left – Full numerical $\Lambda(\Theta, \eta)$ solution (solid) compared to Paczyński $\Lambda_{\rm P83}(\Theta, \eta)$ (dotted) prescription in Eq.(2.7) for the (inverse of the) Rosseland mean free path as a function of temperatures of interest for stellar matter. The dashed line shows the Thomson scattering limit, in which $\Lambda_{\rm Th} = 1$, Eq.(2.5). Fixed degeneracy parameters are color coded, and $\mu_e = 2$; Right – Compton opacity κ and $\kappa_{\rm P83}$, derived from the full and P83 solution, respectively, as in Eq.(2.7), as a function of temperatures of interest for stellar matter. The dashed line shows, again, the Thomson scattering limit, $\kappa_{\rm Th}$, for $\mu_e = 2$, and degeneracy parameter η is fixed and color coded.

Notice, however, that the expected physics is indeed respected: the electron scattering opacity ▶ ***decreases*** at high T due to relativistic electron velocities, which makes the fulfilling of condition Eq.(3.1) more difficult; ▶ ***decreases*** at high density due to electron degeneracy.

3.2.3 The P17 prescription

We finally present a new prescription for the Rosseland mean free path $\Lambda(T, \eta)$, due to J. Poutanen (2017), [Pou17]: we will call it throughout as *P17 prescription*. This represents the newly included prescription in the PARSEC code, and we will discuss the results in the following section, Sec.(3.3).

P17 Prescription

$$\kappa_{\rm P17} = \frac{\overbrace{n_e \sigma_{\rm Th}}^{=\kappa_{\rm Th}}}{\rho} \frac{1}{\Lambda_{\rm P17}\left(\mathrm{T}, \rho\right)} \qquad \text{with}$$
$$\Lambda_{\rm P17}\left(\mathrm{T}, \rho\right) = f_1(\eta) \left[1 + \left(\frac{\mathrm{T}}{\mathrm{T_{br}}}\right)^{\alpha}\right] \tag{3.26}$$

This formula is a sort of combination between the Paczyński's one and another, which was already proposed by Buchler & Yueh; it comprises some parameters and functions which are reported below:

$$
\begin{aligned}
&\mathrm{T_{br}} = \mathrm{T_0}\, f_2(\eta)\,, \\
&\alpha = \alpha_0\, f_3(\eta)\,, \\
&f_i(\eta) = 1 + c_{i1}\,\xi + c_{i2}\,\xi^2\,, \\
&\text{with} \quad i = 1,2,3\,, \\
&\xi = \exp\left(c_{01}\eta + c_{02}\eta^2\right)
\end{aligned}
\tag{3.27}
$$

***Asymptotic* P17**

$$\Lambda_{\mathrm{P17}} \overset{\eta\to-\infty}{\longrightarrow} 1 + \left(\frac{\mathrm{T}}{\mathrm{T_{br}}}\right)^{\alpha}$$

	Rosseland Mean			
Coefficient	$2-40$ keV		$2-300$ keV	
T_0 [keV]	39.4	43.4	41.5	43.3
α_0	0.976	0.902	0.90	0.885
c_{01}		0.777		0.682
c_{01}		-0.0509		-0.0454
c_{11}		0.25		0.24
c_{12}		-0.0045		0.0043
c_{21}		0.0264		0.050
c_{22}		-0.0033		-0.0067
c_{31}		0.0046		-0.037
c_{32}		-0.0009		0.0031

Table 3.1: Coefficients for P17 prescription, Eq.(3.26).

This relatively simple form, together with Paczyński's and the full numerical one, is shown in Fig.(3.6), over the same broad range of temperatures T and electron degeneracies η as Fig.(3.5). We can immediately see the goodness of the fit with respect to the full numerical solution: this for approximates the opacity to better than 7% in the temperature range of $2-300$ keV, and in any case we see a consistent difference between P17 and P83, more pronounced as $\eta \nearrow$.
We shall note that, in case of non-degenerate gas, $\eta \to -\infty$, the expressions above simplify due to $f_i \to 1$, such that a simply ***asymptotic*** form $\Lambda_{\mathrm{P17}} \propto \mathrm{T}^{\alpha}$ can be found.

3.3 Results: P17+COND

We ran the PARSEC code for the stellar models grid described in Sec.(1.4), with the implementation of the new opacity routine in Eq.(3.26). This subsection aims at showing the most interesting *results* of this update, starting with individuating the relevant models and then presenting both the structural and evolutive novelties.

The relevant models Not all of our models are expected to experience high degeneracies in their advanced stages of evolution: we need to single out the *relevant models* to our treatment. This can be done by looking at Fig.(3.7):

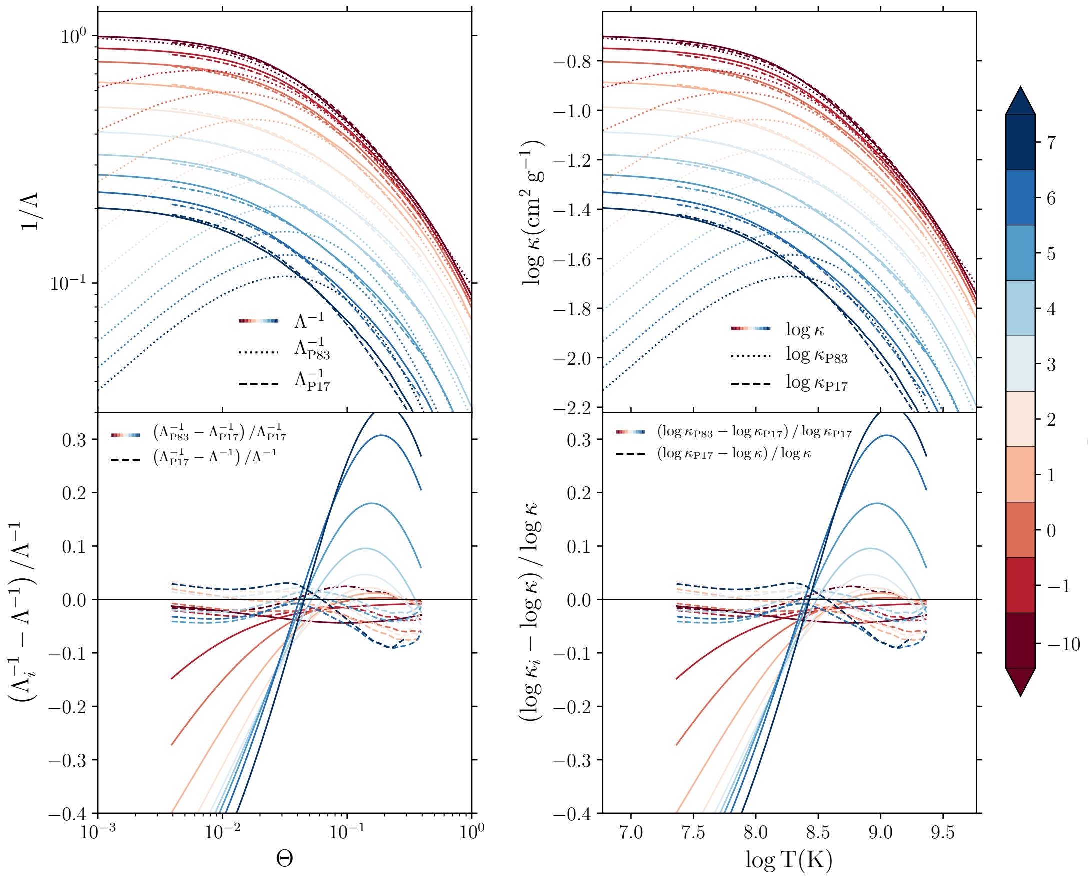

Figure 3.6: Left – Full numerical $\Lambda(\Theta,\eta)$ solution (solid) compared to Paczyński $\Lambda_{\mathrm{P83}}(\Theta,\eta)$ (dotted) and Poutanen $\Lambda_{\mathrm{P17}}(\Theta,\eta)$ (dashed) prescriptions in Eq.(2.7) and Eq.(3.26) for the (inverse of the) Rosseland mean free path as a function of temperatures of interest for stellar matter. The bottom panel shows the relevant relative differences. Fixed degeneracy parameters are color coded, and $\mu_e = 2$; Right – Compton opacity κ, κ_{P83} and κ_{P17}, derived from the full, P83 and P17 solutions, respectively, as in Eq.(2.7) and Eq.(3.26), as a function of temperatures of interest for stellar matter. The bottom panel, again, shows the relevant relative differences for $\mu_e = 2$, and degeneracy parameter η is fixed and color coded.
NB Here we are using the P17 in the complete range of T $2-300$ keV, without using the fit parameters (see Tab.(3.1)) for $2-40$ keV; this is relegated to future works, since in our treatment the PARSEC code ignites the Compton scattering opacity at $\log\mathrm{T} > 8.7 \simeq 43.2$ keV.

- The *left panel* shows the results from **Timmes & Swesty** (1999) electron-positron EoS routine, [TS00], This routine is based on a fast and thermodynamically consistent interpolation of Helmholtz free energy, by means of a biquintic Hermite polynomial as the interpolating function. It is deeply connected with the Timmes EoS, [TA99], implemented in PARSEC, from which it fastly builds up the tables of (ρ, T)

and Helmholtz energy and computes $\eta_{\pm}$ for $\mu_e = 2$. We are showing this as a reference, spanning 17 orderd of magnitudeto alleviate concern about describing all the canonical stellar phenomena.

- The *right panel* shows a **zoom** on the (ρ, T) plane in the area of interest for our models, with Z$= 0.0003$: by plotting the structure $\log \mathrm{T_c} - \log \rho_c$ of stellar masses ranging from 9 $\mathrm{M}_{\odot}$ to 140 $\mathrm{M}_{\odot}$, both with and without (no) Envelope Overshooting (EOv) (solid and dotted, respectively), we can see that only the *less massive objects* achieve $\eta \gtrsim 0$ in their core, during their most advanced phases of evolution.

  This reasoning is not expected to be different when changing the surface properties, i.e. changing Z, though examining different metallicities could give some insights in the evolutionary impact of P17 by singling out the effects due to the Z itself. Indeed, by producing a similar plot to the one of Fig.(3.7 – right) for Z=0.001 and Z=0.014, we conclude that decent (yet not very high though) degeneracies are achieved by the most compact models of our sample: 9 $\mathrm{M}_{\odot}$, 10 $\mathrm{M}_{\odot}$ and 12 $\mathrm{M}_{\odot}$.

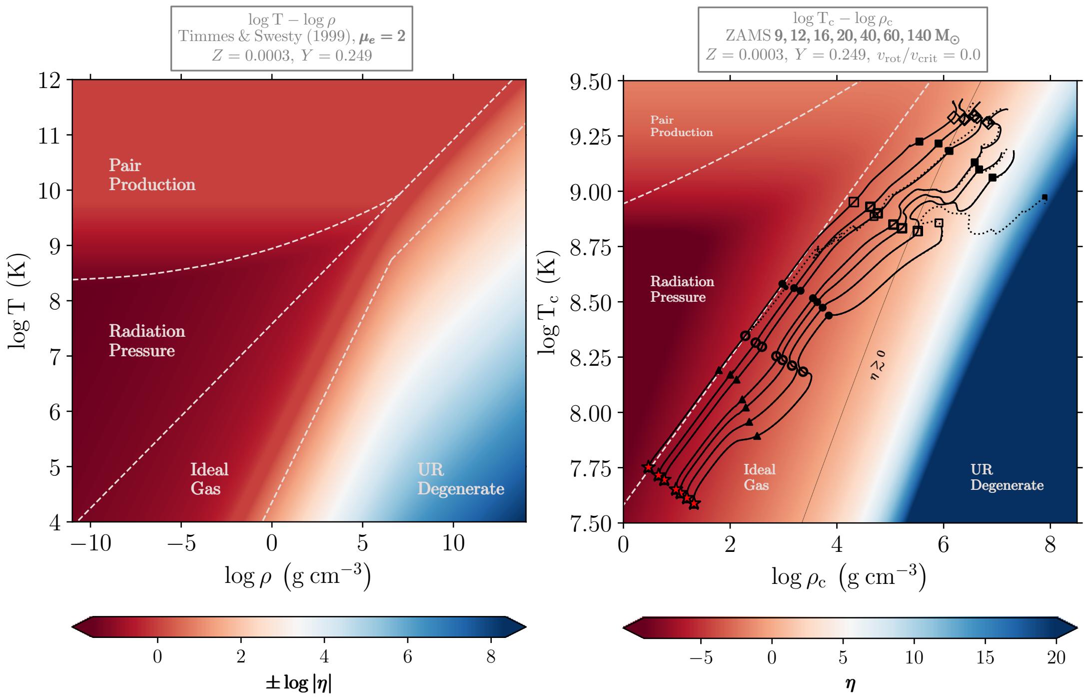

Figure 3.7: Left – Electron degeneracy parameter η in the plane $(\log \rho, \log \mathrm{T})$, as output from EoS electron-positron routine by Timmes & Swesty, [TS00]. The color coding is chosen for a nice plotting: we color-code the following quantity sgn $\eta \times \log |\eta|$; Right – Electron degeneracy parameter η from Timmes & Swesty, this time in the plane $(\log \rho_c, \log \mathrm{T_c})$ of interest for our stellar models, which are reported with Envelope Overshooting (EOv, dotted) and without EOv (thick solid). Approximate boundary regions for EoS are also reported in dashed white, while the countour for $\eta \gtrsim 0$ is in thin solid.

We therefore decide to show the results, both in the structural and evolutionary properties, of our run, with P17 implementation compared to P83, of these relevant models: 9 $\mathrm{M}_{\odot}$, 10

$M_\odot$ and 12 $M_\odot$ (sometimes even 14 $M_\odot$). The first model, unfortunately, did not succeed in going further the C-ignition point in the case of no EOv for any Z, thus the EOv (where available) shall be representative for 9 $M_\odot$; for the same reasons, some other models (see Tab.(3.2) below) will not enter in our discussion.
We are going to refer to the PARSEC code version before the implementation of P17 as **P83**, and as **P17** its new version. An even better version comprising P17, **COND**, will be explained below.

		$v_{rot}/v_{crit} = 0.7$		$v_{rot}/v_{crit} = 0$			
	ZAMS	EOv	no EOv	EOv	no EOv	**P17**	**COND**
Z= 0.0003 **Y**= 0.249	9 $M_\odot$	✗	✓	✓	✗	✓	✓
	10 $M_\odot$	✓	✓	✓	✓	✓	✓
	12 $M_\odot$	✓	✓	✓	✓	✓	✓
	14 $M_\odot$	✓	✓	✓	✓	✓	✓
Z= 0.001 **Y**= 0.250	9 $M_\odot$	✓	✓	✓	✗	✓	✓
	10 $M_\odot$	✓	✓	✗	✗	✓	✓
	12 $M_\odot$	✓	✓	✗	✓	✓	✓
	14 $M_\odot$	✓	✓	✓	✓	✓	✓
Z= 0.014 **Y**= 0.273	9 $M_\odot$	✓	✓	✗	✗	✓	✓
	10 $M_\odot$	✓	✓	✗	✗	✓	✓
	12 $M_\odot$	✓	✓	✗	✓	✓	✓
	14 $M_\odot$	✓	✓	✓	✓	✓	✓

Table 3.2: Selected PARSEC models for the study of the impact of the prescriptions **P17** and **COND** for Compton electron-scattering and conductive opacities. Possible extensions of the present grid, perhaps to intermediate-mass stars, can be relegated to future works.

- ✓ Black checkmarks indicate that the P83 model is relevant to our study, i.e. has entered the degeneracy region;
- ✗ Red-crossed models do not enter the degenerate region, mainly due to numerical difficulties of the solver, thus are not relevant;
- ✓ Green checkmarks label the computed, and considered, tracks with the new prescription, without specifying whether they have entered the degenerate region or not.

In the following, we are taking for granted that the comparisons between tracks from different runs, P17 (COND) and P83, of PARSEC are being made between similar, though not identical, evolutionary stages; *numerical fluctuations* are to be taken into account in all the treatment.

3.3.1 Structure plots at advanced stages

The so called *structure plots* catch the track at a fixed coordinate time, i.e. at a fixed point in the HR diagram, and describe the inner stratification of the star, from the surface to the core. The coordinate we are going to use is the temperature T, which can be not properly monotonic towards the core; however, it is a good proxy for the depth coordinate.

3.3.1.1 The opacity $\log \kappa - \log \mathrm{T}$

Before comparing the P17 and P83 PARSEC's runs, let us look at the general behavior of the total opacity in the proximity to the highest temperatures, i.e. $\log \mathrm{T} \to 8.7$. Fig.(3.8) shows the total opacity, as in Fig.(2.4), with an insert which zooms in our region of interest. We can immediately recognize the expected departure from the Thomson plateaux κ_{Th}, which is predicted by **P83** and **P17** too, as one cas see their excellent agreement (see Fig.(3.8), the red dashed line).
A quite dramatic decrease is, actually, predicted in both cases, approximately after $\log \mathrm{T} \gtrsim 9$: this can be **a)** partly due to the relativistic ***electron velocities***, making the condition Eq.(3.1) more difficult to fulfill, and partly also to **b)** a consisten fraction of ***positrons*** appearing through pair production.

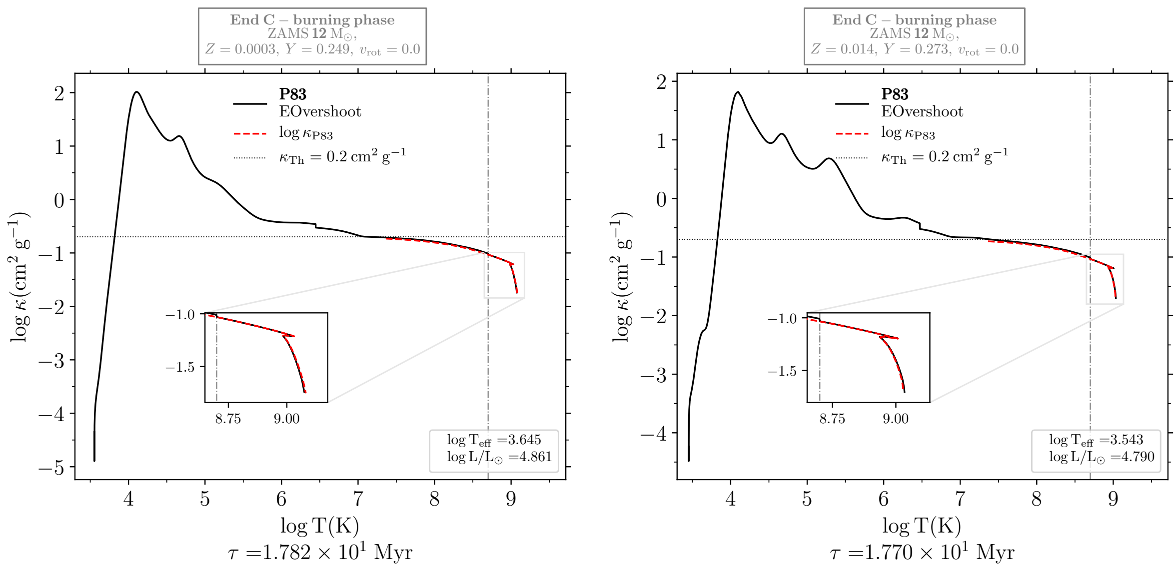

Figure 3.8: Overview of opacity $\log \kappa$, as a function of the stratification temperature $\log \mathrm{T}$, at an evolutionary stage corresponding to the end of core C-burning, with an insert which zooms in the region of interest ($\log \mathrm{T} > 8.7$, thin dot-dashed black line) for our new prescription P17. The Thomson scattering plateaux κ_{Th} is reported (thin, black dotted line), together with the theoretical curve κ_{P83} of Eq.(3.25), red dashed line. Left – PARSEC output for Z=0.0003; Right – PARSEC output for Z=0.014.

The P17 run: summary The opacity $\log\kappa$ of the *P17 run*, in general, shows a consistently different trend as a function of $\log\mathrm{T}$ with respect to the **P83** PARSEC version. The changes, of course, interest the region $\log\mathrm{T} > 8.7$, in which PARSEC shuts down the OPAL opacities and accounts for electron scattering opacity only. We can summarize the main results as

- **$\log\mathrm{T} \gtrsim 8.7$** The P17 opacity are overall in excellent agreement with P83 ones when temperature are not so extreme, namely when the models have just ignited C-burning in the core and $\log\mathrm{T} \gtrsim 8.7$. The agreement is of entity $< 1\%$.
- **$\log\mathrm{T} > 8.7$** Consistent differences arise once the core C-burning turns to the end: the models, in fact, usually enter a higher degeneracy stage, and differences can be as high as 25% for the most compact models (i.e. 9 $\mathrm{M}_\odot$).
- **$7.4 < \log\mathrm{T} < 8.7$** In the range of validity of P17 prescription, i.e. $2\,\mathrm{keV} - 300\,\mathrm{keV}$, the OPAL opacities are better approximated by P17 in every examined case. The difference can be as high as 5%. This is a simple check which confirms the validity of our implementation, since it seems to assure a better junction with the opacity tables from OPAL project.

We tested our completely general routine for different ZAMS M, rotational velocities $v_{\mathrm{rot}}/v_{\mathrm{crit}}$, convective envelope overshooting (EOv or no EOv) and metallicities Z. Only selected results are reported below.

Different ZAMS Fig.(3.9) and Fig.(3.10) show the effect of the new prescriptions as one changes the *Zero Age Main Sequence Mass* M. The figures show

- **Top row** Logarithmic opacity as a function of $\log\mathrm{T}$, for P17 and P83 PARSEC runs, with the analytical curves from Eq.(3.26) and Eq.(3.25). The agreement is excellent for $\log\mathrm{T} \gtrsim 8 - 7$, until higher temperatures ($\log\mathrm{T} \simeq 9$) are reached.
- **Bottom row** Relative differences of the P17 PARSEC run with respect to the theoretical curves from Eq.(3.26) and Eq.(3.25), κ_{P17} and κ_{P83}. The relative difference with κ_{P17}, after $\log\mathrm{T} = 8.7$, is expectedly zero and it's just a check of consistency; the relative departure from κ_{P83} can reach a 28% for the M=10 $\mathrm{M}_\odot$ model.

A different mass influence these features in the following way: for more compact structures, the relative deviations increase and the opacity drops even more below the Thomson plateaux, as expected from Fig.(3.6).

Different Metallicities Z Fig.(3.10) and Fig.(3.11) show the effect of the new prescriptions as on changes the *surface metallicity* Z. One can see that for higher Z the opacity is a bit higher, and the relative differences with respect to κ_{P83} are of slightly different entity: for Z=0.001 we get a 15% in the M=12 $\mathrm{M}_\odot$ case, while in the same case with Z=0.014 the departure reaches at most 12%.
Differences in the EOv and no EOv case of Fig.(3.11) can be deputed to the slightly different evolutive stages of the two PARSEC's runs.

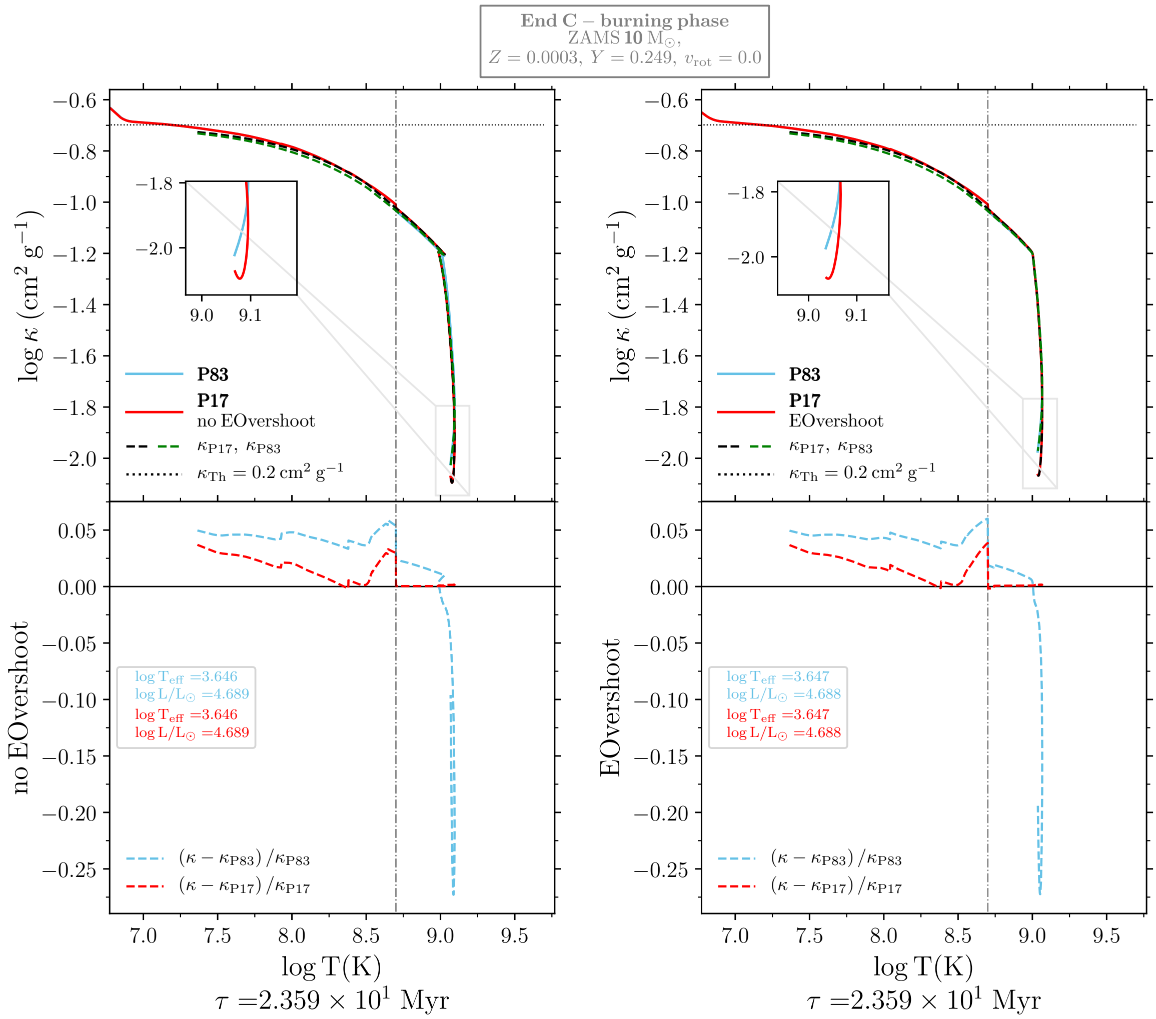

Figure 3.9: Comparative structure $\log\kappa - \log\mathrm{T}$ for a star with ZAMS mass M=10 $M_\odot$, metallicity Z=0.0003 and rotation velocity $v_{\rm rot}/v_{\rm crit} = 0$, with the two prescriptions **P17** and **P83**. The analytic curves for P83 and P17, i.e. 3.26 and 3.25, are also shown in dashed lines. The bottom row, instead, show the relative differences between the PARSEC runs' results and the prescriptions. The two PARSEC's runs, **P17** and **P83** in the text, are caught at similar, though not identical, evolutionary stages, and the age of P17 model is reported below the x-axis. Left – PARSEC output without EOvershooting; Right – same as Left, but with EOvershooting incorporated.

Different Rotational Velocity $v_{\rm rot}/v_{\rm crit}$ Fig.(3.11) and Fig.(3.12) show the effect of the new prescription as one changes the *rotational velocity* $v_{\rm rot}/v_{\rm crit}$. We can immediately recognize the well known fact that rotating stars behave as more massive stars, as we anticipated in Sec.(1.3), fact which reflects in the microphysics too: the rotating M=12 $M_\odot$ model develops a slightly lower opacity in the core, reaching also higher temperatures $\log\mathrm{T} > 9.2$ and with minimal deviations with respect to $\kappa_{\rm P83}$, i.e. 6%. On the contrary, the non rotating model can develop a 12% relative departure from the old prescription.

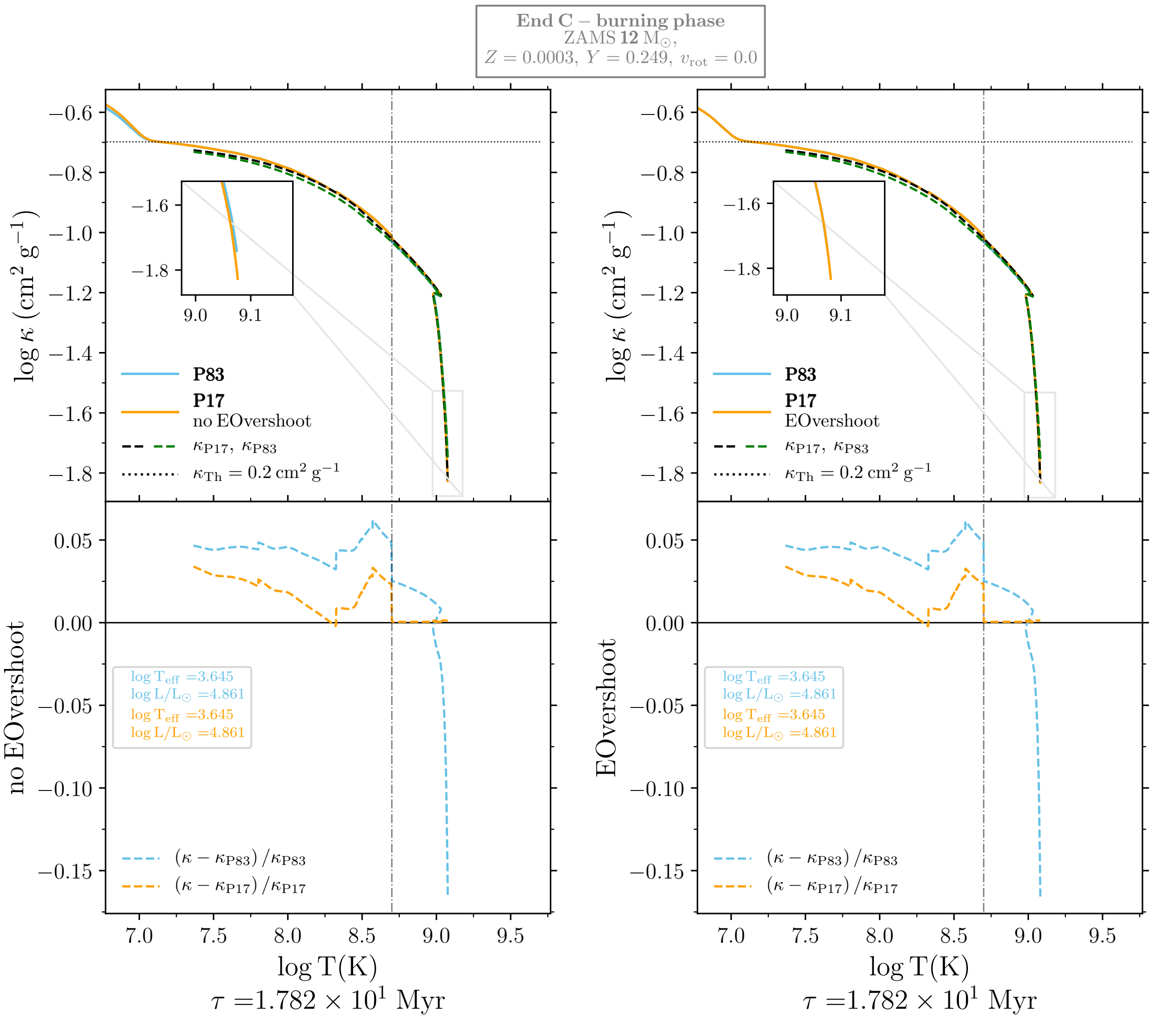

Figure 3.10: Comparative structure $\log\kappa - \log\mathrm{T}$ for a star with ZAMS mass M=12 $\mathrm{M}_\odot$, metallicity Z=0.0003 and rotation velocity $v_{\mathrm{rot}}/v_{\mathrm{crit}} = 0$, with the two prescriptions **P17** and **P83**. Same notations as Fig.(3.9) are employed. Left – PARSEC output without EOvershooting; Right – same as Left, but with EOvershooting incorporated.

Brief comment on stability Without the purpose of a complete performance analysis, which is far beyond the scoper of this work, we have nevertheless tested the smoothness of *logarithmic derivatives*, with respect to the temperature T, of our new prescription P17. This smoothness is of prior importance in any code which solves an EoS, both **1)** to test thermodynamic consistency *and* **2)** assure convergence; also, the proper computation of adiabatic indexes requires them. Our routine outputs:

$$\left.\frac{\partial\log\kappa_{\mathrm{P17}}}{\partial\log\mathrm{T}}\right|_{\mathrm{mesh}}, \qquad \left.\frac{\partial\log\kappa_{\mathrm{P17}}}{\partial\mathrm{P}}\right|_{\mathrm{mesh}},$$

the second one being identically vanishing by virtue of the (first order) non-dependence of κ_{P17} of Eq.(3.26) from ρ. The logarithmic derivative with respect to the temperature has

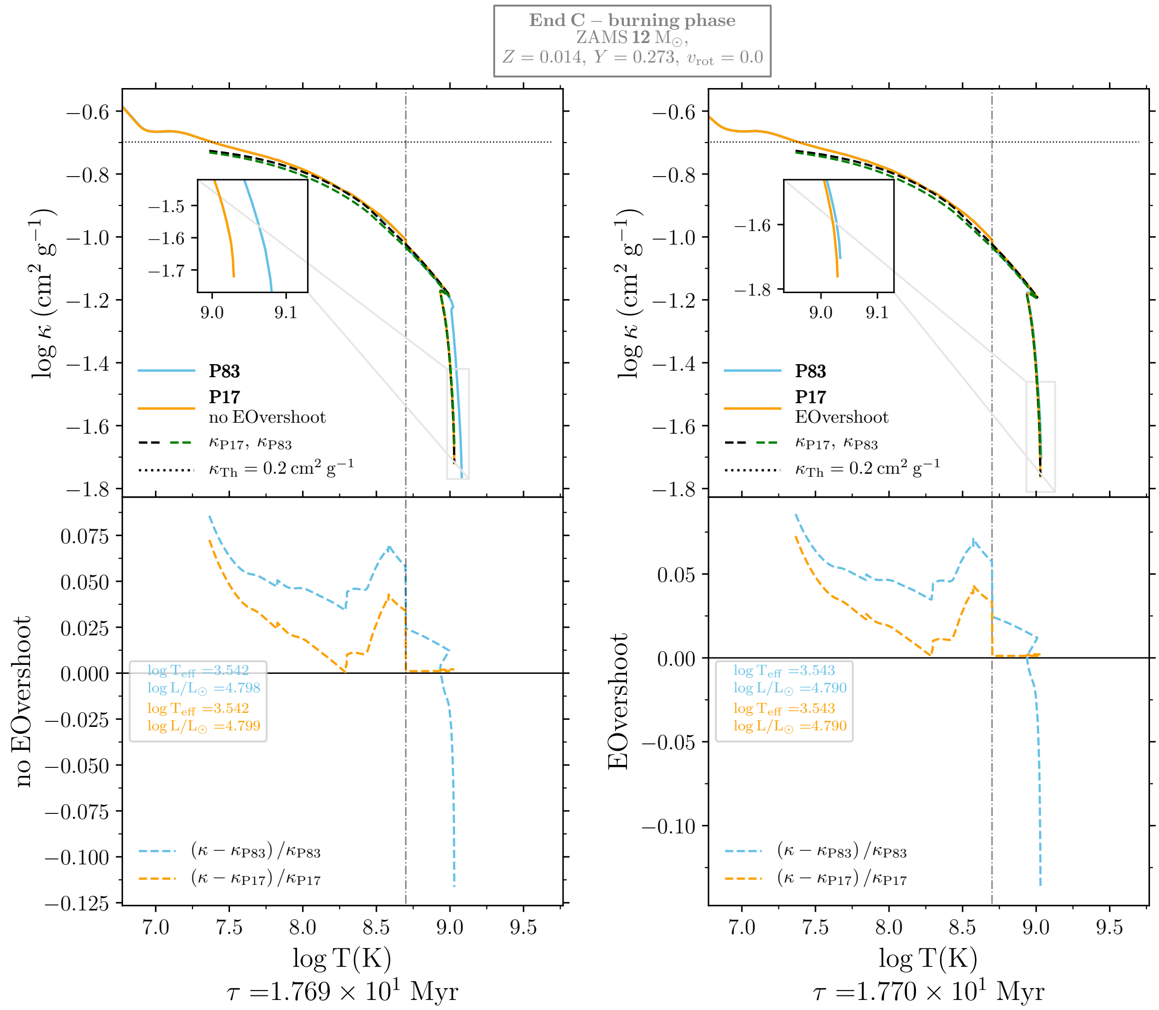

Figure 3.11: Comparative structure $\log\kappa - \log \mathrm{T}$ for a star with ZAMS mass M=12 M$_\odot$, metallicity Z=0.014 and rotation velocity $v_{\rm rot}/v_{\rm crit} = 0$, with the two prescriptions **P17** and **P83**.Same notations as Fig.(3.9) are employed. Left – PARSEC output without EOvershooting; Right – same as Left, but with EOvershooting incorporated.

been tested all over the stellar models grid, with an example showed in Fig.(3.13): we see that P17 gives a slightly closer to zero logarithmic derivative with respect to P83, and the dashed red analytic curve, smoothly calculated from Eq.(3.26), is a check of consistency.

3.3.1.2 Abundances stratification $\log \mathrm{X}_i - \log \mathrm{T}$

Fig.(3.14) shows an example, for M=10 M$_\odot$, $v_{\rm rot}/v_{\rm crit} = 0.$ and Z=0.0003, both with (EOv) and without (no EOv) convective Envelope Overshooting, of *abundances stratification*, in a structure towards the start of core C-burning. No perceivable differences due to the new $\kappa_{\rm P17}$ prescription could be singled out in Fig.(3.14 – Left): the small deviations of colored dotted (P83) from solid (P17) lines could indicate simply numerical fluctuations and slightly

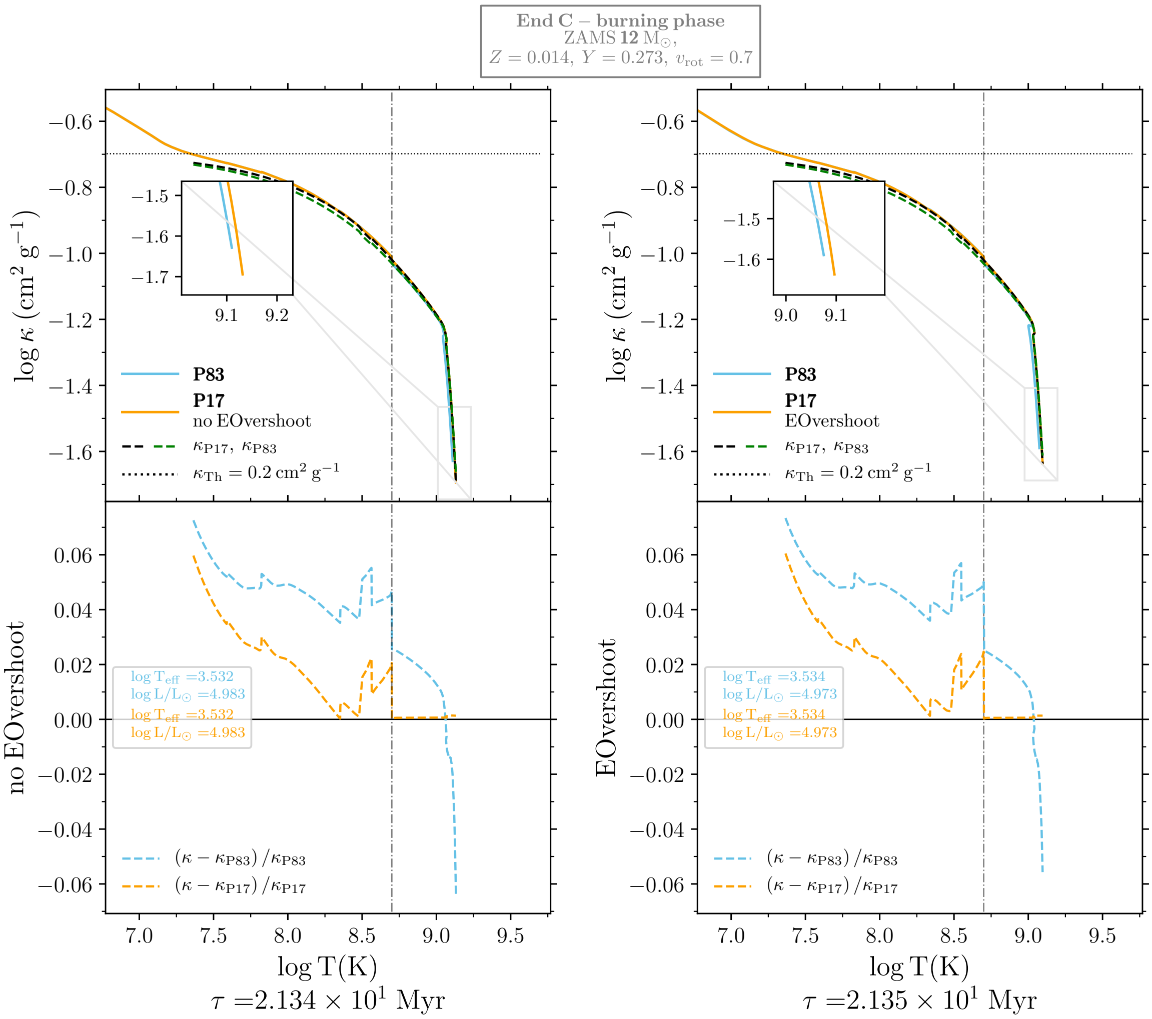

Figure 3.12: Comparative structure $\log\kappa - \log T$ for a star with ZAMS mass M=12 $M_\odot$, metallicity Z=0.014 and rotation velocity $v_{rot}/v_{crit} = 0.7$, with the two prescriptions **P17** and **P83**.Same notations as Fig.(3.9) are employed. Left – PARSEC output without EOvershooting; Right – same as Left, but with EOvershooting incorporated.

different evolutionary stages. The EOv case in Fig.(3.14 – Right) is, instead, perfectly identical. These considerations hold for the entire considered grid of stellar models in Tab.(3.2).

The fact that the opacity prescription is not very relevant in determining the mass fractions stratification comes with some surprise: the opacity has a key role in the energy flux radiating from the core to the surrounding shells, so we should expect that, at advanced stages, the complicated stratification of active shells from C-burning and beyond can change, having even dramatic impacts on the pre-SN stages of the most compact models. We think that, in future works, with an enlarged grid of stellar models and perhaps with tracks catching Ne- (O-) burnings and beyond, some relevant effects could indeed arise.

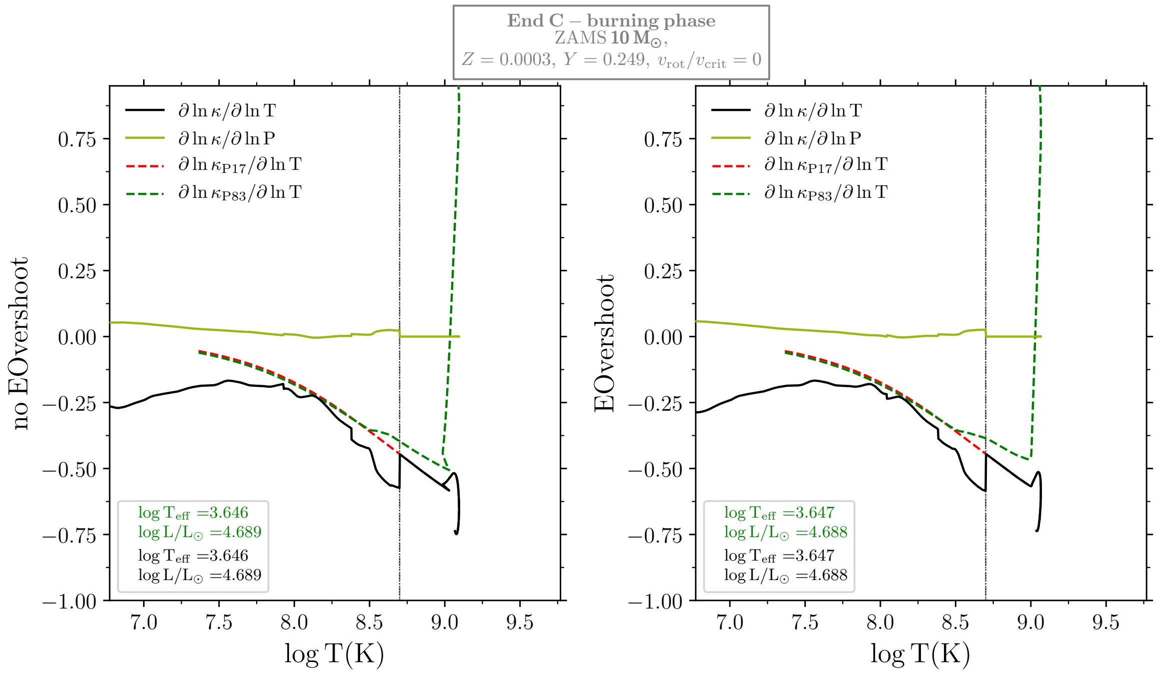

Figure 3.13: Logarithmic derivatives $\partial \log \kappa / \partial \log \mathrm{T}$ (and $\partial \log \kappa / \partial \log \mathrm{P}$) of the opacity output for the P17 PARSEC's run, for a star with ZAMS mass M=10 $\mathrm{M}_{\odot}$, metallicity Z=0.0003 and rotation velocity $v_{\mathrm{rot}}/v_{\mathrm{crit}} = 0.$. The analytical curves, smoothly calculated from Eq.(3.25) and Eq.(3.26), are also reported as a reference. Left – PARSEC output without EOvershooting; Right – same as Left, but with EOvershooting incorporated.

3.3.1.3 Structure plots $\log \mathrm{T} - \log \rho$

No perceivable differences due to the new κ_{P17} prescription's implementation could be resolved in the *structural diagrams* $\log \mathrm{T} - \log \rho$. We think that even the observed small deviations are to be deputed to the slightly different evolutionary stages of P83 and P17 runs.

3.3.2 Evolutionary plots

Now we are going to show some results concerning the *evolutionary plots*, namely the ones following the evolution of the models from the ZAMS to the end of the computation. We will see that not many differences were revealed, in this front, between the runs **P83** and **P17**; therefore, just a tiny selection of plots will be included, mainly one representative at a selected Z, $v_{\mathrm{rot}}/v_{\mathrm{crit}}$ and for the 9-10-12-14 $\mathrm{M}_{\odot}$. The representative Z will be chosen on the basis of the possibility to compare with P83 runs shown in Chp.(1), when possible; the representative rotational velocity is chosen to be $v_{\mathrm{rot}}/v_{\mathrm{crit}} = 0$, by virtue of the fact that the effects of our prescription are of more important entity in the non-rotating counterparts of our models.

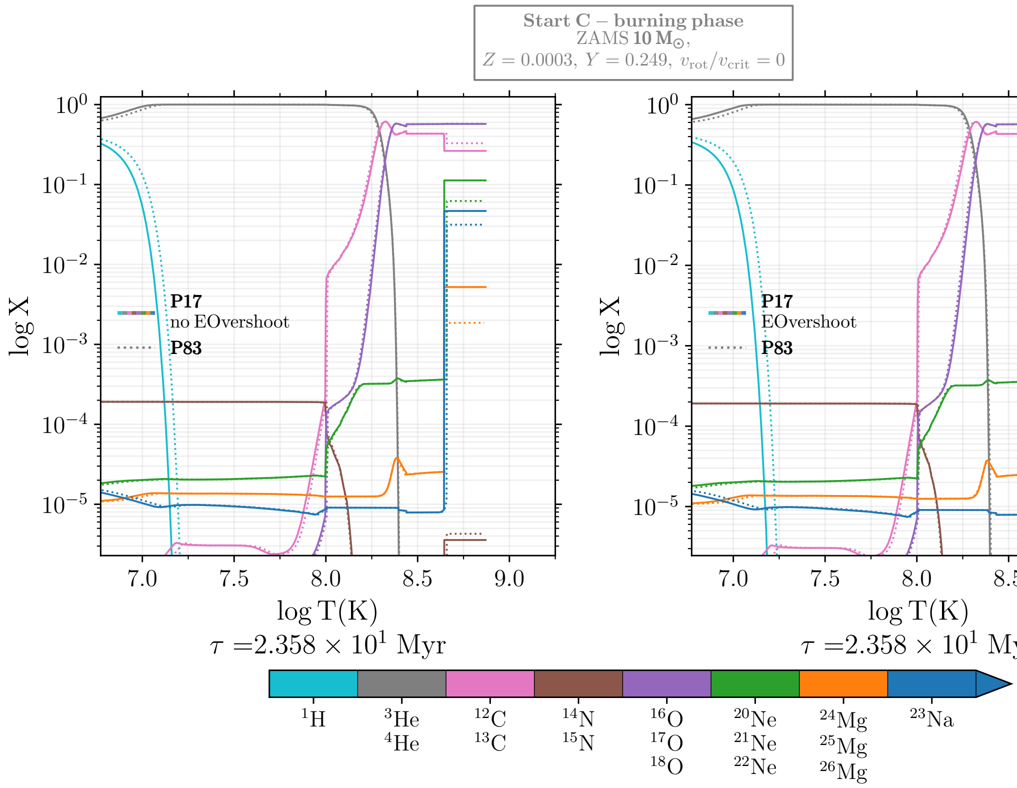

Figure 3.14: Comparative mass fractions $\log X - \log T$ stratification for a star with ZAMS mass M=10 $M_\odot$, metallicity Z=0.0003 and rotation velocity $v_{rot}/v_{crit} = 0.$, with the two prescriptions **P17** and **P83**. The color coding for different elements is reported in the colorbar, and colored dotted (solid) lines refers to P83 (P17) PARSEC's runs. Left – PARSEC output without EOvershooting; Right – same as Left, but with EOvershooting incorporated.

HR diagrams The HR diagrams of the P17 runs showed no apparent difference with the P83 ones. Fig.(3.15) shows the results for the reference set with Z=0.0003; these can be compared with Fig.(1.14) to find excellent agreement in any phase of the evolution. This fact indirectly describes also:

- The $\dot{M}$ behavior, since the mass loss rate prescription depends strongly on the HR region of the track; we met excellent agreement even in this case.
- The **surface abundances $\log X_i$** evolution, whose variation could influence the HR position of the track; no relevant deviations were encountered.

As a proof of the agreement, we reported in inserts of Fig.(3.9), Fig.(3.10), Fig.(3.11) and Fig.(3.12) the HR positions $(\log T_{eff},\ \log L/L_\odot)$ of P83 and P17 runs: we see that these are essentially unchanged.

$\log T_c - \log \rho_c$ diagrams As regards the structure evolution through the $\log T_c - \log \rho_c$, some slight departure of **P17** from **P83** are present and appreciable; a general trend we

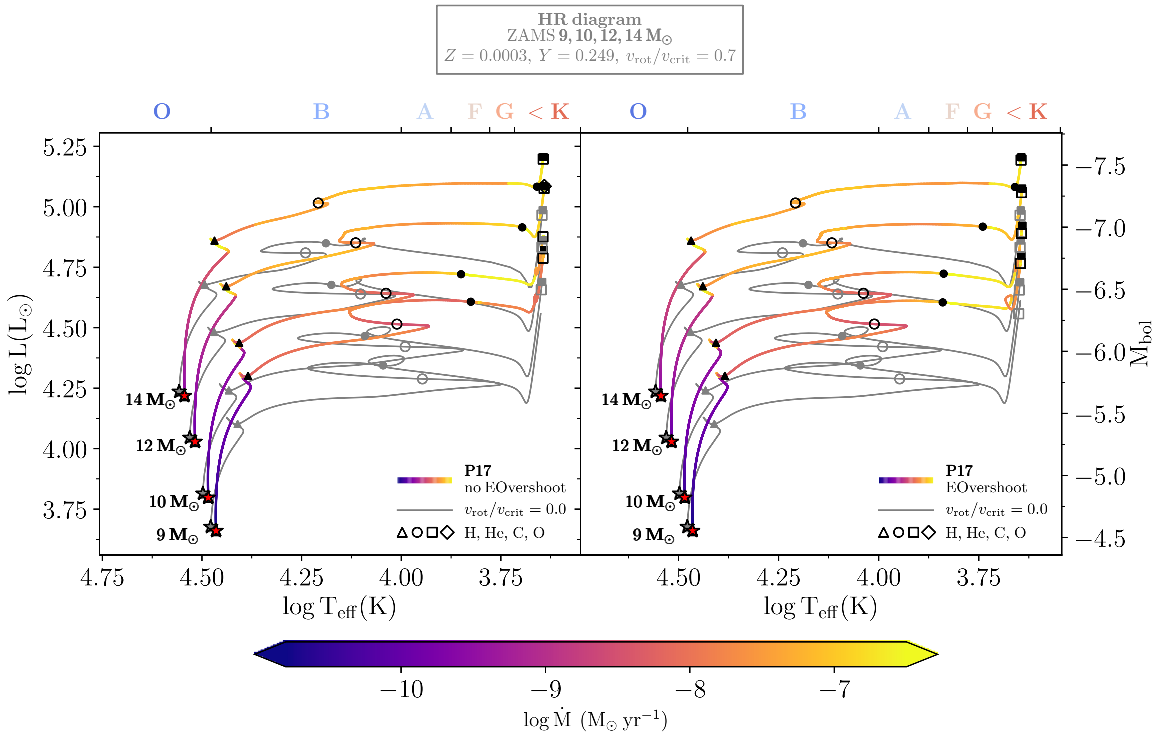

Figure 3.15: Evolutionary track for stars with ZAMS mass M=9-10-12-14 M$_\odot$, metallicity Z=0.0003 and rotation velocity $v_{\rm rot}/v_{\rm crit} = 0.0 - 0.7$, with the prescription **P17**. Similar notation as Fig.(1.14) is adopted, and one can refer to it also as a comparison with the prescription P83: any difference is absolutely negligible. Left – PARSEC output without EOvershooting; Right – same as Left, but with EOvershooting incorporated.

were able to single out, in the comparable stages of tracks, was a difference in the core C-burning ignition temperature. As an example, we report in Fig.(3.16) a zoom on the nearly degenerate region, i.e. towards the C-burning stage, for a M=10 M$_\odot$, Z=0.0003 and no rotation. We see a 1% deviation in the ignition temperatures of C, with the P83 being the cooler one: this can be easily interpreted as, with a consistently lower opacity (see Fig.(3.9) for the equivalent model), the core is warmed up less efficiently since radiative diffusion is effective. Summarizing:

- **Minor deviations** of the structures $\log \mathrm{T_c} - \log \rho_c$ were detected mostly in each case for M=9-10-12-14 M$_\odot$, regardless of the Z or rotational velocity. In some cases, even the more massive models (> 14 M$_\odot$) showed deviations, although for these the probability of them being of numerical nature is higher, giving the difficulties of the solver in following the more advanced stages.
- **Degeneracies** reached, i.e. η, are not that high but not negligible. The M=10 M$_\odot$ in Fig.(3.16) reaches a peak of $\eta \simeq 8$, and in some cases of more massive stars (e.g. M=20 M$_\odot$) the degeneracy parameter in the core drops slightly above $\eta \gtrsim$ even at the starting of C-burning. We can expect that, in a future enlargement of our stellar models grid, both in the massive (with a high Z to favor a more compact pre SN stage)

and low-mass cases, the effects of the **P17** could become even more relevant.

Fig.(3.17) shows an overview of all the considered models, M=9-10-12-14 $M_\odot$, with their rotating counterparts and for different Z as presented in Tab.(3.2).

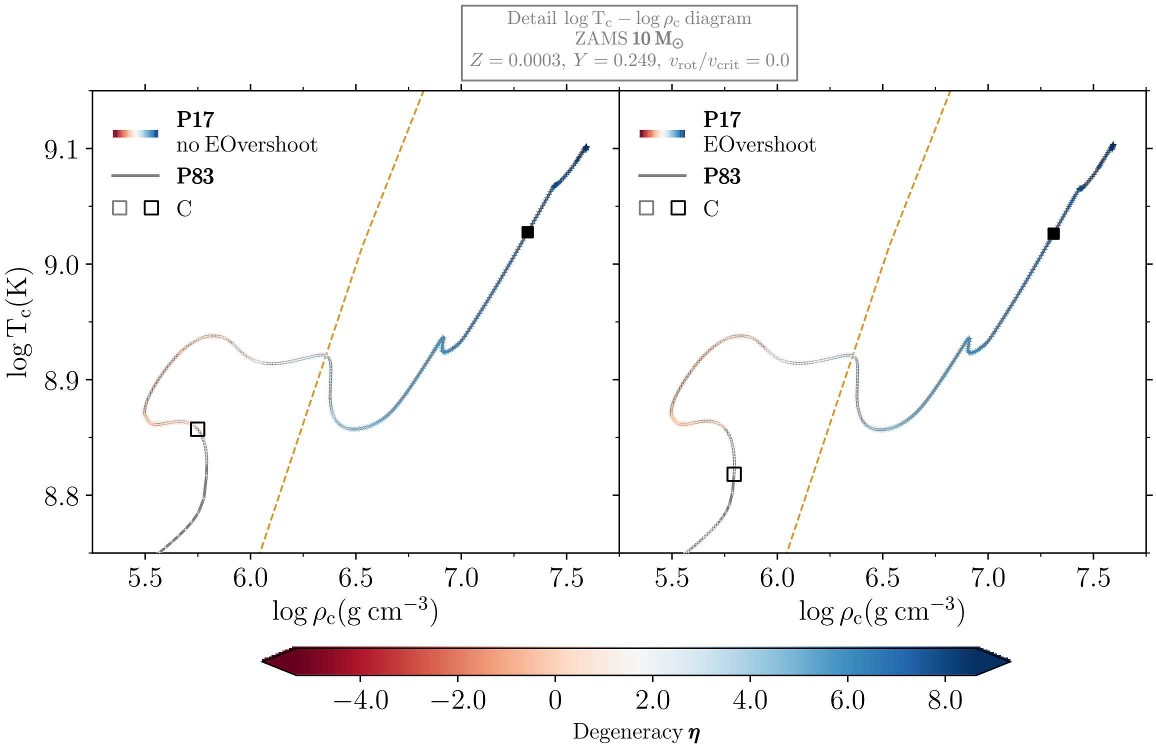

Figure 3.16: Structure $\log T_c - \log \rho_c$ for a star with ZAMS mass M=10 $M_\odot$, metallicity Z=0.0003 and rotation velocity $v_{rot}/v_{crit} = 0.0$, with the prescriptions **P83** (solid gray) and **P17** (scatter plot, color coded with the core degeneracy parameter η). Similar notation for the symbols as Fig.(1.2) is adopted. Left – PARSEC output without EOvershooting; Right – same as Left, but with EOvershooting incorporated.

Kippenhahn diagrams As concerns the mass coordinates of interest for the evolutive history, e.g. the mass of the He or CO core, M_{He} and M_{CO}, respectively, one needs to look at a complete *Kippenhahn diagram*.
We performed this operation all through the stellar models grid, concluding that no relevant deviations appears in the set 9-10-12-14 $M_\odot$, a part from sligth modifications in the convective regions, forming beyond core C-burning, outside the burning areas in the core: these regions are expected to be better sustained by the higher leakage of radiative diffusion from the core, and the active burning shells can be affected too. Indeed some differences were revealed, but giving that our models did not overcome C-burning, we could not appreciate any consequence of these modifications on the relevant mass coordinates. Perhaps a detailed study of mesh-point wise luminosities could even enlight the issue on whether the slight modification are caused by numerical fluctuations or not.

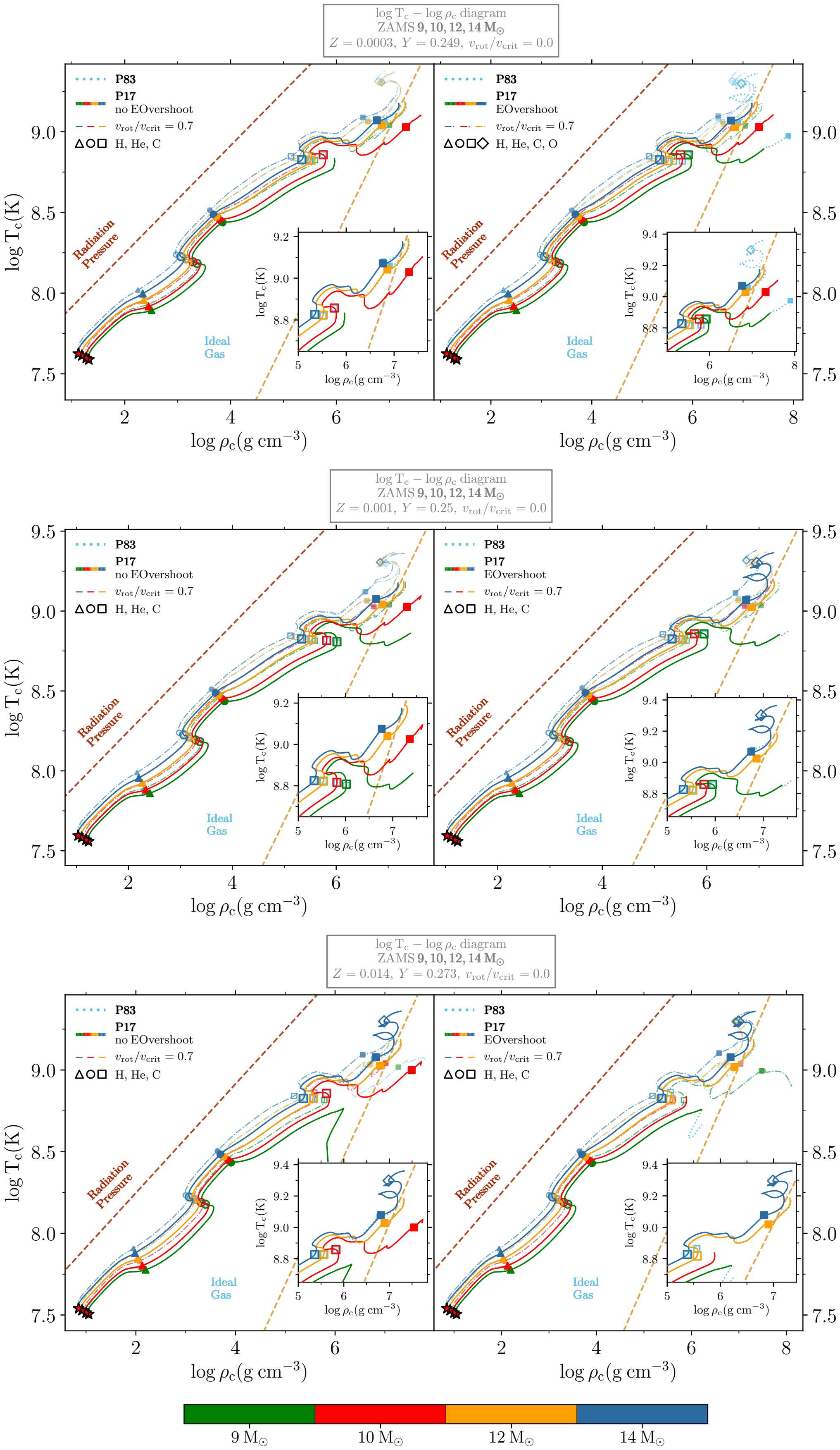

Figure 3.17: See the following page.

Figure 3.17: (Previous page.) Comparative $\log \mathrm{T_c} - \log \rho_\mathrm{c}$ structure for all the models in which we expected the **P17** (**COND**) routine to show some effects. We show the P17 tracks in solid colors, P83 are dotted light blue with their respective phases following the color coding of the colorbar; the rotating counterparts of P17 are in colored dot-dashed lines, while light blue dot-dashed lines correspond to P83 with rotation. The inserts zoom only on the P17 and P83 models without rotation, for clearness. Top row to bottom: Z=0.0003, Z=0.001, Z=0.014. Left – PARSEC output without EOvershooting; Right – same as Left, but with EOvershooting incorporated.

3.3.3 Implementing the Conductive Opacity (COND)

So far we have presented, both theoretically and with quantitative results, our update of the high energy counterpart of radiative opacities in PARSEC, which are expected to be the major contributions to the total opacity in the core of massive stars. We remember from Sec.(2.3) that the state of the art for PARSEC's high energy opacities comprises, by now, **a)** a purely analytical Compton scattering behavior from $\log \mathrm{T} > 8.7$, i.e. our P17, and **b)** OPAL project's tables in the high energy range $4.0 < \log \mathrm{T} < 8.7$. This framework is indeed very good for massive stars.

We want however to provide PARSEC with an update, at the highest energies, which is the more general as possible. To do so, we have implemented a routine for *conductive opacities* and tested it within the entire stellar models grid presented in Sec.(1.4), whose runs will be referred to as **COND**.

The Coulomb coupling parameter Γ_i As already said in Sec.(2.2), the effects of Coulomb scattering of the electrons, in the liquid metal phase of astrophysical matter, by atomic nuclei of species i, $(\mathrm{Z_i},\ \mathrm{A_i})$, become important under some conditions. These conditions regard the density ρ, the temperature T and the chemical properties of the mixture, and are packed together in the *Coulomb coupling parameter* Γ_i, which must lie between

$$\boxed{1 \lesssim \Gamma_i = 0.2275 \, \frac{Z_i^{5/3}}{\mathrm{T_8}} \left(\sum_i \mathrm{X}_j \frac{\mathrm{Z}_j}{\mathrm{A}_j} \, \rho_6 \right)^{1/3} \lesssim 170 \, .} \tag{3.28}$$

Let us thus investigate on the values of the Coulomb parameter in the cores of our models. Fig.(3.18) shows an example of our calculation of Γ_i for the more relevant species of the mixture (the 34 isotoped comprised in PARSEC) at a specific evolutionary stage. We can see that

- The ***core C-burning starting*** stage of our test model M=10 $\mathrm{M}_\odot$, Z=0.0003, $v_\mathrm{rot}/v_\mathrm{crit} = 0$ is characterized by the core abundances reflecting the nuclear reaction network functioning, and we can easily read them in Fig.(3.14):

$$\log \mathrm{X}_{^{16}\mathrm{O}} \gtrsim -0.2 \, , \quad \log \mathrm{X}_{^{12}\mathrm{C}} \gtrsim -0.5 \, ,$$

$$\log \mathrm{X}_{^{20}\mathrm{Ne}} \gtrsim -2 \, , \quad \log \mathrm{X}_{^{24}\mathrm{Mg}} \simeq -3 \, , \quad \log \mathrm{X}_{^{23}\mathrm{Na}} \gtrsim -2 \, .$$

The Coulomb coupling parameter for the most abundant ionic specie, namely ^{16}O, is represented by the light brown curve, and we see that in the core we indeed obtain $\Gamma_{^{16}\mathrm{O}} \gtrsim 0.5$.

- As one proceeds to ***higher densities***, namely advancing in the core C-burning phase, an increase of importance for the abundances of $^{24}\mathrm{Na}$ or $^{20}\mathrm{Ne}$ is expected and, most importantly, this core density increase must happen at *nearly constant* T, due to the sensitivity of thermonuclear reaction rates:

$$\rho_c \nearrow, \mathrm{T} \simeq \mathrm{const} \quad \Rightarrow \quad \mathbf{\Gamma_i} \nearrow .$$

As one can already see from Fig.(3.18), the Γ_i for these species is indeed rising above unity in the core of this massive star too.

NB Notice that Γ_i is the same for a family of isotopes, since the electrostatic properties in electron-scatterings off nuclei are not changed by the amount of neutrons. However, one must apply a suitable average in Eq.(2.13) for A_i, or weight each specie with the adequate X_i.

Itoh et al. (2008) routine By virtue of the above considerations, we proceed in implementing the *Itoh et al. (2008) routine*, [Ito+08], for electron conductive opacities within our new P17 routine. This operation allows us to obtain a more precise and, remarkably, completely general prescription for the highest energies opacity in stellar (core) matter. We notice also that this routine is already implemented in PARSEC (kindly provided by private communication with the supervisor) in all the lower temperature regimes; a better matching with the cooler opacities, thus, motivates further our inclusion. This routine stands out in the inherent literature for the following reasons:

- It includes the ***second Born corrections***, from quantum mechanics scattering theory, for the electrons' elastic scattering with ionic species, which were shown to be fairly necessary to describe $Z \lesssim 26$ in the liquid metal phase;
- It makes use of a ***semianalytical approach***, with respect to the past, purely numerical ones. This allowed the authors to develop a versatile fitting of numerical calculations, with a remarkably suitable Z dependence. The latter one allows their results to be applied in several studies, personalizing them to the needed mixture: this is what has been done in PARSEC, too. The range of validity of their results,

$$0.1 \leq \Gamma \leq 180 \,, \qquad 10^{0.0}\,\mathrm{g\,cm^{-3}} \leq \rho \leq 10^{12.8}\,\mathrm{g\,cm^{-3}} \,,$$

is large enough to comprise fairly common stellar physics phenomena. Of course, their prescription must always be taken within the liquid metal phase regime, i.e. while condition Eq.(3.28) holds.

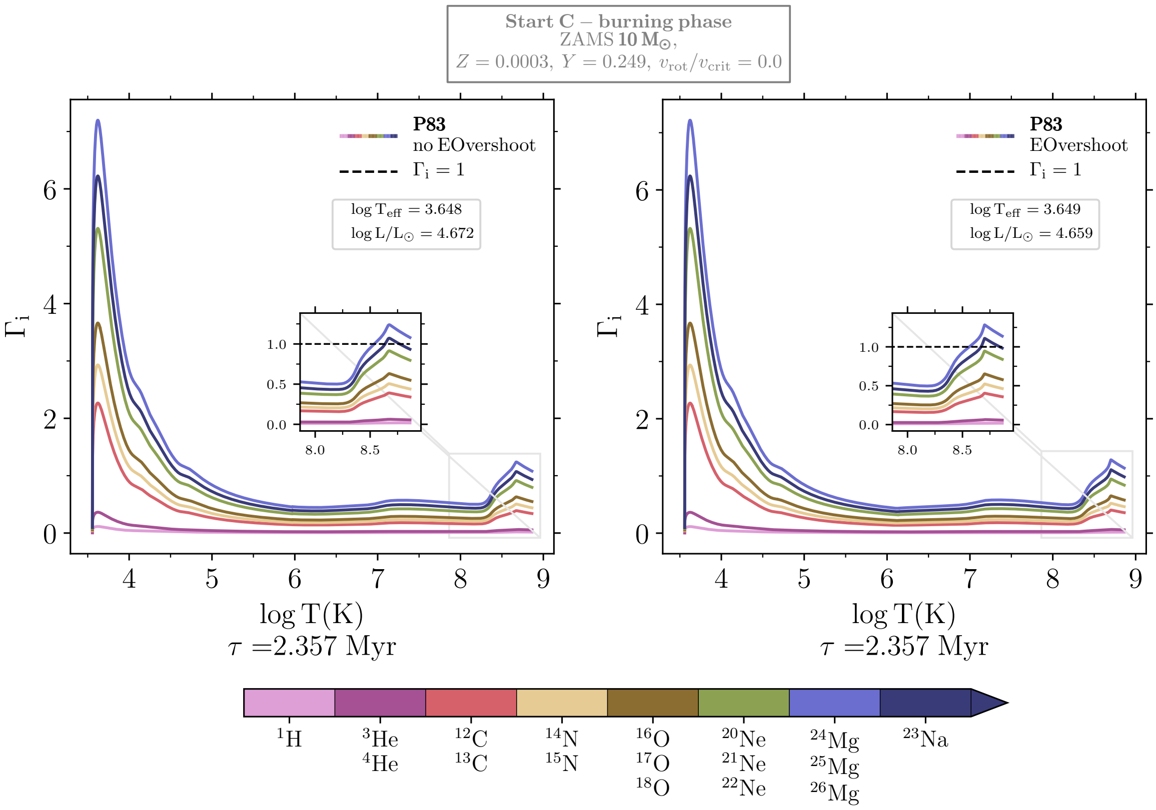

Figure 3.18: Coulomb coupling parameter Γ_i for the nuclear specie $(\mathrm{Z_i},\ \mathrm{A_i})$, as a function of stratification temperature T, for a star with ZAMS mass M=10 $\mathrm{M}_\odot$, metallicity Z=0.0003 and rotation velocity $v_\mathrm{rot}/v_\mathrm{crit} = 0$, with the prescription **P83**; since we pointed out that the stratification abundances for the P17 run are non appreciably different, this is a reference also for the P17 Coulomb parameter. The HR position of the evolutionary stage, i.e. near the core C-burning start, is reported in an insert, and the atomic species are color coded. Left – PARSEC output without EOvershooting; Right – same as Left, but with EOvershooting incorporated.

Their result for the thermal conductivity $\mathrm{K_{cd}}$ can be recast into a result for the **conductive opacity**, κ_cd, by means of an analogy with radiative diffusive processes:

Conductive Opacity

$$\kappa_\mathrm{cd} = \frac{4ac\mathrm{T}^3}{3\mathrm{K_{cd}}\rho} = \frac{4ac\mathrm{T}^3}{3\rho}\Bigg(\underbrace{\frac{2.363\times10^{17}\rho_6\mathrm{T}_8}{1+b^2}\,\frac{\left[\sum_i \mathrm{X}_i\left(\mathrm{Z}_i/\mathrm{A}_i\right)\right]^2}{\sum_j \mathrm{X}_i\left(\mathrm{Z}_j^2/\mathrm{A}_i\right)\,\langle S\rangle_j}}_{=\mathrm{K_{cd}}}\Bigg)^{-1}, \tag{3.29}$$

where $\langle S\rangle_i$ is a suitable integral of the ionic liquid structure factor S_i, see [Ito+08] for the expressions, calculated for the classical One-Component Plasma (OCP); b is the dimensionless relativistic parameter $b \equiv \alpha(9\pi/4)^{1/3}r_s^{-1}$, and the electron density parameter is defined

as $r_s \equiv 1.388 \times 10^{-2}(\mathrm{A/Z})^{1/3}\rho_6^{-1/3}$.
As concerned the actual implementation of this subroutine, we stress that one needs to adjust the formula Eq.(3.29) for $\kappa_{\rm cd}$ to the PARSEC's mixture of elements, which actually comprises much more isotopes than the ones contemplated by Itoh et al; we needed to consider a proper, weighted sum of A_i for each nucleus.

The harmonic sum $1/\kappa$ Once one obtains the $\kappa_{\rm cd}$ from the Itoh's routine, and the $\kappa_{\rm rad} = \kappa_{\rm P17}$ (for the regime $\log\mathrm{T} > 8.7$) from the new prescription Eq.(3.26), all the ingredients for the total opacity are prepared. We performed a *harmonic sum*,

$$\frac{1}{\kappa} = \frac{1}{\kappa_{\rm P17}} + \frac{1}{\kappa_{\rm cd}}\,, \tag{3.30}$$

in the fashion of Eq.(2.11), and then we were ready to test PARSEC new, **COND** outcomes.

3.3.3.1 The opacity $\log\kappa - \log\mathrm{T}$

We are now going to present the results of **COND** runs concerning the structure plots of $\log\kappa - \log\mathrm{T}$. Again, the changes interest the region $\log\mathrm{T} \geq 8.7$, in which PARSEC shuts down the OPAL opacities and account for $\kappa_{\rm P17}$ and $\kappa_{\rm cd}$.
We can summarize the main results as

- **$\log\mathrm{T} \gtrsim 8.7$** As was the case for P17, the COND opacity is overall in excellent agreement with P83 when temperatures are not so extreme: this is probably due to the fact that we are not entering the actual, denser core of the star, in which conduction becomes effective. The agreement is again of entity $< 1\%$.

- **$\log\mathrm{T} > 8.7$** This regime show a ***dramatic*** difference in $\log\kappa$ with respect to P83, at least in the most advanced phases (i.e. end of core C-burning and beyond): the departure can be as high as 40% for the most compact models, whose 25% was solely due to P17 introduction (see Fig.(3.9 – Top row) and Fig.(3.19 – Top row)).
  The opacity has, of course, decreased with respect to the P17 runs, as one can see by looking at Fig.(3.9 – Bottom row) and Fig.(3.19 – Bottom row): this is expected by virtue of the harmonic sum of Eq.(3.30).

- **Different ZAMS** As one can see in Fig.(3.19) and Fig.(3.20), we found similar differences, between **COND** and **P83**, as one increases the ZAMS mass: for higher masses, the deviation diminish. For reasons we are explaining just below, we believe that this behavior is almost exclusively operated by the P17 routine; anyway, since we have just compared structures at some relevant evolutionary points, i.e. core C-burning start or end, happening at fairly similar $\mathrm{T_c}$ coordinates (see Fig.(3.17), the empty (filled) rectangles) but different ρ_c, we also contemplate the possibility that COND contributes to this effects, in a smaller part.

- **Different Metallicity Z and $v_{\rm rot}/v_{\rm crit}$** The same entity of deviations are encountered by varying Z and rotational velocity, which excludes a specific COND behavior's dependence on them.

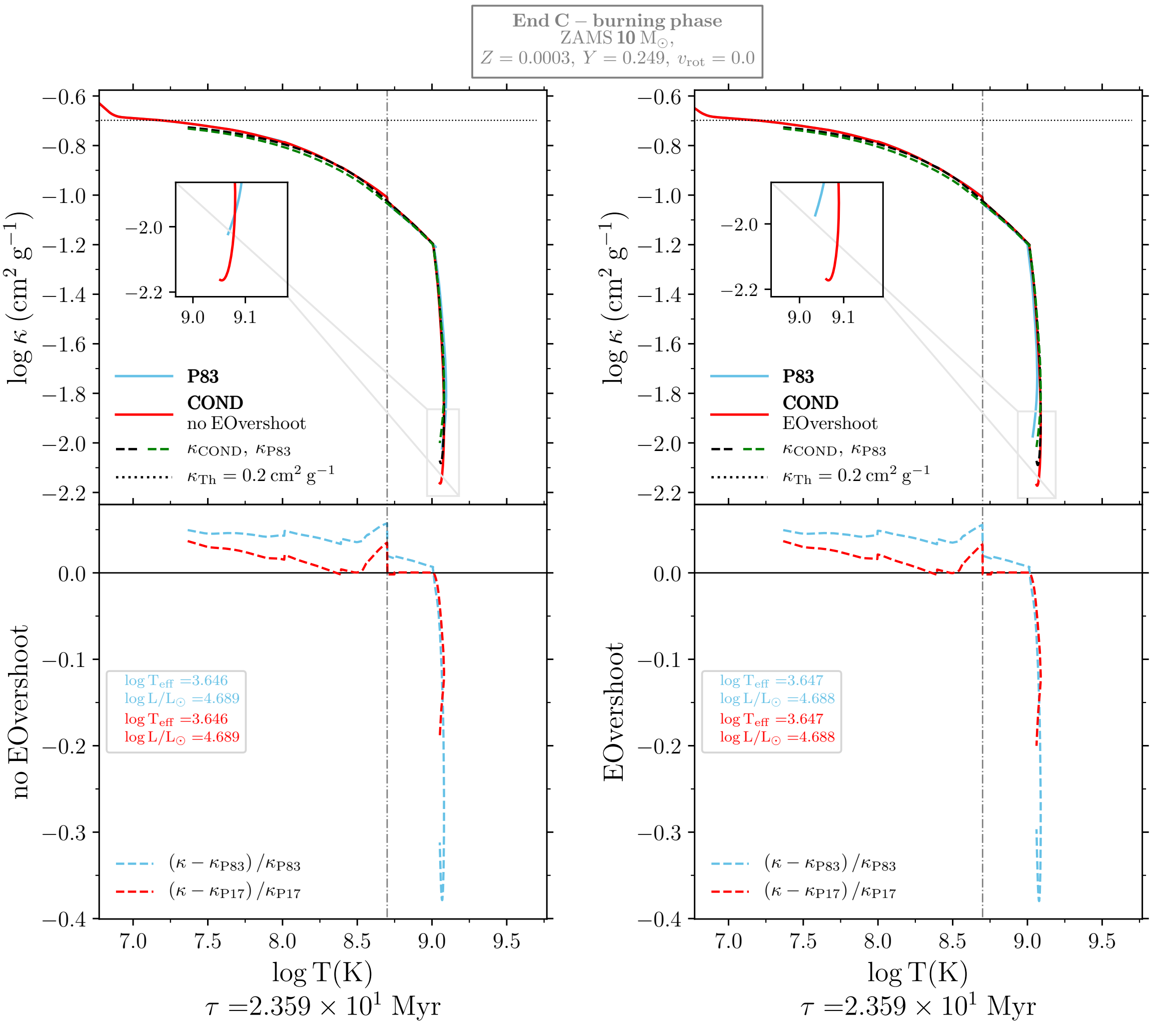

Figure 3.19: Comparative structure $\log\kappa - \log T$ for a star with ZAMS mass M=10 $M_\odot$, metallicity Z=0.0003 and rotation velocity $v_{rot}/v_{crit} = 0$, with the two prescriptions **COND** and **P83**. Same notations as Fig.(3.9) are employed. Here we see that the relative difference of P17 to κ (dashed light blue), i.e. the harmonic sum of conductive and radiative opacities, is not zero, as a contrast to Fig.(3.9), where its representation was just a consistency check. Left – PARSEC output without EOvershooting; Right – same as Left, but with EOvershooting incorporated.

Brief comment stability Again, without the purpose of a complete performance analysis, we have nevertheless tested the smoothness of *logarithmic derivatives* with respect to the temperature T, of our prescription COND as well. In the majority of cases we found a very similar situation to Fig.(3.13), with $\partial \log\kappa/\partial T$ fairly closer to zero than the P17 case.

Evolutionary properties As regards the evolution diagrams and the key evolutive parameters discussed in the previous section, we have basically encountered the same, very slight, deviations. By virtue of this fact, we cannot conclude to have singled out relevant

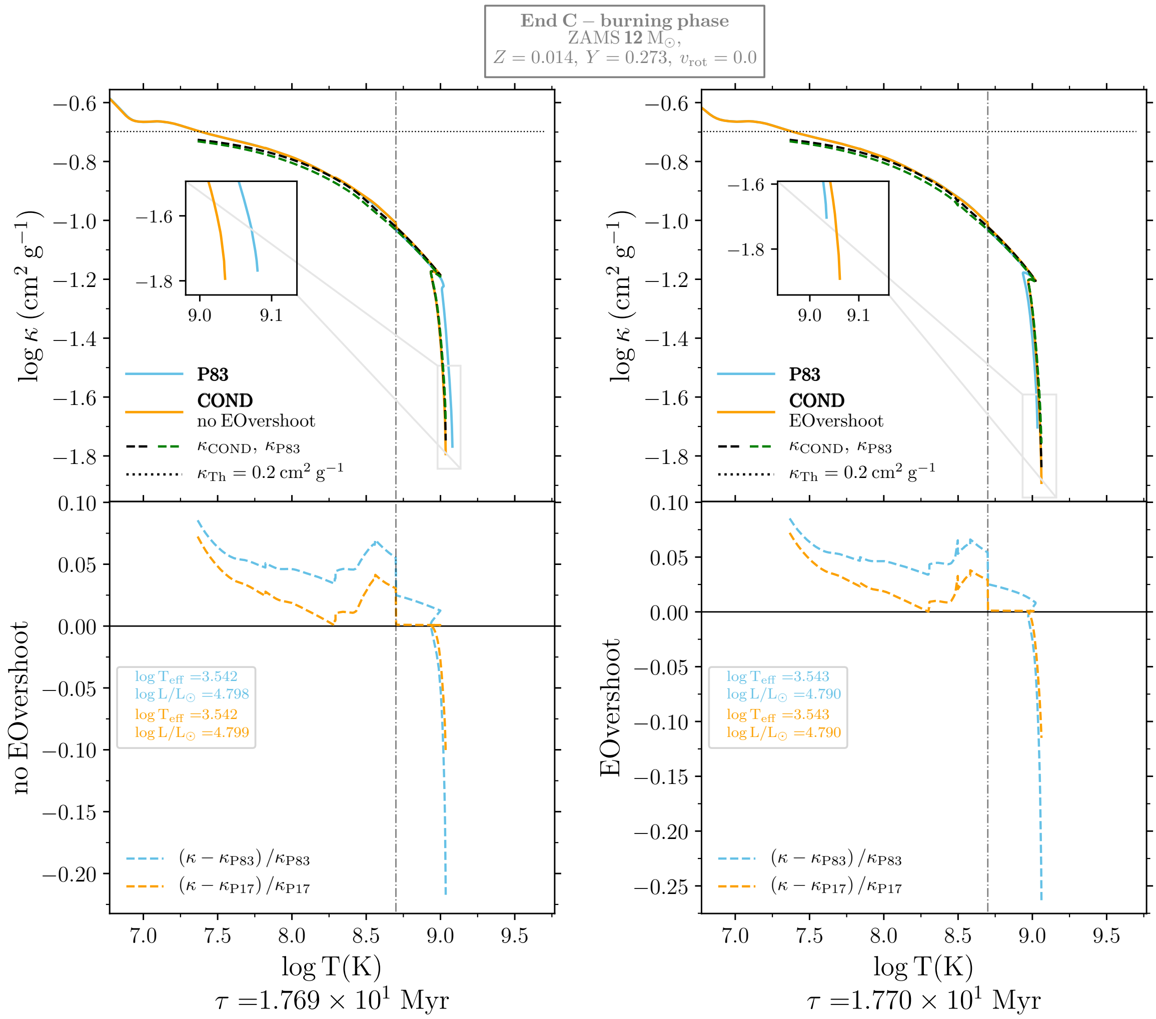

Figure 3.20: Comparative structure $\log \kappa - \log \mathrm{T}$ for a star with ZAMS mass M=12 M$_\odot$, metallicity Z=0.014 and rotation velocity $v_{\rm rot}/v_{\rm crit} = 0$, with the two prescriptions **COND** and **P83**. Same notations as Fig.(3.9) are employed. Left – PARSEC output without EOvershooting; Right – same as Left, but with EOvershooting incorporated.

effects on the evolution caused by the introduction of conductive opacities in the highest temperatures regime $\log \mathrm{T} > 8.7$.

Possible extension to other masses Following the idea outlined in introducing Sec.(3.3), we have performed our analysis in the restricted grid presented in Tab.(3.2), namely by varying ZAMS masses in between M=9-10-12-14 M$_\odot$. The implementation of $\kappa_{\rm cd}$, however, could introduce very interesting features even in the (much) more *and* (much) less massive cases.

- The first case is essentially motivated by the fact that, for **higher masses**, the condition Eq.(3.28) for liquid metal phase in the core at advanced stages (beyond O-burning) could hold as well, even with stronger entity than the $\Gamma_i \gtrsim 1$ we see in

Fig.(3.18); this is especially true when heavier elements, such as $^{28}\mathrm{Si}$ or $^{52}\mathrm{Fe}$, compare in the nuclear reactions network.
This reasoning essentially motivates the fact that we believe the reduction of deviation from P83 with ZAMS mass M $\nearrow$ to be caused mainly by P17 run. Also, an investigation of COND in the context of more massive stars could help singling out the effects of the conductive opacities only, since we know that P17 acts effectively only in the presence of strong degeneracy.

- The **less massive case**, instead, is easier to guess: more compact structures could reach higher density regions, of course always within the cases in which they also reach out a sufficiently heavy mixture composition (and they do not crystallize).

In conclusion, even though we were not able to single out specific evolutionary effects caused by COND, the above aspects certainly need a future, further development, which could reveal indeed something relevant to the evolutive parameters.

4

Opacity: Molecular and Atomic transitions

This chapter focuses on the evolutionary effects of a different opacity prescription in the intermediate temperature range, $4.2 \leq \log \mathrm{T(K)} \leq 8.7$, analyzing the evolutive impact of a more refined input (micro-) physics. The considered T range, in PARSEC, is by now fully covered by the opacity tables from the Opacity Project At Livermore (OPAL) team, see Iglesias & Rogers (1996) [IR96].
A brief description of the *standard treatment*, for atomic and molecular opacities, in stellar evolution codes opens the chapter in Sec.(4.1); following, the *new approach* based on a recent work by Colgan et al. (2016), [Col+16] and P. Marigo (in preparation) is presented in Sec.(4.2); lastly, the *results* from the runs of PARSEC code, with the implementation of a test routine for the new opacities in $4.2 \leq \log \mathrm{T(k)} \leq 8.7$, are extensively described in Sec.(4.3) for selected, interesting case study.

4.1 The standard treatment

Given the well established sensitivity, of stellar structure's and evolution's modeling results, to even modest changes in the opacity, literature has already known several notable efforts in developing refinements of the atomic physics, in the (astrophysical) radiation transport theory front. These efforts have included both recent data and theoretical modeling results, with the aim to provide accessible, updated opacity databases whose usability covers vast areas of astrophysical interest, not limited to SECs only.

Opacity Tables Since there are no direct measurements of the radiative opacity at stellar interior conditions, one must rely on theoretical calculations, which are inherently dependent on EoS state variables (usually $(\mathrm{T},\ \rho)$) and chemical mixtures. The standard approach has always been the construction of *Rosseland mean opacity tables*, which are

- ***Large as possible***, in both T and ρ, to assure complete coverage of astrophysical phenomena, with a good resolution in both dimensions too;
- ***Adaptable to chemical mixtures***, since an accurate interpolation in T, ρ and varying hydrogen and metal mass fractions, H and Z, respectively, needs to be performed;

- ***Included in SECs***, namely easily readable by Stellar Evolution Codes, which either perform interpolations *on the fly* (i.e., during their run and when needed) or prior to their run;
- Accounting for ***updated mycrophysics***, which means that any source, of radiation continuum or lines, present in any mixture has to be treated within the full theoretical framework of atomic / molecular physics, supported, where possible, by laboratory data on cross sections and oscillator strengths of astrophysical interest.

This last requirement is evidently the most challenging, as we understand that the implications of refined treatments of full atomic physics could comprise not just enormous expenses on computing times for SECs, but also the actual lack of laboratory experiments to test the theory.
Fortunately, the astrophysical community is very alive in this front, and large efforts have already been devoted to this refinement, as one can understand by considering the results of the *OPAL Rosseland opacities*, by Iglesias & Rogers (1996), [IR96].

The OPAL opacities (1996) Let us highlight the main features of the major (though not the first nor last!) effort to provide the astrophysical community with versatile and precise Rosseland mean opacities. The efforts were due to the Lawrence Livermore National Laboratory (CA, USA) team who independently responded, in the 90's, to the needs of new calculations, based on improved EoS and atomic physics, emerged from consistent observational discrepancies (e.g., properties of pulsating stars).

a) RANGES OF VALIDITY
OPAL Rosseland mean opacities tables are quite extended in both T and ρ, offering numerical results in almost rectangular ranges of

$$3.75 \leq \log \mathrm{T(K)} \leq 8.7 \,, \quad -8 \leq \log \mathrm{R} \leq +1 \,,$$

where $\mathrm{R} \equiv \log(\rho/\mathrm{T}_6)$ is a proxy for the density ρ, and T_6 is the temperature (in K) scaled by 10^6 K. Some omitted values correspond to the degenerate plasmas that are beyond the range of validity of their calculations, where the energy transport is dominated by conduction. In their paper, a cutoff is indicated around $\eta \simeq 8$.

b) IMPROVED ATOMIC PHYSICS
Detailed treatment of atomic configurations, in the intermediate coupling framework (contrarily to the simple Russel-Saunders used in the past) in the majority of cases, is comprised, and has shown to have major impact in solving mostly *all* of the observational discrepancies which motivated their work. The major refinements regarding

- Inclusion of several **metal lines** there were not previously considered (e.g., the rich spectrum of transitions from the M shell of iron) due to their sufficiently low abundances in normal stellar compositions;
- Updates to **spectral lines** broadening, accounting for **1)** Voigt's profile modifications on the red wings of spectral lines, **2)** collisional broadening by neutrals (H and He), instead of by charged species only;

- Higher order **Coulomb corrections** for the higher densities, to overcome the over simplified Debye-Hückle approximation on weakly coupled plasmas.

c) **Some Molecular Processes**
The quite large range of validity for the OPAL tables, which has a lower limit of $\log \mathrm{T(K)} \geq 3.75$, actually assures that their neglect of molecular absorption do not lead to significant errors. However, some molecular relevant process are indeed included in OPAL tables, and these comprise such important mechanisms as, e.g.,

Rayleigh Scattering	$\mathrm{H_2} + \gamma \rightarrow \mathrm{H_2} + \gamma'$
Inverse Bremsstrahlung	$\mathrm{H_2^+} + e^- + h\nu \rightarrow \mathrm{H_2^+} + e^-$
	$\mathrm{He_2^+} + e^- + h\nu \rightarrow \mathrm{He_2^+} + e^-$

which are expected to play a relevant role at sufficiently high densities and low temperatures; the above cited are not, actually the only ones, since a large variety of processes involving $\mathrm{H_2}$ and $\mathrm{He_2}$ molecules are comprised, all with recent scattering cross sections.

d) **Web Interface**
As regards the availability of the OPAL team data, they developed a free, interactive web mask, [IR], provides a set of pre-computed tables for selected H, He and metal mass fractions, X, Y, Z respectively, with $0 \leq \mathrm{Z} \leq 0.1$, together with the solar composition, α-enhanced and C-O enhanced ones.
Even though most needs for astrophysical opacities can be met with such standard set of tables, there is also the possibility to generate new tables, according to the user's needs, as it is done in PARSEC.

OPAL in the PARSEC code As specified in Sec.(2.3), the PARSEC code, at the date of this work, fully exploits the OPAL team opacity tables in the temperature range $4.2 \leq \log \mathrm{T(K)} \leq 8.7$, where we notice that the upper boundary corresponds to the ignition of our new updates of Chp.(3). The lower boundary is chosen according the validity of the ÆSOPUS tool, [MA09]; the results from the latter and OPAL are shown to perfectly agree in the transition temperature interval.
The PARSEC code uses OPAL tables generated from the interactive web mask, specifying the number fractions of 19 heavy elements (C, N, O, Ne, Na, Mg, Al, Si, P, S, Cl, Ar, K, Ca, Ti, Cr, Mn, Fe, Ni) as needed by their relative abundances $\mathrm{X_i/Z}$. The standard interpolation scheme is performed in R, T, X and Z.

4.2 A new approach

We present here the ideas behind a *new approach* to the usage of opacity tables, which will essentially translate in a refined interpolation scheme accounting for the specific C, N and O mass fractions together with the usual T, ρ (or R), hydrogen and metals fractions H and Z.

A complete formulation of this method is yet to be implemented in PARSEC (see P. Marigo, in preparation), but it is by now fully working for a selected metallicity value of Z=0.0003, very fast and usable for any ZAMS mass supported by the PARSEC code. We will investigate its implications in the following section Sec.(4.3).

The ATOMIC code from LANL (2016) Being in fact the actual releasers of the first opacity tables, and after the independent effort of the OPAL team, the Los Alamos National Laboratory (LANL) has recently presented to the astronomical community a renewed set of opacity tables, the *OPLIB tables*. These are computed with their new ATOMIC *code*, see J. Colgan et al. (2016), [Col+16]. Let us summarize the main novelties of this thorough work:

a) **Ranges of Validity**
ATOMIC code can provide both *monochromatic*, κ_ν, and Rosseland mean, κ, opacities for the elements from Hydrogen to Zinc, and for a wide range of temperatures and densities:

$$3.76 \leq \log \mathrm{T(K)} \leq 9.1\,, \qquad -8 \leq \log \rho\,(\mathrm{g\,cm^{-3}}) \leq 4\,.$$

For a complete opacity calculation, they crucially included a large number of configurations to account for contributions to the total absorption; these configurations are then all split into *fine-structure* levels (as opposed to OPAL, in which fine-structure precision was not assured in all cases).

b) **Improved Atomic Physics**
The ATOMIC code is a multi-purpose opacity and plasma modelling code that can be run both in LTE and non-LTE mode. Atomic data (e.g. occupation numbers, oscillator strengths) calculations are carried with LANL's standard atomic structure codes in the semi-relativistic Hartree-Fock framework. The major strengths of the code comprise:

- Full **configuration interaction (CI)** between all configurations, in the hydrogenoid atoms cases (H-, He- or Li-like), while for multi-electrons stages are treated with a **single-configuration** approximation, within the intermediate coupling option.

- Full **Free-Free contributions** contributions to the opacity are corrected for plasma screening effects and exact for any degeneracy. The incorporation of effects due to multiple electron-ion collisions is also included, e.g. from H^- and C^- ions, these latter contributions being important only at $\log \mathrm{T(K)} \leq 4.1$.

- **Rayleigh** scattering is included, for the low energy side of the lowest energy transition of the ground state of *all* neutral atoms.

- **Line broadening** is thoroughly updated, accounting for **1)** Stark broadening of H- and He-like line, important for opacity calculations; **2)** neutral resonance and van der Waals broadening (or, simply, CIAs, see Sec.(2.1.2)); **3)** Voigt's profile with natural, Doppler, neutral broadening features when Stark's effects are not treated.
  Also, a different treatment of the *red wings*, with respect to OPAL, is adopted, and this can actually make a huge difference to the opacity in certain regions,

e.g. for κ of He around $\log \mathrm{T(K)} \simeq 4.1$, where the bound-bound He transition is essentially the only opacity contributor.

c) **Web Interface**
As regards the availability of the LANL ATOMIC opacity and atomic data, the team updated their existing free, interactive web mask, [Mag]. Their webpage has been recently updated to include access to the new OPLIB opacity tables computed with ATOMIC by the TOPS group at LANL.
On the website, the user may request opacities for *single elements* or *mixtures* of elements, the latter ones being completely arbitrary in the mass fractions of H to Zn, for a total of 30 elements.

The NEW$\boldsymbol{\kappa}$ in PARSEC From the incredibly powerful tool offered by the web mask, [Mag], we may thus obtain ***monochromatic opacities***, encompassing a large photon energy range and providing sufficient density of points; multigroup opacities or Rosseland and Planck means, as needed. Additionally, both the total monochromatic opacities *and* separate absorption and scattering contributions are tabulated. This range of appealing possibilities paves the groundwork for a thorough revision of the PARSEC's opacities in the range $4.2 \leq \log \mathrm{T(K)} \leq 8.7$, where we recall from Sec.(2.3) that OPAL tables were in full operation.

This inspired the work under development at the PARSEC's group in Padua (Marigo et al., in preparation) which shall comprise a completely *renewed opacity treatment*, let us call this **NEW$\boldsymbol{\kappa}$**, in the temperature range where atomic transitions dominate: pre-computed look-up tables of opacities, at a fixed initial reference metallicity Z, are produced and interpolated, by standard schemes, in **7 dimensions**:

$$\mathbf{\log T(K)}\ ,\quad \mathbf{\log \boldsymbol{\rho}}\ ,\quad \mathbf{H}\ ,\ \overbrace{\mathbf{C}\ ,\ \ \mathbf{N}\ ,\ \ \mathbf{O}}^{\text{⚠}}\ ,\quad \mathbf{Z}$$

$$3.2 \leq \log \mathrm{T(K)} \leq 9.1\ , \qquad -8 \leq \log \mathrm{R} \equiv \frac{\rho}{\mathrm{T}_6} \leq 1\ ,$$

and the same fine grid spacing as described in Sec.(2.3), to limit as much as possible the accuracy loss due to subsequent interpolations; also, the interpolations shall be done simultaneously for $\log \kappa$, $\partial \log \kappa / \partial \log \mathrm{T}$ and $\partial \log \kappa / \partial \log \rho$.

One can immediately understand the relevance of such a refinement, since PARSEC shall consequently be able to follow *any* modelled changes of opacity due to C, N, O abundances peculiar evolution, during the history of the tracks, and this is true at *each mesh-point* in the stellar structures. Such peculiar episodes can comprise overshoot/rotational mixing, advanced dredge up episodes and others more. Let us summarize the prospective PARSEC's scenario:

Very High Temperatures $\log T \gtrsim 9.1$	▸ **P17+Itoh et al.** κ_{P17}	[Pou17] [Ito+08]
High-Mid Temperatures $4.2 \lesssim \log T \lesssim 9.1$	▸ TOPS $\kappa_\nu \to$ **NEW**$\boldsymbol{\kappa}$	[Mag] [Marigo, in prep]
Transition Region $4.0 \lesssim \log T \lesssim 4.1$	▸ **NEW**$\boldsymbol{\kappa}$**+ÆSOPUS**	
Low Temperatures $3.2 \lesssim \log T \lesssim 4.1$	▸ **ÆSOPUS**	[MA09]
+ Conductive	▸ **Itoh et al.**	[Ito+08]

Here above we notice the consistent difference with respect to the scenario described in Sec.(2.3), and we have also updated the highest temperature range with our new implementations presented in Chp.(3).

To date of the present work, this drastically improved scenario has not been fully implemented yet, as said above. However, some **test tables** of the Rosseland mean opacity, for fixed metallicity, Z=0.0003, and variable H, C, N, O are already prepared and ready to be tested. The 6-dimensional interpolation in $(\log \mathrm{T(K)},\ \log \mathrm{R},\ \log \mathrm{H},\ \mathrm{C},\ \mathrm{N},\ \mathrm{O})$ is performed through a concatenation of linear interpolations, and mixture values are such that

$$\mathbf{H} \in [0.0,\ 0.0001,\ 0.001,\ 0.1,\ 0.2,\ 0.35,\ 0.5,\ 0.7,\ 0.8]$$

$$\mathbf{C},\ \mathbf{N},\ \mathbf{O} \in [-1.,\ 0.0,\ 0.01,\ 0.03,\ 0.1,\ 0.6,\ 0.95]$$

the negative abundances being set to the reference ones (e.g., solar scaled) and resorted. In the following work, we are precisely going to test these new tables for Z=0.0003 and chosen models of interest, which are comprehended in the enlarged stellar grid shown in Sec.(1.4.1), Tab.(1.1).

4.3 Results: NEW$\boldsymbol{\kappa}$, $\mathbf{Z = 0.0003}$

We ran the PARSEC code for the stellar models grid in Tab.(4.1), with the implementation of the new prescription for atomic-molecular opacities described above. As said above, at the moment, this new prescription is fully working for a single value of the metallicity, i.e. $\mathrm{Z} = 0.0003$. The choice of the masses was driven by the following argument: given the very low $\dot{\mathrm{M}} \propto \mathrm{Z}^{\alpha}$, see Eq.(1.12), the impact of our prescription is expected to be more relevant in the most massive tracks. However, a check on the lower mass $\mathrm{M} = 10\,\mathrm{M}_{\odot}$ could be interesting, due to the possibility of a comparison with the respective rotating model.

Z = 0.0003, Y = 0.249			
ZAMS	10 $M_\odot$	60 $M_\odot$	140 $M_\odot$
$v_{rot}/v_{crit} = 0.0$	✓	✓	✓
$v_{rot}/v_{crit} = 0.7$	✓	✗	✗
EOv	✓	✓	✓
no EOv	✓	✓	✓

Table 4.1: Selected PARSEC models for the study of the impact of the prescription **NEWκ** for atomic opacities. The rotating counterpart of 60 $M_\odot$ and 140 $M_\odot$ are missing: these can be relegated to future works, as well as any other possible extension of the present grid.

This section aims at showing the most interesting results of the **NEWκ** for few selected models; we present singularly each model, with both their structural and evolutionary characteristics. The comparisons are made between them and **OLDκ** results, referring to the PARSEC's models computed prior to the implementation of **NEWκ**.
NB In the following, we are taking for granted that the comparisons of tracks from different runs, OLDκ and NEWκ, of PARSEC are being made between similar, though not identical, evolutionary stages; *numerical fluctuations* are to be taken into account in all the treatment.

4.3.1 10 $M_\odot$, $v_{rot}/v_{crit} = 0.0$

Evolutionary Track Some relevant results of the models are presented in Tab.(4.2). We can start our discussion about M=10 $M_\odot$ by commenting on the *evolutionary track*, which can be seen in Fig.(4.1).

10 $M_\odot$		τ_{MS}	$\tau_{H\text{-}shell}$	τ_{He}	M_{He}	M_{CO}	$^{12}C/^{16}O$
no EOv	**OLDκ**	20.4 Myr	152.8 kyr	1.528 Myr	2.252 $M_\odot$	1.414 $M_\odot$	0.762
	NEWκ	19.4 Myr	143.1 kyr	1.392 Myr	2.275 $M_\odot$	1.326 $M_\odot$	0.774
EOv	**OLDκ**	20.4 Myr	152.8 kyr	1.528 Myr	2.252 $M_\odot$	1.413 $M_\odot$	0.762
	NEWκ	19.4 Myr	143.1 kyr	1.392 Myr	2.275 $M_\odot$	1.326 $M_\odot$	0.774

Table 4.2: 10 $M_\odot$ characteristics from PARSEC with prescriptions **OLDκ** and **NEWκ**. The fraction $^{12}C/^{16}O$ is referred to the stage of the end of He-burning; the M_{He} refers to the end of shell H-burning, while the M_{CO} value refers to the end of He-burning.

I. H-BURNING
The core H-burning phase shows an excellent agreement in the two prescriptions, with just a slight difference of 5% in τ_{MS}, see Tab.(4.2). This is indeed expected, since

the (logarithmic) abundances of C, N, O all remain below 10^{-4} throughout the structure till the end of H-burning. We can lastly notice a slightly hotter *blue hook* as the MS ends in the usual contraction.

II. SHELL H-BURNING
The shell H-burning phase shows a 8% fluctuation in $\tau_{\mathrm{H-shell}}$, see Tab.(4.2), with the **NEWκ** being shorter than **OLDκ**. The star evolves towards the red and, at the start of the Blue Loop, a bluer track from **NEWκ** can be seen: in the core, C and O are indeed rising above 10^{-3}.
At the end of shell H-burning, the minimum mass $\mathrm{M_{He,min}} = 0.3\ \mathrm{M_\odot}$ is obviously reached in both cases, with the following difference:

$$\mathrm{M_{He}^{NEW\kappa}} = 2.275\ \mathrm{M_\odot} \gtrsim \mathrm{M_{He}^{OLD\kappa}} = 2.252\ \mathrm{M_\odot}\ ,$$

namely NEWκ seems to increase (of about 1%) the mass of the He core.

III. HE-BURNING
The Blue Loop shows good agreement in the prescriptions, with just a slight difference of 1% in τ_{He}, see Tab.(4.2). Core He-burning starts when the star is still a BSG. The key evolutionary parameters, $\mathrm{M_{CO}}$ and the central $^{12}\mathrm{C}/^{16}\mathrm{O}$, are, at this stage, determined, and we found for them (in the case without EOv):

$$\mathrm{M_{CO}^{NEW\kappa}} = 1.326\ \mathrm{M_\odot} < \mathrm{M_{CO}^{OLD\kappa}} = 1.414\ \mathrm{M_\odot}\ ,$$

$$^{12}\mathrm{C}/^{16}\mathrm{O}_{\mathrm{NEW}\kappa} = 0.774\ \gtrsim\ ^{12}\mathrm{C}/^{16}\mathrm{O}_{\mathrm{OLD}\kappa} = 0.762\ .$$

- A lower $\mathrm{M_{CO}}$ implies a lesser compact structure in the most advanced stages, which could result in favoring successfull explosions by virtue of the lower *bounce compactness parameter* $\xi_{2.5}$.
- Since $^{12}\mathrm{C}/^{16}\mathrm{O}$ regulates the fuel for all the advanced stages of evolution; a higher $^{12}\mathrm{C} \nearrow$ in the core usually favors less compact structures as well, which has a combined effect with $\mathrm{M_{CO}} \searrow$.

IV. SHELL HE-BURNING
The short lifetimes of the proceeding nuclear burning stages allow for a fair amount of He to burn inside the shell; this can be seen by the increase of $\mathrm{M_{CO}}$ in Fig.(4.3):

$$\mathrm{M_{CO}^{NEW\kappa}} = 1.495\ \mathrm{M_\odot} < \mathrm{M_{CO}^{OLD\kappa}} = 1.532\ \mathrm{M_\odot}\ .$$

We can see that the NEWκ CO core increases, during shell He-burning, by a 11%, while the OLDκ increases a bit less, by a 8%.
The most prominent feature of this stage is the very pronounced ***redward evolution*** of both tracks; the NEWκ one arrives much further in the red, foretelling a development as a RSG along its Hayashi line, and a much larger expansion of the envelope.

V. ADVANCED BURNINGS
The run follows, for both models, the subsequent evolutionary stages at least till the

core C-burning ignition. The position in the HR diagram remains mostly unchanged, due to the rapid evolution after core C-burning. We can see that, after the expected ascending along their Hayashi lines, these stars are expected to explode as **RSGs**, however with consistently different surface properties:

$$\log \mathrm{T}_{\mathrm{eff}}^{\mathrm{NEW}\kappa} \simeq 3.4 \ll \log \mathrm{T}_{\mathrm{eff}}^{\mathrm{OLD}\kappa} \simeq 3.7\,,$$

with advanced spectral types as K and M, in the Morgan-Keenan (MK) system, for **OLDκ** and **NEWκ**, respectively.
We point out also the numerical difficulties of the solver in the last stages: when the star sets in the Asymptotic Giant Branch (AGB), there can be a problematic phase caused by complicated evolution of the multiple active burning shells (see also Fig.(4.3)); we needed to consistently relax the simulation's parameters to obtain convergence.

No appreciable differences can be highlighted between the EOv and no EOv models, so we are going to refer to both of them without being specific, unless otherwise needed.

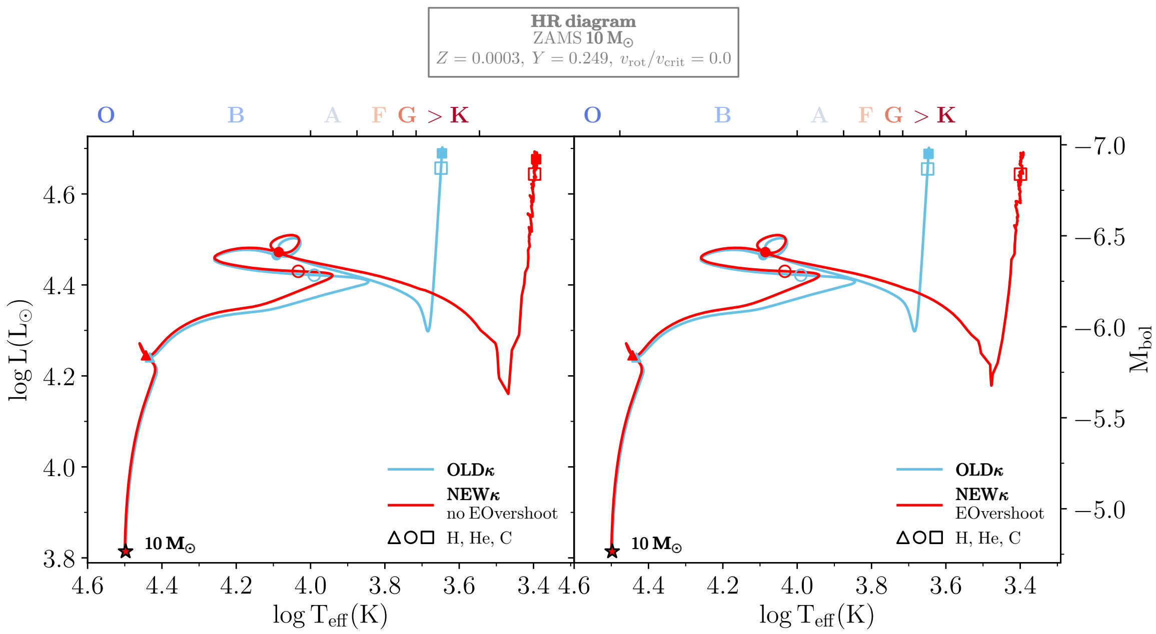

Figure 4.1: Comparative evolutionary tracks for a star with ZAMS mass M = 10 M$_\odot$, metallicity Z=0.0003 and rotation velocity $v_{\rm rot}/v_{\rm crit} = 0$, with the two prescriptions **NEWκ** and **OLDκ**; again, (filled) symbols states the start (end) of corresponding nuclear burning cycle. Spectral types are also highlighted. Left – PARSEC output without convective overshooting of the envelope (EOvershoot); Right – same as Left, but with EOvershooting incorporated.

Central ^{12}C/^{16}O evolution The evolution of the *central* ^{12}C/^{16}O can be seen in Fig.(4.2). We can see that slight differences are present between NEWκ and OLDκ.

- Mildly larger value of $^{12}C/^{16}O$ at *core He depletion*: this essentially supports the higher $M_{CO}^{NEW\kappa}$ highlighted in the previous paragraph, since the $^{12}C(\alpha,\gamma)^{16}O$ reaction has already taken over the role (which was of the triple-α) to produce He ashes, but probably with smaller strength.
- Since the model NEWκ does not proceed beyond the start of C-burning, the last effectively comparable stage is the ignition of core C-burning; the characteristic *lowering of the ratio* in the core is indeed experienced, as the ^{16}O abundance builds up feeding the CO core.

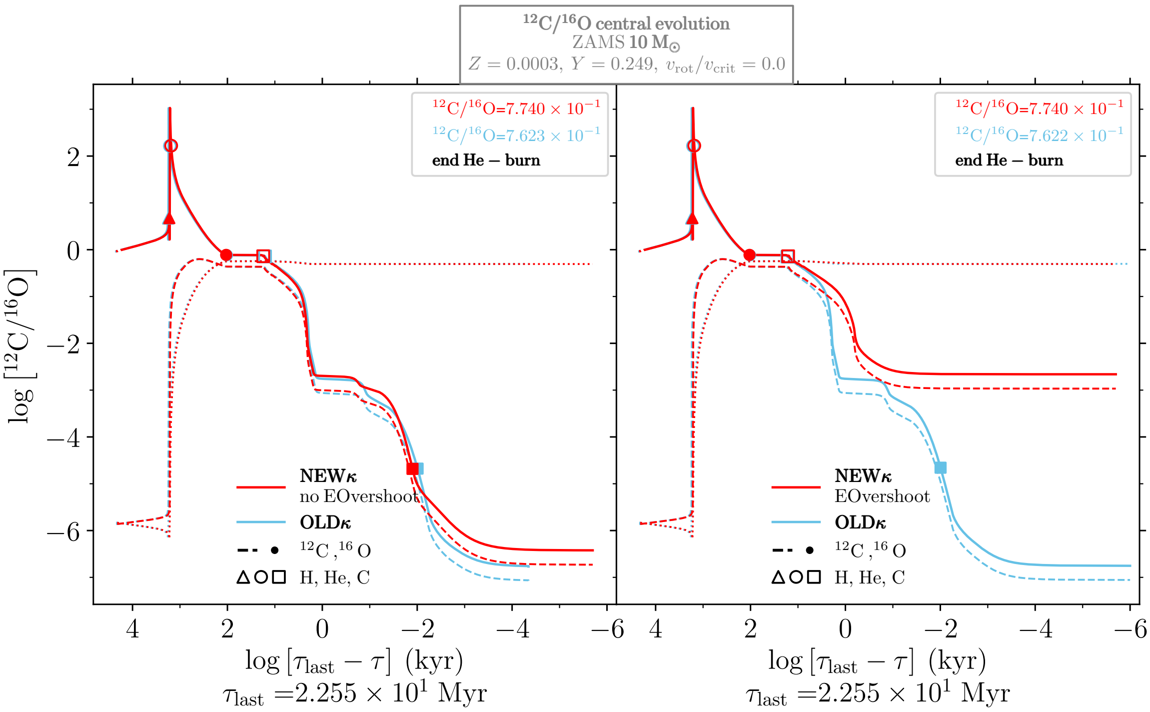

Figure 4.2: Comparative (logarithmic) central ratio $^{12}C/^{16}O$ evolution for a star with ZAMS mass M=10 $M_\odot$, metallicity $Z = 3\times10^{-4}$ and rotation velocity $v_{rot}/v_{crit} = 0$, with the two prescriptions **NEWκ** and **OLDκ**; again, (filled) symbols state the start (end) of corresponding nuclear burning cycle. Single evolution of the (logarithmic) central mass fractions ^{12}C and ^{16}O is also reported, with dashed and dotted linestyle respectively. Lastly, interesting values of the ratio are shown above. Left – PARSEC output without EOvershooting; Right – same as Left, but with EOvershooting incorporated.

Kippenhahn Diagram The so called *Kippenhahn diagram*, i.e. the evolution of some interesting mass coordinates M_i, is presented in Fig.(4.3). We can indeed see the reduction of the convective core, created by the high energy flux of the CNO cycle, as the H-burning proceeds; the core He-burning, instead, is characterized by the expected increase of the convective core, at least until the central He mass fraction drops below ~ 0.5, see M_{Schw}. This latter fact is due to the effects of the $^{12}C(\alpha,\gamma)^{16}O$ reaction, starting to feed the CO core while a H-burning shell is still active.
A very complicated stratification builds up after at the more advanced stages; a convective

tongue is also developed, able to dredge up some CNO cycle ashes e.g. ^{14}N, see also below. The most prominent differences between **OLDκ** and **NEWκ** are

- Slightly lower mass of the convective core $\mathbf{M_{Schw}}$ during He-burning;
- A 7% relative difference between $\mathbf{M_{CO}}$, as already pointed out above.
- A less penetrative bottom of the convective envelope for EOv NEWκ, which does not reach the H-He discontinuity, in contrast to the EOv OLDκ.

Let us also stress that our computations comprise, in each case, the core Ne-burning phase, described by the shift of the CO-burning core in a *off-center shell* turning on an intermediate convective region; this convective zone inside the CO core continuously provides fresh carbon to the burning shell that sustains the overlying layers, thus *delaying the core O-burning* phase.
We can lastly notice that the H-burning shell is completely shut-down after the core He depletion: this is caused by the encountering with the He-H discontinuity (see $\mathrm{M_{H-He}}$), and is expected to cause relevant effects on the onion-skin structure of the pre-SN stage; also, this prevents our M=10 $\mathrm{M_\odot}$ star to undergo *thermal pulses*.

$\log \mathbf{T}_c - \log \boldsymbol{\rho}_c$ The evolution through the $\log \mathrm{T}_c - \log \rho_c$ is shown in Fig.(4.4). No appreciable differences between OLDκ and NEWκ are visible, though probably more advanced stages in NEWκ could reveal some deviations. Both models develop mainly in the ideal gas region, as expected, see Sec.(1.2). Notably, the C-burning is ignited at slightly lower core temperature $\mathrm{T_c}$ and density ρ_c in the **NEWκ**.

Surface Abundances $\log \mathbf{X}_i$ Due to the very weak mass loss rate $\dot{\mathrm{M}}$, which always stays well below $\log \dot{\mathrm{M}} = -8$ for both models, the star does not show any apparent difference in the (logarithmic) *surface abundances* $\log \mathrm{X_i}$ of elements heavier than He. Also, the H abundance never drops below the limiting case of $\log$ H=0.4, thus a WR object is not originated. As pointed out in the previous paragraph, a dredge up happens, during shell He-burning, in both models, lifting some N and modifying the C surface content sensibly:

Before 1DU	$\log^{14}\mathrm{N} \simeq -4.82$	$\log^{12}\mathrm{C} \simeq -4.3$	$\log^{16}\mathrm{O} \simeq -3.8$
After 1DU	$\log^{14}\mathrm{N} \simeq -4.1$	$\log^{12}\mathrm{C} \simeq -5$	$\log^{16}\mathrm{O} \simeq -4$

and these are common values to both **OLDκ** and **NEWκ**; we see that indeed the CNO cycle products are being mixed.

Mass loss rate $\dot{\mathbf{M}}$ evolution A practically null mass loss is experienced by this model throughout all of its life of almost 23 Myr, as one can see by looking at Fig.(4.3). We know that the *mass loss evolution*, the metallicity Z being equal, is determined by the HR region of the star. The major amount of losses is expected when the *dust-driven wind* area is approached, ergo during the most advanced phases; but these stages are very short for our

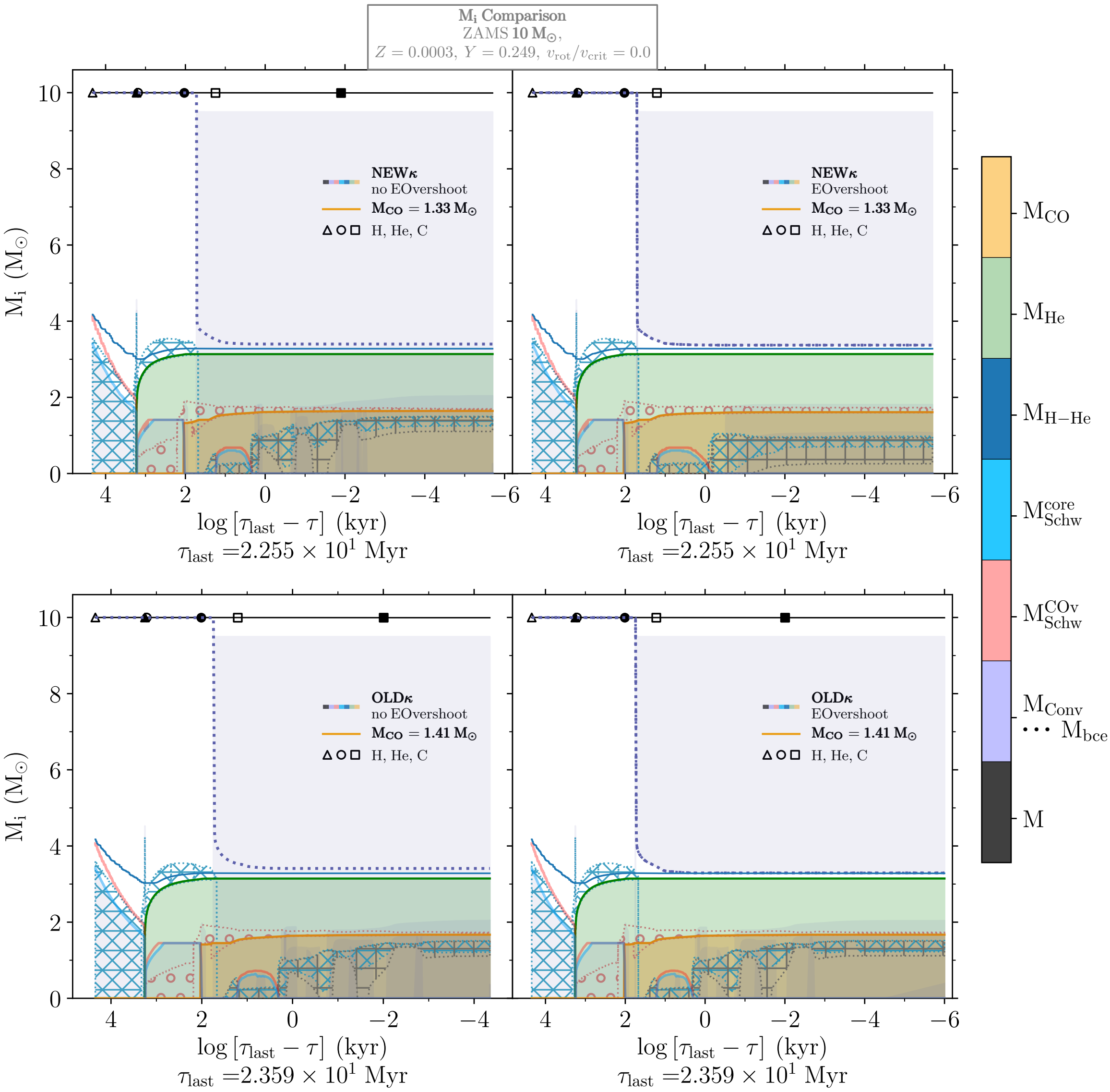

Figure 4.3: Comparative stratification history for a star with ZAMS mass $M = 10\ M_\odot$, metallicity Z=0.0003 and rotation velocity $v_{rot}/v_{crit} = 0.0$, with the two prescriptions **NEW**κ and **OLD**κ. Same notation symbols for phases as in Fig(1.1) are adopted. Respectively, M_{CO}, M_{He}, M_{H-He}, M^{COv}_{Schw}, M_{Conv}, M_{bce} and M stand for the mass coordinates of: final mass of the CO core, mass of He core at H-burning end, mass of the H-He discontinuity, Schwarzschild-unstable convective core, Schwarzschild-unstable convective core with overshooting, mass coordinate of the Bottom of the Convective Envelope (BCE), total mass as a function of (logarithmic) time coordinate, until the last model. The latter is a constant shift of coordinate time τ_{last}, which is different for OLDκ and NEWκ, both reported below x-axis. The first row shows the NEWκ results, while the second row shows OLDκ. Left – PARSEC output without EOvershooting; Right – same as Left, but with EOvershooting incorporated.

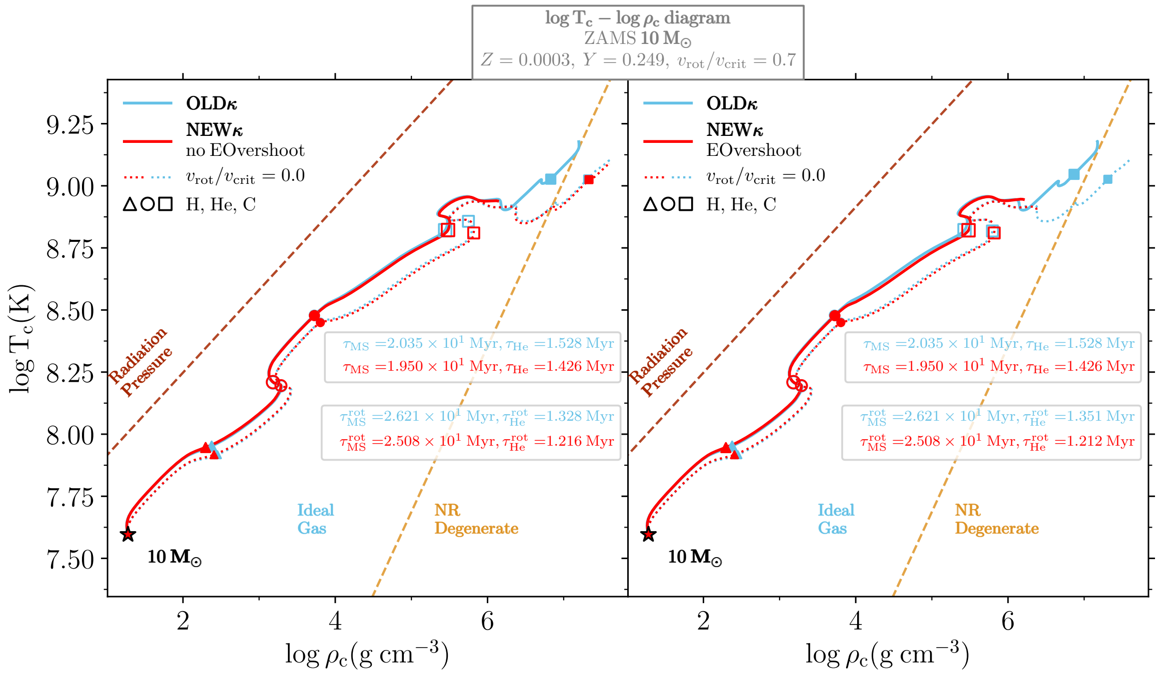

Figure 4.4: Comparative structure $\log T_c - \log \rho_c$ for a star with ZAMS mass $\mathrm{M} = 10\mathrm{M}_\odot$, metallicity Z=0.0003 and rotation velocity $v_{\mathrm{rot}}/v_{\mathrm{crit}} = 0 - 0.7$, with the two prescriptions **NEWκ** and **OLDκ**.Again, (filled) symbols state the start (end) of corresponding nuclear burning cycle. Duration of core H and He burning, τ_{MS} and τ_{He} respectively, are also highlighted. Left – PARSEC output without EOvershooting; Right – same as Left, but with EOvershooting incorporated.

star, such that less than 1‰ is expected to be ejected. More precisely,

NEWκ	$\log \dot{\mathrm{M}} \simeq -7.1$	$\mathrm{M}^{\mathrm{NEW}\kappa}_{\mathrm{C_{start}}} = 9.992\ \mathrm{M}_\odot$
OLDκ	$\log \dot{\mathrm{M}} \simeq -8.0$	$\mathrm{M}^{\mathrm{OLD}\kappa}_{\mathrm{C_{start}}} = 9.994\ \mathrm{M}_\odot$

holding for both no EOv and EOv, see Fig.(4.5). Such low $\dot{\mathrm{M}}$, in turn due to the low Z, indeed allows the models to evolve through advances stages *maintaining their H-rich envelope*, too.

First Dredge Up 1DU As the star evolves towards the red, approaching their RSG phase, convective envelopes of the cooler and cooler external layers penetrate deep into the stars till the H-He discontinuity *and* the He core, originating the *first Dredge Up* 1DU. This is an exclusively opacity-driven mechanism, thus of prior importance for our treatment.
We can catch a glimpse of the evolution of the logarithmic ratio C/O by looking at Fig.(4.6), where we compare two structures, respectively caught near the end of He-burning and the start of C-burning; the 1DU is expected to occur in between these two stages. We note that:

- The **atmospheric ratio C/N** is, at first, above 1, and after the 1DU it decreases to

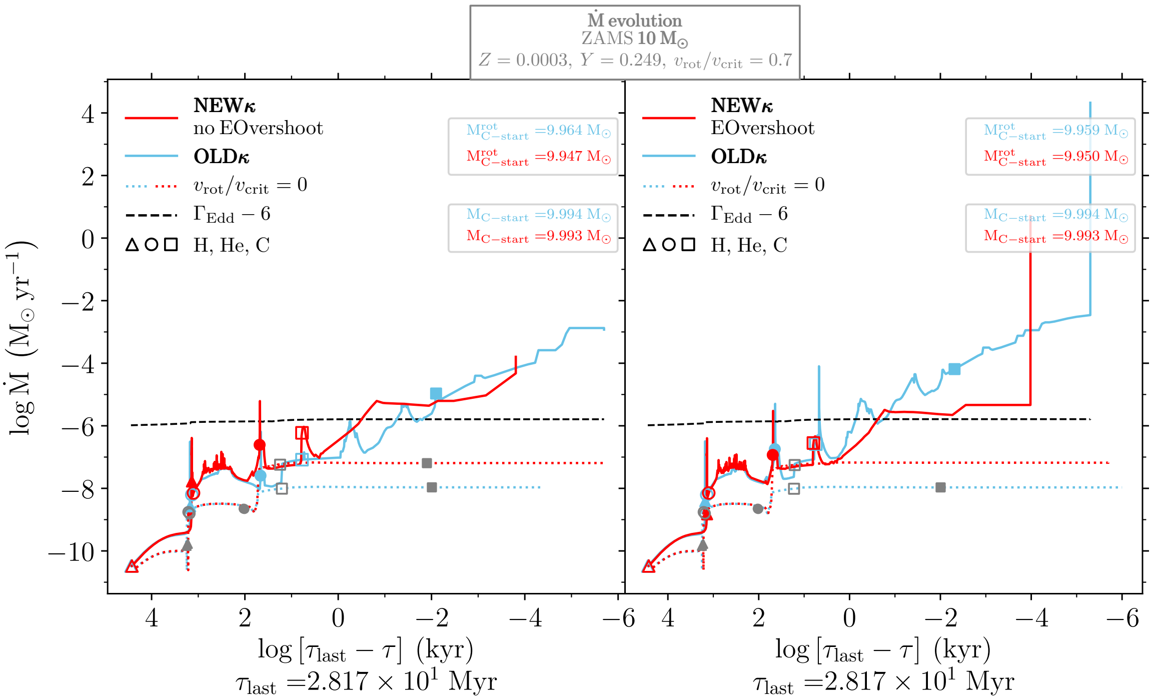

Figure 4.5: Comparative mass loss rate $\dot{\mathrm{M}}$ evolution for a star with ZAMS mass $\mathrm{M} = 10\ \mathrm{M}_\odot$, metallicity Z=0.0003 and rotation velocity $v_{\rm rot}/v_{\rm crit} = 0.0 - 0.7$, with the two prescriptions **NEW**κ and **OLD**κ; the usual convention for the symbols is employed. The usual constant shift of coordinate time $\tau_{\rm last}$, different for OLDκ (not reported) and NEWκ, is reported below the x-axis; the value of the Eddington parameter $\Gamma_{\rm Edd}$, shifted by -6 to let it appear in the plot, is shown for illustrative purposes, see text; lastly, the masses $\mathrm{M}_{\rm O}$ at the end of the last comparable model (O-burning in this case) is printed too. Left – PARSEC output without EOvershooting; Right – same as Left, but with EOvershooting incorporated.

< 0: this is a proof of the dredging up of nitrogen, only possible with a convective envelope penetration towards the CNO-processed regions.

- The **atmospheric ratio C/O** remains always below 1: this confirms our star to be of an M spectral type, as we can see in Fig.(4.1), with an oxygen rich atmosphere. Actually, this key ratio always stays <1 during our computations.
- **After the 1DU**, the opacities from NEWκ and OLDκ are similar, as for before the 1DU. Anyway, there is a difference in the atmospheric opacity: the NEWκ one is **consistently** higher, motivating thus the redder Hayashi line.
- The **NEWκ opacity** shows a peculiar feature, which is not present at all in the OLDκ: an abrupt **rise** in the atmospheric region. We motivate this fact by noticing the inserts in Fig.(4.6 – bottom row), which show the HR diagram positions of the selected structures near the core C-burning start: the $\log \mathrm{T}_{\rm eff}$ of NEWκ are strongly lower.

The latter fact suggests that, in the atmosphere of these models, the conditions (both ρ

and T dependent) for *dust and molecules aggregates* to rise are fulfilled, originating the high cusp right before the H recombination (and H^- opacity) feature. Our hypothesis fall back to the water H_2O, vanadium oxide V_2O_5 or titanium bioxide TiO_2 molecules, but this needs some further investigation. We point out that we are in the regime in which $\log T_{\rm eff} \simeq 3.4$: here, the prescription for opacities is the ÆSOPUS tool from P. Marigo (2009), [MA09].

4.3.2 10 $M_\odot$, $v_{\rm rot}/v_{\rm crit} = 0.7$

Evolutionary Track Some relevant results of the models are presented in Tab.(4.3). We briefly discuss also this rotating, M=10 $M_\odot$ model, since we want to single out possible consequences of the new prescription in case of non-null rotation $v_{\rm rot}/v_{\rm crit} = 0$. Let us start with the *evolutionary track*, which can be seen in Fig.(4.7).

10 $M_\odot$ ROT		$\tau_{\rm MS}$	$\tau_{\rm H\text{-}shell}$	$\tau_{\rm He}$	$M_{\rm He}$	$M_{\rm CO}$	$^{12}C/^{16}O$
no EOv	**OLD**κ	26.2 Myr	112.8 kyr	1.328 Myr	2.797 $M_\odot$	2.165 $M_\odot$	0.64
	NEWκ	25.1 Myr	107.4 kyr	1.216 Myr	2.826 $M_\odot$	2.061 $M_\odot$	0.66
EOv	**OLD**κ	26.2 Myr	112.8 kyr	1.351 Myr	2.801 $M_\odot$	2.180 $M_\odot$	0.62
	NEWκ	25.1 Myr	106.0 kyr	1.212 Myr	2.826 $M_\odot$	2.048 $M_\odot$	0.66

Table 4.3: Rotating 10 $M_\odot$ characteristics from PARSEC with prescriptions **OLD**κ and **NEW**κ. The fraction $^{12}C/^{16}O$ is referred to the stage of the end of He-burning; the $M_{\rm He}$ refers to the end of shell H-burning, while the $M_{\rm CO}$ value refers to the end of He-burning.

I. H-BURNING
The core H-burning phase shows an excellent agreement in the two prescriptions, with just a slight difference of 4% in $\tau_{\rm MS}$, see Tab.(4.3). This is indeed expected, since the (logarithmic) abundances of C, N, O all remain below 0.0002 throughout the structure till the end of H-burning. We can lastly notice a slightly hotter *blue hook* as for the non-rotating models.
The tracks of both **NEW**κ and **OLD**κ are consistently redder and evolve nearly vertical toward higher L, as a consequence of the additional rotational mixing (see Sec.(1.3.4)).

II. SHELL H-BURNING
The shell H-burning phase shows a 5% fluctuation in $\tau_{\rm H-shell}$, see Tab.(4.3), with the **NEW**κ being shorter than **OLD**κ. The star evolves towards the red and, at the start of the Blue Loop, a bluer track from **NEW**κ can be seen: in the core, C and O are indeed rising above 10^{-3}.
At the end of shell H-burning, the minimum mass $M_{\rm He,min} = 0.3\ M_\odot$ is obviously reached in both cases, with the following difference:

$$M_{\rm He}^{\rm NEW\kappa} = 2.826\ M_\odot \gtrsim M_{\rm He}^{\rm OLD\kappa} = 2.797\ M_\odot\ ,$$

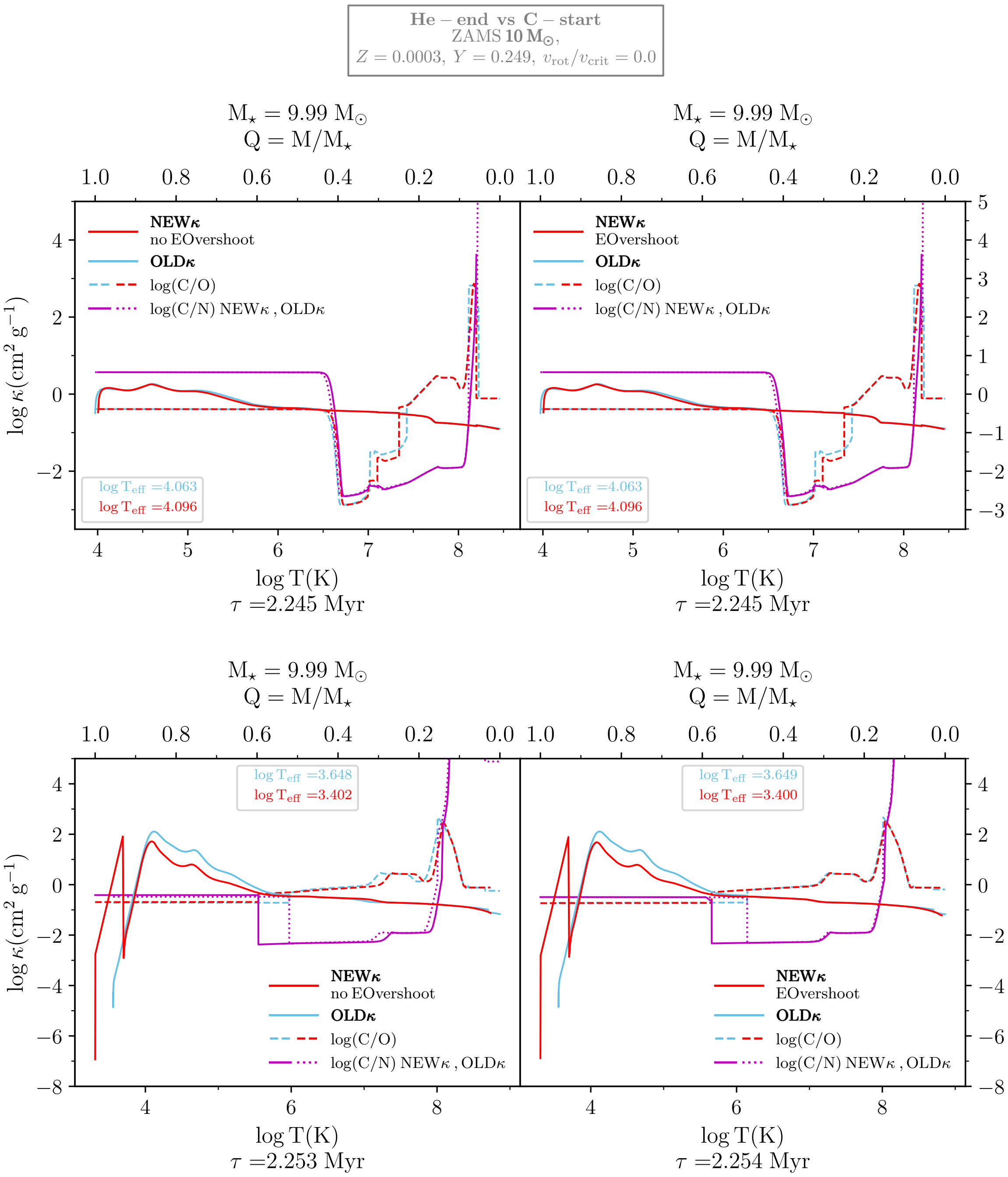

Figure 4.6: Comparative structure $\log \kappa - \log T$ for a star with ZAMS mass M=10 $M_\odot$, metallicity Z=0.0003 and rotation velocity $v_{rot}/v_{crit} = 0$, with the two prescriptions **NEWκ** and **OLDκ**. The logarithmic abundance ratio C/O and C/N are also shown. The top row catches a structure at the end of core He-burning, hence before the 1DU; the bottom row shows a structure at the starting of core C-burning, i.e. after the 1DU. Left – PARSEC output without EOvershooting; Right – same as Left, but with EOvershooting incorporated.

namely NEWκ seems to increase (of about than 1%) the mass of the He core; this effect is present also in the non rotating-models. We see that the evolution during shell H-burning is indeed similar to the non-rotating models' one, but with consistently higher luminosities.

III. HE-BURNING

The Blue Loop shows good agreement in the prescriptions, with a difference of 9% in $\tau_{\rm He}$, see Tab.(4.3); also, the Blue loop seems a bit more extended in the OLDκ case, with redder core H-burning ignition and depletion points. In both cases, core He-burning starts when the star is still a BSG, at a slightly higher $T_{\rm eff}$ for NEWκ. The key evolutionary parameters, $M_{\rm CO}$ and the central $^{12}C/^{16}O$, are, at this stage, determined, and we found for them (in the case without EOv):

$$M_{\rm CO}^{\rm NEW\kappa} = 2.061\ M_\odot < M_{\rm CO}^{\rm OLD\kappa} = 2.165\ M_\odot\ ,$$

$$^{12}C/^{16}O_{\rm NEW\kappa} = 0.66 \gtrsim\ ^{12}C/^{16}O_{\rm OLD\kappa} = 0.64\ .$$

- A lower $M_{\rm CO}$ implies a lesser compact structure in the most advanced stages, which could result in favoring successful explosions by virtue of the lower *bounce compactness parameter* $\xi_{2.5}$.
- Since $^{12}C/^{16}O$ regulates the fuel for all the advanced stages of evolution; a higher $^{12}C \nearrow$ in the core usually favors less compact structures as well, which has a combined effect with $M_{\rm CO} \searrow$.

These two effects are enhanced, in these rotating models, with respect to the $v_{\rm rot}/v_{\rm crit} = 0$ case, as expected by the additional rotation-driven mixing; this holds for both **NEWκ** and **OLDκ**.

IV. SHELL HE-BURNING

The short lifetimes of the proceeding nuclear burning stages allow for a fair amount of He to burn inside the shell; this can be seen by the increase of $M_{\rm CO}$ in Fig.(4.3):

$$M_{\rm CO}^{\rm NEW\kappa} = 1.347\ M_\odot < M_{\rm CO}^{\rm OLD\kappa} = 1.670\ M_\odot\ .$$

We can see that the NEWκ CO core increases, during shell He-burning, by a 3%, while the OLDκ increases by a 4%.

The most prominent feature of these subsequent stages is the very pronounced ***red-ward evolution*** of both tracks; the NEWκ one arrives much further in the red, foretelling a development as a RSG along its Hayashi line, and a much larger expansion of the envelope. For these rotating models, this evolution is performed at much higher L.

V. ADVANCED BURNINGS

The run follows, for both models, the subsequent evolutionary stages at least till the core C-burning ignition. The position in the HR diagram remains mostly unchanged, due to the rapid evolution, after core C-burning. We can see that, after the expected ascending along their Hayashi lines, these stars are expected to explode as **RSGs**, however with consistently different surface properties:

$$\log \mathrm{T}_{\mathrm{eff}}^{\mathrm{NEW}\kappa} \simeq 3.47 \ll \log \mathrm{T}_{\mathrm{eff}}^{\mathrm{OLD}\kappa} \simeq 3.7\,,$$

with advanced spectral types as K and M, in the Morgan-Keenan system, for **OLD$\boldsymbol{\kappa}$** and **NEW$\boldsymbol{\kappa}$**, respectively.
We point out also that much less numerical difficulties were encountered by the solver, with respect to the $v_{\mathrm{rot}}/v_{\mathrm{crit}} = 0$ models; we did not need to relax the simulation's parameters to obtain convergence.

No appreciable differences can be highlighted between the EOv and no EOv models, so we are going to refer to both of them without being specific, unless otherwise needed.

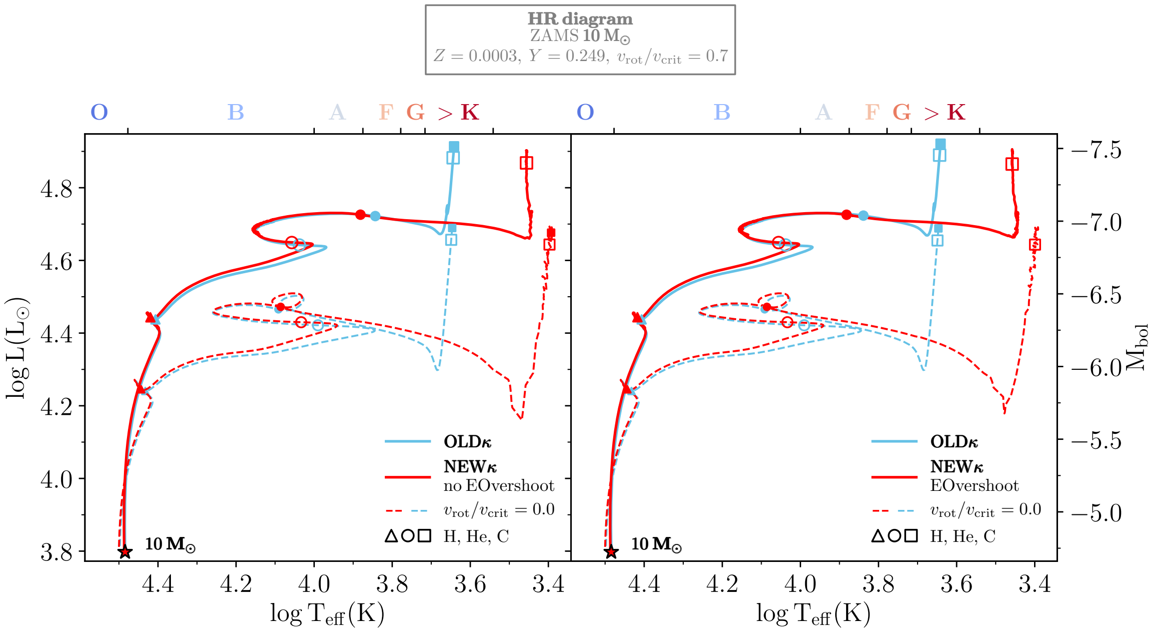

Figure 4.7: Comparative evolutionary tracks for a star with ZAMS mass M = 10 M$_\odot$, metallicity Z=0.0003 and rotation velocity $v_{\mathrm{rot}}/v_{\mathrm{crit}} = 0.7$, with the two prescriptions **NEW$\boldsymbol{\kappa}$** and **OLD$\boldsymbol{\kappa}$**; the usual convention for the symbols is employed, and spectral types are also highlighted. Left – PARSEC output without convective overshooting of the envelope (EOvershoot); Right – same as Left, but with EOvershooting incorporated.

Central ^{12}C/^{16}O evolution The evolution of the *central* ^{12}C/^{16}O essentially presents the same differences between **NEW**κ and **OLD$\boldsymbol{\kappa}$** as the non-rotating model. One can notice that even smaller ^{12}C/^{16}O is expected when rotation acts, and this confirms the effect of rotation-driven mixing.

Kippenhahn Diagram The *Kippenhahn diagram* for the M=10 M$_\odot$ and $v_{\mathrm{rot}}/v_{\mathrm{crit}} = 0.7$ is shown in Fig.(4.8). With respect to the non-rotating model in Fig.(4.3), we can see the enhanced effect of the core overshooting, see $\mathrm{M}_{\mathrm{Schw}}^{\mathrm{COv}}$, due to additional rotational mixing. The

same agent determines a much more extended H-He discontinuity M_{H-He} and, most importantly, the consistently higher M_{He} and M_{CO}, destined to produce more compact structures at pre SN stage.
Mostly the same differences between **NEWκ** and **OLDκ** as the previous section Sec.(4.3.1) are encoutered, with a relative M_{CO} difference of 5%.

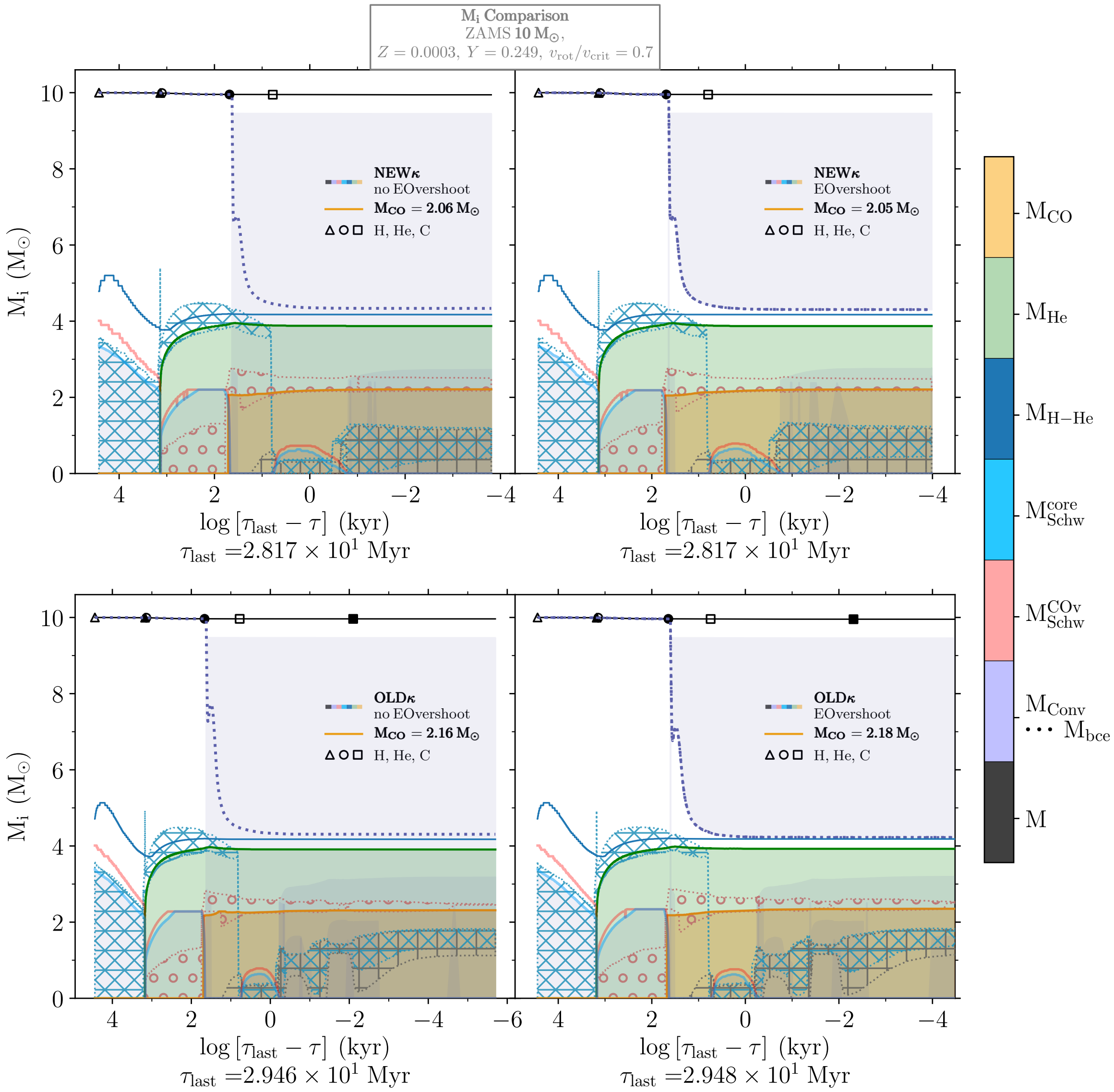

Figure 4.8: Comparative stratification history for a star with ZAMS mass M = 10 $M_\odot$, metallicity Z=0.0003 and rotation velocity v_{rot}/v_{crit} = 0.7, with the two prescriptions **NEW**κ and **OLDκ**; the usual convention for the symbols is employed, as well as same mass coordinates highlighted in Fig.(4.3). The usual constant shift of coordinate time τ_{last}, different for OLDκ (not reported) and NEWκ, is reported below x-axis. Left – PARSEC output without EOvershooting; Right – same as Left, but with EOvershooting incorporated.

$\log T_c - \log \rho_c$ The evolution through the $\log \mathrm{T}_c - \log \rho_c$ is shown in Fig.(4.4), together with its non-rotating counterpart. No appreciable differences between OLDκ and NEWκ are visible, though probably more advanced stages in NEWκ could reveal some deviations, the EOv model suggests. Indeed rotation modifies the $\log \mathrm{T_c} - \log \rho_\mathrm{c}$ locus: all models develop mainly in the ideal gas region, the $v_\mathrm{rot}/v_\mathrm{crit} = 0$ one extending further towards degenerate regions. Notably, for the rotating models the C-burning is ignited at mostly the same core temperature $\mathrm{T_c}$ and density ρ_c in the **NEW$\boldsymbol{\kappa}$**, as a contrast with its non-rotating version.

Surface Abundances $\log \mathbf{X}_i$ The two prescriptions NEWκ and OLDκ do not show any apparent difference in the (logarithmic) *surface abundances* $\log \mathrm{X_i}$. The H mass fraction never drops down below the limiting case of $\log \mathrm{H} = 0.4$, so even in this case a WR object is not created. A dredge up happens, during shell He-burning, in both models, lifting some N and modifying the C surface content slightly:

Before 1DU	$\log^{14}\mathrm{N} \simeq -4.1$	$\log^{12}\mathrm{C} \simeq -4.7$	$\log^{16}\mathrm{O} \simeq -4$
After 1DU	$\log^{14}\mathrm{N} \simeq -3.8$	$\log^{12}\mathrm{C} \simeq -5$	$\log^{16}\mathrm{O} \simeq -4.2$

and these are common values to both **OLD$\boldsymbol{\kappa}$** and **NEW$\boldsymbol{\kappa}$**; we see that indeed the CNO cycle products are being mixed. However, for this rotating case we can notice the effects of the additional mixing agents (rotation, angular momentum transport, see Sec.(1.3.4)), which effectively act during the MS and He-burning, prior to the 1DU.

Mass loss rate $\dot{\mathbf{M}}$ evolution The evolution of the *mass loss rate* $\dot{\mathrm{M}}$ for the rotating M=10M$_\odot$ is shown in Fig.(4.5) together with its non-rotating counterpart. We see that, throughout all of its life of almost 28 Myr, the star loses a small amount of mass, namely less than 1%, which is nevertheless much higher than for the $v_\mathrm{rot}/v_\mathrm{crit} = 0$ case. More precisely,

NEW$\boldsymbol{\kappa}$	$\log \dot{\mathrm{M}} \simeq -6.1$	$\mathrm{M}_{\mathrm{C_{start}}}^{\mathrm{NEW}\kappa} = 9.964\,\mathrm{M}_\odot$
OLDκ	$\log \dot{\mathrm{M}} \simeq -7.1$	$\mathrm{M}_{\mathrm{C_{start}}}^{\mathrm{OLD}\kappa} = 9.947\,\mathrm{M}_\odot$

holding for just no EOv, see Fig.(4.5). Such slightly higher $\dot{\mathrm{M}}$ are of course due to the rotational velocity. We also see that both no EOv and EOv, at the most advanced phases, reach very high values of $\dot{\mathrm{M}}$, and the tendency of higher $\dot{\mathrm{M}}$ for **NEW$\boldsymbol{\kappa}$** is still present, in a smaller measure, until the last comparable stages.

First Dredge Up 1DU We are lastly going to comment on the *first Dredge Up* 1DU for the rotating M=10 M$_\odot$ model. We can see the evolution of the logarithmic ratio C/O by looking at Fig.(4.9), where we compare two structures, respectively caught near the end of He-burning and the start of C-burning; the 1DU is expected to occur in between these two stages. The differences between **NEW$\boldsymbol{\kappa}$** and **OLD$\boldsymbol{\kappa}$** can be explained in the same terms of the previous section, Sec.(4.3.1). We can however add that

- The **atmospheric opacity** has already rise above 0 at the end of He-burning for the rotating models, with a consistent difference between OLDκ and NEWκ; this is due to the fact that rotational mixing modifies the surface abundances prior to the core He-burning stage, adding some metals to the atmosphere already.

4.3.3 60 $M_\odot$, $v_{rot}/v_{crit} = 0.0$

Evolutionary Track Some relevant results of the models are presented in Tab.(4.2). We proceed our discussion with M=60 $M_\odot$ by commenting on the *evolutionary track*, which can be seen in Fig.(4.10). With this high mass, we can expect to observe some effects of $\dot{M}$, regardless of the small metallicity.

60 $M_\odot$		τ_{MS}	$\tau_{H\text{-shell}}$	τ_{He}	M_{He}	M_{CO}	$^{12}C/^{16}O$
no EOv	**OLDκ**	3.469 Myr	16.0 kyr	0.28 Myr	27.609 $M_\odot$	24.624 $M_\odot$	0.237
	NEWκ	3.338 Myr	15.3 kyr	0.27 Myr	27.890 $M_\odot$	24.607 $M_\odot$	0.239
EOv	**OLDκ**	3.469 Myr	16.0 kyr	0.28 Myr	27.609 $M_\odot$	24.624 $M_\odot$	0.237
	NEWκ	3.338 Myr	15.3 kyr	0.27 Myr	27.890 $M_\odot$	24.607 $M_\odot$	0.239

Table 4.4: 60 $M_\odot$ characteristics from PARSEC with prescriptions **OLDκ** and **NEWκ**. The fraction $^{12}C/^{16}O$ is referred to the stage of the end of He-burning; the M_{He} refers to the end of shell H-burning, while the M_{CO} value refers to the end of He-burning.

I. H-BURNING

The core H-burning phase shows an excellent agreement in the two prescriptions, with just a slight difference of 4% in τ_{MS}, see Tab.(4.4). This is indeed expected, since the (logarithmic) abundances of C, N, O all remain below 2×10^{-4} throughout the structure till the end of H-burning.

II. SHELL H-BURNING

The shell H-burning phase shows a 5% fluctuation in $\tau_{H-shell}$, see Tab.(4.4), with the **NEWκ** being shorter than **OLDκ**. The star evolves towards the red, no Blue Loop is performed, and a redder track from **NEWκ** can be seen: in the core, C and O are indeed rising above 10^{-3}.

At the end of shell H-burning, the He-core mass M_{He} has the following differences:

$$M_{He}^{NEW\kappa} = 27.890\ M_\odot \gtrsim M_{He}^{OLD\kappa} = 27.609\ M_\odot\ ,$$

In this case, NEWκ seems to increase (of about 1%) the mass of the He core.

III. HE-BURNING

Core He-burning is ignited at a slightly cooler T, and this phase, lasting τ_{He}, shows just a difference of 4% in the two prescriptions, see Tab.(4.4). Core He-burning starts when the star is still a BSG. The key evolutionary parameters, M_{CO} and the central

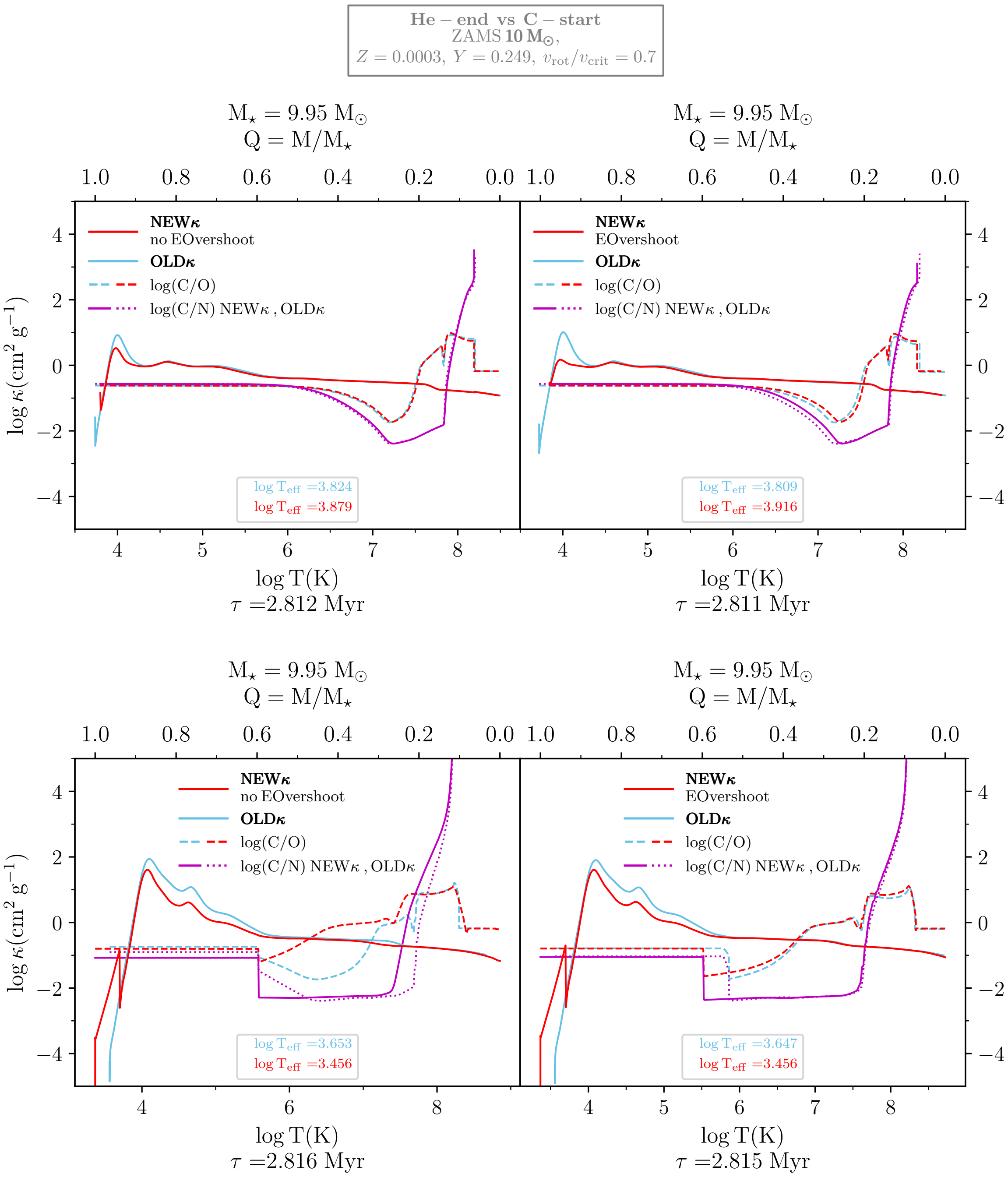

Figure 4.9: Comparative structure $\log\kappa - \log\mathrm{T}$ for a star with ZAMS mass M=10 $\mathrm{M}_\odot$, metallicity Z=0.0003 and rotation velocity $v_{\rm rot}/v_{\rm crit} = 0.7$, with the two prescriptions **NEWκ** and **OLDκ**. The logarithmic abundance ratio C/O and C/N are also shown. The same notation as in Fig.(4.6) is employed. Left – PARSEC output without EOvershooting; Right – same as Left, but with EOvershooting incorporated.

$^{12}\mathrm{C}/^{16}\mathrm{O}$, are, at this stage, determined, and we found for them (in the case with EOv):

$$\mathrm{M}_{\rm CO}^{\rm NEW\kappa} = 24.607\ \mathrm{M}_\odot \lesssim \mathrm{M}_{\rm CO}^{\rm OLD\kappa} = 24.624\ \mathrm{M}_\odot\ ,$$

$$^{12}\mathrm{C}/^{16}\mathrm{O}_{\mathrm{NEW}\kappa} = 0.239 \gtrsim {}^{12}\mathrm{C}/^{16}\mathrm{O}_{\mathrm{OLD}\kappa} = 0.237\ .$$

- A lower $\mathrm{M_{CO}}$ implies a lesser compact structure in the most advanced stages, which could result in favoring successfull explosions by virtue of the lower *bounce compactness parameter* $\xi_{2.5}$.
- Since $^{12}\mathrm{C}/^{16}\mathrm{O}$ regulates the fuel for all the advanced stages of evolution; a higher $^{12}\mathrm{C} \nearrow$ in the core usually favors less compact structures as well, which has a combined effect with $\mathrm{M_{CO}} \searrow$.

IV. **Shell He-burning**
The short lifetimes of the proceeding nuclear burning stages allow for an approximately negligible amount of He to burn inside the shell; this can be seen by the very slight increase of $\mathrm{M_{CO}}$ in Fig.(4.11):

$$\mathrm{M_{CO}^{NEW\kappa}} = 24.607\,\mathrm{M_\odot} < \mathrm{M_{CO}^{OLD\kappa}} = 24.624\,\mathrm{M_\odot}\ .$$

We can see that the NEWκ and OLDκ CO cores are essentially unvaried.
The most prominent feature of this stage is the very pronounced ***redward evolution*** of both tracks; the NEWκ one arrives much further in the red, foretelling a development as a RSG along its Hayashi line, and a much larger expansion of the envelope.

V. **Advanced Burnings**
The run follows, for both models, the subsequent evolutionary stages up till the core O-burning ignition. The position in the HR diagram remains mostly unchanged, due to the rapid evolution after core C-burning. We can see that these stars are expected to explode as **RSGs**, however with consistently different surface properties:

$$\log \mathrm{T_{eff}^{NEW\kappa}} \simeq 3.55 \ll \log \mathrm{T_{eff}^{OLD\kappa}} \simeq 3.72\ ,$$

with advanced spectral types as K and M, in the Morgan-Keenan system, for **OLDκ** and **NEWκ**, respectively. This is in spite of the predicted limiting case $\mathrm{M} \gtrsim 30\,\mathrm{M_\odot}$ to explode as BSG, due to the low $\dot{\mathrm{M}}$.
We point out also that the solver did not encounter numerical difficulties in following the structure evolution until core O-burning stage.

No appreciable differences can be highlighted between the EOv and no EOv models, so we are going to refer to both of them without being specific, unless otherwise needed.

Central $^{12}\mathrm{C}/^{16}\mathrm{O}$ evolution The evolution of the *central* $^{12}\mathrm{C}/^{16}\mathrm{O}$ with NEWκ and OLDκ is not appreciably different, a part from some slight fluctuations in the models after the start of core O-burning. These are indeed difficult to compute for PARSEC, and numerical deviations are expected. The characteristic lowering of the ratio in the core, after the core C-burning start, is of course experienced by both models.

Kippenhahn Diagram The *Kippenhahn diagram* for these models is presented in Fig.(4.11). We can indeed see the reduction of the convective core, created by the high energy flux of

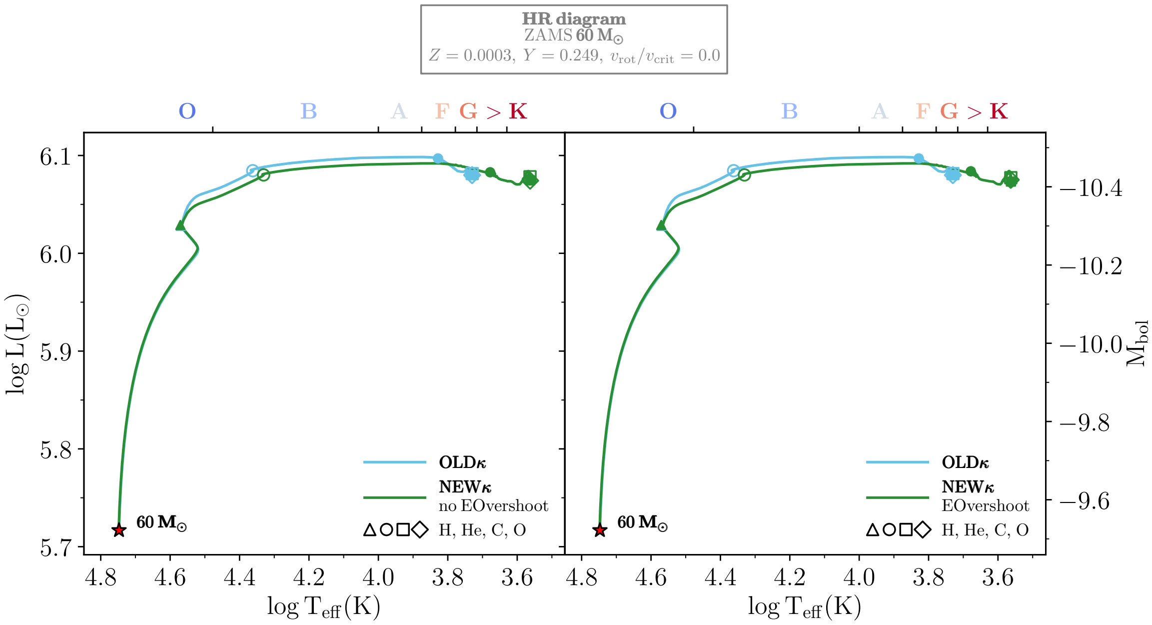

Figure 4.10: Comparative evolutionary tracks for a star with ZAMS mass $M = 60\ M_\odot$, metallicity Z=0.0003 and rotation velocity $v_{\rm rot}/v_{\rm crit} = 0$, with the two prescriptions **NEWκ** and **OLDκ**; the usual convention for the symbols is employed, and spectral types are also highlighted. Left – PARSEC output without convective overshooting of the envelope (EOvershoot); Right – same as Left, but with EOvershooting incorporated. Differences between the EOv and no EOv are completely negligible, while differences between NEWκ and OLDκ are highlighted in text.

the CNO cycle, as the H-burning proceeds; the core He-burning, instead, is characterized by the expected increase of the convective core, at least until the central He mass fraction drops below ~ 0.5, see $M_{\rm Schw}$. A convective pocket in the $M_{\rm CO}$ is also predicted, during core C-burning, in all models, as well as the convective pocket in the $M_{\rm CO}$ during core O-burning.

A slight mass loss is experienced by this model throughout all of its life of almost 4 Myr, as one can see by looking at Fig.(4.11): only 2% of its mass is lost at the end of the PARSEC run. The most prominent features of **NEWκ** and **OLDκ** prescriptions are

- A ***deeper penetration*** of the bottom of the convective envelope, see $M_{\rm bce}$, is present for the NEWκ models, both for EOv and no EOv, after the end of core He-burning; this can be motivated by the much higher atmospheric opacities, see below. However, the penetration is not that deep to mix the C-burning products up on the surface.
- A ***convective tongue*** is developed by both OLDκ and NEWκ, allowing for a first dredge up of CNO processed material, see below.

We can lastly notice that the H-burning shell is completely shut-down after the core He depletion: this is caused by the encountering with the He-H discontinuity (see $M_{\rm H-He}$),

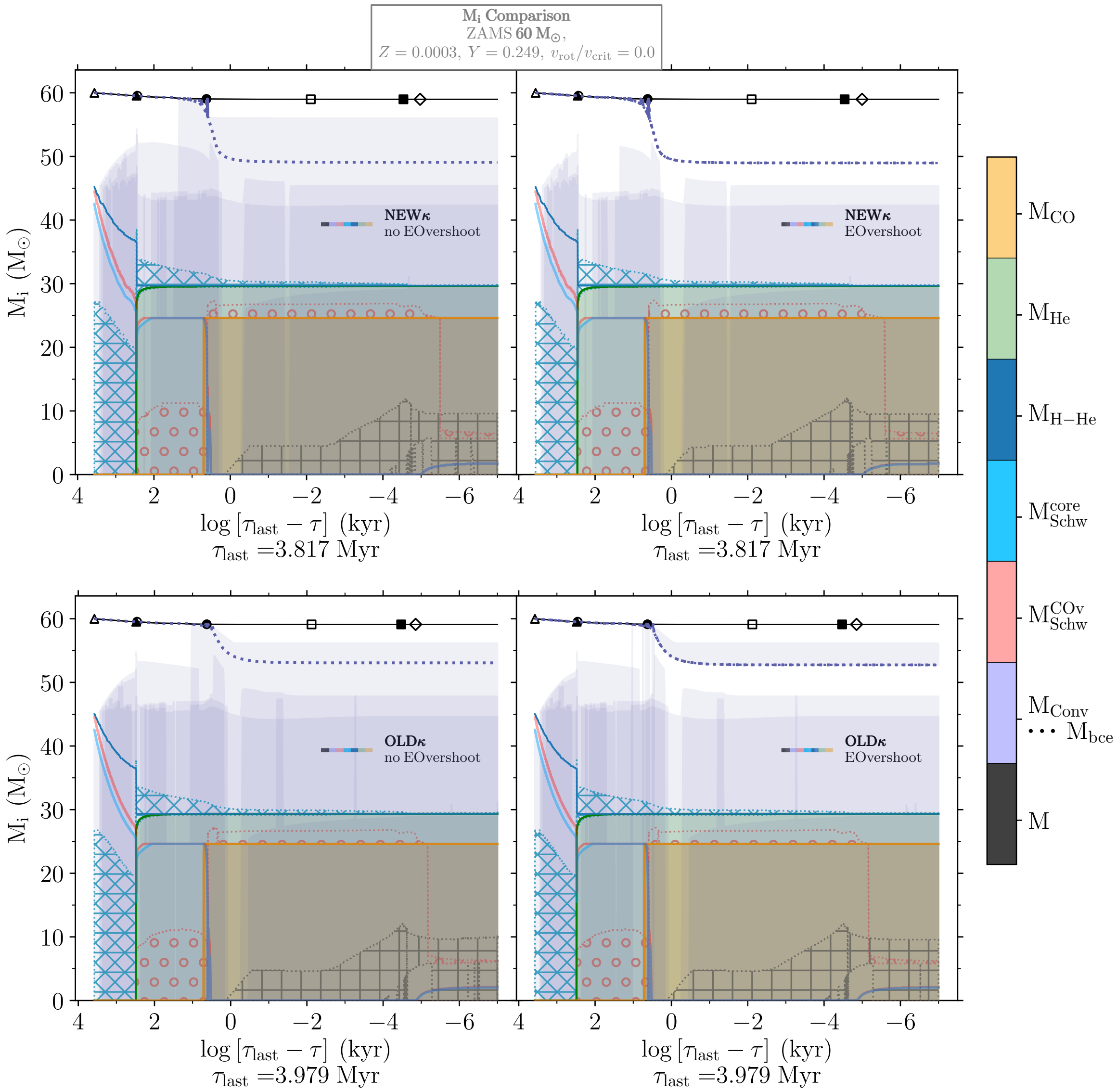

Figure 4.11: Comparative stratification history for a star with ZAMS mass M = 60 $M_\odot$, metallicity Z=0.0003 and rotation velocity $v_{rot}/v_{crit} = 0.0$, with the two prescriptions **NEWκ** and **OLDκ**; the usual convention for the symbols is employed, as well as same mass coordinates highlighted in Fig.(4.3). The usual constant shift of coordinate time τ_{last}, different for OLDκ (not reported) and NEWκ, is reported below x-axis. Left – PARSEC output without EOvershooting; Right – same as Left, but with EOvershooting incorporated.

and is expected to cause relevant effects on the onion-skin structure of the pre-SN stage; also, this prevents our M=60 $M_\odot$ star to undergo *thermal pulses*.

$\log T_c - \log \rho_c$ The evolution through the $\log T_c - \log \rho_c$ shows no appreciable differences between OLDκ and NEWκ. Both models develop mainly in the ideal gas region, as expected; a pronounced homologous trend is maintained throughout all stages until core C-burning end.

Surface Abundances log X_i Due to the quite weak $\dot{M}$ (see below and Fig.(4.13)) the star does not show any apparent difference in the (logarithmic) *surface abundances* $\log X_i$ of H and He; as concerns elements heavier than He, slight differences can be noticed after the core He-burning end, most prominently in the increase of ^{14}N. This latter fact hints at a 1DU in both models, and this needs some further investigation (see below and Fig.(4.14)). More precisely,

Before 1DU	$\log^{14}\mathrm{N} \simeq -4.82$	$\log^{12}\mathrm{C} \simeq -4.3$	$\log^{16}\mathrm{O} \simeq -3.86$
After 1DU	$\log^{14}\mathrm{N} \simeq -4.4$	$\log^{12}\mathrm{C} \simeq -4.4$	$\log^{16}\mathrm{O} \simeq -3.94$

and these are the values regarding **NEWκ** only; we see that indeed the CNO cycle products are being mixed. As concerns the **OLDκ**, no apparent dredge up in these most abundant metals is revealed, while minor modifications after 1DU pertain less abundant species, e.g. ^{13}C. Also, the H abundance never drops below the limiting case of logH=0.4, thus a WR object is not originated.

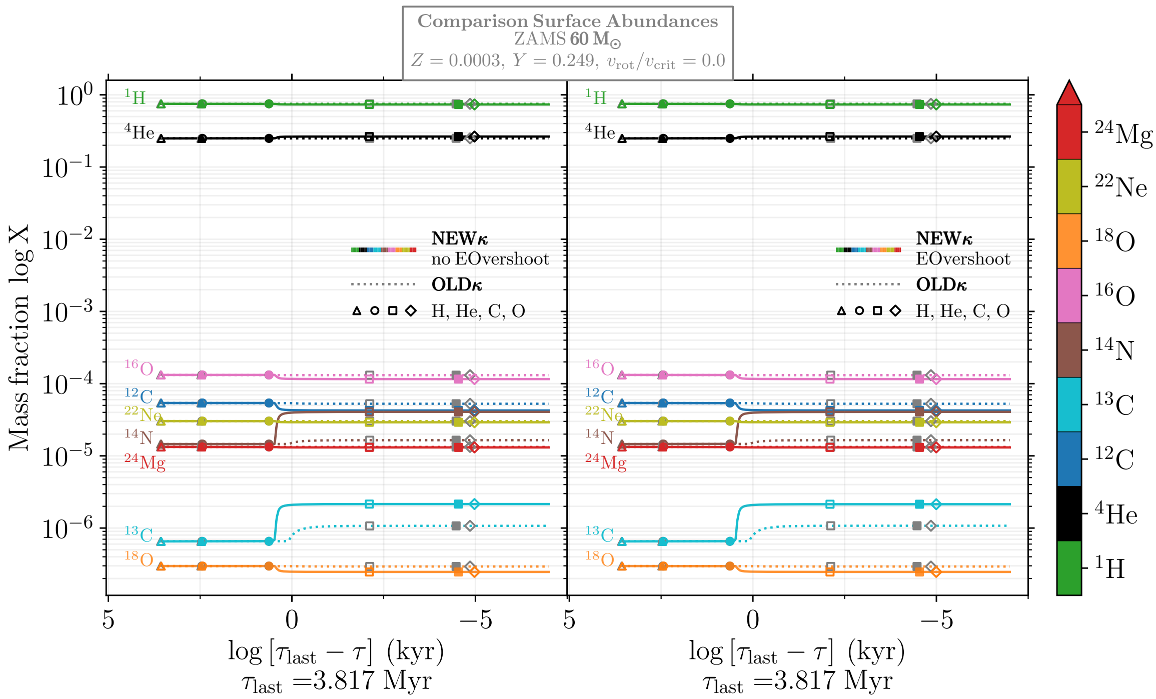

Figure 4.12: Comparative superficial (logarithmic) abundances $\log X_i$ history for a star with ZAMS mass $M = 60\ M_\odot$, metallicity Z=0.0003 and rotation velocity $v_{rot}/v_{crit} = 0.0$, with the two prescriptions **NEW**κ and **OLDκ**; the usual convention for the symbols is employed. The usual constant shift of coordinate time τ_{last}, different for OLDκ (not reported) and NEWκ, is reported below the x-axis. Left – PARSEC output without EOvershooting; Right – same as Left, but with EOvershooting incorporated.

Mass loss rate $\dot{M}$ evolution As already said above, this star loses about 2% of its mass throughout its life of almost 4 Myr, due to a non negligible *mass loss rate* $\dot{M}$. We recall that the $\dot{\mathrm{M}}$ prescription, in PARSEC, for RSGs with $\log \mathrm{T_{eff}} \lesssim 4.1$, is the de Jager's one, Eq.(1.12), which is expected to comprise all the complexities of powerful cool, *dust-driven winds*.

Fig.(4.13) indeed shows the evolution of $\dot{\mathrm{M}}$ through the subsequent phases of our models:

- The **Main Sequence** is in excellent agreement for OLDκ and NEWK, confirming what we can see in the HR diagram, Fig.(4.10); the MS $\dot{\mathrm{M}}$ is not very efficient, but nevertheless succeeds to remove a 1% of the total mass, due to the large timescale $\tau_{\mathrm{MS}} \simeq 3.338$ Myr, see Tab.(4.4).
  In any case, $\dot{\mathrm{M}}$ is not that strong to induce a reduction of the H convective core, see Fig.(4.11), which is expected in more massive (and Z$\nearrow$) models.
- The **He-burning** phase shows a systematically ***higher*** $\dot{\mathrm{M}}$ for the NEWκ model: this can be motivated by the redder $\mathrm{T_{eff}}$ of NEWκ. This stage succeeds in removing the remaining 1% of the total mass. We also notice that both NEWκ and OLDκ enter the dust-driven wind region of the HR diagram very late in the core He-burning stage: this prevents the $\dot{\mathrm{M}}$ to peel off more mass from the envelope and favor a blue evolution of both models.
  In any case, $\dot{\mathrm{M}}$ is not that strong to induce a reduction of the He convective core, see Fig.(4.11), which is expected in more massive (and Z $\nearrow$) models.
- Both models, in the **advanced stages**, share a $\log \dot{\mathrm{M}} \gtrsim -5.3$, but NEW$\kappa$ has a *much* stronger rate: again, the track is indeed much redder. We find:

NEWκ	$\log \dot{\mathrm{M}} \simeq -4.5$	$\mathrm{M}^{\mathrm{NEW}\kappa}_{\mathrm{O_{start}}} = 58.98\ \mathrm{M}_\odot$
OLDκ	$\log \dot{\mathrm{M}} \simeq -5.3$	$\mathrm{M}^{\mathrm{OLD}\kappa}_{\mathrm{O_{start}}} = 59.11\ \mathrm{M}_\odot$

  which holds for the start of O-burning, namely the last stage that is possible to compare in the two **NEWκ** and **OLDκ** prescriptions.
  We can also notice that both models, with excellent agreement, approach a high value of the ***Eddington parameter***, $\Gamma_{\mathrm{Edd}} \simeq 0.6$, see Eq.(1.14); this is indeed expected for such massive stars and it is always in correspondence of notable increases of $\dot{\mathrm{M}}$.

First Dredge Up 1DU Also in this case, we can catch a glimpse of the evolution of the logarithmic ratio C/O by looking at Fig.(4.14), where we compare two structures, respectively caught near the end of He-burning and the start of C-burning; the 1DU is expected to occur in between these two stages. We note that:

- The **atmospheric ratio C/N** is, at first, above 0.5, and after the 1DU it decreases to < 0 for the **NEWκ** case, while for **OLDκ** a mild decrease is only revelead, as one could have guessed by looking at Fig.(4.12).
- The **atmospheric ratio C/O** again remains always below 1: this confirms our star to be of an M spectral type, as we can see in Fig.(4.10), with an oxygen rich atmosphere. This key ratio always stays <1 during our computations.

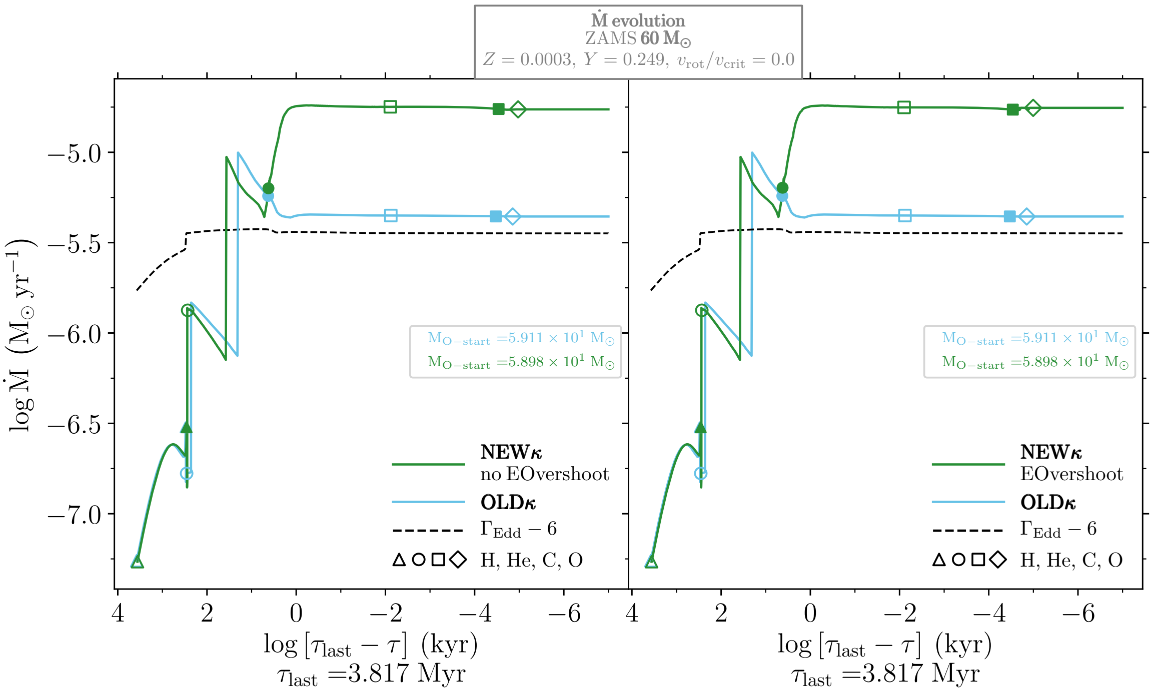

Figure 4.13: Comparative mass loss rate $\dot{\mathrm{M}}$ evolution for a star with ZAMS mass $\mathrm{M} = 60\ \mathrm{M}_\odot$, metallicity Z=0.0003 and rotation velocity $v_{\mathrm{rot}}/v_{\mathrm{crit}} = 0.0$, with the two prescriptions **NEW**κ and **OLD**$\boldsymbol{\kappa}$; the usual convention for the symbols is employed. The usual constant shift of coordinate time τ_{last}, different for OLDκ (not reported) and NEWκ, is reported below the x-axis; the value of the Eddington parameter Γ_{Edd}, shifted by -6 to let it appear in the plot, is shown for illustrative purposes, see text; lastly, the masses M_{O} at the end of the last comparable model (O-burning in this case) is printed too. Left – PARSEC output without EOvershooting; Right – same as Left, but with EOvershooting incorporated.

- **After the 1DU**, the opacities from NEWκ and OLDκ are similar, as for before the 1DU. The same difference in the atmospheric opacity as with the $\mathrm{M} = 10\mathrm{M}_\odot, v_{\mathrm{rot}}/v_{\mathrm{crit}} = 0$ model occurs here, but in a smaller measure: the NEWκ one is slightly higher, motivating thus the redder Hayashi line.
- The **NEW**$\boldsymbol{\kappa}$ **opacity** presents the same abrupt rise, in the atmospheric region, right before the H recombination and H^- opacity feature; in this case, we see this cusp event at the stage of core He-depletion, which should come with no surprise due to the red incursion of our $60\ \mathrm{M}_\odot$ star in the HR diagram, Fig.(4.10). The feature can be explained by the same arguments as the ones for the M=10 $\mathrm{M}_\odot$, non-rotating model.

4.3.4 140 $\mathbf{M}_\odot, \boldsymbol{v}_{\mathbf{rot}}/\boldsymbol{v}_{\mathbf{crit}} = 0.0$

Evolutionary Track Some relevant results of the models are presented in Tab.(4.2). We finish our discussion with the test case M=140 $\mathrm{M}_\odot$, whose *evolutionary track* can be seen

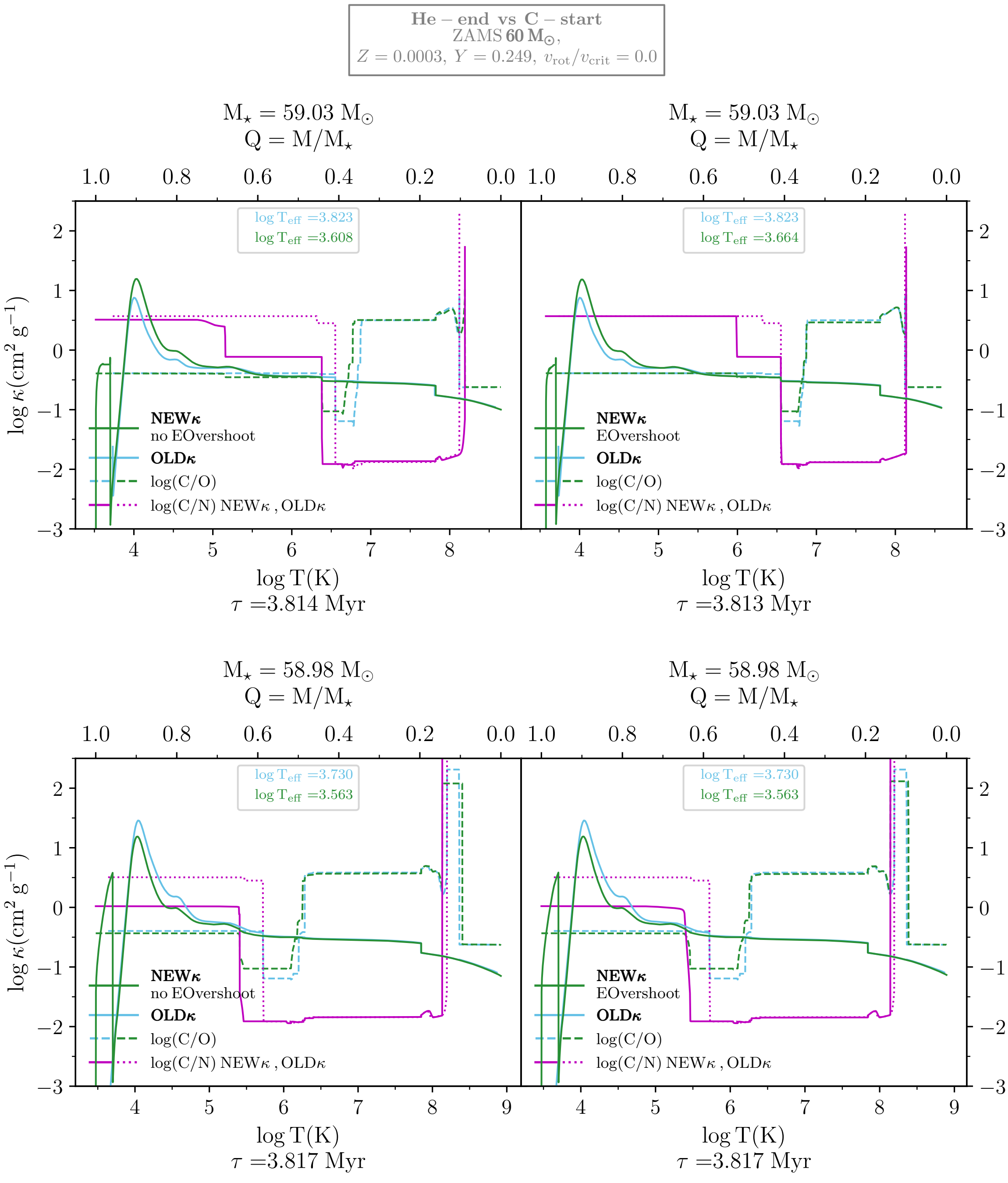

Figure 4.14: Comparative structure $\log\kappa - \log T$ for a star with ZAMS mass M=60 $M_\odot$, metallicity Z=0.0003 and rotation velocity $v_{rot}/v_{crit} = 0$, with the two prescriptions **NEWκ** and **OLDκ**. The logarithmic abundance ratio C/O is also shown, and the same conventions as in Fig.(4.6) are employed. Left – PARSEC output without EOvershooting; Right – same as Left, but with EOvershooting incorporated.

in Fig.(4.15). Even here, we can expect to observe some effects of $\dot{M}$, regardless of the small metallicity.

140 $M_\odot$		τ_{MS}	$\tau_{H\text{-shell}}$	τ_{He}	M_{He}	M_{CO}	$^{12}C/^{16}O$
no EOv	**OLDκ**	2.340 Myr	11.9 kyr	0.196 Myr	75.103 $M_\odot$	71.817 $M_\odot$	0.62
	NEWκ	2.340 Myr	11.8 kyr	0.216 Myr	75.033 $M_\odot$	69.945 $M_\odot$	0.13
EOv	**OLDκ**	2.340 Myr	11.9 kyr	0.216 Myr	75.103 $M_\odot$	46.074 $M_\odot$	0.67
	NEWκ	2.340 Myr	12.3 kyr	0.225 Myr	75.033 $M_\odot$	62.704 $M_\odot$	0.13

Table 4.5: 140 $M_\odot$ characteristics from PARSEC with prescriptions **OLDκ** and **NEWκ**. The fraction $^{12}C/^{16}O$ is referred to the stage of the end of He-burning; the M_{He} refers to the end of shell H-burning, while the M_{CO} value refers to the end of He-burning.

I. H-BURNING

The core H-burning phase shows an excellent agreement in the two prescriptions, with just no apparent difference in τ_{MS}, see Tab.(4.5). This is indeed expected, since the (logarithmic) abundances of C, N, O all remain below 2×10^{-4} throughout the structure till the end of H-burning. We can lastly notice a fairly hotter *blue hook* as the MS ends in the usual contraction.

II. SHELL H-BURNING

The shell H-burning phase shows a maximum of 3% fluctuation in $\tau_{H-shell}$, see Tab.(4.5), with the **NEWκ** being longer than **OLDκ**. The star evolves towards the red, no Blue Loop is performed, and a redder track from **NEWκ** can be seen: in the core, C and O are indeed rising above 10^{-2}.

At the end of shell H-burning, the He-core mass M_{He} has the following differences:

$$M_{He}^{NEW\kappa} = 75.033\ M_\odot \lesssim M_{He}^{OLD\kappa} = 75.103\ M_\odot\ ,$$

In this case, NEWκ seems to decrease (of less than 1‰) the mass of the He core. We can see the prominency of the ***redward evolution*** of both tracks; the NEWκ one arrives much further in the red, foretelling the subsequent development as a RSG along its Hayashi line, and a much larger expansion of the envelope.

III. HE-BURNING

Core He-burning is ignited at a fairly cooler T, and this phase, lasting τ_{He}, shows a maximum difference of 9% in the two prescriptions, see Tab.(4.5). The key evolutionary parameters, M_{CO} and the central $^{12}C/^{16}O$, are, at this stage, determined, and we found for them:

no EOv	$M_{CO}^{NEW\kappa} = 69.945\ M_\odot < M_{CO}^{OLD\kappa} = 71.817\ M_\odot\ ,$ $^{12}C/^{16}O_{NEW\kappa} = 0.13 \ll {}^{12}C/^{16}O_{OLD\kappa} = 0.62\ ,$
EOv	$M_{CO}^{NEW\kappa} = 62.704\ M_\odot < M_{CO}^{OLD\kappa} = 46.074\ M_\odot\ ,$ $^{12}C/^{16}O_{NEW\kappa} = 0.13 \ll {}^{12}C/^{16}O_{OLD\kappa} = 0.67\ .$

Summarizing the key points,

- A lower M_{CO} implies a lesser compact structure in the most advanced stages, which could result in favoring successfull explosions by virtue of the lower *bounce compactness parameter* $\xi_{2.5}$.

- Since $^{12}C/^{16}O$ regulates the fuel for all the advanced stages of evolution; a higher $^{12}C \nearrow$ in the core usually favors less compact structures as well, which, in this case, has a counter-effect with respect to $M_{CO} \searrow$.

- Core He-burning starts when the star is already a RSG, forecasting the occurrence of a 1DU, see below. The tracks lift along the respective ***Hayashi line***, with ingent expansion of the envelopes, and NEWK maintain the higher redness with respecto to OLDκ.

★ A very extended **Blue Loop** is performed by the EOv NEWκ model, while on the contrary the EOv P83 one drops consistently in luminosity, at mostly constant T_{eff}, during core He-burning. This aspect is remarkable, since, usually, for such VMSs Blue Loops are not very extended, and observationally they are mostly suppressed (and, certainly, not that "blue") for $M \gtrsim 12\ M_\odot$. The new opacities are expected to exert a formidable influence in this phase, see below.

IV. SHELL HE-BURNING

While, till now (exception made for the Blue Loop), the EOv and no EOv models where fairly comparable, from towards the end of core He-burning on the two evolve very differently, for both **NEWκ** and **OLDκ**.

- **no EOv** The short lifetime of the shell He-burning allows for an approximately negligible amount of He to burn inside the shell for the case no EOv; this can be seen by the very slight increase of M_{CO} in Fig.(4.17—Left):

$$M_{CO}^{NEW\kappa} = 69.945\ M_\odot < M_{CO}^{OLD\kappa} = 71.817\ M_\odot\ .$$

  We can see that the NEWκ and OLDκ CO cores are essentially unvaried. The position in the HR diagram remains approximately the same in both prescriptions.

- **EOv** Despite the short lifetime of shell He-burning, the OLDκ track shows a peculiar (69%) reduction of $M_{CO}^{OLD\kappa}$ with respect to its value at core He-burning end, while the NEWK $M_{CO}^{NEW\kappa}$ value shows negligible variation:

$$M_{CO}^{NEW\kappa} = 62.704\ M_\odot \gg M_{CO}^{OLD\kappa} = 27.207\ M_\odot\ .$$

  This can be seen in Fig.(4.17—Right), and is motivated by an enhanced $\dot{M}$, see below. Both the OLDκ and NEWκ tracks start to show numerical difficulties of the solver, with ingent fluctuations; this can be connected to problems in following the deepening of the envelope base, see below.

V. ADVANCED BURNINGS The run follows, for both models, the subsequent evolutionary stages up till the core C-burning ignition for **NEWκ**, core O-burning for OLDκ.

▶ **no EOv** The position in the HR diagram remains mostly unchanged, due to the rapid evolution after core C-burning. We can see that these stars are expected to explode as **RSGs**, in spite of the predicted limiting case $\mathrm{M} \gtrsim 30\,\mathrm{M}_\odot$ to explode as BSG: this is due to the low $\dot{\mathrm{M}}$. We obtain, for the final M_{CO} at the end of the computations,

$$\mathrm{M}_{\mathrm{CO}}^{\mathrm{NEW}\kappa} = 69.945\,\mathrm{M}_\odot < \mathrm{M}_{\mathrm{CO}}^{\mathrm{OLD}\kappa} = 71.817\,\mathrm{M}_\odot\,,$$

namely they are essentially unvaried: is indeed motivated by the timescales. The Hayashi lines of the two models lie at fairly different temperatures, though similar luminosities:

$$\log \mathrm{T}_{\mathrm{eff}}^{\mathrm{NEW}\kappa} \simeq 3.7 \;<\; \log \mathrm{T}_{\mathrm{eff}}^{\mathrm{OLD}\kappa} \simeq 3.75\,,$$

with advanced spectral types as G and K, in the Morgan-Keenan system, for **OLD$\boldsymbol{\kappa}$** and **NEW$\boldsymbol{\kappa}$**, respectively.

▶ **EOv** The position in the HR diagram of both tracks evolves sparsely: the OLDκ seems to set into a new, hotter Hayashi line, and continue its evolution by climbing above it; the NEWκ, instead, finishes the very extended Blue Loop to the red. Both **NEW$\boldsymbol{\kappa}$** and **OLD$\boldsymbol{\kappa}$** are expected to explode as RSGs as well.

$$\mathrm{M}_{\mathrm{CO}}^{\mathrm{NEW}\kappa} = 62.724\,\mathrm{M}_\odot \gg \mathrm{M}_{\mathrm{CO}}^{\mathrm{OLD}\kappa} = 26.822\,\mathrm{M}_\odot\,,$$

namely the NEWκ has grown (slightly) its CO core, while OLDκ lost another 1% of its CO core mass due to $\dot{\mathrm{M}}$. Even though we can't properly speak of an Hayashi line for the EOv models, due to the quite sparse evolution, we can compare the start of core C-burning and recognize fairly different surface properties:

$$\log \mathrm{T}_{\mathrm{eff}}^{\mathrm{NEW}\kappa} \simeq 3.8 \;\ll\; \log \mathrm{T}_{\mathrm{eff}}^{\mathrm{OLD}\kappa} \simeq 3.99\,,$$

$$\log \mathrm{L}(\mathrm{L}_\odot)^{\mathrm{NEW}\kappa} \simeq 6.61 \;<\; \log \mathrm{L}(\mathrm{L}_\odot)^{\mathrm{OLD}\kappa} \simeq 6.65\,,$$

and advanced spectral types as A and F, in the Morgan-Keenan system, for **OLD$\boldsymbol{\kappa}$** and **NEW$\boldsymbol{\kappa}$**, respectively.

Central ^{12}C/^{16}O evolution The evolution of the *central* $^{12}\mathrm{C}/^{16}\mathrm{O}$ with NEWκ and OLDκ is appreciably different, as one can observe in Fig.(4.16).

- The ***MS and shell H-burning*** show good agreement for both no EOv and EOv, which agree in showing a lower (of about 30% in logarithmic scale) $^{12}\mathrm{C}/^{16}\mathrm{O}$ ratio for NEWκ, once the star sets towards the start of core He-burning;

- In ***He and shell He-burning***, the difference above is even enhanced, as highlighted in Tab.(4.5), whilst this ratio decreases due to $^{16}\mathrm{O} \nearrow$ in the core.
  The entity of the deviation between NEWκ and OLDκ in the $^{12}\mathrm{C}/^{16}\mathrm{O}$ is *dramatic*: its physical reason has to be individuated in the mixing properties of the structures

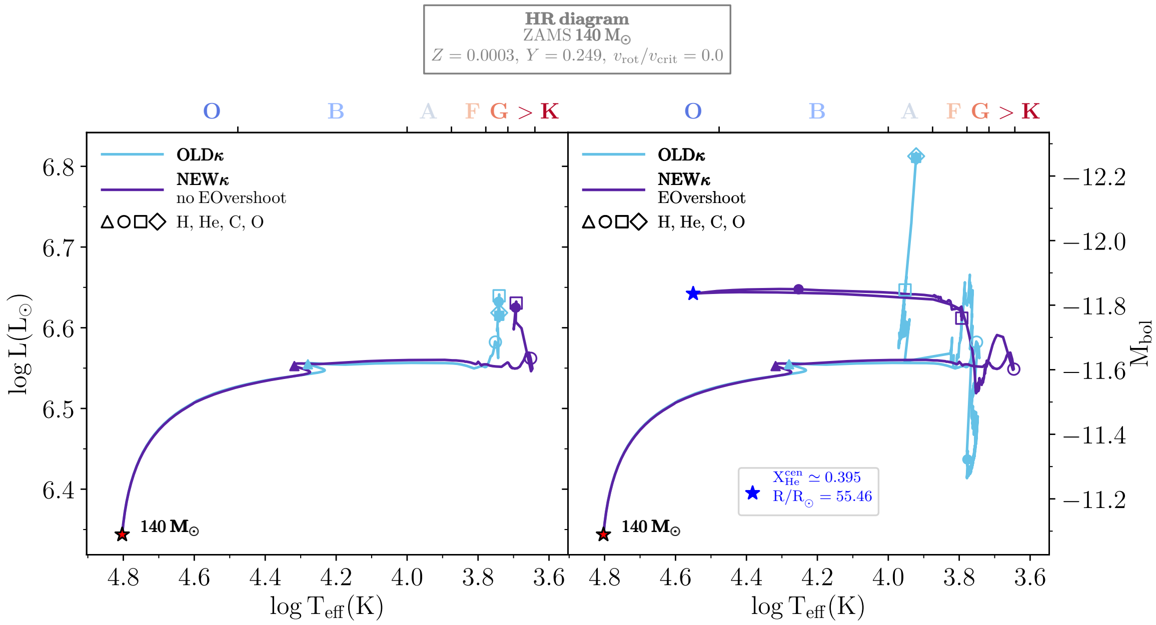

Figure 4.15: Comparative evolutionary tracks for a star with ZAMS mass $M = 140\ M_\odot$, metallicity Z=0.0003 and rotation velocity $v_{rot}/v_{crit} = 0$, with the two prescriptions **NEWκ** and **OLDκ**; the usual convention for the symbols is employed, and spectral types are also highlighted. The insert in the right panel highlights some features of the NEWκ track at the indicated point (blue star scatter point); this will be useful for the subsequent discussion about the *Blue Loop*. Left – PARSEC output without convective overshooting of the envelope (EOvershoot); Right – same as Left, but with EOvershooting incorporated.

solely, since the $^{12}C(\alpha,\gamma)^{16}O$ rate sensitivity to T_c (and ρ_c) has (mostly) nothing to do with that, as one can see in Fig.(4.18) and below.

In fact, we can give a simple motivation: since, during core He-burning (see below), our stars undergo a first dredge up, the quantity of fuel is determined by the chemical gradients, which tend to flatten during a dredge up. Our NEWκ model mixes the ^{16}O towards the core sensibly more (see Fig.(4.22), the ^{16}O line lowering more) in the dredge up: this provides the lower central $^{12}C/^{16}O$ which, at the depletion of He, persists. The mechanism occurs with even more strength in the EOv model, which in fact presents a higher (as 1%) deviation. So, why this enhanced mixing of our NEWκ models? The answer lies in the much cooler Hayashi lines: the structure becomes greatly dependent on the surface details, once convective envelopes arise, and a lower T_{eff} simply means larger convective envelopes. The EOv case is enhanced thanks to the convective overshooting itself!
This also motivates the longer durantion of the core He-burning phase, τ_{He}, highlighted in Tab.(4.5): the fuel is simply larger for NEWκ

- The ***advanced stages*** are determined by the ^{12}C abundance only, at least until O ignites in OLDκ; in this latter case, some numerical fluctuations are visible in both EOv and no EOv, with a seemingly higher depletion of ^{16}O in the no EOv case. We shall also remember that the last comparable phase between OLDκ and NEWκ is core C-burning start.

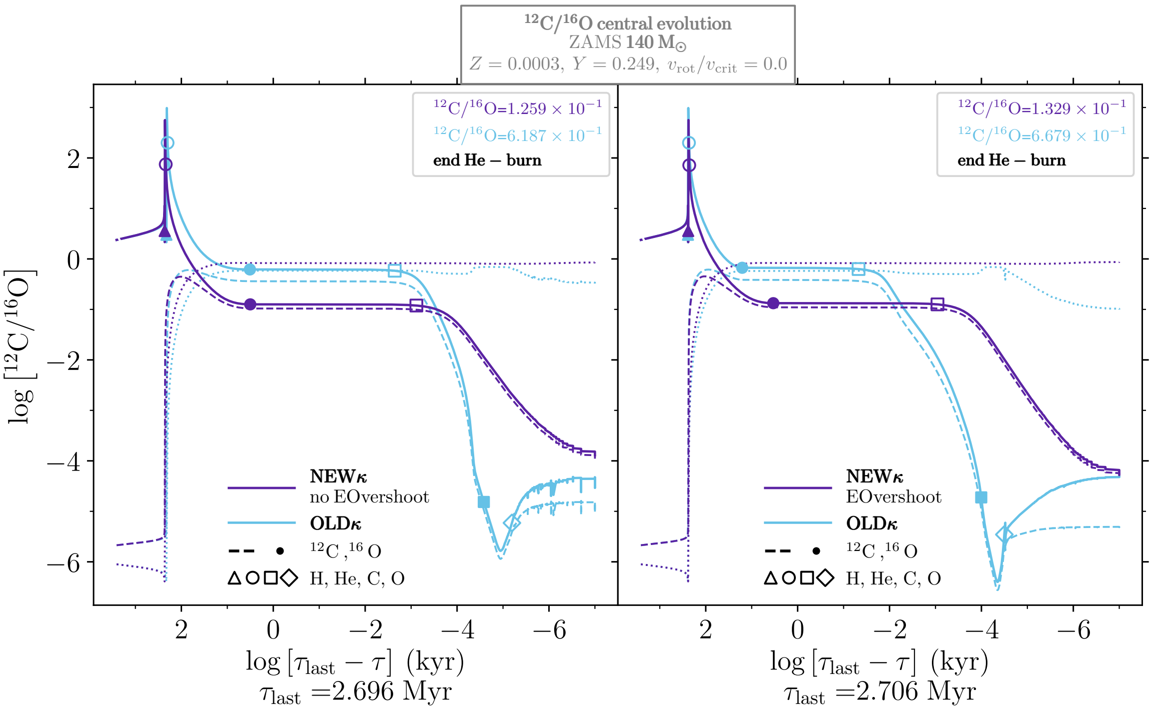

Figure 4.16: Comparative (logarithmic) central ratio $^{12}C/^{16}O$ evolution for a star with ZAMS mass M=140 $M_\odot$, metallicity $Z = 3 \times 10^{-4}$ and rotation velocity $v_{rot}/v_{crit} = 0$, with the two prescriptions **NEWκ** and **OLDκ**; the usual convention for the symbols is employed. Single evolution of the (logarithmic) central mass fractions ^{12}C and ^{16}O is also reported, with dashed and dotted linestyle respectively, as Fig.(4.2). Left – PARSEC output without EOvershooting; Right – same as Left, but with EOvershooting incorporated.

Kippenhahn Diagram An idea of the *structure evolution*, i.e. the evolution of some interesting mass coordinates M_i, is presented in Fig.(4.17). In both OLDκ and NEWKκ, the expected decrease of the convective core occurs during the MS. As concerns the subsequent stages, again, the cases no EOv and EOv deserve different comments:

- **NO EOV**

  Up till the end of core He-burning, OLDκ and NEWκ share the fairly the same stratification history: the standard core He-burning increase of the convective core is fairly evident, see M_{Schw} in Fig.(4.17), at least until the central He mass fraction drops below ~ 0.5. The most prominent differences in **NEWκ** and **OLDκ** are:

  a) The M_{CO} value at which NEWκ sets during shell He-burning, slightly lower than OLDκ's, with a 3% difference;

  b) Convective envelope's extension differs after core He depletion: this determines a more efficient mixing in the NEWκ, which explains the reduced central $^{12}C/^{16}O$ ratio.

c) Sensibly larger H- and He-burning shells for the NEWκ run: this can be motivated by a slightly higher opacity, in NEWκ, thanks to which the shells are well sustained.

- **EOv**
The excellent agreement of the two prescriptions, here, interrupts abruptly as the MS ends: the $\dot{\mathrm{M}}$ of OLDκ is much higher (see below and Fig.(4.23)); $\mathrm{M_{He}}$ decreases in both cases, but for OLDκ the reduction is drastic, and we know that this is due to a first dredge up event (see also below); the same does not hold for the $\mathrm{M_{CO}}$, which for NEWκ decreases slightly, while in OLDκ lower dramatically, as highlighted in Tab.(4.5). This last aspect hints at a *second dredge up*, we will investigate it further below.
We also see that there are some numerical difficulties in following a complicated evolution, up and down, of the ***bottom of the convective envelope***, see $\mathrm{M_{bce}}$, and this is true for both **NEWκ** and **OLDκ** during the first dredge up, i.e. right after core He-burning ignition, and for the P83 only in the case of the second dredge up, i.e. right after core He depletion.

  We can lastly notice that, in the OLDκ, the burning shells of He and H are not even recognizable, if even present, due to the deep penetration of the convective envelope, while this does not happen in the NEWκ model, though even here the H-burning shell is very thin (due to the proximity of the He-H discontinuity, see $\mathrm{M_{H-He}}$). These facts is expected to have a great impact on the final, ***onion-skin*** structure of the pre-SN stage. The narrowness of the H shell in principle does not prevent our M=140 $\mathrm{M_\odot}$ star to undergo *thermal pulses*, but we did not appreciated this phenomenon in the Kippenhahn diagram.

A convective pocket in the $\mathrm{M_{CO}}$ after core C-burning end is also predicted in both OLDκ models.

$\log \mathbf{T}_c - \log \rho_c$ The evolution through the $\log \mathrm{T}_c - \log \rho_c$ shows some appreciable differences between **OLDκ** and **NEWκ** only in the EOv case, as one can see in Fig.(4.18). Both models develop mainly in the ideal gas region, but the NEWκ ones are more slanted towards the radiation pressure region; a pronounced homologous trend is maintained throughout all stages until, approximately, core C-burning start.

We can give an explanation for the non-homologous behavior in the EOv case, Fig.(4.18 – Right), by looking at the Kippenhahn diagram in Fig.(4.17 – Right column) and at the structure plot of energy rates in Fig.(4.20 – Right). We shall add the following two arguments, which have a combined effect:

I. As we noted, during the shell He-burning, the NEWκ model has two active shells, well sustained by a ***large core*** which already started its C-burning (we stress that, in our calculations, we imposed a threshold of a diminishing fuel $\sim 5\%$ for the acknolodging of the start of a burning cycle); the OLDκ, instead, has a much narrower C-burning core, which needs to contract more (with respect to NEWκ, and to a quasi-homologous trend) to ignite core C-burning.

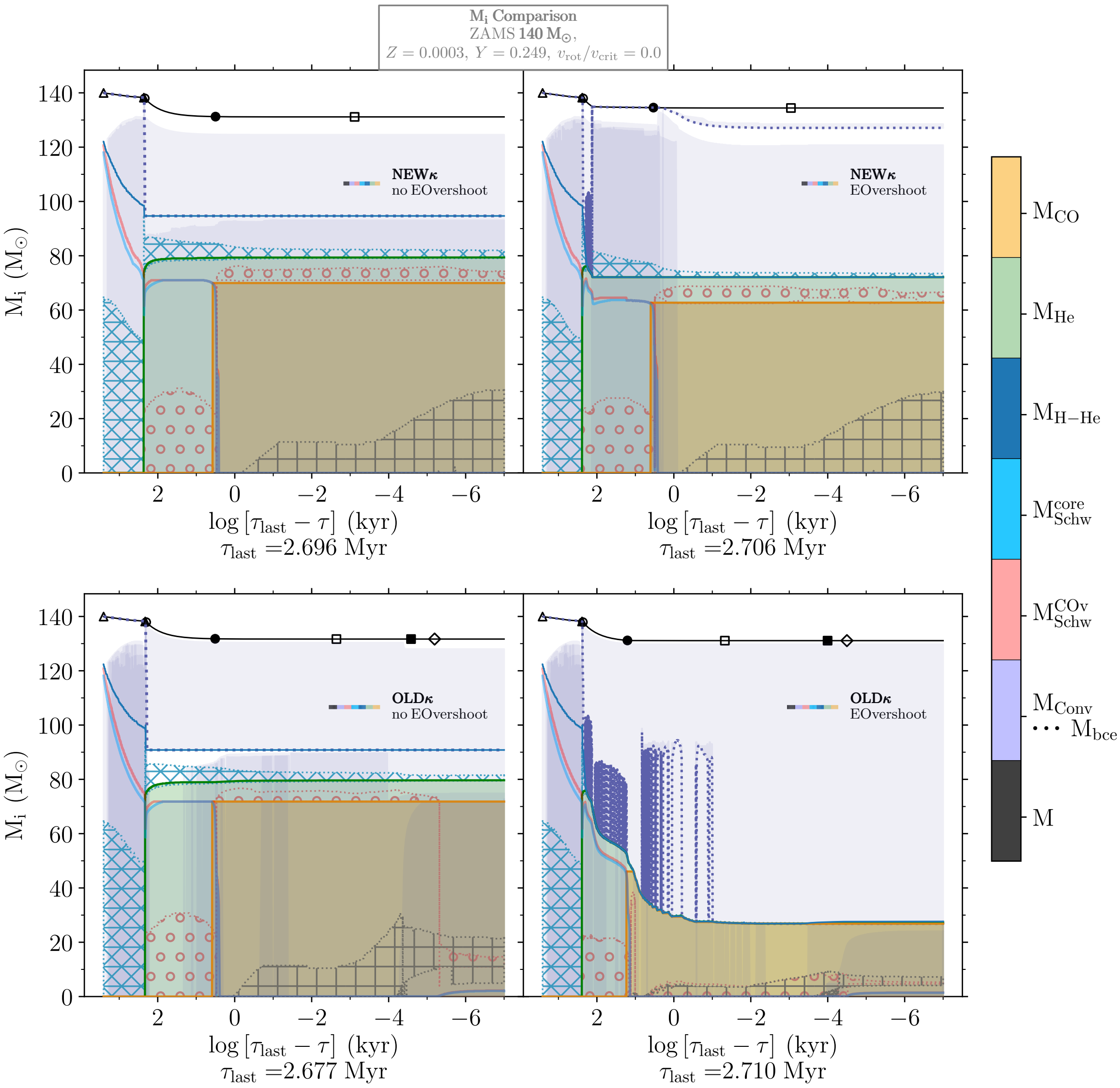

Figure 4.17: Comparative stratification history for a star with ZAMS mass $M = 140\,M_\odot$, metallicity Z=0.0003 and rotation velocity $v_{rot}/v_{crit} = 0.0$, with the two prescriptions **NEW**κ and **OLD**$\boldsymbol{\kappa}$; the usual convention for the symbols is employed, as well as same mass coordinates highlighted in Fig.(4.3). The usual constant shift of coordinate time τ_{last}, different for OLDκ (not reported) and NEWκ, is reported below x-axis. Left – PARSEC output without EOvershooting; Right – same as Left, but with EOvershooting incorporated.

II. As we can see in Fig.(4.20 – Right), at the start of core C-burning the ***neutrino losses*** are dramatic both in the NEWκ and OLDκ cases, but a order of magnitude larger for OLDκ in the core: this determines a larger net cooling for the latter model, enhancing the effect I.

After the start of core C-burning, the EOv OLDκ model seems to follow a quasi-homologous trend again, and the eventual other departures can be explained by the usual non-monotonic behaviors expected when new fuels are ignited and convective cores are formed.

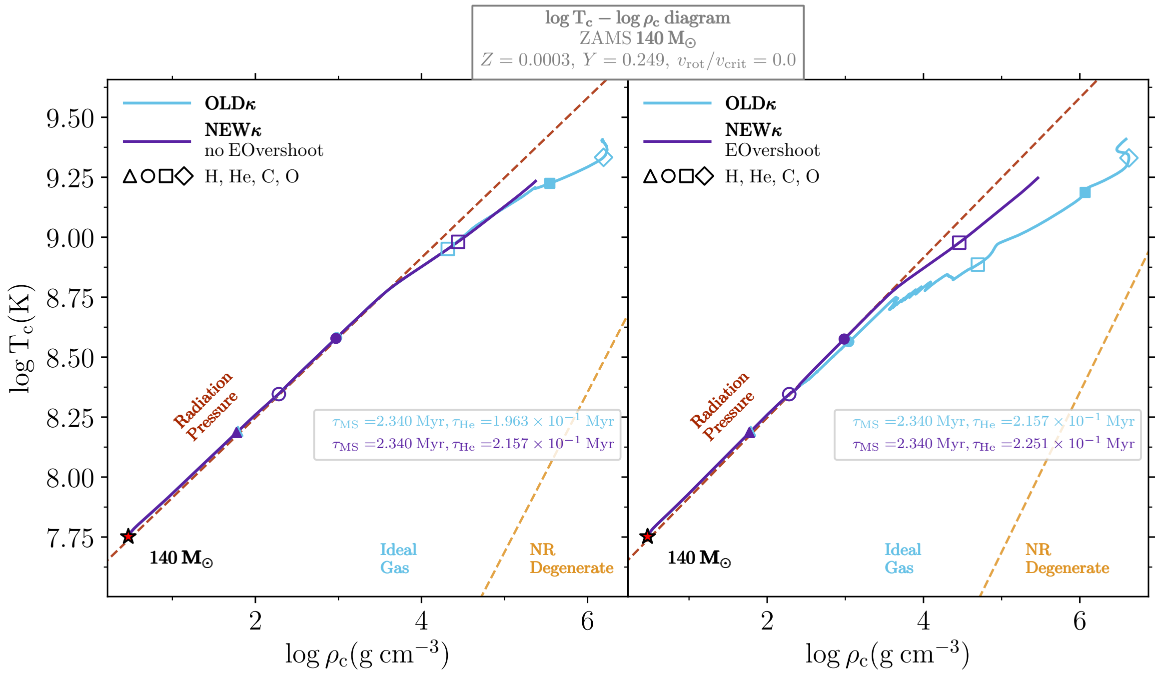

Figure 4.18: Comparative structure $\log T_c - \log \rho_c$ for a star with ZAMS mass $\mathrm{M} = 140\ \mathrm{M}_\odot$, metallicity Z=0.0003 and rotation velocity $v_{\mathrm{rot}}/v_{\mathrm{crit}} = 0$, with the two prescriptions **NEWκ** and **OLDκ**; the usual convention for the symbols is employed. Duration of core H and He burning, τ_{MS} and τ_{He} respectively, are also highlighted. Left – PARSEC output without EOvershooting; Right – same as Left, but with EOvershooting incorporated.

Radius evolution $\mathrm{R}/\mathrm{R}_\odot$ Fig.(4.19) shows the evolution of the stellar total radius $\mathrm{R}/\mathrm{R}_\odot$. We find this peculiarly interesting, since the models differ consistently, and this behavior is strictly connected to the surface properties (HR diagram, Fig.(4.15)) and allows us to enlight some stratification aspects (Kippenhahn diagram, Fig.(4.17)).

We see that the evolutive history of the stellar radius is quite standard, and in excellent agreement, from the MS to the core He-burning start, in both EOv and no EOv runs of the two prescriptions: to a quiet MS a drastic expansion follows during shell H-burning, until He is ignited in the core when the star, after a 1DU, has already ascended their respective Hayashi lines and is already a RGs. At the start of core He-burning, the evolution becomes quite different in EOv and no EOv cases.

- No EOv
  The stars set in the RGB, at the core He-burning start, with a quite different radius, the NEWκ being more expanded thanks to the cooler envelope. Right after, the NEWκ starts to contract due to the well known ***mirror principle***, but this contraction is slender (we stress that, in Fig.(4.19), the scale is not logarithmic!), corresponding to the brief phase in which the He-burning core is still growing (see Fig.(4.17 after the empty circle).
  Soon after, both NEWκ and OLDκ set in a fairly constant $\log \mathrm{T}_{\mathrm{eff}} - \log \mathrm{L}/\mathrm{L}_\odot$ position

in the HR diagram, which translates, in Fig.(4.19), in an unchanged plateaux for the stellar radius. The outer envelope has barely the time to respond to the core rapid changes, so this comes with no surprise.

- EOv
  The stars set in the RGB, at the core He-burning start, again with a quite different radius. Right after, the **NEWκ** model contracts drastically: as the 1DU occurs, the M_{He} is reduced (see Fig.(4.17) and Tab.(4.5)); the H-burning shell is suddenly quenched (see also below, Fig.(4.21), the L_H); the star performs the large Blue Loop (see also below) and changes its spectral type from K to O, the increase of T_{eff} being the final agent to shut down the dredge up; lastly, the star re-sets in the coolest part of the diagram, with the consequent (gentle) expansion due to its Hayashi line proximity and to the double-mirror of the two active burning shells, see Fig.(4.17).

  As for the **OLDκ**, the contraction after core He-burning start is not as dramatic: the star undergoes a very deep 1DU, which is able to quench the H-burning shell (see Fig.(4.21), the L_H).

  After the core He-depletion, the Kippenhahn diagram does not allow to appreciate the actual presence of a surviving, very thin H-burning shell, which is instead evident in Fig.(4.20 – Right): here, the energy generation rates ϵ of equation Eq.(1.2) are shown, and we can see a single peak in ϵ_{nuc} towards the stellar core. Thus, a ***single*** (not double, as for NEWκ) mirror effect acts, and the star expands as it ascends the RGB. Another contraction phase occurs (see the luminosity drop in Fig.(4.15)), as the star is setting towards the start of core C-burning, during which a *second dredge up* happens (see below): we see that the OLDκ sets, at core C-burning, with a much compact structure than the NEWκ one, see the envelope's gravo-thermal energy ϵ_{grav} in Fig.(4.20). Lastly, the ascension on a (slightly modified) RGB is characterized by a radius increase, as expected.

Integrated luminosities log L($L_\odot$) Since, in the later stages of the evolution of our EOv models, both NEWκ and OLDκ deviate consistently from their respective Hayashi line, we wanted to briefly comment also on the *integrated luminosities* L($L_\odot$) evolution in Fig.(4.21). For (almost) completely convective stars, in fact, it is well known that the total luminosity is practically *independent of their structure*, being sensitive just to the T_{eff}. This fact is indeed not true anymore when stars depart from their fully-convective locus in the HR diagram, as it happens to NEWκ in particular, during the Blue Loop.
Though quite difficult to an immediate interpretation, we have already noticed in Fig.(4.21) the quenching of H-burning shell due to the 1DU, which is expressed by a pronounced lowering of L_H; other prominent features are:

- The much higher **neutrino luminosity** for OLDκ, which we have already stressed to be partly responsible for a non-homologous trend in Fig.(4.18). Notice that the L_ν is reported with an absolute value, so it would be upside down in reality;

- The presence of a non-zero, and quite high though, **He luminosity**, developing in OLDκ a bit after the core C-burning start (i.e., after the stage of single H-burning

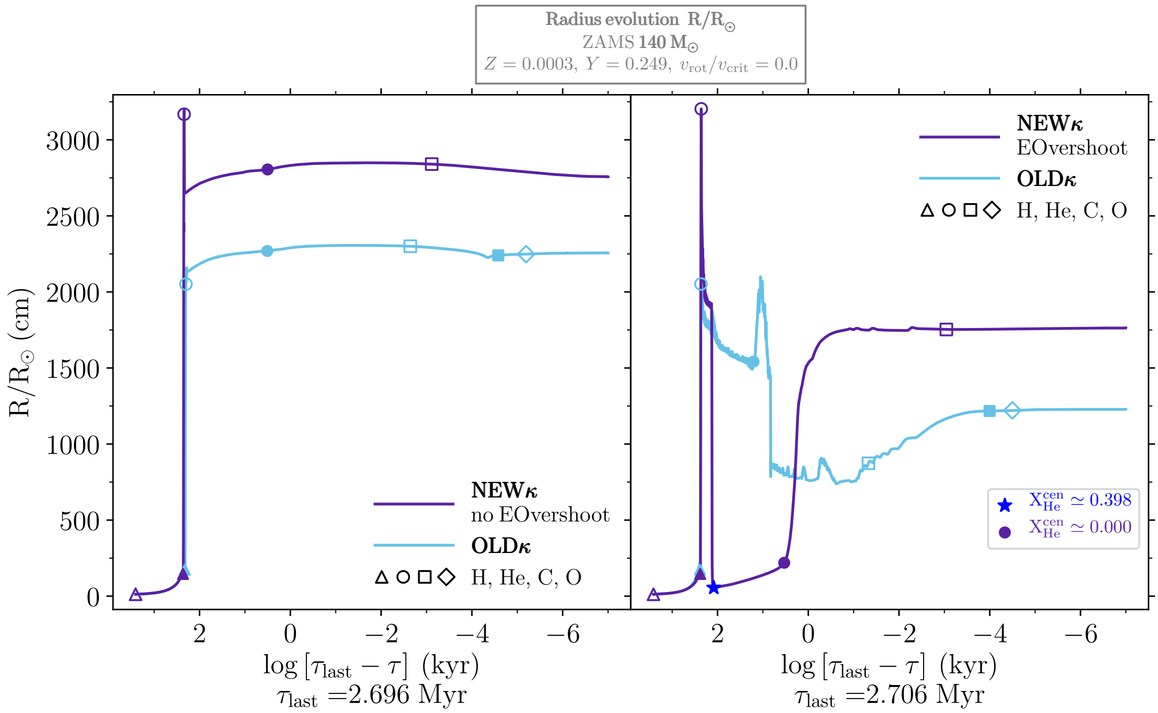

Figure 4.19: Comparative radius R/R$_\odot$ evolution for a star with ZAMS mass M = 140 M$_\odot$, metallicity Z=0.0003 and rotation velocity $v_{\rm rot}/v_{\rm crit} = 0.0$, with the two prescriptions **NEWκ** and **OLDκ**; the usual convention for the symbols and time coordinate shift is employed. The y-axis scale is, on purpose, non logarithmic: the aim, here, is to enhance the slight differences, and not the orders of magnitude. An insert, in the EOv (right) panel, shows the value of central Helium mass fraction at two interesting points of the track for **NEWκ** run: these are commented in the Blue Loop paragraph. Left – PARSEC output without EOvershooting; Right – same as Left, but with EOvershooting incorporated.

shell captured by Fig.(4.20)); this hints at a *double shell phase* even for this model, which is supported by the slight increase of radius in Fig.(4.19 – Right), see after the empty rectangle. This is interesting, and it was not appreciable by solely looking at the Kippenhahn diagram.

- The **gravitational luminosity** is not reported for clearness' sake: it shows large fluctuations in all models, particularly for the last stages of EOv OLDκ and NEWκ. Fortunately, the information about the surface's expansion and contraction history can be glimpsed by the radius evolution.

Surface Abundances log X_i We can see the evolution of the *surface abundances*, log X_i, in Fig.(4.22). The no EOv models show no outstanding differences, a part from small deviations in the ^{16}O and ^{14}N abundances, a little lower and higher, respectively, in **NEWκ** and **OLDκ**. Nevertheless, as we already highlighted, this deviation in ^{16}O, right after the 1DU, is key to determine the central ^{12}C/^{16}O ratio difference in the two models.

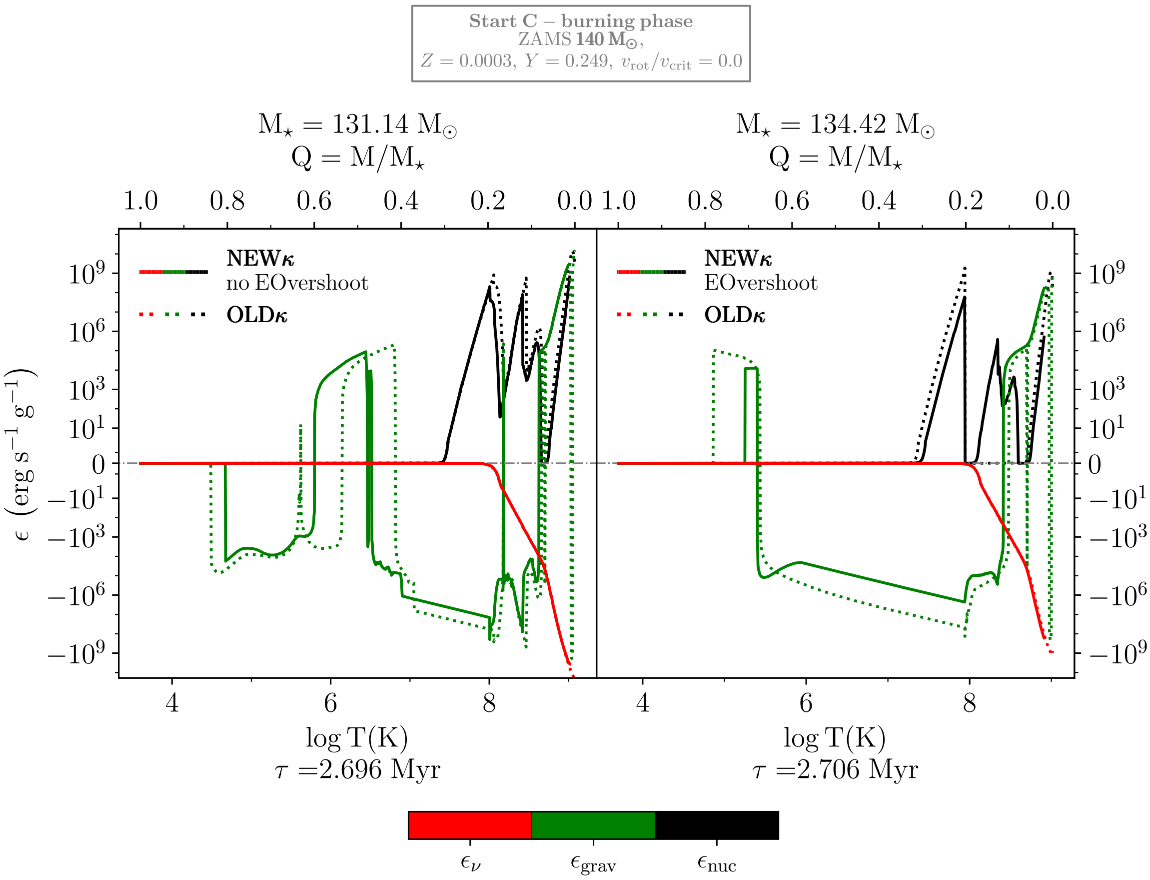

Figure 4.20: Comparative energy generation rates $\epsilon - \log\mathrm{T}$, at the selected evolutionary stage of the start of C-burning, for a star with ZAMS mass $\mathrm{M} = 140\ \mathrm{M}_{\odot}$, metallicity Z=0.0003 and rotation velocity $v_{\mathrm{rot}}/v_{\mathrm{crit}} = 0.0$, with the two prescriptions **NEWκ** and **OLDκ**. The time coordinate at which the NEWκ structure is captured is reported below the x-axis (the same information for P83 is not reported). a second x-axis on the top give an idea of the normalized mass coordinate Q$\in [0, 1]$, which runs from the core to the surface of the star and is normalized to the value of $\mathrm{M}_{\star}$ (reported above for NEWκ). Notice that the y-axis scale is a ***symmetric logarithm***: the negative energy rates are mapped below the zero (dot-dashed gray line) logarithmically, as well as the positive ones, with a small range of linear scales around 0. Left – PARSEC output without EOvershooting; Right – same as Left, but with EOvershooting incorporated.

As for the EOv models, an interesting evolution is evident:

- The ***MS and shell H-burning*** show excellent agreement between the two prescriptions. As said above, towards the end of shell H-burning, the tracks go towards their respective Hayashi line, and a first dredge up is indeed expected;
- In ***He-burning***, an evident dredge up happens: in the **OLDκ** track, the H surface mass fraction drops below $\log\mathrm{H} = 0.3$ and $\log\mathrm{He} \gtrsim 0.6$, creating a WR object of the WNL subclass; the **NEWκ** track evolves as well towards a WR-NL object, but the surface H depletion is less dramatic, with $\log\mathrm{H} \lesssim 0.4$. Summarizing,

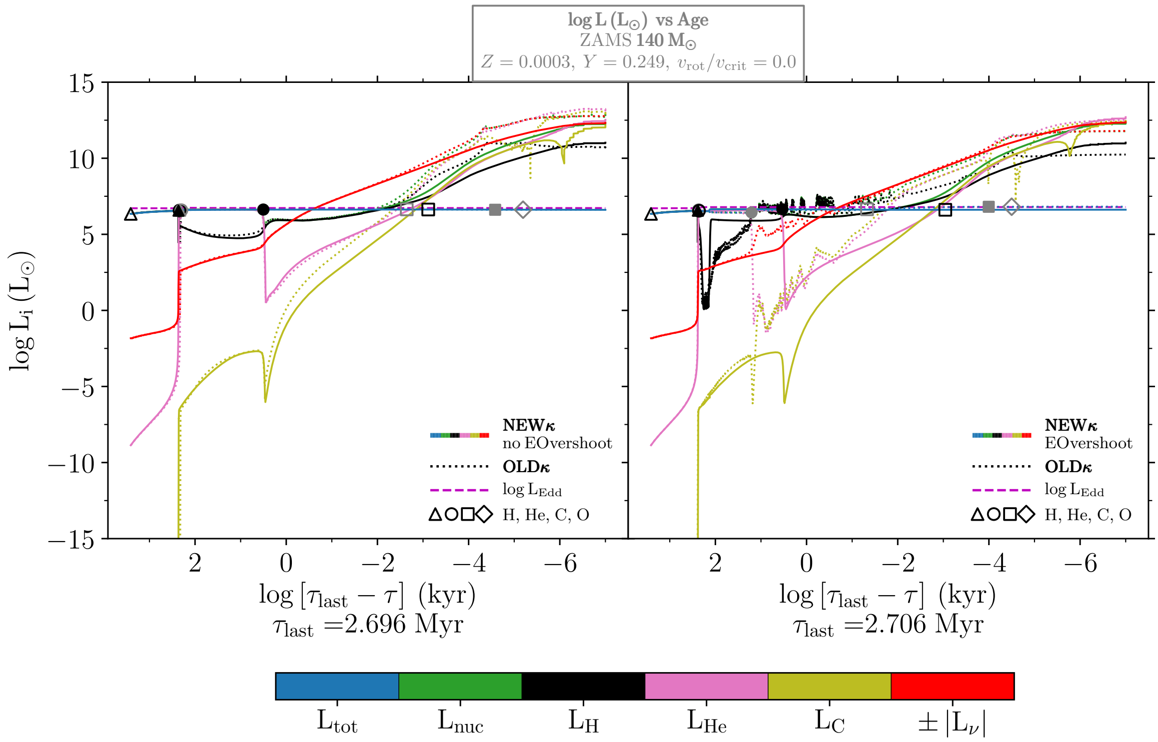

Figure 4.21: Comparative integrated (logarithmic) luminosities $\log \mathrm{L_i}$ for a star with ZAMS mass $\mathrm{M} = 140\ \mathrm{M_\odot}$, metallicity Z=0.0003 and rotation velocity $v_{\mathrm{rot}}/v_{\mathrm{crit}} = 0.0$, with the two prescriptions **NEWκ** and **OLDκ**; the usual convention for the symbols is employed. The usual constant shift of coordinate time τ_{last}, different for OLDκ (not reported) and NEWκ, is reported as a legend. Left – PARSEC output without EOvershooting; Right – same as Left, but with EOvershooting incorporated.

OLDκ He end	$\mathrm{M_{WR}^{OLD\kappa}} = 131.17\ \mathrm{M_\odot}$ $\mathrm{X} \simeq 0.3 \quad \mathrm{Y} \gtrsim 0.6 \quad \log\ {}^{12}\mathrm{C} \gtrsim 0.07$	$\Longrightarrow$	**WNL**
NEWκ He end	$\mathrm{M_{WR}^{OLD\kappa}} = 134.56\ \mathrm{M_\odot}$ $\mathrm{X} \lesssim 0.4 \quad \mathrm{Y} \gtrsim 0.6 \quad \log\ {}^{14}\mathrm{N} \gtrsim 0.0001$	$\Longrightarrow$	**WNL**

- During ***shell He-burning***, the NEWκ surface abundances are stabilized and no other unexpected event happens: this supports the scenario provided in Fig.(4.17). On the other hand, the OLDκ experience another dramatic enhancing of mass fractions of heavier elements, leaning towards a WR object of WO subclass; we will see below how the occurrence of a ***second dredge up*** is the major cause for this effect, with $\dot{\mathrm{M}}$

partly participating, too.

OLDκ C start	$\mathrm{M}_{\mathrm{WR}}^{\mathrm{OLD}\kappa} = 131.1\,\mathrm{M}_\odot$ $X \simeq 0.003 \quad Y \gtrsim 0.6 \quad \log\,^{16}\mathrm{O} \gtrsim 0.02$	$\Longrightarrow$	**WO**
NEWκ C start	$\mathrm{M}_{\mathrm{WR}}^{\mathrm{OLD}\kappa} = 134.4\,\mathrm{M}_\odot$ $X \lesssim 0.4 \quad Y \gtrsim 0.6 \quad \log\,^{14}\mathrm{N} \lesssim 0.0001$	$\Longrightarrow$	**WNL**

Let us lastly make a summary of the most important surface abundances changes during the evolutive history of EOv models:

	$\log^{12}$ C		$\log^{14}$ N		$\log^{16}$ O	
	NEWκ	**OLDκ**	**NEWκ**	**OLDκ**	**NEWκ**	**OLDκ**
Before 1DU	5×10^{-5}	5×10^{-5}	1.5×10^{-5}	1.5×10^{-5}	1.5×10^{-4}	1.5×10^{-4}
After 1DU	8×10^{-6}	7×10^{-2}	1.8×10^{-4}	3×10^{-2}	2×10^{-5}	2×10^{-2}
	$\searrow$	$\nearrow\nearrow$	$\nearrow$	$\nearrow\nearrow$	$\searrow$	$\nearrow\nearrow$
After 2DU	5×10^{-6}	2×10^{-2}	1.9×10^{-4}	5×10^{-1}	0.25×10^{-5}	2.5×10^{-1}
	$\searrow$	$\searrow$	$\nearrow$	$\nearrow\nearrow$	$\searrow$	$\nearrow\nearrow$

Table 4.6: Summary of surface mass fractions of H, He and most important metals for a star with ZAMS mass $\mathrm{M} = 140\,\mathrm{M}_\odot$, metallicity Z=0.0003 and rotation velocity $v_{\mathrm{rot}}/v_{\mathrm{crit}} = 0.0$, with the two prescriptions **NEWκ** and **OLDκ**. These are caught before and after the two dredge ups characterizing (at least one of) the models. The upper (lower) slanted green (red) arrows indicate an increase (lowering) of the logarithmic abundance.

Mass loss rate $\dot{\mathrm{M}}$ evolution This star loses a (maximum) minimum of (7%) 4% for EOv NEWκ (OLDκ) of its mass throughout its life of almost 3 Myr. This is caused by an intense *mass loss rate* $\dot{\mathrm{M}}$, which influences all evolutionary stages. As one can see in Fig.(4.23), the no EOv models are in excellent agreement in all stages, maintaining a fairly high $\dot{\mathrm{M}} \simeq -4.5$. The only, mild difference one can notice concerns the core H depletion, see Fig.(4.23 – Left), the filled triangles, which is simply due to the slightly hotter blue hook in the HR diagram; this difference is present also for the EOv models, Fig.(4.23 – Right).

As concerns the EOv case:

- **Core He depletion**
  The end of He burning phase shows a prominently ***lower*** $\dot{\mathrm{M}}$ for the NEWκ model: this can be motivated by the bluer $\mathrm{T}_{\mathrm{eff}}$ of NEWκ, which is actually undergoing the Blue Loop (see below). Nevertheless, this stage succeeds in removing mostly all 4% of the total mass, due to the non negligible duration of τ_{He}. Thanks to the Blue Loop, the NEWκ EOv model loses quite less mass, in this stage, with respect to the no EOv one, see Fig.(4.17).

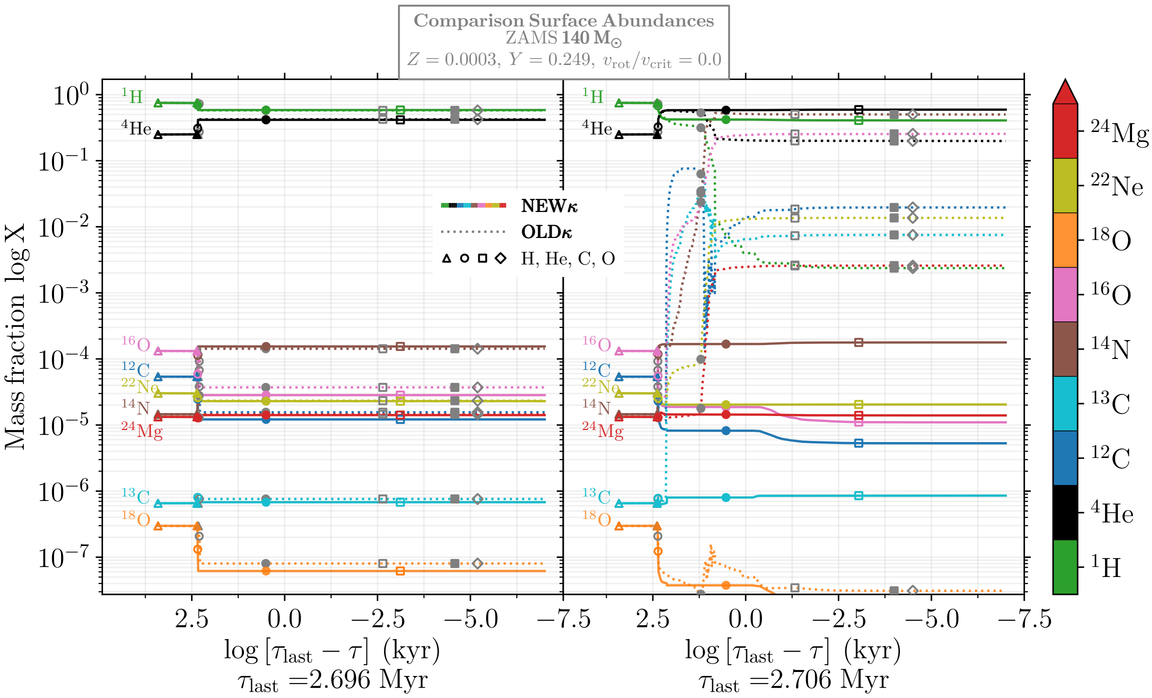

Figure 4.22: Comparative superficial (logarithmic) abundances $\log X_i$ history for a star with ZAMS mass $M = 140\,M_\odot$, metallicity Z=0.0003 and rotation velocity $v_{rot}/v_{crit} = 0.0$, with the two prescriptions **NEWκ** and **OLDκ**; the usual convention for the symbols is employed. The usual constant shift of coordinate time τ_{last}, different for OLDκ (not reported) and NEWκ, is reported as a legend. Left – PARSEC output without EOvershooting; Right – same as Left, but with EOvershooting incorporated.

We also notice that both NEWκ and OLDκ enter the dust-driven wind region of the HR diagram very late in the core He-burning stage: this, however, does **not** prevent the $\dot{M}$ to peel off more mass from the envelope and favor the bluer evolution of the NEWκ EOv model.

In the OLDκ case $\dot{M}$ is, conversely, still very strong: this is caused by the fact that the star remains along its Hayashi line, undergoing the 1DU, all along this stage, as one can see in the HR diagram Fig.(4.15).

► **Advanced stages**

Both models, in the advanced stages, share a very high $\log \dot{M}$, but NEWκ has a *much* stronger rate: the track now, is actually much redder than the OLDκ one. We find:

NEWκ	$\log \dot{M} \simeq -4.5$	$M_{C_{start}}^{NEW\kappa} = 134.4\,M_\odot$
OLDκ	$\log \dot{M} \lesssim -5.5$	$M_{C_{start}}^{OLD\kappa} = 131.1\,M_\odot$

which holds for the start of C-burning, i.e. the last stage that is possible to compare in the two **NEWκ** and **OLDκ** prescriptions. Numerical difficulties of the solver are

clearly visible, too.
Lastly, we notice that both models, with not much agreement, approach a high value of the ***Eddington parameter***, $\Gamma_{\mathrm{Edd}} \simeq 0.6$, see Eq.(1.14); this is indeed expected for such massive stars and it is always in correspondence of notable increases of $\dot{\mathrm{M}}$; also, this is shown even by Fig.(4.21), where the total luminosity $\mathrm{L_{tot}}$ is at all times very close to the Eddington's value $\mathrm{L_{Edd}}$.

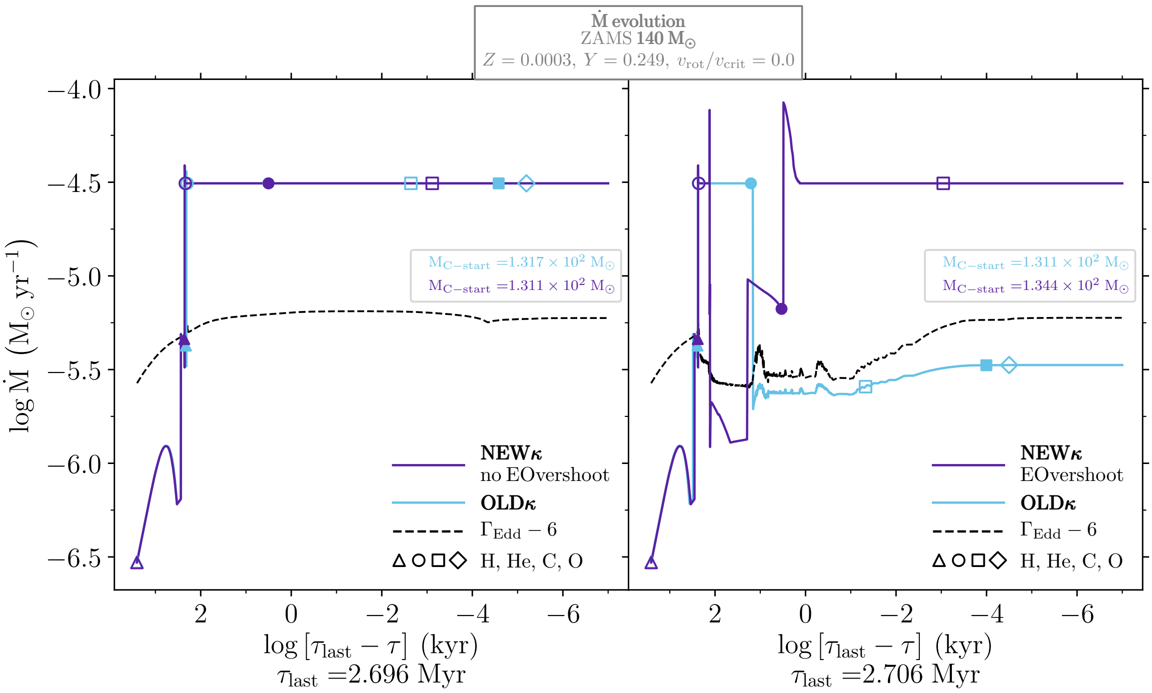

Figure 4.23: Comparative mass loss rate $\dot{\mathrm{M}}$ evolution for a star with ZAMS mass $\mathrm{M} = 140\ \mathrm{M}_\odot$, metallicity Z=0.0003 and rotation velocity $v_{\mathrm{rot}}/v_{\mathrm{crit}} = 0.0$, with the two prescriptions **NEW**κ and **OLD**κ; the usual convention for the symbols is employed. The usual constant shift of coordinate time τ_{last}, different for OLDκ (not reported) and NEWκ, is reported below the x-axis; the value of the Eddington parameter Γ_{Edd}, shifted by -6 to let it appear in the plot, is shown for illustrative purposes, see text; lastly, the masses $\mathrm{M_O}$ at the end of the last comparable model (O-burning in this case) is printed too. Left – PARSEC output without EOvershooting; Right – same as Left, but with EOvershooting incorporated.

First Dredge Up 1DU Let us now give a look at Fig.(4.24), where the usual comparison between two structures at two different evolutionary stages is performed. The top row shows the opacity of NEWκ and OLDκ at the start of the core He-burning, while the bottom row shows the same quantities towards the end of core He-burning: between these stages, the *firts dredge up* 1DU is expected to happen.

Let us highlight the most prominent features:

- The **atmospheric ratio C/N**, which is represented by the purple lines, is, on the top row, above 1; after the 1DU it decreases to < 0 for the no EOv models, while in the

EOv case the OLDκ maintains a C/N ratio above unity, actually even enhanced. A part from this latter case, the lowering of C/N at the atmosphere is the proof of the dredge up of nitrogen, only possible with a convective envelope penetration towards the CNO-processed regions.
As for the **OLDκ** case with EOv: the enhancement is definitely another proof of 1DU, since the higher value of atmospheric C/N is simply due to the great enrichment of ^{12}C in the surface, see Tab.(4.6).

- The **atmospheric ratio C/O** remains always below 1, of course with the exception of the OLDκ model after the 1DU. The C/O$<$ 1 confirms our stars, at the core He-burning end, to be of an advanced spectral type, with oxygen rich atmospheres.
  As for the **OLDκ** case with EOv: this model, at the end of He-burning, is expected to present an atmosphere rich in carbonaceous grains (i.e. graphite).

- **After the 1DU**, the opacities from NEWκ and OLDκ are similar, in the no EOv case. Anyway, we see that the NEWκ atmospheric opacities are fairly *higher*, and this essentially motivates the prediction of a redder Hayashi line.

  As regards the **EOv case**: while the opacities were only mildly different before the 1DU, we see a *dramatic* departure of these after the 1DU. This was actually quite predictable, since we already saw that the predicted evolutive history of these models are completely different, and not quite comparable, already from the core He-burning start. The NEWκ opacity is so lower that the envelope is not even convective (see also below, Fig.(4.25)), and the star undergoes a Blue Loop instead of a deep, drastic 2DU.

- The **NEWκ opacity** essentially presents the same peculiar features highlighted for the less massive models (see Fig.(4.6), Fig.(4.9) and Fig.(4.14), the bottom panels!). The abrupt rise of atmospheric opacity is analogously motivated, being in this case actually less pronounced due to slightly hotter Hayashi lines.

The Blue Loop for NEWκ EOv We have already individuated this peculiarity of the NEWκ track with Envelope Overshooting; let us elaborate a bit further on the *Blue Loop*. The Blue Loops are well established results of numerical computation for intermediate to relatively (M $\lesssim$ 12 M$_\odot$) massive stars, actually a bit peculiar on the VMS cases. We can describe our peculiar Blue Loop by steps:

I. **After the 1DU**
In correspondence to the empty circle in Fig.(4.15 – Right), the star is burning He in the core and is set in the RGB. The envelope contracts, thanks to the mirror principle (Fig.(4.17)), and the stellar radius decreases (Fig.(4.19)). The luminosity also decreases, initially, as the envelope is mostly convective, and the star is thus forced to move along its Hayashi line.

II. **Radiative envelope**
The star's envelope, subsequently, becomes radiative, and the star departs from its Hayashi line to higher effective temperatures. The evolution proceeds towards the

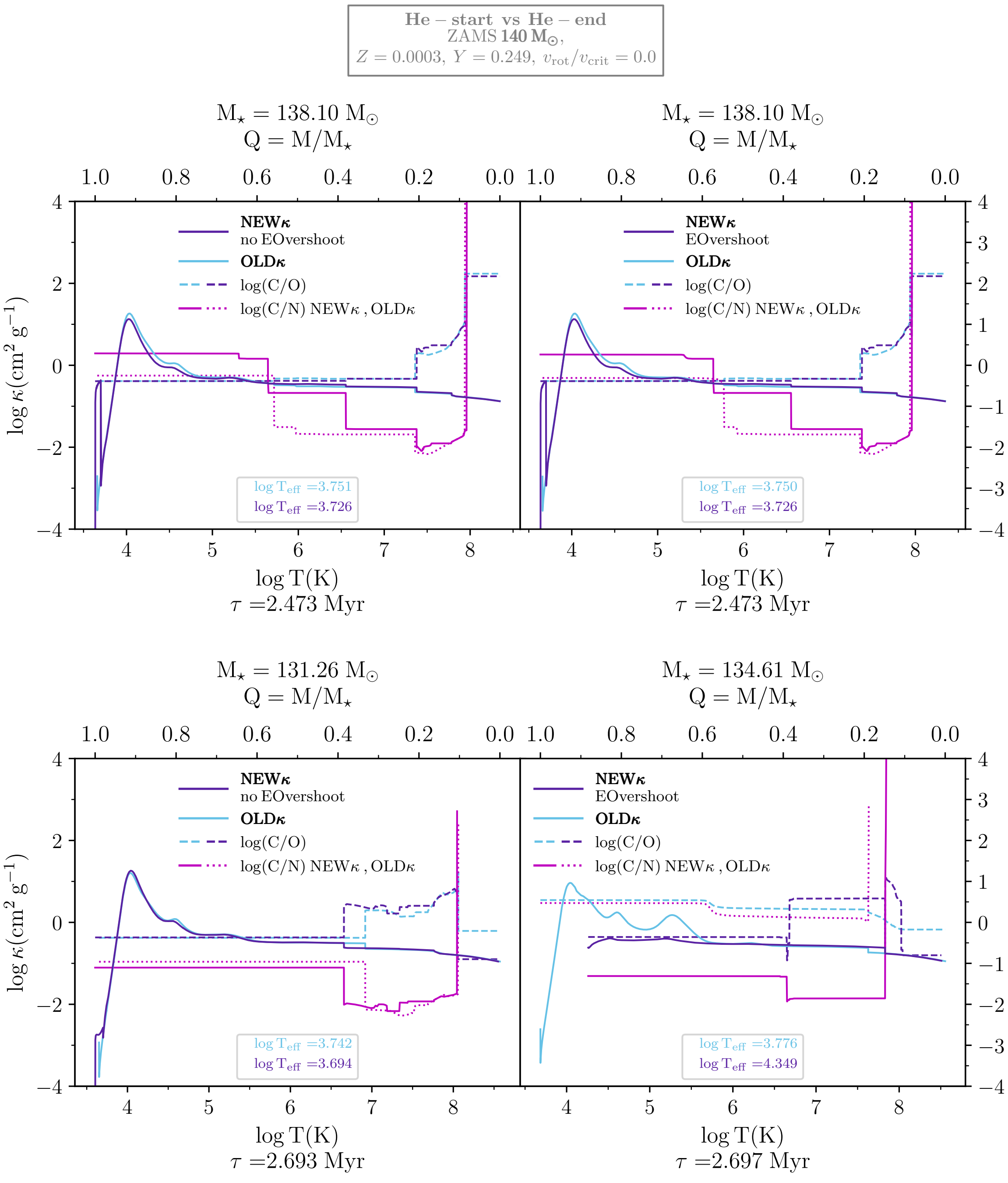

Figure 4.24: Comparative structure $\log\kappa - \log \mathrm{T}$ for a star with ZAMS mass M=140 M$_\odot$, metallicity Z=0.0003 and rotation velocity $v_{\rm rot}/v_{\rm crit} = 0$, with the two prescriptions **NEWκ** and **OLDκ**. The logarithmic abundance ratio C/O is also shown. The top row catches a structure at the start of core He-burning, hence before a 1DU; the bottom row shows a structure at the end of core He-burning, i.e. after the 1DU. Left – PARSEC output without EOvershooting; Right – same as Left, but with EOvershooting incorporated.

point of maximum $\log \mathrm{T_{eff}}$, minimum stellar radius $\mathrm{R/R_\odot}$ and depletion of central

He such as

$$\log T_{\rm eff}{}^{\bigstar} \simeq 4.55\,, \qquad R^{\bigstar} \simeq 55.5\,R_{\odot}\,, \qquad Y_{\rm cen}{}^{\bigstar} \simeq 0.395\,,$$

see also the insert in Fig.(4.15 – Right). After this point, the stellar envelope starts to expand again and the star walk towards the red. Fig.(4.25) precisely captures a moment in which the star is at the core He depletion: in the right panel, we see that still the condition for radiative envelopes, $\nabla_{\rm rad} < \nabla_{\rm ad}$, holds at this stage, on the contrary to what happens to the no EOv cases and to the EOv OLDκ counterpart.

III. To Hayashi line again
After the ★ point and the core He depletion, the star starts expanding again, Fig.(4.19), approaching the the RGB and turning to a very close point with respect to the Blue Loop beginning, right towards the core C-burning start.

We lastly recall that the Blue Loops, being a fairly slow, nuclear time-scaled phase of evolution, are expected to correspond to well populated HR diagram regions. The fact that, with our refined NEWκ prescription, this VM model is predicted to undergo such a peculiar evolutionary stage might have huge impacts on observational tests of both the highly suppressed *population of VMS* and convective overshooting *calibrations*.
This is actually a quite surprising feature, predicted solely by a different, more reliable, microphysics prescription.

Second Dredge Up 2DU We are now briefly commenting on the *second dredge up* 2DU, occurring only in the cases with Envelope Overshooting due to the reasons largely explained above. Fig.(4.26) catches the stellar structures at two different evolutionary stages; the top row shows the opacity of NEWκ and OLDκ at the end of the core He-burning (essentially, the same as the bottom row in Fig.(4.24)), while the bottom row shows the same quantities towards the start of core C-burning: the 2DU is expected to happen in between these stages, see also Fig.(4.22) and Fig.(4.17).

Let us highlight the most prominent features:

- The **atmospheric ratio C/N**, represented by the purple lines, remains unvaried in the no EOv cases, as expected; as for the EOv, Fig.(4.26 – Right), we see a dramatic decrease for OLDκ, essentially motivated by the drastic increase of ^{14}N in the atmosphere (see also Tab.(4.6)); the NEWκ case, instead, shows just a slight decrease after the 2DU, since the dredge up is milder.

- The **atmospheric ratio C/O** remains in fairly good agreement, after the 2DU, in the no EOv cases, while the EOv models show a peculiar behavior: since, in the OLDκ model, the atmospheric ^{12}C drops a bit while the ^{16}O remains very abundant, the C/O ratio returns below 1 after the 2DU, as it was prior to the first one. This confirms our star, at the core C-burning start, to appear as an advanced spectral type (A) object, with an O-rich atmosphere.
  As for the **NEWκ** model, this ratio increases a bit, see Tab.(4.6), but always staying below the unity.

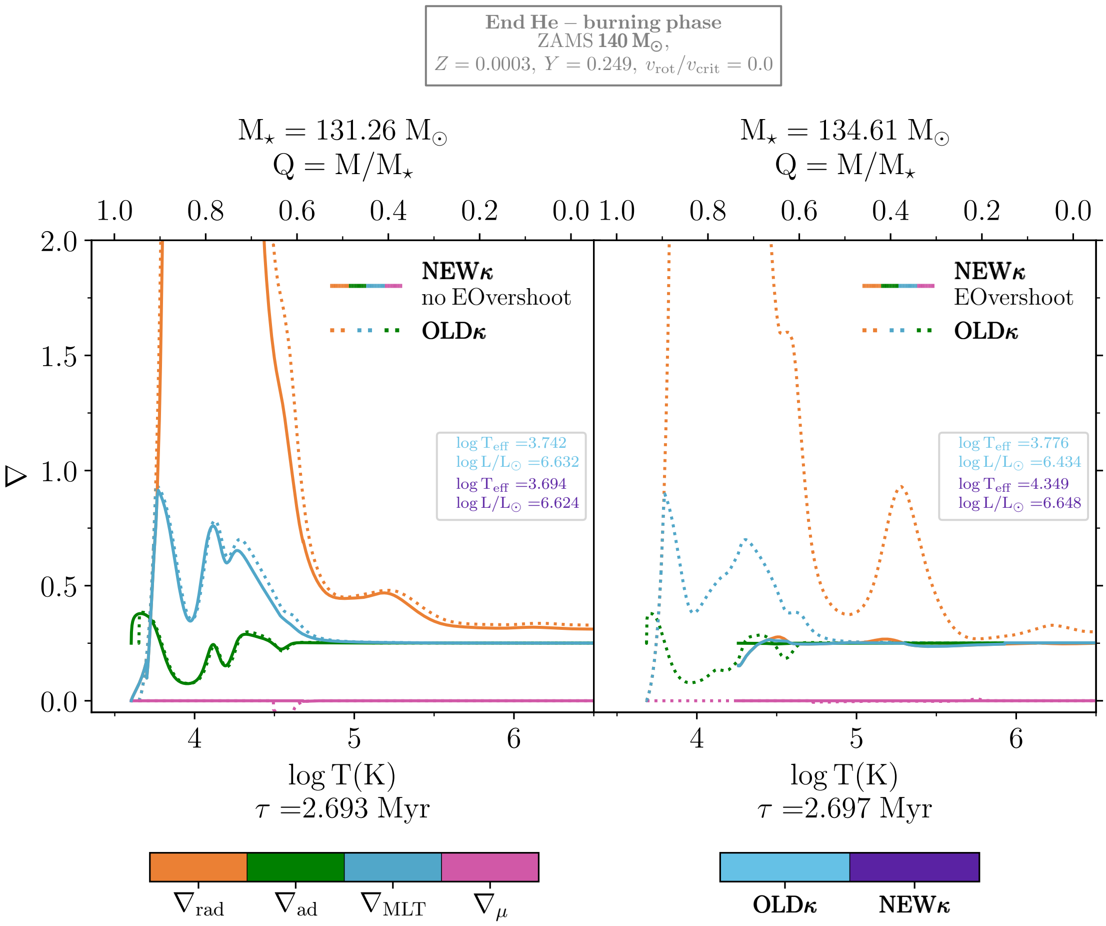

Figure 4.25: Comparative structure $\nabla_{\rm i} - \log \rm T$ for a star with ZAMS mass M=140 $\rm M_{\odot}$, metallicity Z=0.0003 and rotation velocity $v_{\rm rot}/v_{\rm crit} = 0$, with the two prescriptions **NEWκ** and **OLDκ**. The solid (dotted) lines, for NEWκ and OLDκ respectively, follow the color code explicit in one colorbar to the left; the inserts show the HR diagram positions of the selected model, towards the end of He-burning phase, and follow a second colorbar, to the right. Left – PARSEC output without EOvershooting; Right – same as Left, but with EOvershooting incorporated.

▶ **After the 2DU**, a great similarity of opacities in the no EOv cases (with the usual difference in the atmospheric regions which motivates the cooler Hayashi lines), a major opposition is opposed in the EOv cases. Again, we stress that these very different curves are at the basis of two ***completely different*** evolutive histories as the ones in Fig.(4.15), so this comes at no surprise; we see that the OLDκ opacities are lower in the atmospheric zones, and show some known features highlighted in Chp.(2) for hotter temperatures than the NEWκ ones.

First Adiabatic Index $\langle \Gamma_1 \rangle_{\rm tot}$ We are lastly going to follow the analysis given by G. Costa et al. (2020), [Cos+20], as concerns the *First Adiabatic Index* Γ_1; this is interesting in this test case of M=140 $\rm M_{\odot}$ since this VMS falls in the range (given that some mass loss

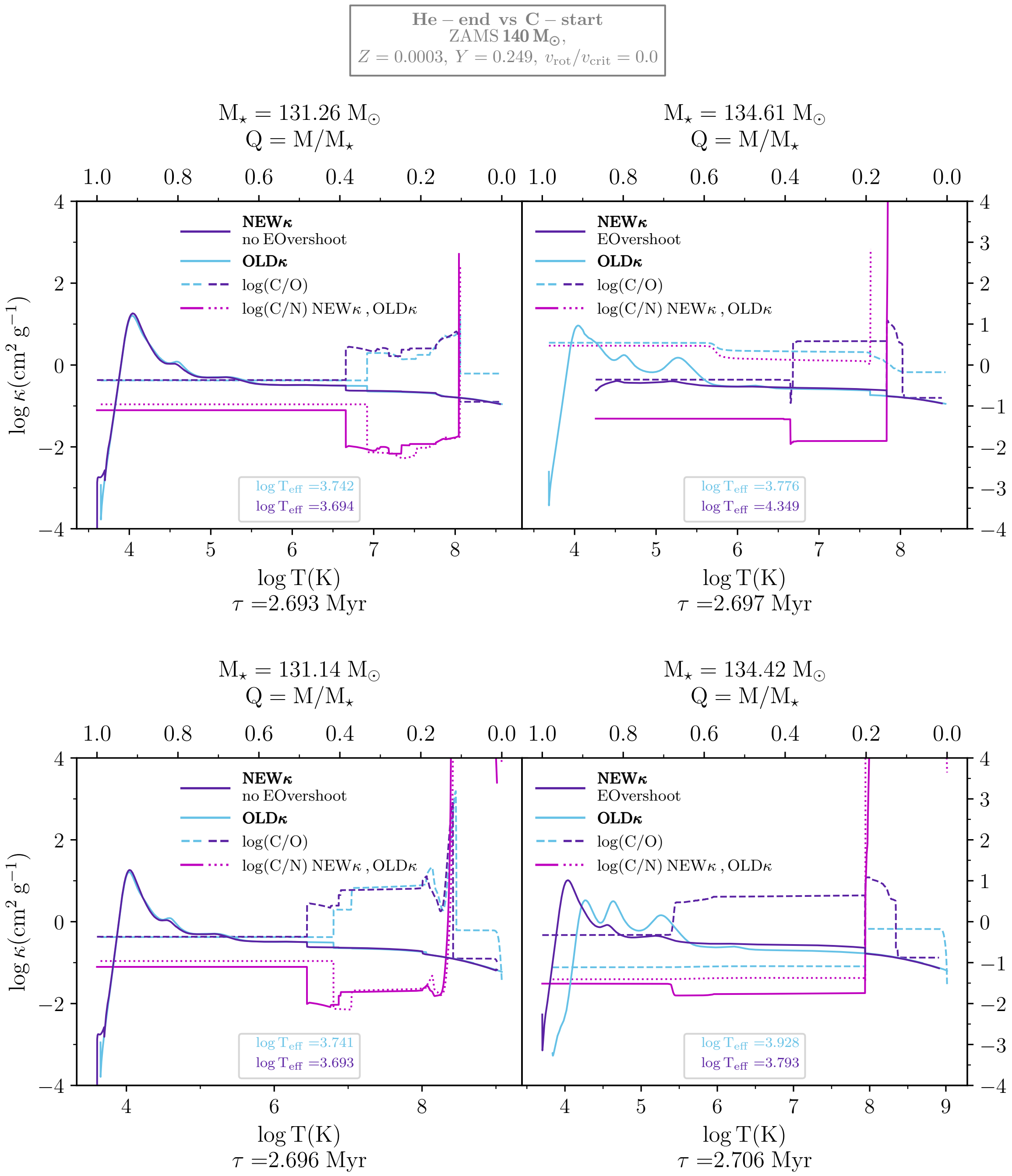

Figure 4.26: Comparative structure $\log\kappa - \log T$ for a star with ZAMS mass M=140 $M_\odot$, metallicity Z=0.0003 and rotation velocity $v_{rot}/v_{crit} = 0$, with the two prescriptions **NEWκ** and **OLDκ**. The logarithmic abundance ratio C/O is also shown, and the same conventions as in Fig.(4.6) are employed. Left – PARSEC output without EOvershooting; Right – same as Left, but with EOvershooting incorporated.

indeed happens) of interest for the investigation about the ***Pair Instability SuperNovae***

(PISN), which are expected to create a well known *mass gap*,

Pair Instability Mass Gap

$$40 - 65 \lesssim \mathrm{M_{He}}/\mathrm{M_\odot} \lesssim 120$$
$$\text{i.e.} \quad 95 \lesssim \mathrm{M}/\mathrm{M_\odot} \lesssim 260\,,$$

in the BHs spectrum. This mass gap have been recently challenged by GWs detections (e.g., the event GW190521) from theoretical progenitors with primary masses of about $\mathrm{M}{=}85^{+21}_{-14}\,\mathrm{M_\odot}$.

As one can see in Fig.(4.17), see the $\mathrm{M_{He}}$, our models can, in principle, be good candidates for a PISN event at the end of their lives, with the exception of OLDκ with Envelope Overshooting model. To be more precise, we need to evaluate the **first adiabatic index** for the models and perform a complete stability analysis at each mesh point, seeking for the onset of dynamical instability. The standard, simple way to deal with this, otherwise incredibly complicated, analysis, is to refer to the Stothers criterion,

Stothers Instability Criterion

$$\langle\Gamma_1\rangle = \frac{\int_0^{\mathrm{M}} \Gamma_1 \dfrac{P}{\rho}\,\mathrm{d}m}{\int_0^{\mathrm{M}} \dfrac{P}{\rho}\,\mathrm{d}m} < \frac{4}{3}\,,$$

see Stothers (1999), [Sto99]. This stability criterion account for a weighted mean of the Γ_1 over all the stellar object: P and ρ are the pressure and density at the mass coordinate m, within the mass integration measure $\mathrm{d}m$. As G. Costa in [Cos+20], we decided to study this integral as performed within all the stellar matter, from the core to the star's surface, and call this quantity as $\langle\Gamma_1\rangle_{\mathrm{tot}}$. The outcome is shown in Fig.(4.27). The figure shows the comparison of NEWκ and OLDκ runs' mean first adiabatic index $\langle\Gamma_1\rangle_{\mathrm{tot}}$, together with the Stothers' limiting case of $4/3 \simeq 1.333$; a gray shaded area represents a tolerance of 0.01 with respect to the instability onset value, to be conservative. Let us summarize the main points:

- **No EOv**
  Good agreement is shown until the last comparable stage, the start of core C-burning. Both PARSEC's computations end in the gray shaded area, the NEWκ one with a quite stronger degree of affidability: this labels both of the models as good **PISN** candidates, expected to undergo a powerful, single pulse which disrupts completely the object, with *no compact remnant* left.

- **EOv**
  Any shade of agreement between the two prescriptions completely vanish after the 1DU: the stars follow a completely different history. The OLDκ ends with a greatly reduced $\mathrm{M_{He}}$, which traslates into consistent departure from the NEWκ's $\langle\Gamma_1\rangle_{\mathrm{tot}}$ behavior and, in the end, by the avoidance of the instability region. This fact labels the OLDκ model as a good candidate for a *compact remnant* progenitor, via a Pulsation Pair Instability SuperNova (**PPISN**).

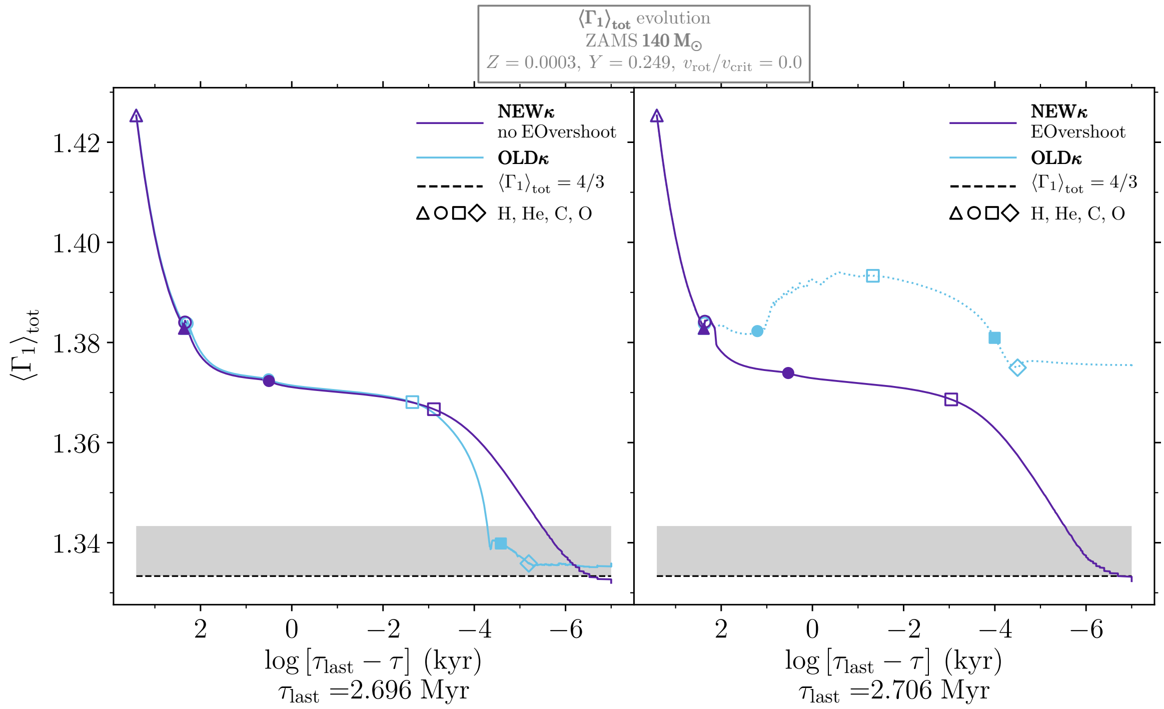

Figure 4.27: Comparative (averaged) first adiabatic index $\langle\Gamma_1\rangle_{tot}$ for a star with ZAMS mass M=140 $M_\odot$, metallicity Z=0.0003 and rotation velocity $v_{rot}/v_{crit} = 0$, with the two prescriptions **NEWκ** and **OLDκ**. The Stothers limiting case of $4/3$ is also shown, and the same conventions for the symbols as in Fig.(4.1) are employed. Left – PARSEC output without EOvershooting; Right – same as Left, but with EOvershooting incorporated.

As for the NEWκ model, we see that the star indeed advance in the pair-instability region in its latest stages, and this again confirms our model to be a good **PISN** candidate.

We see that, while the OLDκ were interestingly favoring a possible closure of the PI-BH mass gap, the inclusion of refined opacities in this front is not equally favorable, and our test case of M=140 $M_\odot$ confirms the evolutive scenario predicted by the past literature.

Conclusions

The purpose of this work was an in-depth analysis of the stellar matter resistance to energy transport, the ***opacity***, in the context of massive stars with Zero Age Main Sequence (ZAMS) mass M>9 $M_\odot$. This property of astrophysical plasmas has a special interest, greatly affecting model predictions of structural as well as evolutionary properties of stellar objects; by virtue of this paramount role, we studied in details the opacity both as a stand-alone micro-physical process *and* as the possible origin of consistent evolutionary effects.

I. STELLAR MODELS GRID
A meticulous review of well established literature's results about massive stars' evolutive history, Chp.(1), allowed the author to test model tracks from PARSEC runs, confirming the Padova-Trieste code's stability into convergence, rapidity and well suited outputs; a *stellar models grid* with variable ZAMS masses, metallicities Z, rotational rate and convective Envelope Overshooting (EOv) was built and served as test sample for comparisons.

II. ELECTRON SCATTERING **P17**
From the new theoretical framework of the Relativistic Kinetic Equation (RKE) formalism, the author re-derived a suitable, refined prescription [Pou17] for *free-electron scattering opacity* at the highest energies, Compton limit, and implemented it in PARSEC code as the P17 subroutine routine for $\log \mathrm{T(K)} \geq 8.7$. The study of structural and evolutionary consequences followed, comprising the most compact models of the built grid, to single out the effects in sufficiently degenerate ($\eta \gtrsim 0$) stars.
Most relevant findings are the dramatic departures of the new Compton opacities from the Thomson plateaux, peaking at even 25% relative departure with respect to previous PARSEC's runs, in the most compact ZAMS M$\simeq$ 10 $M_\odot$ objects, at the start of core C-burning; rotating models seems to be quite less affected, while a higher Z enhances such deviation.
Resulting effects on the stratification history, i.e. Kippenhahn diagrams, are indeed expected once models reach more advanced stages, due to the expected influence on the convective history of near-core layers.

III. THERMAL CONDUCTION **COND**
The author furtherly argued about the *thermal conductivity* impact, at the highest energies, in the considered compact models ZAMS M$\gtrsim$ 10 $M_\odot$. From the well established theoretical framework of scattering theory in Quantum-Mechanics and liquid metals structures, the subroutine from [Ito+08] is consequently implemented in PARSEC as the COND subroutine for $\log \mathrm{T(K)} \geq 8.7$. The findings were in agreement

with those of **I.** and even drastically enhanced, for fixed M and Z, in the most advanced stages of evolution: relative departures from Thomson plateaux with respect to previous PARSEC's runs reach 40% entity.
Resulting effects on both more and less massive models are indeed expected, as non negligible values of the Coulomb coupling parameter can supervene with a (ρ, T) dependent conditions which cannot be solely described by a constraint on the degeneracy parameter η.

IV. <u>Atoms & Molecules</u> **NEWκ**
The author lastly expands on the substantial, work-in-progress revision of *atomic and molecular transition* opacities at work within the Padova group [Marigo et al., in prep.], not yet fully operational but under development. A series of test opacity tables for Z=0.0003 are employed, implemented and ran, in a prototype new-PARSEC code version, as the NEWκ subroutine for $3.2 \leq \log \mathrm{T(K)} \leq 9.1$, to be compared with the OLDκ existing version prior to the present work.
Model tracks of selected ZAMS from our grid are comprehensively described, case by case, as a comparison to OLDκ, giving great insights on NEWκ evolutionary effects and, where possible, explanations of the physics behind them. Most relevant findings are exceptionally substantial redward excursions, after the shell He-burning phase, of all NEWκ models, much more pronouced with respect to OLDκ; this basically translates in a fairly different evolutive history, with distinc dredge-up (DU) patterns, mass loss rates $\dot{\mathrm{M}}$ and predicted compactness of pre-SuperNova (SN) structures. A test case of ZAMS M=140 $\mathrm{M}_{\odot}$ resulted the most peculiar, due to its dramatic dredge-up episodes and pair-creation (in-)stability history; this latter confirms the well known scenario for a BH mass gap (recently thought to be relaxable [Cos+20]), reiterating this existing puzzle in the astrophysical community.

This work **a)** aligns with the need of a substantial revision of the opacity treatment in the PAdova TRieSte Evolutionary Code (PARSEC) over the entire relevant temperature range, standing up as first step into a thorough effort which will be surely put in full operation in the future; **b)** serves the purpose of the study of evolutionary effects, in the context of massive stars, of some first, but key, updates to the new PARSEC's opacities, gaining insights on the future prolific opportunities.

The author highlights the appealing possibilities of <u>*micro-physics improvements*</u> at the highest energies: Møller's scattering of free electrons and Compton-like process off positrons could constitute interesting radiative opaqueness counterparts, especially in the cores of massive stars during the most advanced evolutionary stages, e.g. towards the region of pair-instability onset. Any enlargement of <u>*stellar models grid*</u> in the future will certainly open invaluable perspectives, particularly regarding the effects of NEWκ, which are indeed to be explored within a more general coverage of models: this will allow considerable insights about, e.g., Blue Loops populations, metallicity Z effects on the atmospheric opacities, Very Massive Stars (VMS) final fates.

Bibliography

Book Sources

[BPL15] **V B Berestetskii, L. P. Pitaevskii, and E.M. Lifshitz**. *Quantum Electrodynamics: Volume 4 (Course of Theoretical Physics)*. English. Paperback. Butterworth-Heinemann, **Jan. 15**. ISBN: 978-0750633710.

[Gro80] **Sybren Ruurds de Groot**. *Relativistic kinetic theory : principles and applications*. Amsterdam New York: North-Holland Pub. Co. Sole distributors for the USA and Canada, Elsevier North-Holland, **1980**. ISBN: 0444854533.

[PP29] **Gerald C. Pomraning and Physics**. *The Equations of Radiation Hydrodynamics (Dover Books on Physics)*. English. Paperback. Dover Publications, **Nov. 29**. ISBN: 978-0486445991.

Articles

[BKD10] **D Bahena, J Klapp, and H Dehnen**. "Nuclear reaction rates and opacity in massive star evolution calculations". In: *Journal of Physics: Conference Series* **239** (**2010**), p. 012004. DOI: 10.1088/1742-6596/239/1/012004.

[Bre+12] **A. Bressan et al.** "PARSEC: stellar tracks and isochrones with the PAdova and TRieste Stellar Evolution Code". In: *Monthly Notices of the Royal Astronomical Society* **427**.1 (**2012**), 127–145. ISSN: 1365-2966. DOI: 10.1111/j.1365-2966.2012.21948.x.

[BY76] **J. R. Buchler and W. R. Yueh**. "Compton scattering opacities in a partially degenerate electron plasma at high temperatures." In: *The Astrophysical Journal* **210** (**Dec. 1976**), pp. 440–446. DOI: 10.1086/154847.

[Caf+11] **E. Caffau et al.** "Solar Chemical Abundances Determined with a CO5BOLD 3D Model Atmosphere". In: *Solar Physics* **268**.2 (**Feb. 2011**), pp. 255–269. DOI: 10.1007/s11207-010-9541-4. arXiv: 1003.1190 [astro-ph.SR].

[Col+16] **J. Colgan et al.** "A NEW GENERATION OF LOS ALAMOS OPACITY TABLES". In: *The Astrophysical Journal* **817**.2 (**2016**), p. 116. ISSN: 1538-4357. DOI: 10.3847/0004-637x/817/2/116.

[Cos+20] **G. Costa et al.** "Formation of GW190521 from stellar evolution: the impact of the hydrogen-rich envelope, dredge-up, and 12C(α, γ)16O rate on the pair-instability black hole mass gap". In: *Monthly Notices of the Royal Astronomical Society* **501**.3 (**2020**), 4514–4533. ISSN: 1365-2966. DOI: 10.1093/mnras/staa3916.

[Cos+19] **Guglielmo Costa et al.** "Mixing by overshooting and rotation in intermediate-mass stars". In: *Monthly Notices of the Royal Astronomical Society* **485**.4 (**2019**), 4641–4657. ISSN: 1365-2966. DOI: 10.1093/mnras/stz728.

[Cyb+10] **R H Cyburt et al.** "THE JINA REACLIB DATABASE: ITS RECENT UPDATES AND IMPACT ON TYPE-I X-RAY BURSTS". In: *Astrophysical Journal, Supplement Series* **189**.1 (**Aug. 2010**). ISSN: 0067-0049. DOI: 10.1088/0067-0049/189/1/240.

[DDW09] **J. Daszyńska-Daszkiewicz and P. Walczak**. "Constraints on opacities from complex asteroseismology of B-type pulsators: the β Cephei star ϑ Ophiuchi". In: *Monthly Notices of the Royal Astronomical Society* **398**.4 (**Sept. 2009**), pp. 1961–1969. ISSN: 0035-8711. DOI: 10.1111/j.1365-2966.2009.15229.x. eprint: https://academic.oup.com/mnras/article-pdf/398/4/1961/3054032/mnras0398-1961.pdf.

[Fis+16] **J. Fisák et al.** "Rayleigh scattering in the atmospheres of hot stars". In: *Astronomy & Astrophysics* **590**, A95 (**May 2016**), A95. DOI: 10.1051/0004-6361/201628291. arXiv: 1605.02623 [astro-ph.SR].

[Fu+18] **Xiaoting Fu et al.** "New PARSEC database of α-enhanced stellar evolutionary tracks and isochrones – I. Calibration with 47 Tuc (NGC 104) and the improvement on RGB bump". In: *Monthly Notices of the Royal Astronomical Society* **476**.1 (**2018**), 496–511. ISSN: 1365-2966. DOI: 10.1093/mnras/sty235.

[GFF18] **Joyce Guzik, Christopher Fontes, and Chris Fryer**. "Opacity Effects on Pulsations of Main-Sequence A-Type Stars". In: *Atoms* **6**.2 (**June 2018**). DOI: 10.3390/atoms6020031.

[IR96] **Carlos A. Iglesias and Forrest J. Rogers**. "Updated Opal Opacities". In: *The Astrophysical Journal* **464** (**June 1996**), p. 943. DOI: 10.1086/177381.

[Ito+08] **Naoki Itoh et al.** "The Second Born Corrections to the Electrical and Thermal Conductivities of Dense Matter in the Liquid Metal Phase". In: *The Astrophysical Journal* **677**.1 (**2008**), 495–502. ISSN: 1538-4357. DOI: 10.1086/529367.

[JNH88] **C. de Jager, H. Nieuwenhuijzen, and K.A. van der Hucht**. "Mass loss rates in the Hertzsprung-Russell diagram." In: *Astronomy & Astrophysics* **72** (**Feb. 1988**), pp. 259–289.

[Joh88] **T. L. John**. "Continuous absorption by the negative hydrogen ion reconsidered". In: *Astronomy & Astrophysics* **193**.1-2 (**Mar. 1988**), pp. 189–192.

[KN29] **O. Klein and T. Nishina**. "Über die Streuung von Strahlung durch freie Elektronen nach der neuen relativistischen Quantendynamik von Dirac". In: *Zeitschrift fur Physik* **52**.11-12 (**Nov. 1929**), pp. 853–868. DOI: 10.1007/BF01366453.

[MA09] **P. Marigo and B. Aringer**. "Low-temperature gas opacity". In: *Astronomy & Astrophysics* **508**.3 (**2009**), 1539–1569. ISSN: 1432-0746. DOI: 10.1051/0004-6361/200912598.

[Pac83] **B. Paczynski**. "Models of X-ray bursters with radius expansion". In: *The Astrophysical Journal* **267** (**Apr. 1983**), pp. 315–321. DOI: 10.1086/160870.

[Pou17] **Juri Poutanen**. "Rosseland and Flux Mean Opacities for Compton Scattering". In: *The Astrophysical Journal* **835**.2 (**2017**), p. 119. ISSN: 1538-4357. DOI: 10.3847/1538-4357/835/2/119.

[Rot+05] **L.S. Rothman et al.** "The HITRAN 2004 molecular spectroscopic database". In: *Journal of Quantitative Spectroscopy and Radiative Transfer* **96** (**Dec. 2005**), pp. 139–204. DOI: 10.1016/j.jqsrt.2004.10.008.

[Sea+94] **M. J. Seaton et al.** "Opacities for stellar envelopes". In: *Monthly Notices of the Royal Astronomical Society* **266**.4 (**Feb. 1994**), pp. 805–828. ISSN: 0035-8711. DOI: 10.1093/mnras/266.4.805. eprint: https://academic.oup.com/mnras/article-pdf/266/4/805/3050789/mnras266-0805.pdf.

[Ser+09] **Aldo M. Serenelli et al.** "NEW SOLAR COMPOSITION: THE PROBLEM WITH SOLAR MODELS REVISITED". In: *The Astrophysical Journal* **705**.2 (**2009**), L123–L127. ISSN: 1538-4357. DOI: 10.1088/0004-637x/705/2/l123.

[Sto99] **Richard B. Stothers**. "Criterion for the dynamical stability of a non-adiabatic spherical self-gravitating body". In: *Monthly Notices of the Royal Astronomical Society* **305**.2 (**May 1999**), pp. 365–372. ISSN: 0035-8711. DOI: 10.1046/j.1365-8711.1999.02444.x. eprint: https://academic.oup.com/mnras/article-pdf/305/2/365/18630859/305-2-365.pdf.

[TA99] **F. X. Timmes and Dave Arnett**. "The Accuracy, Consistency, and Speed of Five Equations of State for Stellar Hydrodynamics". In: *The Astrophysical Journal Supplement Series* **125**.1 (**1999**), pp. 277–294. DOI: 10.1086/313271.

[TS00] **F.X. Timmes and F. Douglas Swesty**. "The Accuracy, Consistency, and Speed of an Electron-Positron Equation of State Based on Table Interpolation of the Helmholtz Free Energy". In: *The Astrophysical Journal, Supplement* **126**.2 (**Feb. 2000**), pp. 501–516. DOI: 10.1086/313304.

[Vin11] **Jorick S. Vink**. "The theory of stellar winds". In: *Astrophysics & Space Science* **336**.1 (**Nov. 2011**), pp. 163–167. DOI: 10.1007/s10509-011-0636-7. arXiv: 1112.0952 [astro-ph.SR].

[VKL01] **Jorick S. Vink, A. de Koter, and H. J. G. L. M. Lamers**. "Mass-loss predictions for O and B stars as a function of metallicity". In: *Astronomy & Astrophysics* **369**.2 (**2001**), 574–588. ISSN: 1432-0746. DOI: 10.1051/0004-6361:20010127.

[von24] **H. von Zeipel**. "The radiative equilibrium of a rotating system of gaseous masses". In: *Monthly Notices of the Royal Astronomical Society* **84** (**June 1924**), pp. 665–683. DOI: 10.1093/mnras/84.9.665.

Web Sources

[IR] **Carlos A. Iglesias and Forrest J. Rogers**. *Generate New Opal Opacity Tables.* https://opalopacity.llnl.gov, as accessed in 28/08/2021.

[Irw] **A. W. Irwin**. *FreeEOS.* http://freeeos.sourceforge.net/, as accessed in 28/08/2021.

[Mag] **N. H. et al. Magee**. *TOPS Opacities. Opacities of mixtures (calculated by TOPS using ATOMIC or LEDCOP elemental opacities).* https://aphysics2.lanl.gov/apps/, as accessed in 28/08/2021.

[Mar] **P. Marigo**. *ÆSOPUS: Low-temperature Rosseland mean opacities on demand.* http://stev.oapd.inaf.it/cgi-bin/aesopus, as accessed in 28/08/2021.